Combustion dynamics of premixed swirling flames with different injectors

Am Fachbereich Maschinenbau
an der Technischen Universität Darmstadt
zur
Erlangung des Grades eines Doktor-Ingenieurs (Dr.-Ing.)
eingereichte

Dissertation

vorgelegt von

Marco Gatti, M. Sc.

aus Bergamo, Italy

Berichterstatter:	Prof. Dr. A. Dreizler
Mitberichterstatter:	Prof. Dr. A. Sadiki
Mitberichterstatter:	Prof. Dr. T. Schuller
Tag der Einreichung:	28.12.2019
Tag der mündlichen Prüfung:	18.10.2019

Darmstadt 2019

D17

université PARIS-SACLAY

CentraleSupélec

TECHNISCHE UNIVERSITÄT DARMSTADT

NNT : 2019SACLC070

Thèse de doctorat

Combustion dynamics of premixed swirling flames with different injectors

Thèse de doctorat de l'Université Paris-Saclay
préparée à CentraleSupélec

École doctorale n°579 Sciences mécaniques et énergétiques, matériaux et géosciences (SMEMAG)
Spécialité de doctorat : Combustion

Thèse présentée et soutenue à Gif-sur-Yvette, le 18/10/2019, par

MARCO GATTI

Composition du Jury :

Bruno Renou Professeur, INSA-Rouen	Président
Laurent Gicquel Senior scientist, CERFACS	Rapporteur
James Dawson Professeur, NTNU	Rapporteur
Thierry Schuller Professeur, CentraleSupélec - IMFT/CNRS	Directeur de thèse
Clément Mirat Ingenieur de recherche, CentraleSupélec	Co-directeur de thèse
Amsini Sadiki Professeur, Technische Universität Darmstadt	Co-directeur de thèse
Andreas Dreizler Professeur, Technische Universität Darmstadt	Invité
Cameron Tropea Professeur, Technische Universität Darmstadt	Invité

Remerciements

This thesis is part of the CLEAN-Gas European Joint Doctorate and all the work done was possible thanks to the funding received from the European Union's Horizon 2020 research and innovation programme under the Marie Sklodowska-Curie grant agreement No 643134. I want to first thank all the people involved in the organization of the yearly meetings we had over the three years of thesis and particularly Isabella Branca for coordinating the project.

I want to thank all the members of the jury for accepting to review my thesis manuscript.
A big thank goes to my thesis directors, starting from Thierry Schuller, that four years ago let me start my Ph.D. at the EM2C Laboratory, despite my lack of knowledge of any laboratory equipment at all. He has always been supportive and comprehensive, even in those moments when it would have been easier to be angry or disappointed. Most of all, I appreciated his enthusiastic approach to bring out the best in each of his students. I thank Clément Mirat for the great help that he gave me to solve all the technical problems I encountered. He taught me all the aspect of conducting laboratory experiments and he was always available when I needed help. I also thank Laurent Zimmer for teaching me laser diagnostics, from application to post-processing. I really valued the chance to work with such an expert in this field. I want to thank Prof. Amsini Sadiki for welcoming me at TU Darmstadt during my secondment period in Germany and for the fruitful discussions we had about my manuscript.

Renaud Gaudron was the person I spent most of my time with during my three years at the EM2C laboratory, considering that we shared both the same experimental room and the same office. I have to and I am very happy to thank him, not only for his guidance during my first weeks at the lab, for showing me a lot of interesting engineering tricks, for teaching me a bit of the french language, for a lot of interesting discussion related and not related to the job, for the help he gave me in preparing articles and presentation for conferences, but mostly for coping with me despite my terrible taste in music.

None of the work done in this thesis would have been possible without the help from all the technical and administrative staff of the EM2C laboratory, that

deserve a great thank.

I also want to thank all the researchers and Ph.D. students of the EM2C laboratory and at TU Darmstadt, for creating such good workplace environments.

At last, the biggest thanks of all goes to my family, for having supported me during all these years. In particular I want to thank Gloria for having followed me in France, quitting her job and family to share this experience with me. I will make anything I can to be sure she will never regret this choice.

Abstract

Lean premixed (LP) combustors, burning mixtures of natural gas and air at an equivalence ratio well below the stoichiometric value, are one of the best known technologies for the reduction of green house gases emissions and pollutant emission levels from the combustion of fossil fuels. Unfortunately, these technologies are highly sensitive to dynamical phenomena. Performance improvement of LP systems has been hindered for many years now by their susceptibility to lean blowout, flashback and combustion instabilities. Most LP gas turbine combustors use swirling flows to stabilize compact flames for efficient and clean combustion at high power densities. A better knowledge of the mechanisms of unsteady combustion of lean premixed swirled mixtures is then of practical as well as fundamental interest.

The Noisedyn burner was specifically designed during this work to fulfill this objective. The geometry of this burner can easily be modified to test the effects of a series of modifications of the injection unit on the combustion properties. Among these, the effects of an annular swirling vane and a central bluff body are scrutinized. The analysis starts by examining the effects of the radial swirling vane for the injection units equipped with the central bluff body.

The swirl number S is known to control the topology of the swirling flow and, in this respect, it also controls flame stabilization. For a low level of swirl ($S < 0.50$ in this work), flames are close to blowoff with an elongated shape, while for an excessive swirl level ($S > 0.80$), the risk of flashback increases drastically. For intermediate swirl numbers, well-stabilized compact flames were obtained.

The swirl number S also largely determines the response of swirling flames to acoustic perturbations. It is shown that at low swirl levels, the Flame Transfer Function (FTF) approaches that of wedge flames, with large gain values exceeding unity at low frequencies. As the swirl level increases, the FTFs are characterized by a saw tooth pattern, with a maximum response directly followed by a large drop in the same frequency range. It is also shown that a regular reduction of the minimum flame response is obtained when the swirl number is progressively increased, up to a threshold level above which flashback triggered by the acoustic forcing is observed for highly swirled flames. Modifica-

tions of the bulk flow velocity or of the axial position of the swirling vane, with a constant swirl number, lead to a shift of the frequencies at which the FTF gain extrema are observed, but don't change the FTF values at these extrema. These information are used to rescale the FTF of swirled flames as a function of a Strouhal number, based on the bulk flow velocity and on an effective length including the flame length and the swirler-to-injector-outlet distance.

It is shown that a proper tuning of the modifications of the injection unit, along with modifications of the acoustic properties of the combustion chamber, e.g. by a change of the length of the exhaust tube, is a way to passively control thermo-acoustic instabilities that are observed in the NoiseDyn combustor. In particular, when a strong instability is observed at a frequency corresponding to a high FTF flame response, the oscillations can be damped by adjusting the injection system to have a low flame response at that specific frequency.

The analysis proceeds by examining mechanisms leading to FTF maximum and minimum gain values, by conducting a detailed experimental and a numerical analysis of the flow and flame dynamics at these specific forcing frequencies. It is shown that the maximum response of swirled flames, stabilized by a central bluff-body, is controlled by the formation of large vortical structures in the external shear layer of the flow that later rollup the flame tip. At the minimum flame response, this mechanism of flame rollup around a vortex is strongly attenuated, mainly due to the absence of large vortical structures shed from the burner lip. It is demonstrated experimentally and confirmed by numerical simulations, that this is not the result of interfering mechanisms between the vortex growth and the flapping motion of the flame, since these vortical structures are already absent in the cold flow.

The cold flow dynamics is shown to be controlled by complex interactions between azimuthal vortical waves and acoustic longitudinal waves. These waves combine, leading to large swirl number fluctuations by well described mechanisms, but they also lead to a strong reduction of toroidal vortical structures of the cold flow response by a mechanism that remains to be fully elucidated. This, in turn, leads to the conclusion that the strong reduction of the FTF gain of swirled flames, stabilized by a central bluff body, is only the consequence of the cold flow injector dynamics. This opens the path to new ways of controlling the response of these flames.

The last contribution of this work is the examination of the role of the central bluff body in this process. Experiments are conducted for two flames featuring the same swirl level, equivalence ratio and bulk velocity, but while one is anchored on a central bluff body, the other is fully aerodynamically stabilized by removing this component and by slightly reducing the diameter of the injection tube. It is found that the strong reduction of the FTF gain observed

for the bluff-body swirled stabilized flame is not present in the FTF gain of the fully aerodynamically stabilized flame. It is shown, in this latter case, that the dynamics of the internal recirculation region, featuring large axial oscillations, drastically differs from the one of the bluff-body stabilized swirled flame. The formation of vortical structures in the external shear layer of the cold flow response is also strongly altered due to the oscillation of the central vortex bubble, indicating that the cold flow response of swirled injectors with and without central body also drastically differs.

As a conclusion, three main mechanisms determining the response of LP swirled flames to acoustic waves were identified in this work. They are all associated to the cold flow dynamics of the injection unit. The first one, leading to high FTF gains, is the formation of large toroidal vortical structures in the external shear layer of the swirled flow. The second one, possibly leading to reductions of the FTF gain, is the interference of longitudinal acoustic waves and azimuthal convective waves generated by the swirling vane and leading to large swirl number oscillations. The last one is the response of the internal recirculation bubble to acoustic forcing, that exhibits large axial displacements for aerodynamically stabilized flames. Controlling the dynamics of these three mechanisms, by analyzing the cold flow injector response to sound waves, appears as a promising way to shape the FTF of LP swirled flames.

Résumé

Les systèmes de combustion à prémélange pauvre (PP), qui brûlent du gaz naturel avec un excès important d'air par rapport à la stoechiométrie, sont l'une des technologies les mieux adaptées pour la réduction des émissions de gaz à effet de serre et des émissions de polluants résultant de la combustion de ressources fossiles. Malheureusement, ces technologies sont très sensibles aux phénomènes dynamiques. L'amélioration des performances des systèmes PP est entravée depuis de nombreuses années par leur vulnérabilité aux phénomènes d'extinction, aux retours de flamme (flashback) dans l'injecteur et aux instabilités de combustion. La plupart des chambres de combustion des turbines à gaz utilisent des vrilles pour mettre en rotation l'écoulement. On parle de tourbillonneurs ou de swirleurs pour stabiliser des flammes compactes et permettre une combustion efficace et propre avec des densités de puissance élevée. Une meilleure connaissance des mécanismes de la dynamique de la combustion d'écoulements swirlés PP présente un intérêt aussi bien pratique que fondamental.

Le brûleur Noisedyn a été spécialement conçu lors de ces travaux pour répondre à cet objectif. La géométrie de ce brûleur peut être facilement modifiée pour tester les effets d'une série de modifications du système d'injection sur l'état de la combustion. Parmi ceux-ci, les effets d'un swirleur annulaire et d'un insert sur l'axe de l'injecteur sont examinés. L'analyse débute par un examen des effets du swirleur radial équipant le système d'injection avec un insert central.

Le nombre de swirl S est connu pour contrôler la topologie de l'écoulement résultant et, à cet égard, il contrôle également la stabilisation de la flamme. Pour un faible niveau de swirl ($S < 0.50$ dans ce travail), les flammes prennent une forme allongée et sont proches de l'extinction, alors que pour un niveau de swirl excessif ($S > 0.80$), le risque de flashback augmente considérablement. Pour des nombres de swirl intermédiaires, des flammes compactes bien stabilisées sont obtenues dans le foyer Noisedyn.

Le nombre de swirl S détermine également largement la réponse des flammes swirlées aux perturbations acoustiques. Lorsque le niveau de swirl est faible, la fonction de transfert de flamme (FTF) se rapproche de celle d'une flammes

stabilisée dans le sillage de l'insert central avec des valeurs de gain élevées dépassant l'unité sur une large plage de basses fréquences. Au fur et à mesure que le niveau de swirl augmente, les FTF sont caractérisées par un motif en dents de scie, avec une réponse maximale directement suivie d'une chute importante de cette réponse dans la même gamme de fréquences. Il est également montré qu'une réduction régulière de la réponse minimale de la flamme est obtenue lorsque le nombre de swirl augmente progressivement, jusqu'à un niveau supérieur au seuil au-dessus duquel un retour de flamme dans l'injecteur déclenché par le forçage acoustique est observé pour les flammes fortement swirlées. Les modifications de la vitesse d'injection du mélange combustible ou de la position de l'aube tourbillonnante, tout en maintenant un nombre de swirl constant, produisent un décalage en fréquence des extrema de gain de la FTF sans modifier les valeurs de ces extrema. Ces informations sont utilisées pour redimensionner la FTF des flammes swirlées en fonction d'un nombre de Strouhal basé sur la vitesse d'injection et sur une longueur effective incluant la longueur de la flamme et la distance de la vrille à la sortie de l'injecteur.

Il est montré qu'un bon réglage de l'unité d'injection, ainsi que des modifications des propriétés acoustiques de la chambre de combustion, par exemple en changeant la longueur du tube d'échappement, permettent de réduire ou de déclencher des instabilités thermo-acoustiques observées dans la chambre de combustion NoiseDyn. En particulier, lorsqu'une forte instabilité est observée à une fréquence correspondant à une réponse élevée de la FTF, les oscillations peuvent être amorties en ajustant le système d'injection de sorte à obtenir une réponse faible de la FTF à cette même fréquence.

L'analyse procède ensuite à l'examen des mécanismes conduisant aux valeurs de gain maximum et minimum de la FTF grâce à une étude expérimentale et numérique fouillée de la dynamique de l'écoulement et de la flamme à ces fréquences de forçage spécifiques. On montre que la réponse maximale des flammes swirlées stabilisées par un insert central est contrôlée par la formation de grandes structures tourbillonnaires dans la couche de cisaillement externe du jet issu de l'injecteur. Ces structures sont convectées et enroulent ensuite la pointe de la flamme. Au minimum de réponse de la FTF, ce mécanisme d'enroulement de la flamme autour d'un vortex est fortement atténué, principalement en raison de l'absence de grandes structures tourbillonnaires libérées au niveau des lèvres du brûleur. Il est démontré expérimentalement et confirmé par des simulations numériques que cela n'est pas le résultat de mécanismes d'interférence entre la croissance du vortex et le mouvement de battement de la flamme, car ces structures tourbillonnaires sont également absentes dans l'écoulement sans réaction de combustion.

La dynamique de l'écoulement à froid est contrôlée par des interactions complexes entre des ondes de vorticité azimutales et des ondes acoustiques longi-

tudinales. La combinaison de ces ondes conduit à des fluctuations importantes du nombre de swirl par des mécanismes désormais bien décrits, mais elles entraînent également une forte réduction des structures tourbillonnaires toroïdales libérées dans l'écoulement par un mécanisme qui reste à élucider complètement. Ceci conduit à conclure que la forte réduction du gain de la FTF des flammes swirlées stabilisées par un corps central résulte uniquement de la dynamique de l'injecteur à froid. Modifier cette dynamique en agissant sur l'injecteur ouvre la voie à de nouvelles façons de contrôler la réponse de ces flammes.

La dernière contribution de ce travail consiste à examiner le rôle de l'insert central dans ce processus. Des expériences sont menées sur des flammes présentant le même niveau de swirl, la même richesse et la même vitesse d'injection du mélange combustible, mais l'une est ancrée sur le corps central de l'insert tandis que l'autre est stabilisée aérodynamiquement en retirant ce composant et en réduisant légèrement le diamètre du tube d'injection. On constate que la forte réduction du gain de la FTF observée pour la flamme stabilisée swirlée avec un insert central n'est pas présente dans les résultats pour la FTF de la flamme entièrement stabilisée aérodynamiquement. Il est montré dans ce dernier cas que la dynamique de la région de recirculation interne présente de grandes oscillations axiales et diffère radicalement de celle de la flamme stabilisée par le swirl et l'insert central. La formation de structures tourbillonnaires dans la couche de cisaillement externe du jet froid issu de l'injecteur est également fortement modifiée en raison de l'oscillation de la zone de recirculation centrale. Ces éléments indiquent que la réponse à froid d'injecteurs swirlées avec et sans corps central diffère également considérablement.

En conclusion, trois mécanismes importants ont été identifiés dans ce travail qui déterminent la réponse de flammes swirlées aux ondes acoustiques. Ils sont tous associés à la dynamique de l'écoulement à froid à travers le système d'injection. Le premier qui se traduit par des gains élevés de FTF est la formation de grandes structures tourbillonnaires toroïdales dans la couche de cisaillement externe du jet swirlé. Le second qui est associé à un processus de réduction de gain de la FTF sont des mécanismes d'interférence entre les ondes acoustiques longitudinales et des ondes de vorticité azimutales générées par le tourbillonneur, ce qui entraîne de fortes oscillations du nombre de swirl. Le dernier est la réponse de la bulle de recirculation centrale au forçage acoustique. Celle-ci présente de grands déplacements axiaux pour les flammes stabilisées aérodynamiquement. Contrôler la dynamique de ces trois mécanismes en analysant la réponse des injecteurs aux ondes sonores de l'écoulement à froid apparaît comme un moyen prometteur pour modeler la forme des FTF de flammes swirlées PP.

Zusammenfassung

Magervorgemischte (im Englischen, Lean Premixed (LP)) Brennkammern, in denen Erdgas und Luft in einem Äquivalenzverhältnis weit unter dem stöchiometrischen Wert verbrannt werden, sind eine der bekanntesten Technologien zur Reduzierung der Treibhausgasemissionen und der Schadstoffemissionen bei der Verbrennung fossiler Brennstoffe. Leider sind diese Technologien sehr empfindlich gegenüber dynamischen Phänomenen. Leistungs-verbesserung solcher LP Systeme wird seit vielen Jahren durch ihre Anfälligkeit für Blowout, Flashback und Verbrennungsinstabilitäten erschwert.
Die meisten LP-Gasturbinenbrenner verwenden verdrallte Strömungen, um kompakte Flammen effizient und better bei hohen Leistungsdichten zu stabilisieren. Bessere Kenntnis der Mechanismen der instationären Verbrennungsvorgänge in magervorgemischt verdrallten Flammen ist daher von großer praktischer Bedeutung.

In diesem Zusammenhang wurde der Noisedyn-Brenner im Rahmen dieser Arbeit speziell entwickelt. Dabei wurde der Brenner so konzipiert, dass leichte Änderungen der Injektor-Geometrie ermöglicht werden, um ihre Auswirkungen auf die Verbrennungseigenschaften zu evaluieren. Es wurden die Wirkung einer ringförmigen verdrallten Schaufel (Vane) und der Einfluss eines zentralen Staukörpers untersucht.

Zunächst wurde die Untersuchung der Effekte der radial verdrallten Schaufel der mit einem zentralen Staukörper ausgestatteten Injektionseinheit durchgeführt. Da die Drallzahl S die Topologie der verdrallten Strömung und in dieser Hinsicht auch die Flammenstabilisierung determiniert, wurde die Drallzahl variiert. Bei nidriegen Drallzahlen ($S<0.50$) brennen die Flammen nahe des Blowoffs und weisen eine löngliche Form auf. Bei sehr hohen Drallzahlen ($S>0.80$) nimmt die Gefahr eines Rückschlags/Flashbacks drastisch zu, während gut stabilisierte kompakte Flammen bei mäßigen Drallzahlen erhalten werden.

Die Drallzahl S bestimmt auch maßgeblich die Antwort der verdrallten Flammen auf akustische Störungen. Es konnte gezeigt werden, dass bei niedrigen Drallzahlwerten die Flammenübertragungsfunktion (im Englischen "Flame-Transfer-Function" (FTF)) nähert sich diejenige von Keilflammen mit großen

Verstärkungswerten über Eins bei niedrigen Frequenzen. Mit zunehmender Drallstärke zeichnen sich die FTF durch ein Sägezahnmuster aus, welche durch eine maximale Antwort charakterisiert ist, die unmittelbar durch einen starken Druckabfall im gleichen Frequenzbereich gefolgt wird. Es wurde auch festgestellt, dass eine regelmäßige Reduzierung der Flammenantwort erzielt wird, wenn die Drallzahl schrittweise bis zu einem Schwellenwert erhöht wird. Über diesen Wert wird ein Flashback ausgelöst, welcher durch eine akustische Anregung bei stark verdrallten Flammen zu beobachten ist. Die hier gewonnene Information wurde verwendet, um die FTF von verdrallten Flammen in Abhängigkeit von der Strouhal-Zahl auf der Grundlage der Strömungsgeschwindigkeit und einer effektiven Länge einschließlich der Flammenlänge und des Abstands zwischen dem Swirler und dem Injektorauslass neu zu skalieren.

Es wurde gezeigt, dass eine richtige Einstellung der Änderung der Injektoreinheit zusammen mit Modifikationen der akustischen Eigenschaften der Brennkammer, z. B. durch eine Änderung der Länge des Abgasrohrs, können thermoakustische Instabilitäten, die in der NoiseDyn-Brennkammer beobachtet wurden, passiv kontrolliert werden. Insbesondere wenn eine starke Instabilität bei einer bestimmten Frequenz beobachtet wird, die einer hohen FTF-Flammenantwort entspricht, können Oszillationen gedämpft werden, indem das Injektorsystem so eingestellt wird, dass es bei dieser spezifischen Frequenz eine niedrige Flammenantwort aufweist.

Diese Analyse wurde fortgesetzt, indem Mechanismen untersucht wurden, die zu maximalen und minimalen FTF-Werten führen. Hierzu wurden detaillierte experimentelle und numerische Analyse der Strömungs- und Flammendynamik bei diesen spezifisch erzwingenden Frequenzen durchgeführt.

Es wurde gezeigt, dass eine maximale Antwort der verdrallten Flammen, die durch einen zentralen Staukörper stabilisiert werden, durch die Bildung großer Wirbelstrukturen in der äußeren Scherschicht der Strömung gesteuert wird, welche sich später in die Flammenspitze entwicklen. Bei einer minimalen Flammenantwort wird dieser Mechanismus stark gedämpft, hauptsächlich aufgrund der nicht auftretenden großen Wirbelstrukturen. Experimentell wurde gezeigt, und durch numerische Simulationen bestätigt, dass das Ergebnis nicht von Interferenzmechanismen zwischen dem Wirbelwachstum und der Flappingbewegung der Flamme zurückzuführen ist, da die Wirbelstrukturen bereits in der kalten Strömung nicht auftreten.

Es wurde ferner gezeigt, dass die Dynamik der kalten Strömung durch komplexe Wechselwirkungen zwischen azimuthalen Wirbelwellen und akustischen Longitudinalwellen gesteuert wird. Zusammen führen diese Wellen durch gut beschriebene Mechanismen, zum einen, zu großen Schwankungen der Drallzahlen, und zum anderen, zu einer starken Reduzierung der toroidalen Wirbel-

strukturen der Antwort der kalten Strömung durch einen Mechanismus, der noch vollständig aufgeklärt werden muss. Es ließ sicht schlussfolgern, dass die starke Reduzierung der FTF-Verstärkung von verdrallten Flammen, die durch einen zentralen Staukörper stabilisiert wird, nur die Folge der Dynamik des Injektors der kalten Strömung ist. Dies öffnet den Weg zu neuen Möglichkeiten, die Antwort der Flammen zu kontrollieren.

Der letzte Beitrag dieser Arbeit bestand in der Untersuchung der Rolle des zentralen Staukörpers in diesem Prozess. Es wurden Versuche mit zwei Flammen durchgeführt, die den gleichen Drallgrad, das gleiche äquivalenzverhältnis und die gleiche Strömungsgeschwindigkeit aufweisen. Jedoch wurde eine Flamme an einem zentralen Staukörper verankert, während die andere Flamme durch Entfernen dieser Komponente und leichtes Verringern des Durchmessers des Einspritzrohrs vollständig aerodynamisch stabilisiert wurde. Es konnte festgestellt werden, dass die starke Verringerung der FTF-Verstärkung, welche für die durch Staukörper verdrallt stabilisierte Flamme beobachtet wurde, bei der vollständig aerodynamisch stabilisierten Flamme nicht stattfindet.

In diesem letzteren Fall wurde gezeigt, dass die Dynamik des internen Rezirkulationsbereichs, der große axiale Schwankung aufweist, unterscheidet sich drastisch von derjenigen der mit Staukörpern stabilisierten Drallflamme. Die Bildung von Wirbelstrukturen in der äußeren Scherschicht verändert sich stark aufgrund der Oszillation der zentralen Wirbelblase, was darauf hinweist, dass sich die Antwort der kalten Strömung aus den verwirbelten Injektoren mit und ohne Zentralkörper ebenfalls drastisch unterscheidet.

Zusammenfassend wurden in dieser Arbeit drei Hauptmechanismen identifiziert, die die Antworte von LP-Flammen auf akustische Wellen bestimmen. Sie hängen alle mit der Dynamik der kalten Strömung der Injektoreinheit zusammen. Die erste, die zu hohen FTF-Verstärkung führt, ist die Bildung großer toroidaler Wirbelstrukturen in der äußeren Scherschicht der verdrallten Strömung. Die zweite, die möglicherweise zu einer Verringerung der FTF führt, ist die Interferenz von longitudinalen akustischen Wellen und azimuthalen Konvektionswellen, die von der Wirbelschaufel erzeugt werden und zu Schwankungen mit großer Drallzahl führen. Die letzte ist die Antwort der internen Rezirkulationsblase auf akustische Störungen, die große axiale Verschiebungen für aerodynamisch stabilisierte Flammen aufweisen. Das Kontrollieren der Dynamik dieser drei Mechanismen durch eine Analyse der Antwort des kalten Strömungsinjektors auf akustischen Wellen scheint eine vielversprechende Möglichkeit zu sein, die FTF von LP verdrallten Flammen zu modellieren bzw. zu formulieren.

Contents

Introduction

Context

Between 1971 and 2015, the world energy production and consumption more than doubled (IEA, 2017a). The development of renewable energy sources remains too slow and the combustion of fossil fuels still accounts for more than 80% of this production in 2015 (Fig. 1) and this trend is not expected to abruptly change in the next decades (IEA, 2017b). A well known drawback of the combustion of hydrocarbon fuels is the production of greenhouse gases, since carbon dioxide CO_2 is the main product of the combustion reaction, together with water vapor. Combustion also produces traces of other pollutants, like unburned hydrocarbons HC, nitric oxides NO_x and carbon monoxide CO.
The requirements to reduce pollutant emissions are more and more stringent and actions against the climate change trend, caused by fossil fuel burning, are urgently needed. On 12 December 2015, as an outcome of the 2015 United Nations Climate Change Conference, the 196 countries involved signed the Paris Agreement. For the first time, all the nations involved were brought into a common cause to undertake ambitious efforts to combat climate change and adapt to its effects. The central aim is to strengthen the global response to

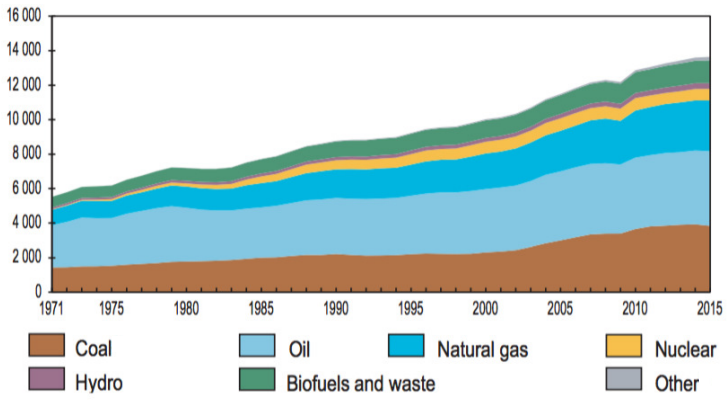

Figure 1: *World total primary energy supply by fuel (Mtoe) from 1971 to 2015. Adapted from IEA, 2017a.*

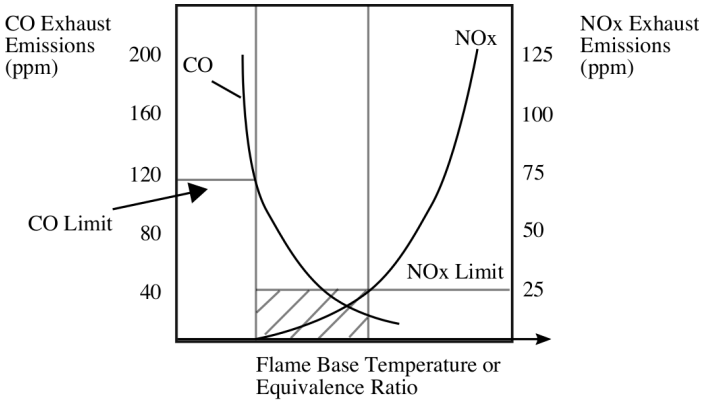

Figure 2: *Typical CO and NOx production from lean premixed combustion of methane. Adapted from Brown, D., 1995.*

the threat of climate change, by keeping a global temperature rise this century well below 2 degrees Celsius above pre-industrial levels and to pursue efforts to limit the temperature increase even further to 1.5 degrees Celsius.
In this sense, the advantages of natural gas compared to other fossil fuels are well known. For example CO_2 emissions (per unit of Joule produced) from natural gas are on average around 40% lower than coal combustion and around 20% lower than burning of oil (IEA, 2016). Due to this environmental benefits and also to its widespread availability, the share of natural gas among other fossil fuels has increased in these last decades, as illustrated in Fig. 1.

To cope with the increasingly strict regulations for pollutant emissions, with particular attention to NO_x production (Correa, 1993; Bahr, D, 1996), the gas turbine industry moved towards new combustion technologies, e.g. staged combustion, oxy-fuel combustion or flameless combustion. Among these technologies, lean premixed (LP) combustion offers several advantages. In LP systems, fuel and air are premixed before entering the burner at a well controlled equivalence ratio, to avoid the formation of stoichiometric regions. The combustion zone is operated with a large excess of air, with respect to stoichiometric values, to reduce the flame temperature. The typical evolution of main pollutant formations for a lean mixture of methane, which is the main compound of natural gas, and air is shown in Fig. 2. NO_x and CO emissions follow opposite trends. On one hand, at low flame temperatures or equivalence ratios, NO_x production is low, but it then increases exponentially with temperature. On the other hand low temperatures prevent the complete oxidation of CO and generate unburned HC. In an ideal case, one tries to drive the system towards the optimum point where both CO and NO_x levels will be minimum. In an industrial context, the objective is to cope with emission limits imposed by the legislation, but one is limited by the machine performance that needs to deliver the desired power, preserve the components integrity and be as versatile as possible. Therefore,

the control system has to operate the combustor in a range of equivalence ratios avoiding the rapid increase of CO and NO_x (Docquier and Candel, 2002) among many other factors altering its behavior.

Lean premixed swirled injectors

The stabilization of flames in LP systems and many other modern combustion systems is achieved by imparting an azimuthal component to the flow, usually by passing the air or the combustible mixture stream through a swirling vane or a set of swirlers (Candel et al., 2012). The swirl intensity is usually characterized by the swirl number S, defined as the ratio of the axial flux of the tangential momentum to the product of the axial momentum flux and a characteristic radius R of the injector (Gupta et al., 1984). By neglecting the pressure term in the axial momentum flux (Beer and Chigier, 1972), the swirl number is defined as:

$$S = \frac{1}{R}\frac{\int u_\theta u_z r^2 dr}{\int u_z^2 r dr}. \tag{1}$$

where u_z and u_θ are the axial and azimuthal velocity components, r the radius and R a characteristic outer radius. When a sufficient amount of rotation is imparted to the flow, a high adverse axial pressure gradient is achieved which leads to a flow reversal and generates a Central or Inner Recirculation Zone (IRZ) (Huang and Yang, 2009). Figure 3 shows a comparison of the streamline patterns and mean temperature fields of a low ($S < 0.6$) and an high ($S > 0.6$) swirling flame. In both cases, an Outer Recirculation Zone (ORZ) is present due to the sudden expansion of the cross section area when the flow leaves the burner and enters the combustion chamber. In the low-swirl number case with $S = 0.44$ in Fig. 3, the recirculating flow in the central region is mainly due to a small wake recirculation zone (WRZ) behind the bluff-body. In the absence of swirl, only these two zones would exist. With the addition of swirl, vortex breakdown takes place (Fig. 4) for a sufficiently large swirl level and leads to the formation of the IRZ.

As the swirl number exceeds a threshold, generally taken equal to $S > 0.60$ (Lucca-Negro and O'Doherty, 2001), the inner recirculation zone IRZ moves upstream and merges with the wake recirculation zone WRZ. The flow region of vortex breakdown provides the dominant flame stabilization mechanism. Thanks to this mechanism, LP systems can sustain compact flames in high speed flows even under lean conditions (Huang and Yang, 2005).

Dynamical phenomena, however, hinder the performance of combustors equipped with swirled injectors. At first, these systems are often operated near the lean blowoff limit, meaning that a small fluctuation of the flowrate could cause

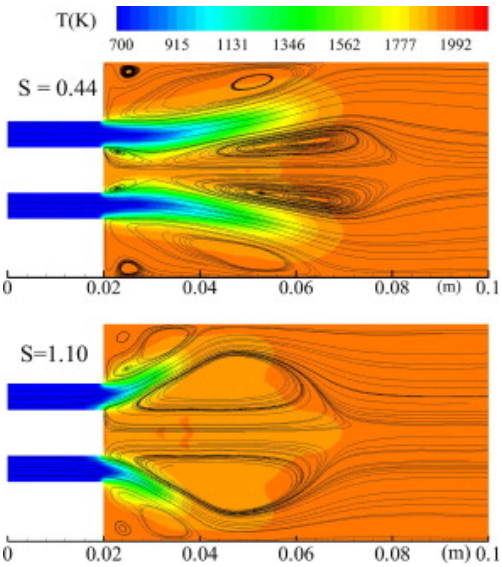

Figure 3: *Mean temperature fields and streamline patterns for two different swirl numbers. Reproduced from Huang and Yang, 2005.*

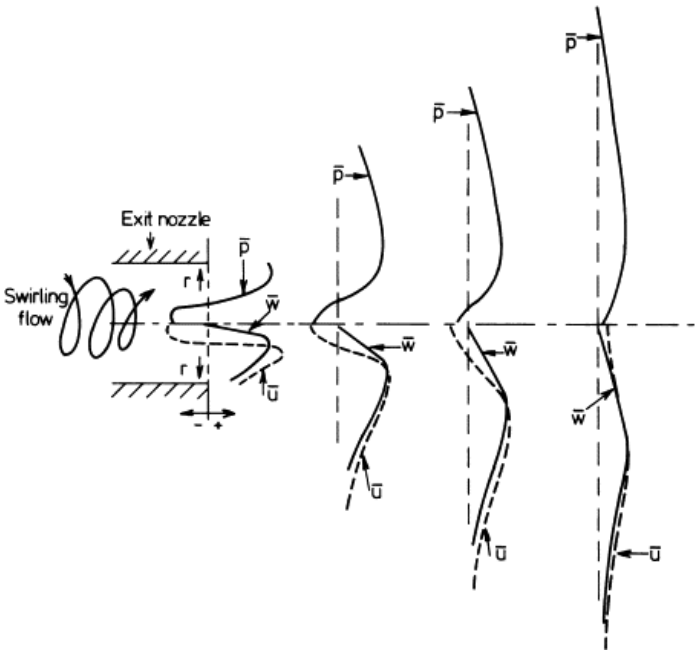

Figure 4: *Schematic diagram of processes leading to the formation of an IRZ: large tangential velocities create a centrifugal pressure gradient and sub-atmospheric pressure near the central axis; axial decay of tangential velocity causes decay of radial distribution of centrifugal pressure gradient in axial direction; thus, an axial pressure gradient is set up in the central region towards the swirl burner, causing reverse flow. Reproduced from Syred, 2006.*

flame extinction. Secondly, when operated at larger equivalence ratios, a small flow oscillation could cause the IRZ to enter the injector, possibly resulting in flame flashback. Among these problems, that of combustion instabilities has drawn a considerable amount of attention since last century (Crocco, 1951) and still constitutes a difficult challenge for designers (Keller, 1995; Lieuwen and Zinn, 2005; Poinsot, 2017). LP systems are particularly prone to this problem. One of the major differences in design, between lean-premixed and diffusion-flame type combustion systems, is the absence in the former of perforated liners around the combustor (Candel et al., 2012). In diffusion controlled combustion burners, a substantial fraction of air enters through the liner. This not only help in decreasing the temperature of the combustion products before entering the turbine, but also serves as damping of acoustic waves (Keller, 1995). Acoustic damping is reduced in LP systems because the perforated liners are mostly eliminated in modern premixed combustors, increasing their sensitivity to acoustic feedback and combustion instabilities.

Combustion instabilities

Extensive review of combustion instability phenomena can be found in the literature, from fundamental mechanisms (Candel, 2002) to application for real engines (Poinsot, 2017). Only a very brief presentation is provided in this section, while readers are referred to these references and to the textbooks from Lieuwen and Yang, 2005 and Poinsot and Veynante, 2005 for more details.
Thermoacoustic instabilities results from the complex dynamic interactions between acoustic waves and unsteady heat release (Fig. 5). When the heat release is provided by combustion, they are also designated as combustion instabilities. They can cause structural vibrations, augmented heat fluxes to the chamber walls, flame quenching or flashback and often lead to severe damage (Lieuwen and Yang, 2005). Combustion instabilities can appear in almost any combustion system and have been observed in the development of propulsion systems, like liquid rocket engines, solid rocket motors, ramjet and scramjet engines and many domestic and industrial boilers or furnaces (Huang and Yang, 2009).

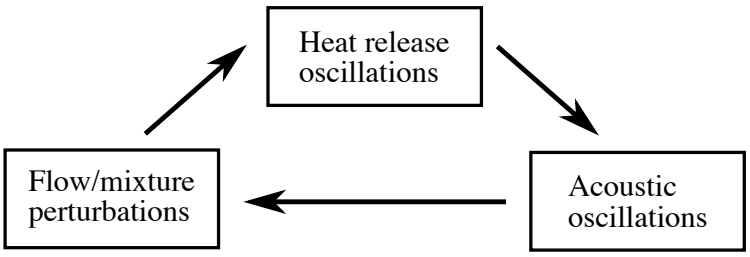

Figure 5: *Feedback loop between acoustics and combustion leading to combustion instabilities. Adapted from Lieuwen and Zinn, 2005.*

This phenomenon has been known for more than a century. Rayleigh, 1878, first stated the conditions under which unsteady heat release adds energy to the acoustic field: if heat is released when a pressure oscillation is near its maximum, the pressure fluctuation increases in amplitude; on the other hand, if heat release occurs when the pressure oscillation is at a minimum point, the pressure fluctuation is attenuated. This is a necessary but not sufficient condition for combustion instabilities to arise, since the energy added to the acoustic field by combustion must overcome that dissipated within the burner and/or transmitted through its boundaries (Cantrell and Hart, 1964). Mathematically, this criterion can be expressed as an acoustic energy balance (Dowling and Morgans, 2005; Nicoud and Poinsot, 2005; Durox et al., 2009; Brear et al., 2012):

$$\frac{\gamma-1}{\rho c^2}\frac{1}{T}\int_V\int_T p'\dot{q}'dtdV \geq \frac{1}{T}\int_{\partial V}\int_T p'u'dtdS + \frac{1}{T}\int_V\int_T \zeta_a dtdV \tag{2}$$

where p', u', $\dot{q}'$, V, ∂V, T and ζ_a are, respectively, the acoustic pressure, velocity and volumetric rate of heat-release oscillations, volume and volume boundaries, period of oscillations, and acoustic energy loss processes within the flow (see Howe, 1998).

Pressure fluctuations indirectly lead to perturbations of the heat-release through three main mechanisms (Ducruix et al., 2003):

- Equivalence-ratio oscillations: this can happen when the air and fuel injection line respond differently to the pressure perturbation. A mixture of oscillating equivalence ratio is then convected to the flame producing the heat-release oscillation. This mechanism does not concern fully premixed systems featuring a common air-fuel injection line.
- Flame surface variation: pressure perturbations are associated with acoustic velocity oscillations that modify the flame surface and thus the heat release.
- Flame-vortex interaction: when the acoustic velocity oscillation reach the burner rim, vortical structures are generated and then convected towards the flame. The interaction rapidly changes the flame surface area and thus the heat release.

Some methods were developed during the years to suppress or attenuate combustion instabilities and can be divided into active or passive (McManus et al., 1993; Candel, 2002; Lieuwen and Yang, 2005).
In active control techniques, the instability is dynamically detected and corrected using a feedback control loop to modify one or more input parameters. Passive control involves changes of fuel or geometry designs (for example, in the composition or types of reactants, fuel injection devices and chamber geometry, or the installation of acoustic dampers), either to reduce the rate at which energy is transferred to unsteady motions (reduce the left term in Eq. (2)), or

to increase losses of energy (increase the right term in Eq. (2)), such as by the use of suitable resonators to introduce a dissipative process.
One of the earliest examples of passive control was applied during the development of the F1 rocket engine (Oefelein and Yang, 1993). The strong instabilities observed during the design process were eventually suppressed by substantial modifications of the injection system geometry. But this was obtained after a costly trial and error process with almost 2000 full-scale tests.
Much progress has been made in the field of combustion instabilities since that experience. It is nowadays possible to predict the thermoacoustic stability of practical systems, at a limited computational cost, by combining descriptions of the burner acoustic field with that of the combustion response (Dowling and Stow, 2003; Sattelmayer and Polifke, 2003; Nicoud et al., 2007; Noiray et al., 2008) even in systems featuring multiple burners such as annular combustors (Laera et al., 2017) and in real annular engines (Bothien et al., 2015).
The main issue in these different descriptions of the combustor dynamics remains that of providing a proper representation of the response of the flame to acoustic waves.

Flame Transfer Functions

In many low-order models used to predict stability maps of combustion systems, the flame frequency response to acoustic waves can be described by a flame transfer function FTF. If one restricts the analysis to fully premixed systems at constant equivalence ratio, the FTF defines as (Ducruix et al., 2003):

$$\mathcal{F}(f) = \frac{\dot{Q}'/\overline{\dot{Q}}}{u'/\overline{u}} = G(f)\exp(i\varphi(f)) \tag{3}$$

The FTF relates the heat release rate fluctuations to incoming acoustic modulations, as function of the excitation frequency f. It is often expressed as a complex number, in terms of a gain G and a phase difference φ. In the case of complete premixed combustion with constant mixture equivalence ratio, the flame surface A and light emission I are directly proportional to the heat release rate (Hurle et al., 1968; Schuller et al., 2002) and one may write (Ducruix et al., 2000):

$$\mathcal{F}(f) = \frac{A'/\overline{A}}{u'/\overline{u}} = \frac{I'/\overline{I}}{u'/\overline{u}} = G(f)\exp(i\varphi(f)) \tag{4}$$

The FTF of swirling flames can be measured experimentally (Kulsheimer and Buchner, 2002; Kim et al., 2010a) or obtained numerically through Large Eddy Simulations (LES) (Freitag and Janicka, 2007; Komarek and Polifke, 2010; Merk et al., 2018a). Attempts were also made to theoretically model this response (Borghesi et al., 2009; Palies et al., 2011d; Han and Hochgreb, 2015). In this work, we will concentrate more on experimentally determined FTFs.

From a practical point of view, following Eq. (4), it is possible to measure FTFs by determining the mean $\overline{I}$ and fluctuating I' flame luminosity, by gathering light from the whole combustion region and then comparing these signals with a reference velocity (see Durox et al., 2009).

Once the FTF is determined, its combination with a description of the system acoustics let one determine eigenmodes and growth rates of an eventual instability (Dowling, 1995). This linear analyses is unfortunately restricted to small perturbations and cannot account for the limit cycle oscillations observed in many experiments. To overcome this issue, one has to substitute the FTF with its non-linear extension, the flame describing function FDF (Dowling, 1999). In this new expression, the gain G and phase lag φ depend on both the frequency f and the amplitude $|u'|$ of the perturbation (Noiray et al., 2008):

$$\mathcal{F}(f,|u'|) = \frac{\dot{Q}'/\overline{\dot{Q}}}{u'/\overline{u}} = G(f,|u'|)\exp(i\varphi(f,|u'|)) \tag{5}$$

Examples of experimentally determined FDFs are reported in Fig. 6 for a non-swirling V-flame (left, Durox et al., 2005) and for a swirling flame (right, Palies et al., 2010a). It is first evident that non linearities appear in both cases as the amplitude level $|u'|$ increases. For the laminar V-flame in Fig. 6-left, it is even difficult to define a linear regime for the flame response (Schuller et al., 2003). One also note that for these fully premixed systems, nonlinearities are

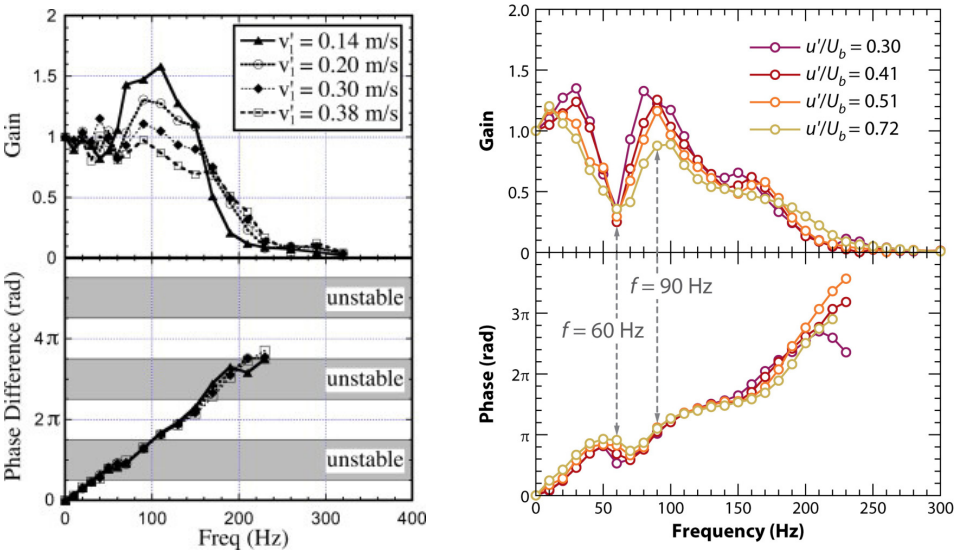

Figure 6: *Flame describing function measurements for a non-swirling (left, Durox et al., 2005) and a swirling flame (right, Palies et al., 2010a) anchored on a central bluff body.*

restricted to the gain of the FDF (Candel et al., 2014). As the forcing level increases, the gain of the FDF decreases due to saturating mechanisms (Lee and Santavicca, 2003; Balachandran et al., 2005; Bellows et al., 2006; Oberleithner et al., 2015). On the other side, the phase difference between velocity and light intensity signals evolves almost linearly with frequency, independently of the forcing level.

An important difference between non-swirling and swirling flames, is evident from the comparison of FDF shapes. The FDF gain of non-swirling V-flames behaves as a low-pass filter, with a large frequency range over which the gain exceeds unity (Schuller et al., 2003). It then regularly decreases towards zero for increasing frequencies. The FDF of swirling flames is characterized by an alternating behavior of the gain with maximum and minimum values and by an inflection point in the phase lag curve around the frequency where the gain features a minimum value ($f = 60$ Hz in Fig. 6-right). It is also observed, that the non linearity is strongest at the FDF gain maximum frequencies, while it is almost suppressed at the gain minimum frequency for swirling flames.
These different responses are the consequence of different mechanisms acting for non-swirling and swirling flames. It is worth remembering that both the non swirling flame in Fig. 6-left and the swirling flame in Fig. 6-right are anchored on a central insert in the burner.

Overview of the main mechanisms controlling the flame response to acoustic perturbations

Flame transfer functions FTF and flame describing functions FDF are very powerful concepts for engineers to determine the system dynamics and the trajectories of unstable modes, but they do not give access to any qualitative information about the physical mechanisms resulting in this flame response. An improved comprehension of the mechanisms of unstable combustion in lean premixed burners is still needed for the development of robust systems. To accomplish this task, FTF/FDF measurements should be completed by supplementary diagnostics or numerical simulations analyzing the flame motion or, when possible, by proper modeling of the flame response. Several research groups have put an effort into this direction. In the following, a brief overview of the main mechanisms altering the flame response to acoustic perturbations is presented. We consider only results referring to fully premixed systems, without considering fluctuations of the equivalence ratio (Lieuwen and Zinn, 2005), and where only one flame is stabilized in the combustion chamber, like those studied in this work.

Non-linear flame-vortex interactions

One of the first experimental efforts, dedicated to the characterization of the non-linear response of swirl-stabilized flames to flow perturbations and to the exploration of the underlying mechanisms for saturation, is that of Bellows et al., 2007. They performed experiments on an atmospheric, swirl-stabilized burner, sketched in Fig. 7. The acoustic oscillations were provided by two loudspeakers mounted in the inlet section. Acoustic velocity disturbances were deduced using the two microphone method (Abom and Boden, 1988). The relative magnitude of the combustion heat release rate oscillations were obtained from global CH* chemiluminescence measurements, with a photomultiplier fitted with a 10 nm bandwidth filter centered at 430 nm. OH planar laser-induced fluorescence (PLIF), was also used to obtain instantaneous two-dimensional slices of the flame and analyze the flame motion in an axial plane of the burner. Bellows et al., 2007 don't provide full data for the FTF in their measurements. They chose to focus on two conditions leading to a non-linear flame response.

For a forcing frequency $f = 130$ Hz, they observed a linear behavior of the flame response up to a forcing amplitude u'/u_0 of nearly 100%, as shown in Fig. 8-left. A significant amplitude dependence of the phase-lag curve between the u' and CH*' signals was in this case also observed. Saturation takes place at a much lower amplitude for $u'/u_0 \simeq 0.35$, when the flow is forced at $f = 410$ Hz. Figure 8-right shows that, in this second case, the phase-lag is almost independent of the forcing level. Figure 8 thus indicates that the nonlinear dynamics of swirled flames could be very complex.

The mechanisms leading to this flame response were analyzed with OH PLIF images of the flame motion at the two forcing frequencies. Results are reported

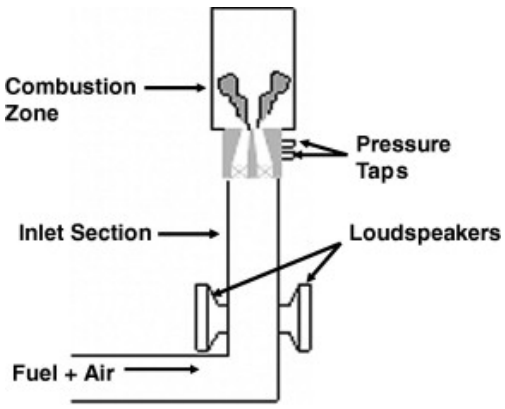

Figure 7: *Schematic of the swirl-stabilized combustor used in the analysis of Bellows et al., 2007.*

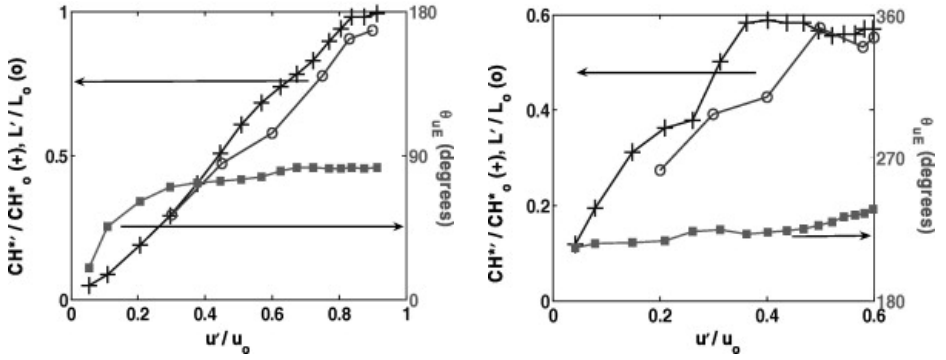

Figure 8: *Dependence of CH* oscillation amplitude and length, L, of the flame front, and u'-CH*' phase angle upon velocity oscillation amplitude. Left: $f = 130$ Hz. Right: $f = 410$ Hz. Reproduced from Bellows et al., 2007.*

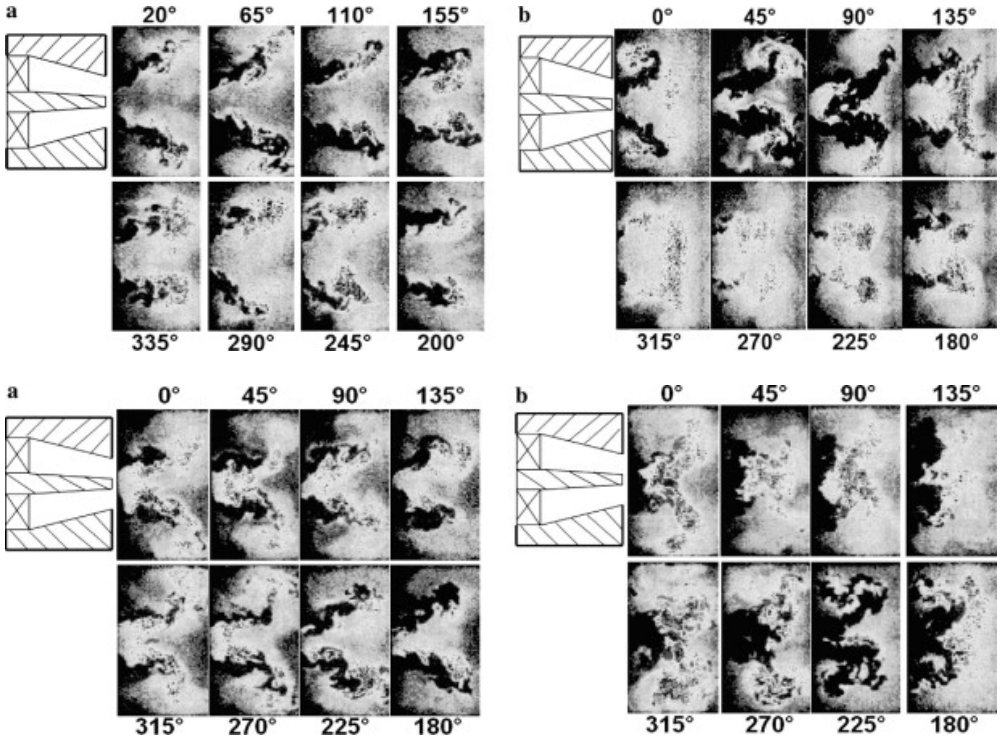

Figure 9: *Instantaneous OH PLIF images showing evolution of flame dynamics over one cycle of acoustic forcing for (a) low and (b) high velocity oscillation amplitudes. Top: $f = 130$ Hz. Bottom: $f = 410$ Hz. Reproduced from Bellows et al., 2007.*

in Fig. 9. At a frequency of $f = 130$ Hz, they identified flame-vortex interaction as a main mechanism for non-linearity. The consequent roll-up of the flame causes a very rapid reduction in its area and, therefore, in heat release rate, as already demonstrated for laminar non swirling V-flames (Durox et al., 2005). The flame heat release response does not increase proportionally with

the velocity perturbation amplitude, and saturation occurs. The same type of mechanism was observed for non-swirling flames, as previously reported by Balachandran et al., 2005 for turbulent V-flames and Durox et al., 2005 for laminar V-flames.
A different mechanism was identified at a forcing frequency $f = 410$ Hz. At this frequency, non-linearities were triggered by an oscillation of the internal recirculation region, causing an unsteady liftoff of the flame, with a consequent reduction of its area (Fig. 9-bottom).

A similar analysis was conducted by Paschereit's group at TU Berlin. The atmospheric combustor test rig used for their investigation is shown schematically in Fig. 10 and fully described in Schimek et al., 2011. The combustor was run in a perfectly premixed mode, with a fixed equivalence ratio of $\phi = 0.70$.
FDF measurements are presented for forcing frequencies between 50 and 400 Hz in Oberleithner et al., 2015 and reported in Fig. 11. The acoustic forcing was provided by two loudspeakers. The OH*-chemiluminescence was in this case preferred to determine the heat release rate. It was measured by a photomultiplier with a 307 nm band-pass filter. The velocity fluctuation was measured with a 2-component LDV system (Fig. 10). The FDF displayed in Fig. 11 shows a strong non-linear behavior with respect to the forcing amplitude. The saturation of the flame response is most emphasized around the peak frequency of the linear (or low amplitude forcing) FTF, indicating that the mechanism that causes this peak becomes increasingly less effective with higher forcing amplitudes. The FTF phase-lag in Fig. 11-b, is here again found to be almost independent of the forcing level and confirms many other experiments (Palies et al., 2011c). The fact that a different behavior is observed in the study of Bellows et al., 2007 might be due to the use of the CH* radical, which is more sensitive to soot observation than OH* emission, to detect heat release rate fluctuations.

The saturation process was further investigated by forcing the flame at different amplitudes at the constant frequency of $f = 254$ Hz and by OH* imaging and PIV measurements of the flow and flame responses. Figure 12 shows results at different forcing amplitudes. An isocontour of the Q criterion is superimposed onto the phase-averaged OH* images highlighting the development of coherent flow structures during one forcing cycle. A vortex ring is generated at the outer edge of the burner mouth, it propagates along the outer shear layer, it impinges on the flame and roll-up its tip. As Bellows *et al.*, these authors identify flame-vortex interaction as one of the leading mechanism for the non-linear response of swirling flames.

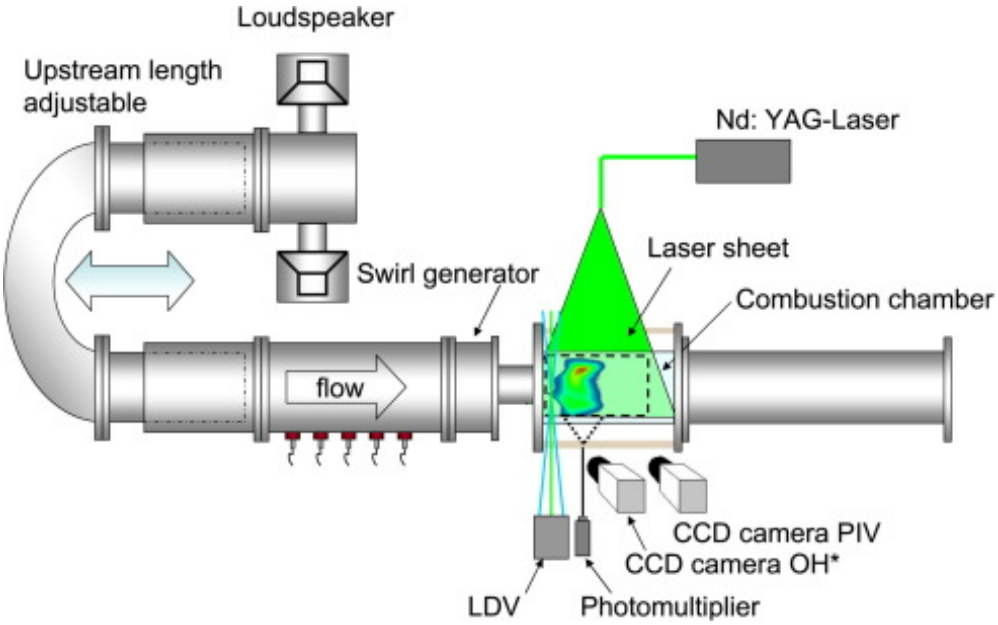

Figure 10: *Test rig used at TU Berlin with measurement devices. Reproduced from Schimek et al., 2011.*

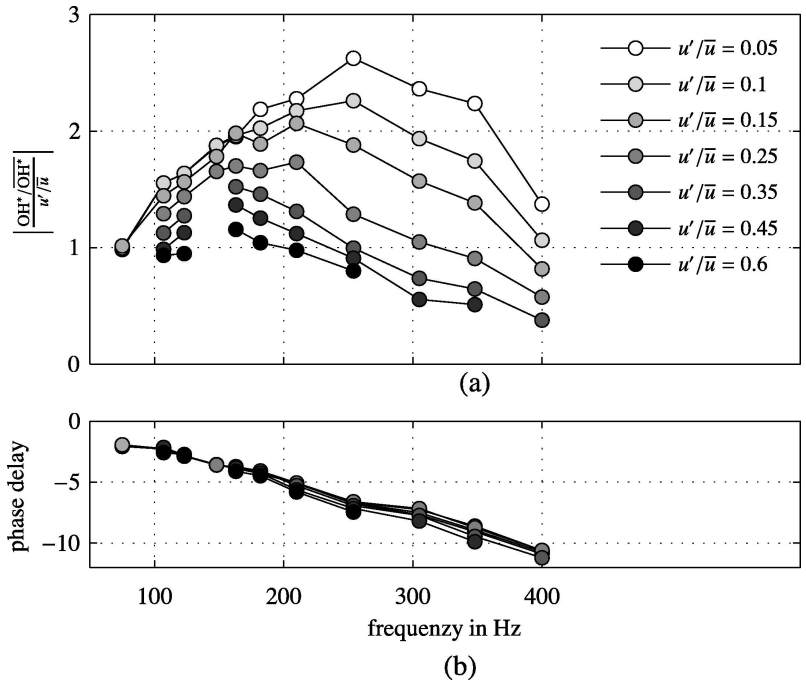

Figure 11: *(a) Amplitude of the flame describing function (FDF) of the perfectly premixed swirl-stabilized flame. (b) Phase delay between the inlet perturbation and the global heat release rate fluctuation. Reproduced from Oberleithner et al., 2015.*

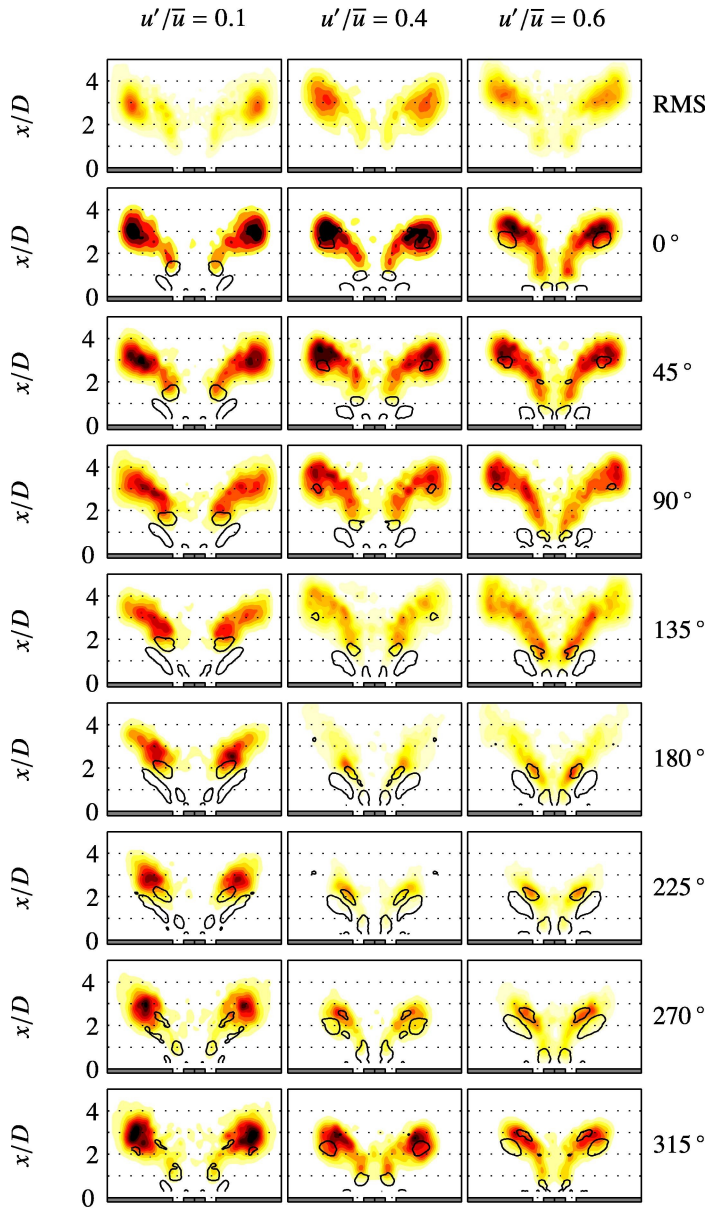

Figure 12: *Color-coded contours of the phase-averaged OH* images of the flame forced at 254 Hz. The contour lines represent an isocontour of the Q-criterion derived from phase-averaged PIV snapshots. The first row shows the root mean square of the OH* fluctuations indicating regions of highest heat release rate fluctuations. Reproduced from Oberleithner et al., 2015.*

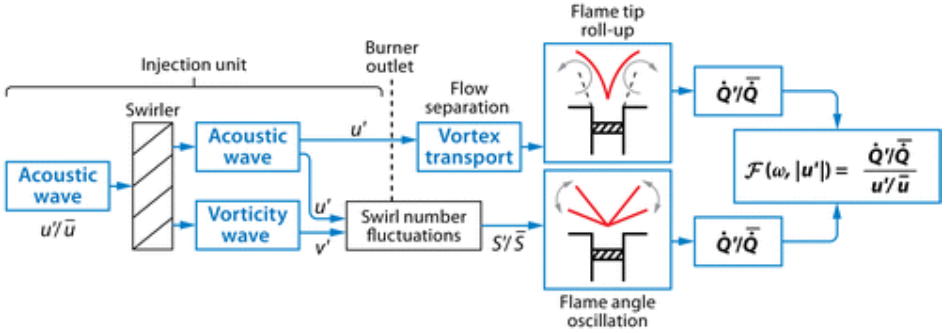

Figure 13: *Block diagram representation of mechanisms generating heat release rate fluctuations in swirling flows. Reproduced from Candel et al., 2014.*

Swirl fluctuations

Another important mechanism, which is at the origin of the differences observed in Fig. 6 between the responses of non-swirling and swirling flames, is the interference between acoustic and azimuthal convective perturbations.
Let us consider the schematic in Fig. 13. When an acoustic wave impinges on a swirler, on the downstream side of the swirler, one still finds a transmitted acoustic wave, but also a generated vorticity wave. These two waves travel at a different speed, the former being acoustic in nature and thus travelling at the local speed of sound, the latter being convective in nature and thus travelling at the local mean flow speed. The interaction between these acoustic and convective perturbations eventually give rise to swirl number oscillations (Palies et al., 2011a).

Komarek and Polifke, 2010 specifically designed an experimental setup to analyze the impact of fluctuations of the swirl number on the heat release rate of a fully premixed flame. Figure 14 shows a sketch of the experimental setup they used. The burner featured an axial swirl generator with variable axial position.

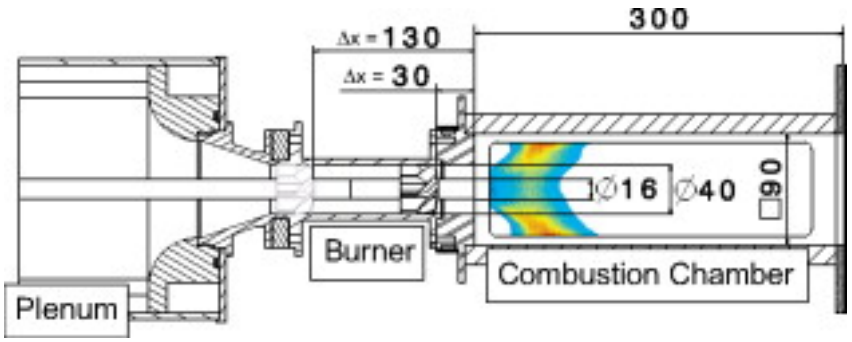

Figure 14: *Sketch of the burner used for the analysis of Komarek and Polifke, 2010.*

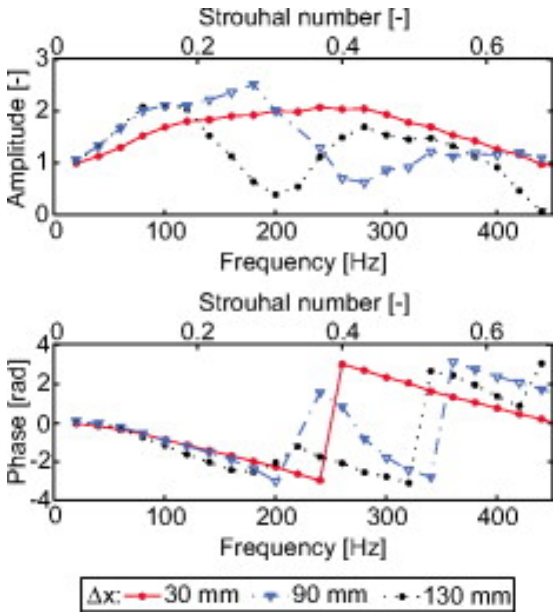

Figure 15: *FTFs for three different positions of the axial swirl generator. Reproduced from Komarek and Polifke, 2010.*

It was then possible to change the relative phase of the swirl fluctuations and to study the impact on the dynamic flame response. By increasing the distance of the swirler to the flame, the time required for convective transport of a fluctuation in swirl number to the flame was also increased.
Their FTF data are reported in Fig. 15. The excitation was realized by a siren that modulated the flow rate of the incoming mixture to the plenum. The velocity signal was obtained by a Constant Temperature Anemometer and the heat release signal was deduced with a photomultiplier in combination with an interference filter to determine the OH* emission.
When measuring the FTF for different positions of the swirl generator, a strong impact on the response of the flame was observed. The flame response is characterized by a series of local minimum and maximum values in Fig. 15. With increasing time lag (increasing distance between the swirler and the flame), the prominent local minimum of the FTF gain moved to lower frequencies. For the swirler mounted closer to the flame ($\Delta x = 30$ mm in Fig. 15) only a local maximum of the flame response was observed, but it is likely that a local minimum would appear at an higher frequency.

An important outcome of the analysis of Komarek and Polifke, 2010, is that the interaction between acoustic and convective waves, leading to swirl fluctuations, is responsible for the shift in the frequency range of the FTF gain curve. The next step was to investigate the conditions leading to a maximum or a minimum flame response.

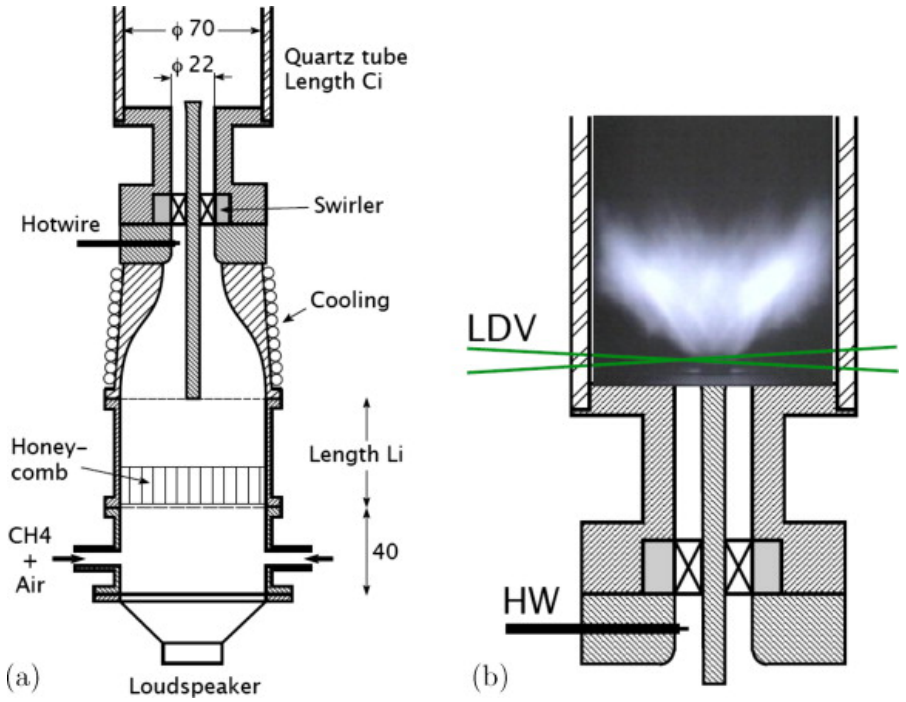

Figure 16: *(a) Schematic view of the burner and diagnostics used for measurements made by Palies et al., 2010b. (b) Close-up view of the upper part of the burner. All size are in millimeters. Reproduced from Palies et al., 2010b.*

The current interpretation follows the analysis described by Palies and co-workers in a series of articles based on experimental, numerical and theoretical work (Palies et al., 2010b; Palies et al., 2011e; Palies et al., 2011d). Their interpretation is based on the constructive/destructive interference of swirl number fluctuations and vortex shedding. The experimental setup used for their analyses is sketched in Fig. 16.

The burner was fed by a methane and air mixture at a fixed equivalence ratio of $\phi = 0.70$. Two operating conditions with two bulk velocities of $U_b = 2.67$ m/s and $U_b = 4.13$ m/s were considered. The acoustic forcing was provided by a loudspeaker mounted at the bottom of the burner. The velocity fluctuation was measured with an hot wire probe below the swirling vane and the heat release rate oscillations with a photomultiplier equipped with an OH* filter. The FDF measurements, performed for the two operating conditions they explored, are reported in Fig. 17. Both FDFs are characterized by maximum and minimum FDF gain values. As for the results of Komarek and Polifke, 2010, by increasing the time required for the convective transport of a fluctuation in swirl number to the flame, the local minimum of the FTF gain moved to lower frequencies. In Palies et al., 2010b, this was obtained by reducing the bulk flow velocity. The non-linear behavior of the flame response was also observed for both operating

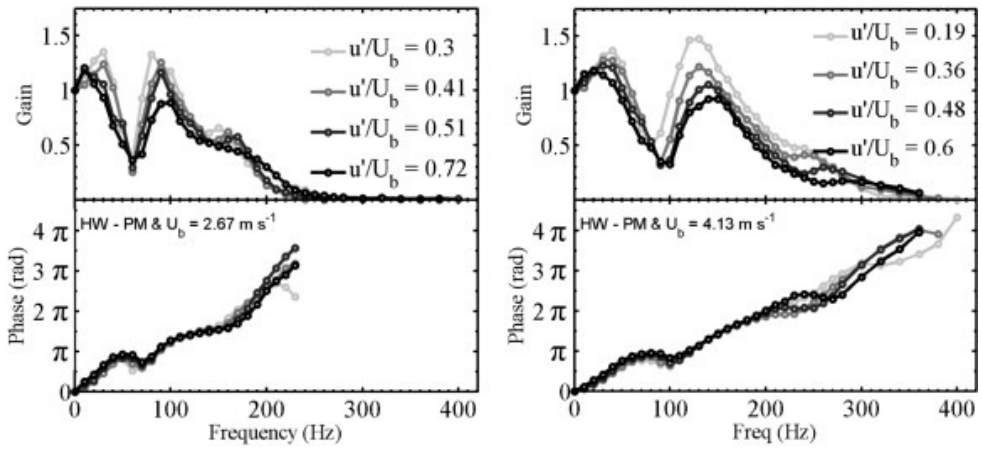

Figure 17: *Flame describing function for two different bulk flow velocities. Reproduced from Palies et al., 2010b.*

conditions, with stronger non-linearities at the FDF gain maximum values. The mechanisms leading to a high or low response was further questioned, by analyzing the flame motion through phase-conditioned emission images with respect to the forcing signal. These images were separated in two interrogation windows, as shown in Fig. 18, to decipher the respective contributions to the heat release rate perturbation of the flame base and tip. Most of the heat release rate fluctuation detected in the lower window LW was the consequence of swirl fluctuations leading to an angular deflection of the flame, while the flame tip was mostly perturbed by interaction with vortical structures. Palies et al., 2010b observed that, for a modulation frequency $f = 60$ Hz, corresponding to a minimum FTF gain in Fig. 17-left, the signals detected in the two windows were essentially out of phase (Fig. 19-left). Since the lower and upper parts of the flame responded in opposition, the global response of the flame was low. At $f = 90$ Hz, corresponding to a maximum FTF gain in Fig. 17-left, the signals from the lower and upper parts of the flame were nearly in phase and the whole flame contributed coherently to the fluctuation in heat release rate. In a subsequent numerical analysis, Palies et al., 2011e showed that, at the frequency corresponding to a minimum FTF gain level, the vortex shedding and flame tip roll-up process was less intense, due to a stronger interaction between the flapping flame base and the flow at the injector rim. All these mechanisms are synthesized in Fig. 13 reproduced from Candel et al., 2014.

These interpretations have been later questioned by Bunce et al., 2013. The experimental setup used for their analysis is sketched in Fig. 20. The burner was fed by mixtures of natural gas and air for different bulk velocities and equivalence ratios. They performed several FTF measurements and observed a qualitative similarity of the response for all the operating conditions. An

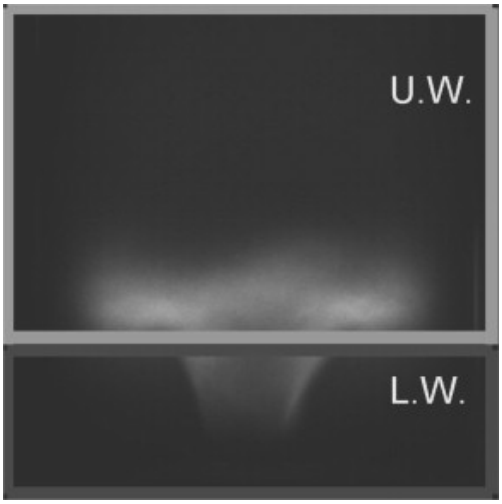

Figure 18: *View of the two interrogation windows superimposed on flame A at* $f = 60$ *Hz. UW and LW respectively designate the upper and lower windows. Reproduced from Palies et al., 2010b.*

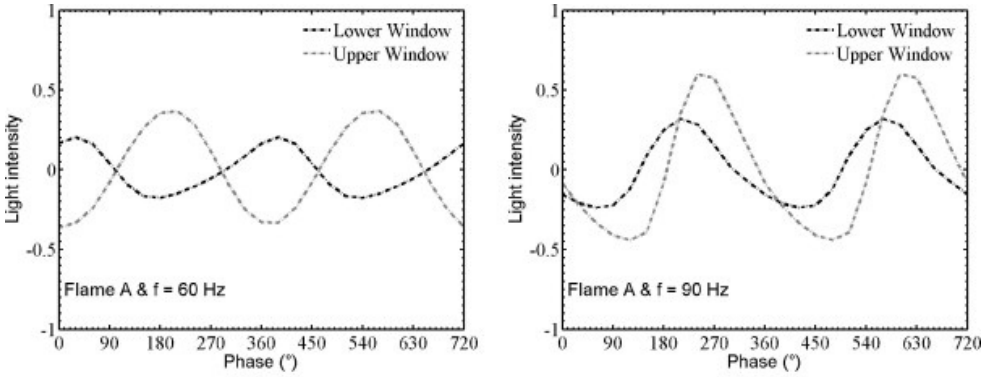

Figure 19: *Heat release rate signals reconstructed from the light emission detected in the upper and lower windows. Reproduced from Palies et al., 2010b.*

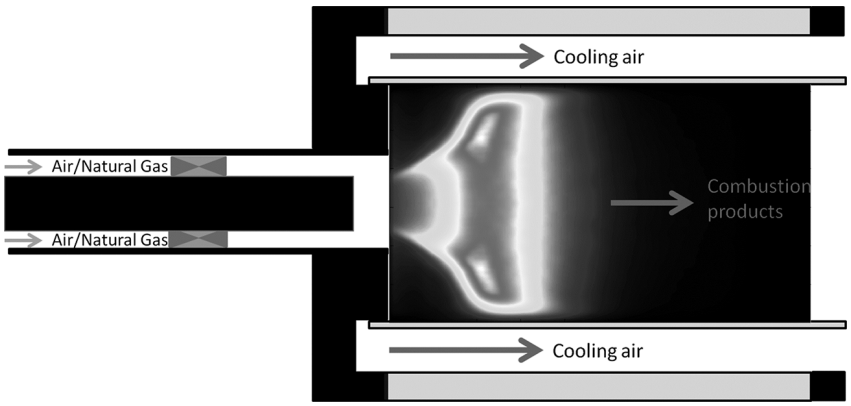

Figure 20: *Cross section of the nozzle and combustion chamber. Reproduced from Bunce et al., 2013.*

example of such response is reported in Fig. 21. As for the results of Komarek and Polifke, 2010 and Palies et al., 2010b, the FTF is characterized by two local maximum gain values and a local minimum in between. The phase lag feature an inflection point close to the frequency where the gain is at its minimum.

They further analyzed the flame response mechanism with the same windowing method applied by Palies et al., 2010b. First, they investigated the sensitivity of the results upon the window division location, and regardless of this choice, constructive interference between the heat release fluctuations in the upper and lower regions of the flame could not be seen.

The envelope of the mean flame position fluctuations was determined at the flame transfer function gain extrema frequencies and is shown in Fig. 22. They

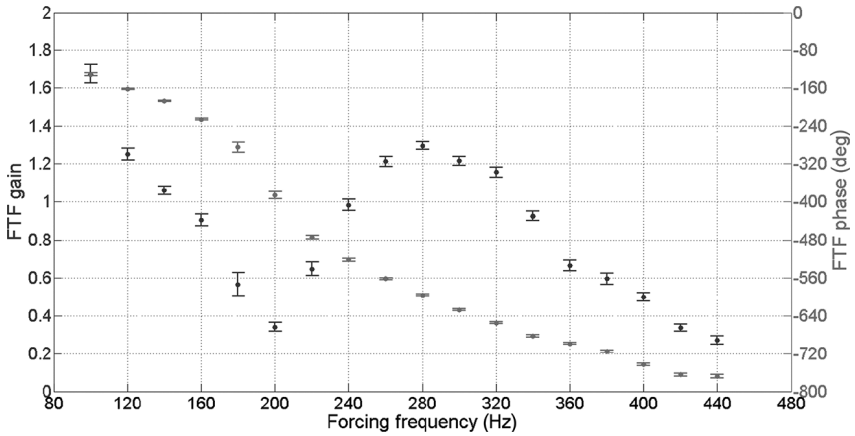

Figure 21: *Flame transfer function gain and phase versus the forcing frequency. Reproduced from Bunce et al., 2013.*

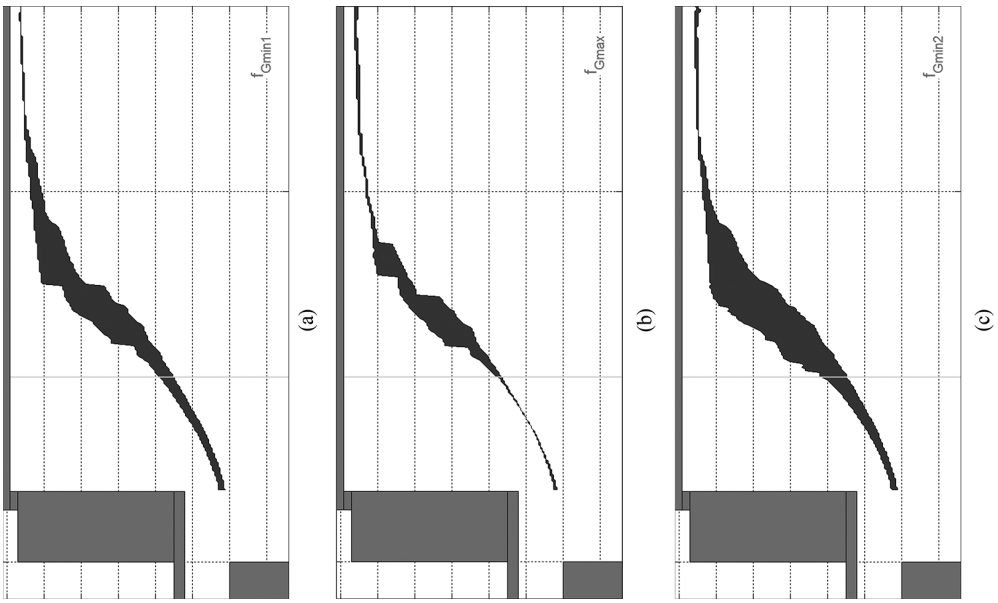

Figure 22: *Envelope of the mean flame position over one period of forcing at (a) the first gain minimum, (b) the gain maximum and (c) the second gain minimum. Reproduced from Bunce et al., 2013.*

found that, at gain minima frequencies, fluctuations in mean flame position near the flame base were present, indicating the presence of swirl number fluctuations at these frequencies. In contrast, fluctuations in the mean flame position near the flame base were much lower at the gain maximum frequency (middle image in Fig. 22).

These results from Bunce *et al.* confirm those from Palies *et al.* in terms of destructive interference between flame angle fluctuations and vortex rollup at the minimum gain frequency, but question the constructive interference at the frequency corresponding to a FTF gain maximum, since flame angle fluctuations were seen not to exist at that particular frequency in the measurements of Bunce et al., 2013.

Upstream and downstream forcing

In all the examples shown until now, the FTF or FDF ware determined by introducing acoustic perturbations coming from the upstream side of the flame. In practical systems, the interference between acoustic waves and the flame can happen from both the upstream and downstream sides. It is then interesting to compare FTF results obtained by submitting the flame to perturbations coming from its downstream side (Hochgreb et al., 2013; Gaudron et al., 2018).
We focus here on the results from Gaudron et al., 2018. The experimental setup used for their analysis is sketched in Fig. 23. The burner is fed by a

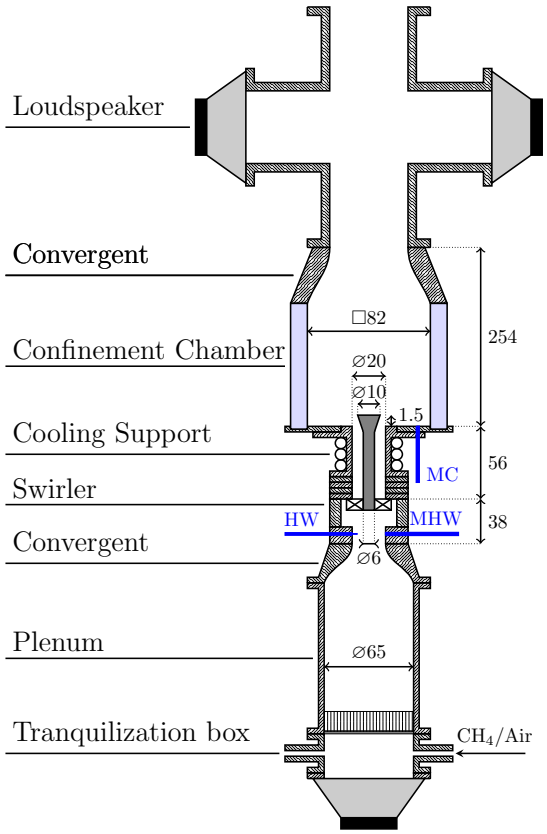

Figure 23: *Experimental setup used by Gaudron et al., 2018.*

mixture of methane and air at fixed equivalence ratio ($\phi = 0.82$) and bulk velocity ($U_b = 5.4$ m/s). In these experiments, the flame is forced either by a loudspeaker connected to the bottom of the burner in the fresh gas region or by a set of loudspeakers connected to the combustion chamber exhaust tube in the burnt gas region.

They compared several FDFs with different reference signals. The results reported in Fig. 24 were obtained by measuring the velocity fluctuations with a hot wire probe (*HW* in Fig. 23) located below the swirler and the heat release rate fluctuation with a photomultiplier equipped with an OH* filter. At first it was shown that the FDFs measured with the two different forcing methods, shown in Fig. 24, follow the same trends. The peculiar shape of swirling flame FDFs is retrieved in both cases and maximum and minimum values of the gain are the same and appear at the same frequencies. Also the non-linear behavior for the gain and linear behavior for the phase was confirmed.

The experimental campaign was followed by a theoretical analysis. From Fig. 24, one can see that slight differences are observed in the two FDF gain

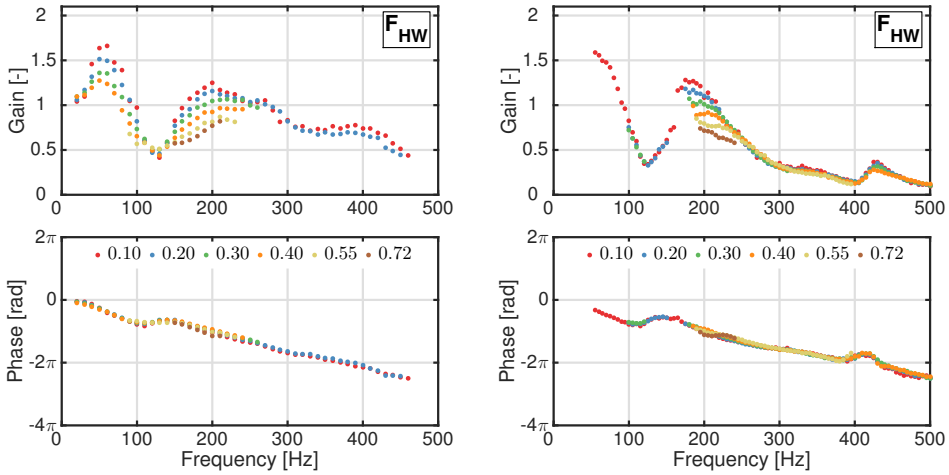

Figure 24: *Flame describing functions obtained with upstream (left) or downstream forcing (right) for six different forcing levels u'/u at the hot wire location. Reproduced from Gaudron et al., 2018.*

curves. This was attributed to the fact that the upstream and downstream acoustic boundary conditions are modified depending on the type of forcing used to excite the flame, which in turn modifies the acoustic fields inside the system. In these experiments, the forcing level u'/u is fixed at the hot wire location, for both upstream and downstream excitation. Thus, it does not correspond to the forcing level seen by the flame at the injector outlet. It was shown that a large acoustic pressure drop, due to acoustic losses, is generated across the swirler in the case of upstream forcing. This acoustic pressure is much lower in the case of downstream forcing. By taking into account this acoustic pressure drop to reconstruct the acoustic velocity at the burner outlet, Gaudron et al., 2018 were able to obtain an almost perfect match between describing functions measured with upstream or downstream forcing at all frequencies and forcing levels. This proves that the mechanisms acting on the flame to determine its response are the same, regardless of the direction of incoming acoustic waves. When the correct velocity signal at the injector outlet is used to determine the FTF/FDF, quantitative results are also independent of the direction of incoming acoustic waves. It is however difficult in many systems to measure this signal directly at the burner outlet and the FTF/FDF are often determined with a reference signal away from the injector outlet. In these cases, reconstruction rules of the FTF at the burner outlet, presented in Gaudron et al., 2018, should be used.

Aerodynamically stabilized flames

For all the previously presented cases, a central bluff body was used to help flame stabilization. Flame transfer function measurements, for swirling flames fully aerodynamically stabilized away from all solid components, as in many real engines, are less well documented. One example of such measurements is provided by Durox et al., 2013. They performed tests on the burner sketched in Fig. 25, with a methane-air mixture, with $\phi = 0.70$ and $U_b = 11$ m/s. A radial swirler, with variable blade angles, is used for flame stabilization. When the blade angle is varied, striking changes in the flame configuration were observed, as shown in Fig. 26. When the swirl number takes large values (i.e., for high blade angles), a characteristic swirling flame shape with a conical root lying on the burner axis, was obtained. Gradually, as the angle decreases the flame was positioned further downstream in the combustion chamber. The FTF is in turn strongly affected by a change in blade angle, as reported in Fig. 27. In this study, the velocity fluctuation is measured by LDV at the burner outlet and the heat release rate deduced from the OH* signal measured by a photomultiplier gathering light from the whole flame. The gain features large values up to 200 Hz, followed by a large drop, regardless of the blade angle. Except for results presented for a blade angle of 61^o, one cannot distinguish a clear drop of the FTF gain at low forcing frequencies. The phase of the FTF increases almost linearly with frequency, for all the blade angles, with a phase lag that regularly increases as the blade angle drops. No attempt was made to investigate the mechanisms controlling the response of these aerodynamically stabilized flames.

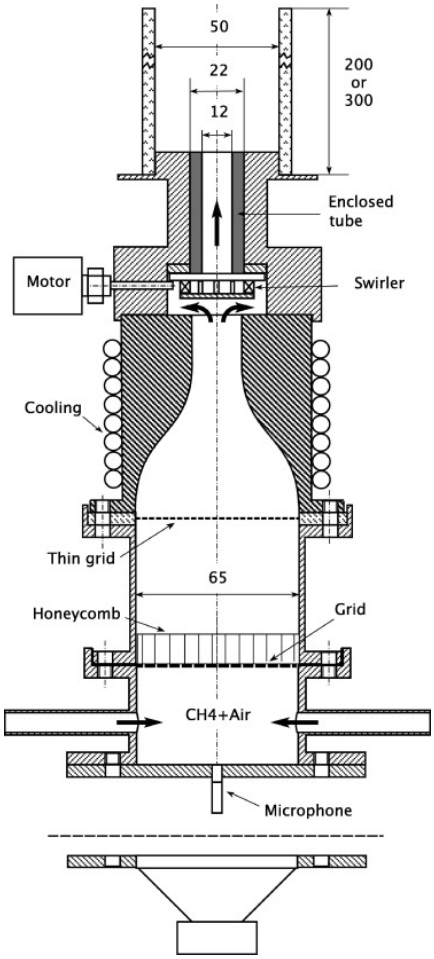

Figure 25: *Experimental setup used for the study of fully aerodinamically stabilized swirling flames in Durox et al., 2013.*

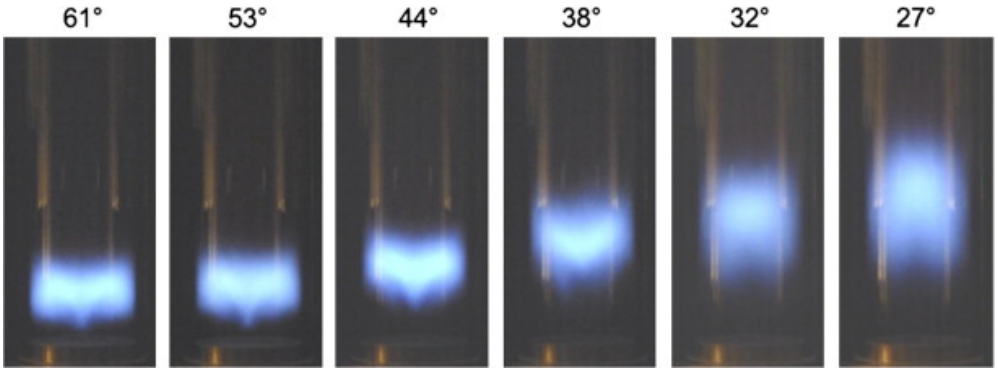

Figure 26: *Long exposure time flame images as a function of the swirler blade angle. Reproduced from Durox et al., 2013.*

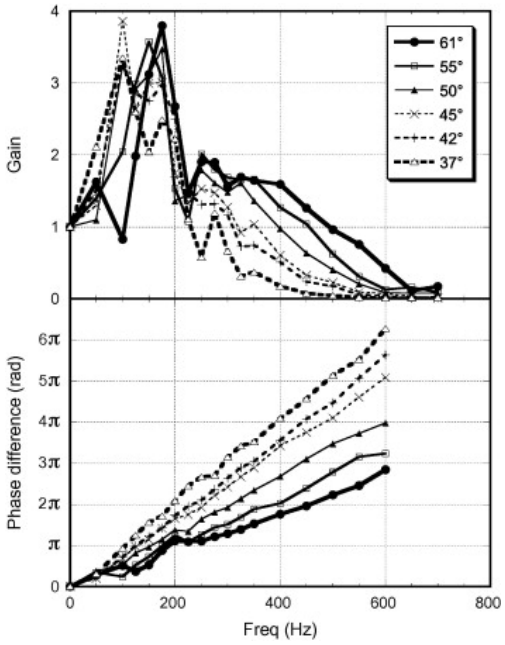

Figure 27: *Flame Transfer Function for different swirler blade angles. Reproduced from Durox et al., 2013.*

Thesis objectives and contents

This brief literature review indicates that the mechanisms determining the response of premixed swirled flames to acoustic perturbations are still not fully understood. In particular, effects of the swirl level, conditions leading to a drop of the FTF gain and effects of the central insert remain to be elucidated.
This thesis is dedicated to the study of the response of lean premixed swirling flames to acoustic perturbations, for different configurations of the swirling injector. A laboratory-scale model gas turbine combustor, powered by turbulent premixed flames at different lean injection conditions and operated at atmospheric pressure, is adapted from a previous setup for this purpose.
The problem is tackled from a fundamental point of view, analyzing the elementary processes associated to changes of the injector design, leading to a reduction of the flame response to acoustic perturbations in a simplified configuration, portraying the combustion dynamics of real systems.
This manuscript is made of nine chapters, which content is briefly described in the following.

Chapter 1 to 3: Burner details and applied methodologies

This first part is dedicated to the description of the burner geometry and of the main diagnostics applied in the process of this work. Chapter 1 first focuses on the experimental setup, which is there described in detail. As this work

is mainly dedicated to the assessment of the effects of different swirling injection conditions on the mean and dynamic properties of lean-premixed swirling flames, a burner with some easily replaceable components was designed. In chapter 1 details of the different injectors developed in this study are given. Chapter 2 is dedicated to a rapid description of the main acoustical and optical diagnostics used in this study, with also some examples of measurements. First, the technique used to measure FTFs is presented. The flow fields properties obtained for different injection conditions are analyzed through Laser Doppler Velocimetry (LDV) and Particle Image Velocimetry (PIV) measurements. Some examples of flame shapes under steady and forced conditions obtained with an ICCD camera are then presented. To close this first part, chapter 3 presents the numerical solver and the meshed geometry used for the Large Eddy Simulation (LES) analysis that was carried out in conjunction with the experiments.

Chapter 4 and 5: Influence of the injection conditions on the mean flow and flame properties and on thermoacoustic instabilities

The second part of the manuscript focuses on the description of the results obtained for the different swirling injection conditions tested. Chapter 4 present flow and flame properties. The investigated geometry modifications cover effects of radial swirler, injector and bluff-body main dimensions. Also the mixture flow rate is modified. A stabilization chart of the burner is shown to be divided into three regions separating the blowoff regime from the flashback regime and well-stabilized flames. Flow fields properties in cold flow conditions and flame shapes in reactive conditions, are then analyzed for the different injectors tested. Chapter 5 reports measurements when the system features combustion instabilities. These instabilities are triggered by modifying the length of the exhaust tube. Effects of modifications of the swirler design and of the distance between the swirler and the combustion chamber backplane are examined.

Chapter 6: Influence of the injection conditions on the transfer function of lean-premixed swirling flames

The third part of the manuscript, covered in chapter 6, is dedicated to the presentation of FTF/FDF measurements obtained by submitting flames to acoustic perturbations, generated by a loudspeaker mounted on the upstream side of the flame. Effects of different injection conditions are considered. The typical shape of the FDF of swirling flame is retrieved. All the geometrical configurations tested confirmed that a decrease of the minimum gain of the FTF can be obtained by an increase of the swirl number S. A limit is reached when an excessive swirl number leads to flashback of the flame into the injector. For a fixed swirl level S and modifying the mean flow velocity or the swirler to

chamber backplane distance, the FTF curve gets shifted in the frequency range without modifications of the gain level.

Chapter 7 to 9: Mechanisms controlling the FTF shape

This last part is dedicated to the interpretation of results presented in chapters 5 and 6. In chapter 7, phase locked ICCD and PIV measurements and LES are carried out at peculiar frequencies deduced from the FTF results of chapter 6. It is first shown that the motion of the flame is quantitatively but not qualitatively different at frequencies corresponding to a minimum or a maximum gain value. Strong swirl number fluctuations are observed at both frequencies, in simulations as well as in experiments. The flame response is dominated by the interaction with vortical structures generated at the burner rim. The strength of these structures is attenuated at the minimum FTF gain frequency, even in cold flow conditions. This is attributed to the different phase shift between acoustic and convective perturbations travelling from the swirler exit to the flame, that eventually lead to a different velocity profile at the chamber backplane, resulting in different strength of vortical structures generated there. Chapter 8 then proposes a scaling of the FTF results by properly accounting for the different time scales of (i) the convection of azimuthal velocity perturbations from the swirler exit to the chamber backplane and (ii) the convection of vortical structures from the burner rim to the flame.
Chapter 9 finally present the differences in terms of flame response mechanisms, when the flame stabilization mechanism is modified. In particular, three cases are considered: (i) a non-swirling flame stabilized behind a bluff-body, (ii) a swirling flame stabilized with the help of the same bluff-body and (iii) an aerodynamically stabilized flame without bluff-body. In these two last cases, the swirl is kept roughly to the same level. It is shown that the response of the aerodynamically stabilized flame shows a low-pass filter behavior, without any reduction of the gain in the intermediate frequency range. Surprisingly, its response is closer to that of a non-swirling flame. Three competing mechanisms defines the dynamics of these flames: flame-vortex interaction, flame angle oscillations and vertical oscillations of the flame root position when the bluff-body is removed. The dominant one depends upon the flame stabilization mechanism. The reduction of flame response to acoustic waves in the intermediate frequency range, possibly reducing the sensitivity of LPM systems to dynamic phenomena, could only be observed for the configuration where flames are stabilized thanks to a swirling stream and with the help of a bluff-body.

List of publications

Journal articles

- *Impact of swirl and bluff-body on the transfer function of premixed flames*
  M. Gatti, R. Gaudron, C. Mirat, L. Zimmer, T. Schuller
  Proceedings of the Combustion Institute, *In Press*, 2018.

- *Flame describing functions of a confined premixed swirled combustor with upstream and downstream forcing*
  R. Gaudron, M. Gatti, C. Mirat, T. Schuller
  Journal of Engineering for Gas Turbines and Power, *Accepted Manuscript*, 2018.

- *Impact of the acoustic forcing level on the transfer matrix of a turbulent swirling combustor with and without flame*
  R. Gaudron, M. Gatti, C. Mirat, T. Schuller
  Flow, Turbulence and Combustion *Submitted*, 2018.

- *Impact of the injector size on the transfer functions of premixed laminar conical flames*
  R. Gaudron, M. Gatti, C. Mirat, T. Schuller
  Combustion and Flame 179, pp. 138-153, 2017.

- *Direct Assessment of the Acoustic Scattering Matrix of a Turbulent Swirl Combustor by Combining System Identification, Large Eddy Simulation and Analytical Approaches*
  M. Merk, C. Silva, W. Polifke, R. Gaudron, M. Gatti, C. Mirat, T. Schuller
  Journal of Engineering for Gas Turbines and Power, 141(2), 021035, 2018.

- *Prediction of combustion noise of an enclosed flame by simultaneous identification of noise source and flame dynamics*
  M. Merk, R. Gaudron, C. Silva, M. Gatti, C. Mirat, T. Schuller, W. Polifke
  Proceedings of the Combustion Institute, *In Press*, 2018.

- *Measurement and Simulation of Combustion Noise and Dynamics of a Confined Swirl Flame*
  M. Merk, W. Polifke, R. Gaudron, M. Gatti, C. Mirat, T. Schuller
  AIAA Journal, Vol. 56, No. 5, pp. 1930-1942, 2018.

Conference Proceedings

- *A Comparison of the Transfer Functions and Flow Fields of Flames With Increasing Swirl Number*
  M. Gatti, R. Gaudron, C. Mirat, L. Zimmer, T. Schuller
  Proceedings of the ASME Turbo Expo 2018, GT2018-76105, 2018.
- *Effects of the Injector Design on the Transfer Function of Premixed Swirling Flames*
  M. Gatti, R. Gaudron, C. Mirat, T. Schuller
  Proceedings of the ASME Turbo Expo 2017, GT2017-63874, 2017.
- *Injection system design impact on the stabilization and acoustic response of premixed swirling flames*
  M. Gatti, R. Gaudron, C. Mirat, T. Schuller
  8th European Combustion Meeting, 2017.
- *Analysis of the transfer function of large and small premixed laminar conical flames*
  R. Gaudron, M. Gatti, C. Mirat, T. Schuller
  Proceedings of the ASME Turbo Expo 2017, GT2017-64231, 2017.

Chapter 1

Experimental setup

The NoiseDyn setup has been designed with the objective of exploiting it for various type of combustion analyses. Due to its versatility, it has been used, for instance, for the analysis of laminar conical flames dynamics, for the analysis of swirling flames dynamics and also for the analysis of combustion noise. In this work, only the components needed for the analysis of the dynamics of swirling flames are presented. Information about other analyses conducted with this setup can be found in the Ph.D. thesis manuscripts from R. Gaudron (Gaudron, 2018) and M. Merk (Merk, 2018). This chapter introduces the geometrical details of the burner. A general description is given in Section 1.1, followed by a more detailed characterization of some replaceable components in Section 1.2.

1.1 Burner geometry

The setup used for the analyses conducted in this study is schematically sketched in Fig. 1.1, also showing the air and methane supply lines. A picture of the burner, together with the design drawn with the CAD software Autodesk Inventor, are shown in Fig. 1.2.
Fully premixed methane and air are injected from two diametrically opposed apertures positioned at the burner base. The air and the methane are supplied separately to a mixing box, at ambient temperature, by a series of pipes connected to an air compressor and to a pressurized gas tank, located outside the experimental room. The mass flow rates of methane and air injected are controlled by Bronkhorst F-Series mass flow controllers. The mixing box is located far upstream the burner bottom apertures, in order to assure a complete premixing of the reactants before their injection in the burner.

When the mixture enters at the bottom of the burner in a 65 mm diameter cylindrical tube, it first crosses a perforated grid, to homogenize the flow and prevent the risk of flame flashback into the pipes and an honeycomb structure

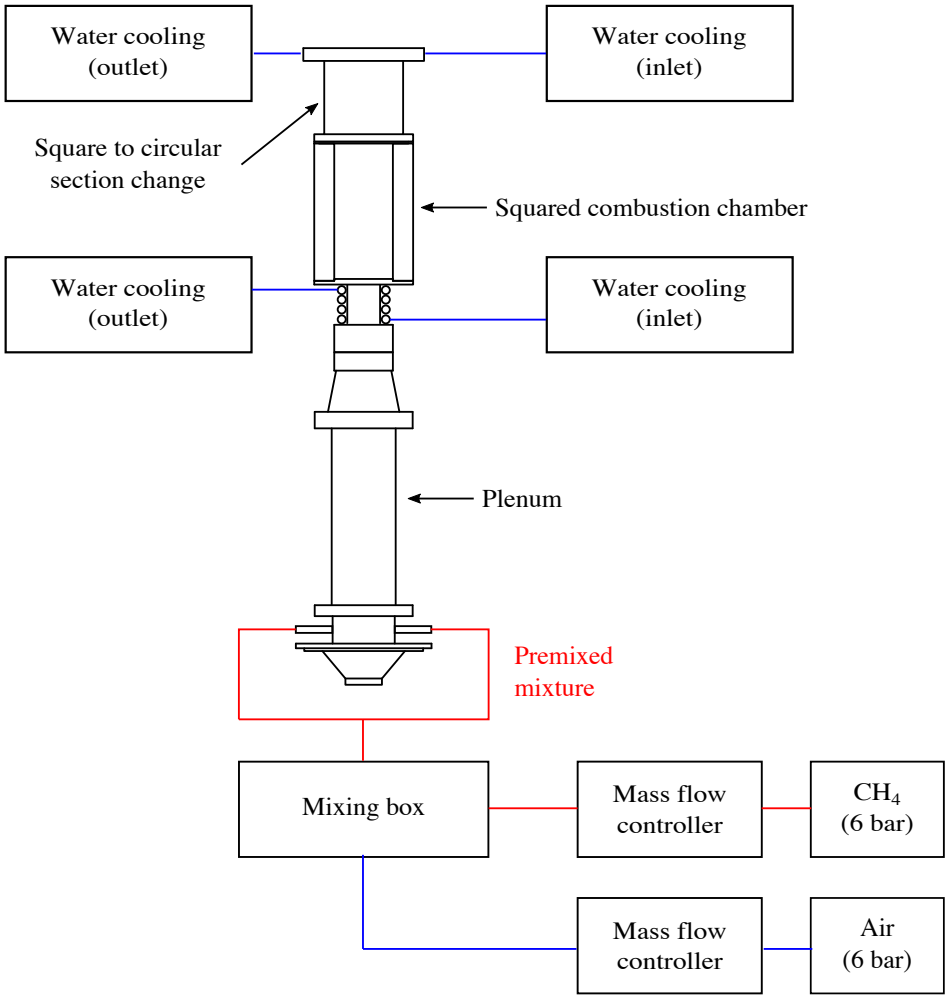

Figure 1.1: *Burner sketch with alimentation system.*

that breaks the largest turbulent scales. It then flows through an upstream plenum of 65 mm diameter featuring some wall pressure taps for acoustic pressure measurements. These and the other internal components of the burner are highlighted in Fig. 1.3, showing a longitudinal cut of the geometry through its central axis.

The mixture then travels along the upstream plenum to reach a first convergent unit (contraction ratio: 8.73). At the outlet of the nozzle of 22 mm diameter, a top-hat velocity profile is obtained. The values of the bulk flow velocity U_b presented all along this work, will always be referred to this section ($\varnothing$ = 22 mm, T_u = 293 K, p_u = 1 atm). At the same axial location, a microphone and a hot wire anemometer probe are used to measure the local flow velocity outside the boundary layer and the acoustic pressure.

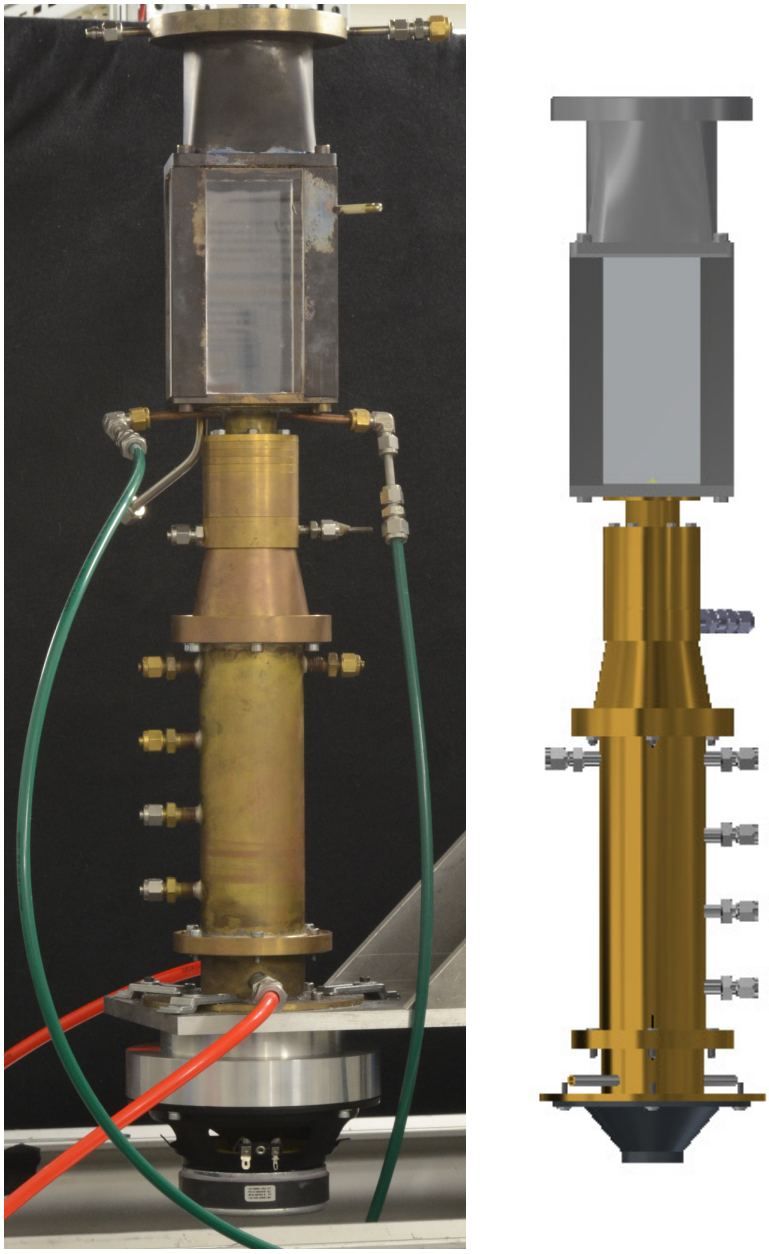

Figure 1.2: *Picture of the NoiseDyn burner (left) and corresponding view obtained with the CAD software Inventor (right).*

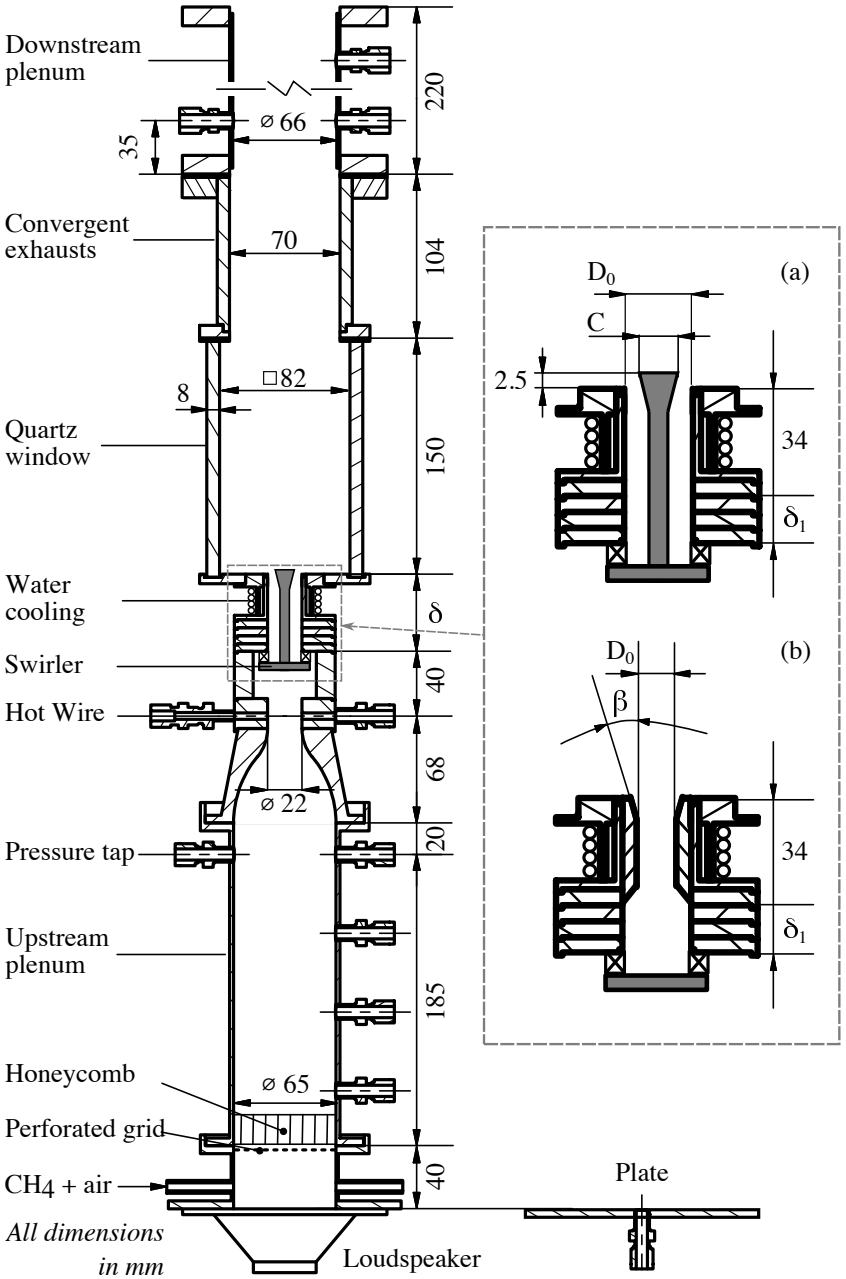

Figure 1.3: *Burner geometrical details. The main dimensions are indicated in millimeters. The loudspeaker used to modulate the flow can be replaced by a plate used to close the bottom of the burner to analyze thermo-acoustic instabilities. Details of the injectors used to stabilize flames with the help of a bluff-body (a) or fully aerodynamically (b) are highlighted in the rectangle.*

An enlargement of the passage section is then necessary to mount the swirling device. More details about the geometry of the swirler units are given in Section 1.2. The swirler unit imparts a certain amount of rotation to the flow. On the downstream side of the swirler, up to the combustion chamber, the injector geometry is highly adjustable and many different configurations were tested during this work, as detailed in Section 1.2. The temperature of the top of the burner is kept as close as possible to the ambient value by water cooling. The mixture then exhaust in the combustion chamber through an enlargement of the cross section.

The squared combustion chamber is made of four transparent quartz windows to allow optical access. The four windows are kept in position by four steel rods at each corner of the chamber. Between the rods and the quartz, high temperature seals exclude the risk of air leakage or external air intrusion. A high-voltage spark igniter (7 kV and 30 mA), inserted through a small hole in one of the steel rods on the corner of the chamber, is used to initiate combustion. A second convergent unit (contraction ratio: 1.27), changing the cross section from squared to circular, is placed on top of the combustion chamber to guide the hot combustion products out of the burner into the atmosphere. The burner is operated at atmospheric pressure.

The geometry of the bottom and top parts of the burner, before the upstream plenum and after the exhaust convergent unit, is modified according to the type of analysis to be conducted. For flame dynamics analysis under external acoustic excitation, a loudspeaker (Monacor SP-6/108PRO, 100 Watts RMS) is mounted at the bottom of the burner and used to introduce acoustic excitations of different frequency and amplitudes in the flow. For measurements in the absence of external forcing or thermo-acoustic instabilities characterization, the bottom side of the burner is closed by a plate equipped with a microphone, as shown in Fig. 1.3, while exhaust pipes of different lengths can be mounted downstream the second convergent unit. More details about these components are given in the following.

1.2 Burner replaceable components

One of the most important characteristics of the NoiseDyn setup is its versatility. Many of the burner components can be demounted and substituted or simply removed from the test-rig, to test the effects of different burner geometries on the combustion properties. In some cases, components are substituted to perform different type of analyses, as for the measurements with or without external acoustic excitation. The following sections of this chapter are dedicated to the description of the main burner replaceable components.

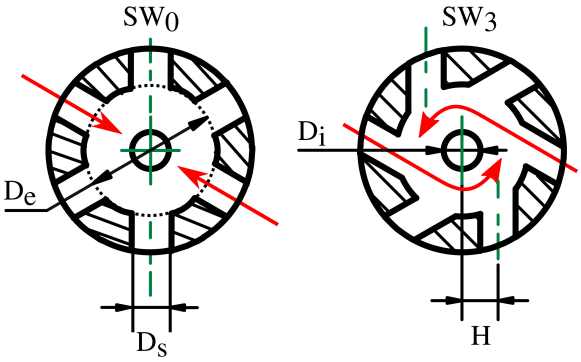

	D_S [mm]	H [mm]	n
SW_0	6	0	6
SW_1	5.6	3.5	6
SW_2	5.6	4.5	6
SW_3	6	6	6
SW_4	4	7	10

Figure 1.4: *Swirler sample geometry and parameters of the different swirlers tested.*

1.2.1 Swirlers

The swirlers used for the experiments conducted in this study are radial vanes with tangential inlets. A total of five different swirlers were designed. A picture of one of these components is shown in Fig. 1.4 together with a sketch of two representative designs and a table reporting the parameters modified in the five different geometries tested. The number n of the tangential inlets, the diameter D_s of these tangential inlets and the semi-distance H between the axes of two diametrically opposed inlets (Fig. 1.4), are modified to select the rotation rate imparted to the flow. The design of swirlers SW_0 and SW_3 only differs by the distance H in Fig. 1.4. In the first device, designated as SW_0, the swirling vanes are aligned with the radial direction ($H = 0$ mm). In the second one, designated as SW_3, the vanes are shifted from the radial direction by $H = 6$ mm, to impart a strong rotation to the flow. The values of H, D_s and n for the other swirlers tested in this study are reported in the table in Fig. 1.4. The dimensions of the external ($D_e = 22$ mm) and internal ($D_i = 6$ mm) diameter of the annular channel shown in Fig. 1.4, are fixed for all the swirler designs. As shown in Fig. 1.3, a central insert of diameter $D_i = 6$ mm ending with a top cone of diameter C, is generally fixed to the swirler. For the analysis of aerodynamically stabilized flames without the help of a central insert, reported in chapter 9, the central hole of diameter $D_i = 6$ mm is closed with a screw.

The rate of rotation imparted to the flow is characterized by the swirl number S, comparing the axial flux of tangential momentum G_θ to the axial momentum

flux G_z, $S = 2G_\theta/(D_o G_z)$, where D_o is the outer diameter of the injector, as shown in Fig. 1.3. Neglecting the pressure term in the axial momentum flux (Beer and Chigier, 1972), the swirl number S is expressed in the form:

$$S = \frac{2}{D_o} \frac{\int u_\theta u_z r^2 dr}{\int u_z^2 r dr} \tag{1.1}$$

The swirl number should, when possible, be determined from measured values of the axial, u_z, and azimuthal, u_θ, velocity profiles, but this is obviously not possible during the design stage of a swirler. In this case, S can be estimated with analytical expressions, taking into account the swirler and injector geometries and making assumptions about the axial and azimuthal velocity components. One should however keep in mind that such estimates can notably differ from values deduced from experiments (Palies, 2010; Durox et al., 2013).
From Fig. 1.5, a mass balance yields the ratio between the axial velocity $\bar{u}_z$ and the velocity inside the swirler injection channels $\bar{u}_h$:

$$\frac{\bar{u}_h}{\bar{u}_z} = \frac{1}{n} \frac{R_o^2 - R_i^2}{R_s^2} \tag{1.2}$$

where $R_s = D_s/2$, $R_o = D_o/2$ and $R_i = D_i/2 = 3$ mm is the radius of the central rod, shown in Fig. 1.3-a. It is then straightforward, from trigonometric considerations, to get the ratio between axial and azimuthal velocities:

$$\frac{\bar{u}_\theta}{\bar{u}_z} = \frac{\sin\alpha}{n} \frac{R_o^2 - R_i^2}{R_s^2} \tag{1.3}$$

where $\sin\alpha = H/R_o$.

To make estimates of the swirl number, one can further make assumptions about the axial and azimuthal velocity components. One possibility is to assume a uniform axial flow profile $u_z(r) = \bar{u}_z$ and a solid body rotation profile for the

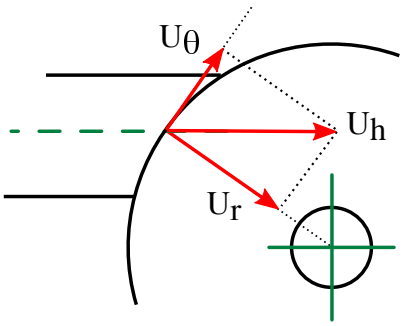

Figure 1.5: *Sketch showing the velocities used for the swirl number estimation.*

azimuthal velocity component $u_\theta(r) = \bar{u}_\theta(r/R_o)$. The swirl number can finally be estimated by integration of Eq. (1.1) as:

$$S \simeq \frac{\sin\alpha}{2n}\frac{R_o^4 - R_i^4}{R_s^2 R_o^2} \tag{1.4}$$

Analytical estimates obtained with this assumptions are shown in Fig. 1.6 for swirler SW_1 and SW_3 as a function of the injector exit radius R_o. As expected, S increases for increasing values of H leading to higher azimuthal velocities and for increasing values of R_o leading to smaller axial velocities.
The swirl number was also determined by Laser Doppler Velocimetry (LDV) or Particle Image Velocimetry (PIV) measurements for the main configurations of the injector investigated in this work. Details about these measurements are given in chapter 2, but it is already interesting to compare them with the analytical estimates just introduced.

LDV measurements of the axial and azimuthal velocity components are presented in Fig. 1.7 for swirlers SW_1 and SW_3, in an injector with an outlet radius $R_o = 10$ mm and a central insert terminated by a cone of $C = 12$ mm diameter. The measurements are conducted in cold flow conditions at 1.5 mm above the top cone of the central bluff-body, corresponding to a distance of 4.0 mm from the combustion chamber backplane (Fig. 1.3). The corresponding bulk flow velocity at the hot wire location is $U_b = 5.44$ m/s. The axial velocity components are almost superposed for the two swirlers SW_1 and SW_3 in the left in Fig. 1.7. In these two cases, the swirler designs are too close (see Fig. 1.4) to obtain a major modification of the axial flow component. On the other hand, in the right plot in Fig. 1.7 showing the azimuthal velocity component, the $\bar{u}_\theta$ profile reaches slightly higher values for SW_3 than for SW_1. This is due to the higher value of the distance H between two diametrically opposed swirler inlets, leading to a higher rotation rate.

The swirl numbers $SW_3 = 0.73$ and $SW_1 = 0.63$ are deduced from Eq. (1.1) and are superposed in Fig. 1.6 on top of the analytical estimates. One can see that Eq. (1.4), considering a constant axial and a linear azimuthal flow component, leads to an underestimation of the experimental swirl number. As a matter of fact, the axial velocity profile shown in Fig. 1.7 is not uniform along the distance going from the central rod at $R_i = 6$ mm to the injector rim at $R_o = 10$ mm. In this case, a better prediction of the swirl number could be obtained by considering a linear axial velocity evolution $u_z(r) = \bar{u}_z(r/R_o)$ and a solid body rotation for the azimuthal velocity profile $u_\theta(r) = \bar{u}_\theta(r/R_o)$. With this new assumption, integration of Eq. (1.1) leads to:

$$S \simeq \frac{4}{5}\frac{\sin\alpha}{n}\frac{1}{R_o R_s^2}\frac{R_o^5 - R_i^5}{R_s^2 + R_o^2} \tag{1.5}$$

Swirl estimates obtained with these new approximations are reported as dashed

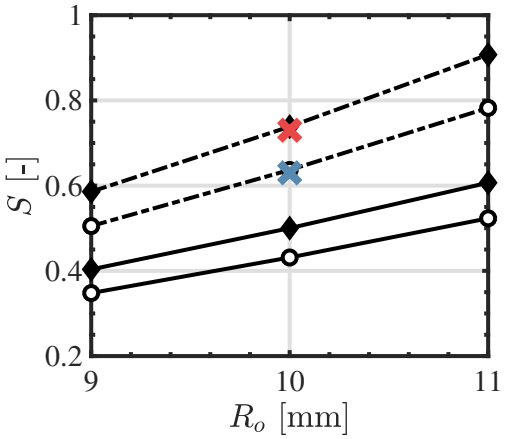

Figure 1.6: *Swirl number analytical estimates (Eq. (1.4)) for swirlers SW_1 (white circles) and SW_3 (black diamonds). Solid lines: estimates obtained with a uniform axial velocity profile and a linear azimuthal velocity profile. Dashed dotted lines: estimates with linear axial and azimuthal velocity profiles (Eq. (1.5)). Superposed as blue (SW_1) and red (SW_3) crosses, the swirl numbers measured by LDV.*

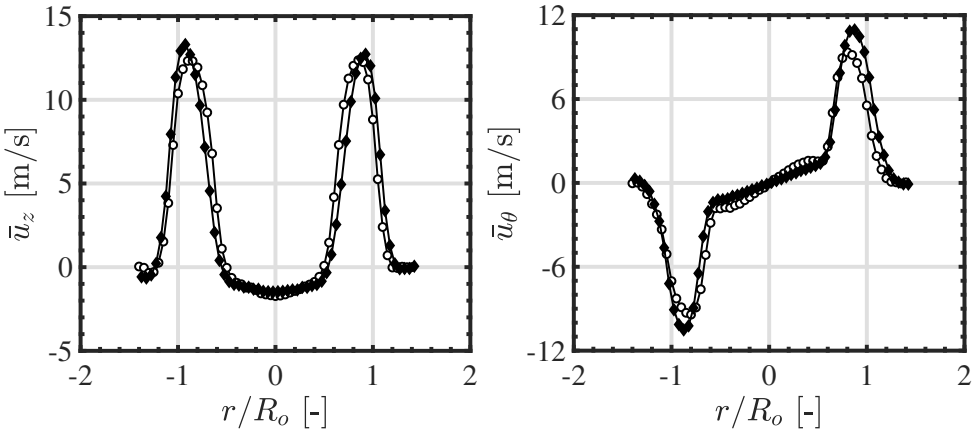

Figure 1.7: *Axial (left) and azimuthal (right) velocity components measured by LDV 4.0 mm above the injector outlet for swirlers SW_1 (white circles) and SW_3 (black diamonds), with an injector of $R_o = 10$ mm and $C = 12$ mm and for a bulk flow velocity $U_b = 5.44$ m/s.*

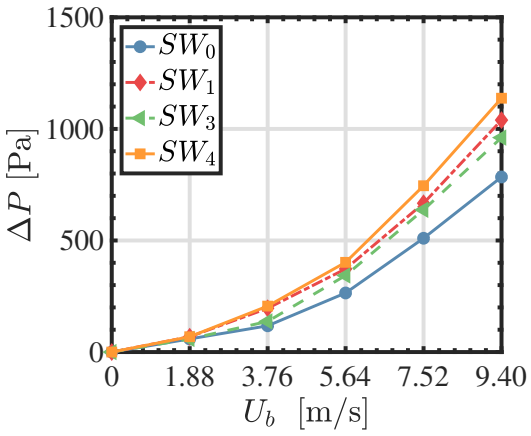

Figure 1.8: *Pressure loss measurements for different swirler designs and fixed injector geometries ($D_o = 22$ mm, $C = 14$ mm).*

dotted lines in Fig. 1.6. They show a better agreement with the experimentally determined values. This later formula is retained to estimate the swirl numbers in this work when they were not determined from LDV or PIV measurements.

A change of the geometrical parameters of the swirler does not only modify the rotation rate of the flow, but also the pressure drop across the swirler unit. This loss was measured for the different swirler designs between the upstream plenum and the atmosphere with a liquid column U-tube manometer. One of the port of the manometer was connected to the pressure tap in the upstream plenum closest to the swirler (Fig. 1.3), while the other was exposed to the atmosphere. Results are shown in Fig. 1.8. These measurements were conducted in cold flow conditions by injecting increasing air mass flow rates in the burner. The bulk velocity U_b indicated in Fig. 1.8 is evaluated at the convergent outlet of 22 mm diameter from the air mass flow rate by assuming an atmospheric pressure value $p_{atm} = 101.325$ kPa and a temperature $T = 293$ K. As expected, the pressure loss increases with the bulk velocity and is lowest for swirler SW_0, featuring injection channels aligned with the radial direction of the reactant injection tube ($H = 0$, Fig. 1.4). The pressure drop ΔP is the highest for SW_4 featuring injection channels the farthest apart from each other ($H = 7$ mm) and the lowest flow passage area $A = n\pi D_s^2/4$. The maximum pressure loss for SW_4 almost reaches 1200 Pa in Fig. 1.8. For the experiments conducted in this work, the bulk velocity was always equal or lower than $U_b = 5.44$ m/s, giving a negligible ΔP always lower than 400 Pa. In this respect, one can neglect effects of the pressure drop through the swirler, since $\Delta p/p < 1\%$ in this study.

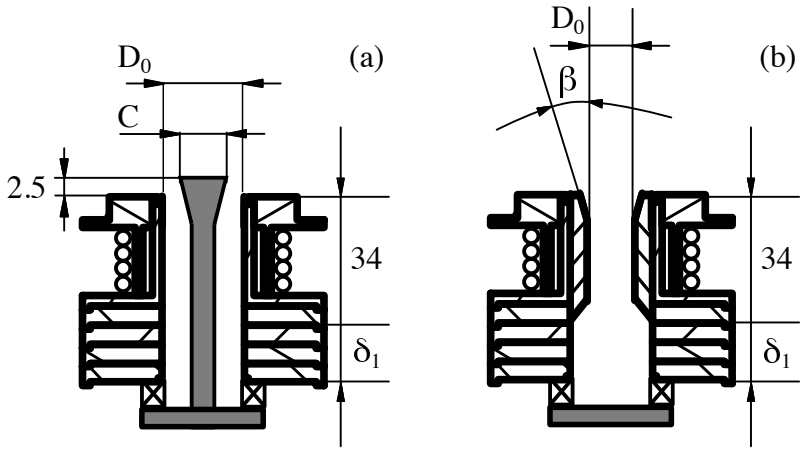

Figure 1.9: *Details of the injectors used to stabilize flames with the help of a bluff-body (a) or fully aerodynamically (b).*

1.2.2 Central injection unit

The flow exits the swirler into a central injection tube (Fig. 1.9-a). The injector geometry, from downstream the swirler up to the combustion chamber backplane, is highly adjustable. The diameter of this tube is $D = 22$ mm, over a first section of variable length δ_1, followed by a central insert of length 34 mm, and diameter D_o. The outer diameter D_o of the injector can be modified by substituting this central insert, shown in Fig. 1.10-a. A central rod of diameter $D_i = 6$ mm, ending with a cone of variable diameter at the top $C = 10$, 12 or 14 mm (Fig. 1.10-b), is inserted in the injection tube to ease stabilization of the flame. The distance between the swirler exit and the combustion chamber backplane can also be modified by 5 mm increments: $\delta = 35$, 40, 45 or 50 mm using a set of spacers of height 5 mm shown in Fig. 1.10-c. To modify the distance δ, one can use from one to four spacers. This configuration with a central rod in Fig. 1.9-a is the one which is retained all along this study, except in chapter 9 where the injector in Fig. 1.9-b is used to analyze the response of fully aerodynamically stabilized flames. In this second case, the central insert with diameter $D_o = 12$ mm is terminated by a diverging cup with an half angle $\beta = 15°$ (Fig. 1.9-b).

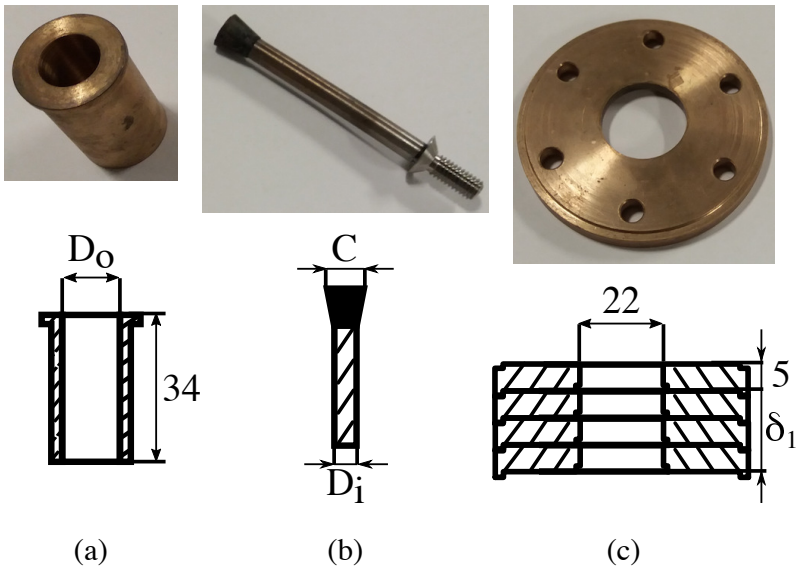

Figure 1.10: *Pictures and geometrical details of the replaceable components of the injection unit. Dimensions in mm.*

1.3 Conclusions

The setup developed in this study allows studying the dynamics of swirling flames with and without acoustic forcing for a wide set of injector configurations. Two main classes can be defined giving that the injector features or does not feature a central insert to help stabilizing the swirled flames. The injector without insert is used in chapter 9 to analyze the dynamics of fully aerodynamically stabilized flames. The other injectors with a central insert are used in the rest of this work. A parametric analysis has been conducted with this second class of injectors for which 28 configurations, indicated in table 1.1, were tested by changing the swirling vane (SW_0, SW_1, SW_2, SW_3, SW_4), the injector outlet diameter varying from $D_o = 18$ to 22 mm, the diameter of the conical end piece $C = 10$ to 14 mm, the distance δ between the swirler and the injector outlet from 35 to 40 mm and the bulk flow velocity from $U_b = 2.72$ to 5.44 m/s. The resulting flow was characterized by LDV or PIV under cold flow conditions in 12 configurations. These data were used to determine the swirl number S. In the 16 other cases the swirl number was deduced with analytic approximations (Eq. (1.5)).

Table 1.1: *Configurations explored. SW: Swirler design: D_o: injection tube diameter [mm], C: conical end piece diameter [mm], δ : distance between the swirler exit and the injection plane outlet [mm], U_b: velocity at the hot-wire location [m/s]. S^* : Estimated swirl number (Eq. (1.5)). S : Swirl number deduced from LDV or PIV measurements.*

SW	D_o	C	δ	U_b	S
0	22	14	50	5.44	0.20
1	18	12	50	5.44	0.54*
1	18	14	50	5.44	0.48*
1	20	12	50	5.44	0.63
1	22	10	50	5.44	0.75*
1	22	12	50	5.44	0.71
1	22	14	50	5.44	0.65*
2	18	12	50	5.44	0.59
2	18	14	50	5.44	0.52*
2	20	10	50	5.44	0.73
2	20	12	50	5.44	0.69
2	20	14	50	5.44	0.63
2	22	10	50	5.44	0.84*
2	22	12	50	5.44	0.79
3	18	12	50	5.44	0.60
3	18	14	50	5.44	0.55*
3	20	10	35	5.44	0.80*
3	20	10	40	5.44	0.80*
3	20	10	45	5.44	0.80*
3	20	10	50	5.44	0.80
3	20	12	50	2.72	0.73*
3	20	12	50	4.08	0.73*
3	20	12	50	5.44	0.73
3	20	14	50	5.44	0.64*
3	22	10	50	5.44	0.86*
3	22	12	50	5.44	0.81
3	22	14	50	5.44	0.80
4	22	14	50	5.44	0.95*

Chapter 2

Diagnostics

The main measurement techniques applied within the scope of this work are introduced in this chapter. Techniques used to force the flame and determine the velocity and heat release rate fluctuations for flame transfer function (FTF) calculations are described in the first part. A constant temperature anemometer probe (HW) and a photomultiplier (PM) equipped with an OH filter are used for this purpose. In Sec. 2.2, Laser Doppler Velocimetry (LDV) used to measure axial, azimuthal and radial velocity components, as close as possible to the injector exit, is briefly described. Particle Image Velocimetry (PIV), adopted for the characterization of velocity fields in different planes inside the combustion chamber in steady and pulsated conditions, is presented in Sec. 2.3. For steady conditions, PIV measurements are performed in cold and reactive conditions. Lastly, Sec. 2.4 describes the optical arrangement used to characterize the steady and forced flame structures.*

2.1 Flame transfer function measurements

A consistent part of the work conducted in this thesis is dedicated to analyze the effects of geometrical modifications of some injector components on the flame response to incoming acoustic perturbations. This response is characterized by measuring the flame transfer function or flame describing function linking velocity fluctuations at some location upstream the flame and heat release rate fluctuations. For this scope, the burner is equipped with a loudspeaker (Monacor SP-6/108PRO, 100 Watts RMS) mounted at the bottom of the burner. A homemade LabVIEW routine generates a digital harmonic signal, which is converted to an analog signal and sent first to an amplifier and then to the loudspeaker. The forcing signal is generated at different amplitudes and frequencies. The excitation level produced by the loudspeaker is controlled by a hot wire (HW in Fig. 2.1). The hot wire measurement is then fed back to the routine and the forcing signal amplitude is adjusted until the desired $u'/\bar{u}$ level is obtained, where u' denotes the root-mean-square value and $\bar{u}$ the av-

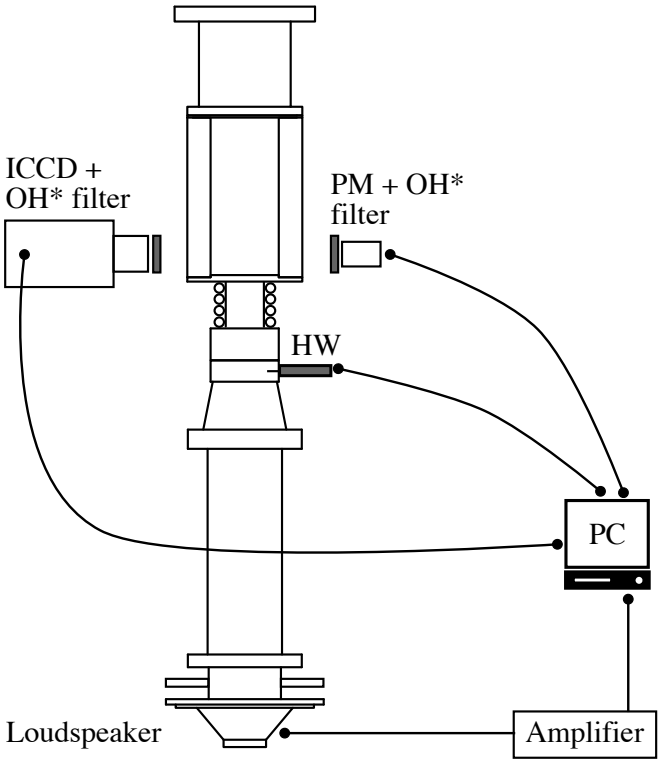

Figure 2.1: *Schematic of the main components used for flame transfer functions measurements and for flame imaging.*

erage value of the signal measured by the hot wire. Signals are generated and recorded by a National Instrument data acquisition card (PCI-MIO-16E-4) and post processed by the homemade LabVIEW routine. For these measurements, signals are sampled at a frequency $f_s = 8192$ Hz during $t = 4$ s.

2.1.1 Hot Wire anemometry

A constant temperature hot wire anemometer probe (Dantec Dynamics - Probe 55P16 with a mini-CTA 54T30) is used to measure the axial velocity component in the 22 mm diameter section downstream the first convergent unit shown in the schematic in Fig. 1.3. One recalls that the probes of the hot wire lie outside the boundary layer of the laminar flow in the region where the axial velocity has a top-hat profile. The distance between this probe and the swirler exit is 40 mm. Figure 2.2 shows two samples over 5 forcing periods of the velocity signals measured by the hot wire at $f = 120$ Hz and $f = 200$ Hz for a forcing level $u'/\overline{u} = 0.30$ RMS. The power spectral density shown at the bottom in Fig. 2.2 indicate that the velocity forcing signal is harmonic, with a small harmonic content of at least two orders of magnitude lower than the forcing level at the forcing frequency. The velocity on the left and the right in the top

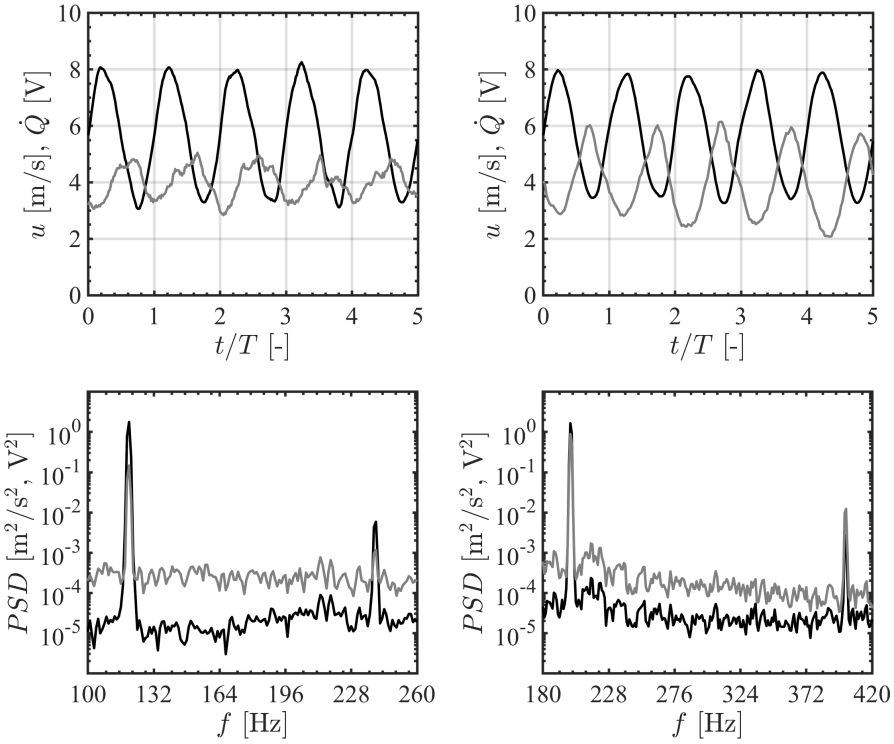

Figure 2.2: *Top: Examples of signals measured by the HW (black) and the PM (gray) for forcing frequencies $f = 120$ Hz (left) and $f = 200$ Hz (right) and for a forcing level $u'/\overline{u} = 0.30$ RMS. Bottom: corresponding power spectral densities.*

in Fig. 2.2 are also very close, indicating that the LabVIEW routine controlling the forcing level behaves well. One may conclude that the velocity modulation obeys to: $u(t) = \bar{u} + u'\sqrt{2}sin(\omega t)$. The calibration of the hot wire probe was carried out with a mixture of pure air. It was shown by Guiberti, 2015 that the response of the hot wire probe is nearly superimposed for mixtures of methane/air or for pure air mixtures, since the kinetic viscosity and the thermal conductivity of methane and air are close.

2.1.2 OH* chemiluminescence

For perfectly premixed conditions like those studied in this work, the OH* radical emission of the flame is a good measure of its heat release rate. This has also been verified for swirling premixed flames (Palies et al., 2010b) for which it has been checked that $\dot{Q}'/\bar{\dot{Q}} = I'_{OH^*}/\bar{I}_{OH^*}$, where I_{OH^*} is the light intensity collected. A photomultiplier (Hamamatsu H5784-04) equipped with a bandpass interferometric filter (Asahi Spectra ZBPA310) centered on 310 nm, with a 10 nm bandwidth, corresponding to the OH* emission wavelength (Gaydon, 1957), records light from the full combustion region. Examples of the

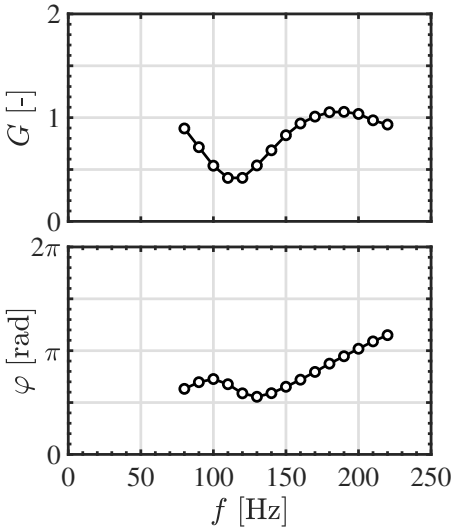

Figure 2.3: *Example of Flame Transfer Function result from the signals shown in Fig. 2.2. The forcing level is* $u'/\bar{u} = 0.30$ *RMS.*

signals measured by the PM are also shown in Fig. 2.2-top. Measurements are reported for forcing frequencies $f = 120$ Hz (left) and $f = 200$ Hz (right) and for a forcing level $u'/\bar{u} = 0.30$ RMS. In contrast to velocity signals, the heat release rate perturbations strongly differ in the two plots, both in terms of amplitude of perturbation and of phase shift with respect to the velocity signal. This is due to the delayed response of the flame to incoming perturbations (Crocco, 1951) and to the nonlinear response of combustion to flow perturbations (Bellows et al., 2006; Durox et al., 2009). These signals feature a larger harmonic content in the power spectra shown in Fig. 2.2. The main peak remains however at least one order of magnitude larger than the second harmonic. This will be reflected in different values for the gain and phase of the FTF. It is also evident that signals can be affected by noise. It is then necessary to apply proper signal processing in order to extract useful information from the signals recorded.

2.1.3 Signals post-processing

Once the desired forcing level is applied, the heat release rate and velocity fluctuations are recorded simultaneously to obtain the Flame Transfer Function (FTF). When this procedure is repeated for different forcing levels, the Flame Describing Function (FDF) is obtained. For all the FTF measurements conducted in this study, the signals from the HW and the PM are recorded over a duration $t = 4$ s at a sampling frequency $f_s = 8192$ Hz. The Cross Power Spectral Density (CPSD) and the Power Spectral Density (PSD) of these signals are obtained with a modified Welch periodogram method, dividing the signal into at least 8 segments windowed with an Hanning window and using a 50% overlap. This assures that at least 50 periods of oscillation are considered for

the average for each measurement, which is very important since signals are affected by noise. Examples of PSD from HW and PM measurements are shown in Fig. 2.2-bottom for forcing frequencies $f = 120$ Hz (left) and $f = 200$ Hz (right). As for the velocity power spectra, the heat release rate power spectra show a strong PSD peak at the excitation frequency. A smaller peak is observed at the first harmonic, at double the forcing frequency. The heat release rate fluctuation is stronger at $f = 200$ Hz than at $f = 120$ Hz, which reflects the complexity of the flame response to low frequency acoustic perturbations. This is best seen by determining the FTF/FDF as:

$$FDF = \frac{S_{xy}}{S_{xx}} = G(\omega, u'/\bar{u})exp(i\varphi(\omega, u'/\bar{u})) \tag{2.1}$$

where S_{xy} is the cross-power spectral density (CPSD) between the velocity $\bar{u}$ and the heat release rate I_{OH^*} signals and S_{xx} is the power spectral density (PSD) of the velocity signal. An example of FTF result is shown in Fig. 2.3. The gain of the FTF is much higher at $f = 200$ Hz than at $f = 120$ Hz as could be deduced from Fig. 2.2. At $f = 120$ Hz the FTF gain is at its minimum value, while it is almost maximum at $f = 200$ Hz. The phase-lag value are also different at the two frequencies. At $f = 200$ Hz, signals from the HW and the PM are in phase opposition ($\varphi = \pi$), while $\varphi \simeq \pi/2$ at $f = 120$ Hz.

2.2 LDV measurements

A 2-components LDV system, similar to the one used by Providakis, 2011; Mirat, 2015; Gaudron, 2018, is used to measure the axial, azimuthal and radial velocity downstream the outlet of the injector for selected configurations.

The two laser components of wavelengths $\lambda = 514.5$ nm (green component, axial velocity) and $\lambda = 488$ nm (blue component, azimuthal/radial velocity) are generated by a continuous 3 W Argon laser. Figure 2.4 shows a sketch of the LDV system from lateral (a) and top (b) views. Measurements with two laser components are conducted simultaneously 1.5 mm downstream the conical end piece of the central insert, which means that either the axial and azimuthal or the axial and radial velocities could be recorded at the same time. The burner is displaced along the axis 1 or 2 (Fig. 2.4) by an automatic controller by steps of 0.5 mm in the radial direction. The transmitting optical system is equipped with a Bragg cell at 40 MHz to discriminate negative and positive velocities. The laser leaves this system through an achromatic lens of focal length 250 mm. The distance between the two laser beams is 40 mm at the exit of the transmitting optic. This generates interference fringes spaced of 3.23 μm for $\lambda = 514.5$ nm (Mirat, 2015).

The flow is seeded with micrometric oil droplets of 3 μm diameter by a nebulizer fully described by Durox et al., 1999. When these particles cross the measure-

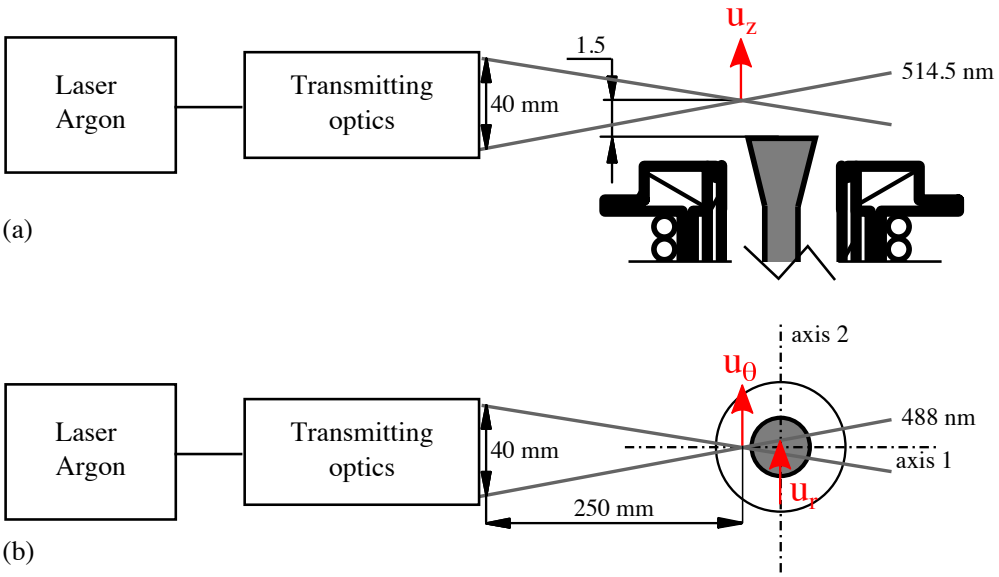

Figure 2.4: *Schematic of the setup used for the LDV measurements. (a) Lateral view showing the $\lambda = 514.5$ nm laser component used to measure the axial velocity. (b) Top view showing the $\lambda = 488$ nm laser component used to measure the azimuthal and radial velocities.*

ment volume, the scattered Mie signal is collected by the receiving optic of focal length 300 mm, placed at an angle of 30° with respect to the laser beam, by photomultipliers with narrow-band interference filters centered on the laser wavelengths. A frequency counter is used to deduce the velocity from Doppler bursts resulting from the droplets passage across the interfering region. The data collection rate is always greater than 10000 s^{-1} and for each measurement point at least 250.10^3 particles are considered, in order to obtain fully converged mean and root-mean-square (rms) values for the different components of velocity. The statistical bias is corrected by the transit time of each particle (Mirat, 2015).

An example of LDV measurements is reported in Fig. 2.5 for swirler SW_3 and an injector with $D_o = 20$ mm and $C = 10$ mm (Fig. 1.3). The maximum values of the axial and azimuthal velocity components are close to 10 m/s. These measurements also well highlight a recirculation region with negative axial velocities in the center of the jet. The corresponding swirl number deduced from Eq. (1.1) is $S = 0.80$. The shape of the RMS profiles of velocities, plotted in the left in Fig. 2.5, is the same for the three components. High RMS values are measured close to the injector outlet and close to the cone rim, while lower values are obtained in the central region of the jet, just behind the bluff-body.

It is important to underline that all the LDV measurements conducted in this

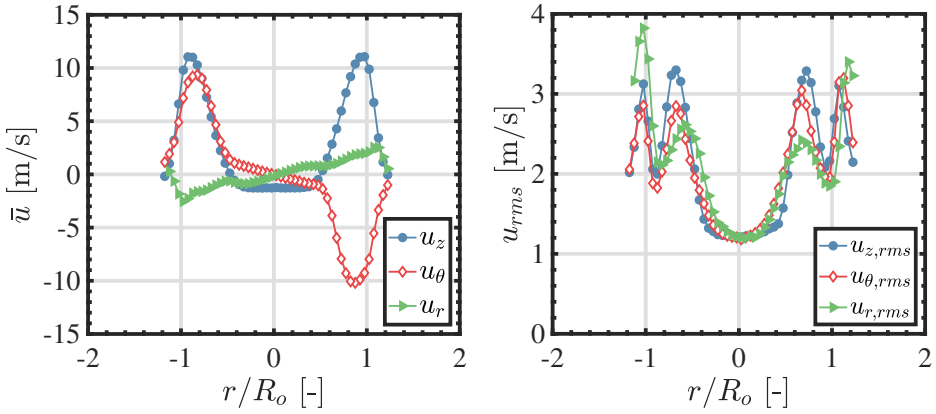

Figure 2.5: *Mean $\overline{u}$ and root mean square u_{rms} values of the axial, azimuthal and radial velocity components for steady operating conditions, measured by LDV at a distance of 1.5 mm from the top cone of the central rod. Measurements refer to a geometrical configuration with SW_3, $D_o = 20$ mm and $C = 10$ mm and to a bulk flow velocity $U_b = 5.44$ m/s.*

study are done without confinement, meaning that all the burner components downstream the injector exit are removed from the setup. This was necessary to get a good optical access to this region and have a good signal to noise ratio. The receiving optics is placed at an angle of 30° with respect to the laser beam and a large fraction of the field of view would be obstructed by the steel rods at the corner of the combustion chamber. LDV measurements are conducted only in cold flow conditions. Measurements performed in cold flow conditions in this study, are conducted with pure air. When these measurements are done to analyze the flow in reactive conditions, the missing mass flow rate of CH_4 is accounted for by increasing the mass flow rate of air, in order to keep a constant volume flow rate and the same bulk flow velocity U_b in the 22 mm diameter section at the convergent outlet.

2.3 PIV measurements

Particle Image Velocimetry (PIV) is used in this work to analyze the structure of the velocity field in different two-dimensional planes. This technique is widely used in fluid-dynamics and combustion and well described in the literature. The reader is referred for instance to the textbook from Raffel et al., 2007 for further information. In the following, only the specific settings of our setup are described.

To do PIV measurements, it is first necessary to seed the flow with particles. In this study, PIV measurements are conducted at steady conditions with and without combustion and also in cold conditions under external acoustic excitation. For measurements without combustion the same oil particles as for LDV

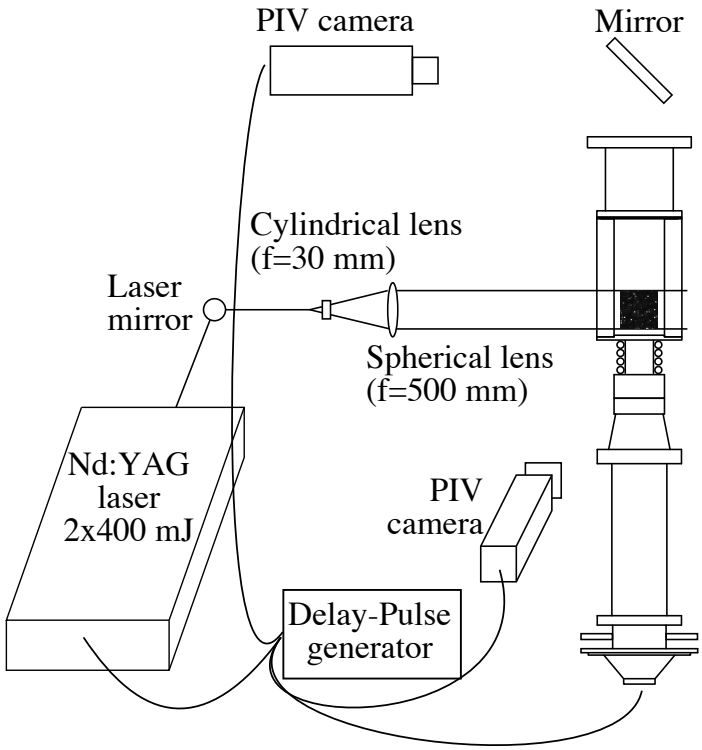

Figure 2.6: *PIV setup*

measurements are used to seed the flow. These liquid particles could not be used for measurements under reactive conditions since they evaporate through the flame front. In this case, flow seeding is obtained with solid ZrO_2 (Zirconium dioxide) particles of diameter $d \simeq 3$ μm, having a melting temperature of $T = 2988$ K. The Stokes number of these ZrO_2 and oil particles is small ($S_t \ll 1$), so that the velocity measured can be considered sufficiently close to the flow velocity.

The basic principles of the technique is described as follows. Two laser pulses, separated by a well controlled time delay Δt, illuminate the particles in a measuring plane. This plane is made by expanding the laser beam with a cylindrical ($f = 30$ mm) and a spherical ($f = 500$ mm) lens in a laser sheet of about 50 mm height and 1.5 mm width. A dual-shot CCD camera takes a picture at each of this two instances. One Mie scattering image for an axial and a transverse plane through the setup is shown in Fig. 2.7 when the cold flow is seeded with oil particles. A Mie scattering image is also shown in Fig. 2.8 for an axial plane with ZrO_2 particles. Figure 2.7 shows that seeding is distributed homogeneously in the cold flow. Figure 2.8 highlights that in the hot region of the flow the number of particles detected drops significantly due to thermal expansion of the flow through the flame. This leads to relatively low seeding

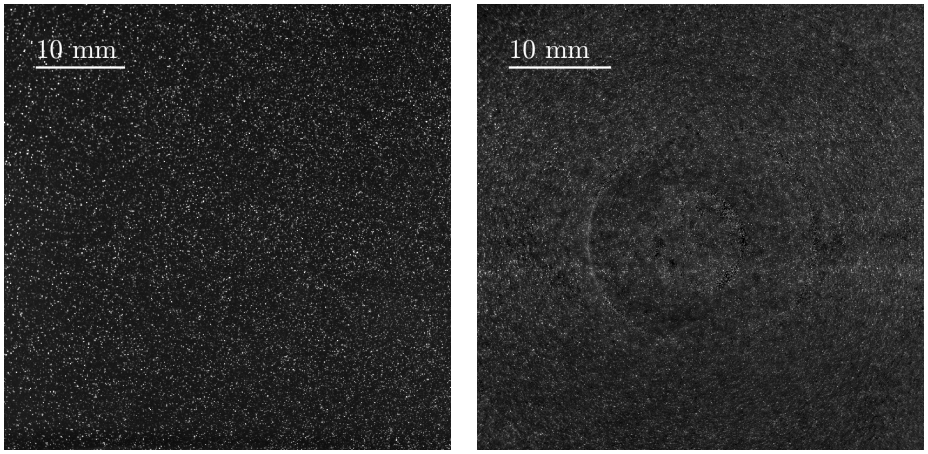

Figure 2.7: *Examples of Mie scattering images obtained under non-reactive conditions using oil seeding in an axial (left) or a transverse plane (right).*

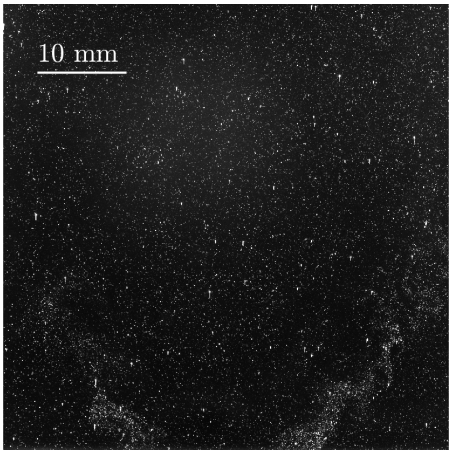

Figure 2.8: *Examples of Mie scattering images obtained under reactive conditions using ZrO_2 as seeding in an axial plane.*

rates in the central region of the flow. These pictures are then post-processed by a specific software. In particular, they are divided into a certain number of overlapping windows, each window having a certain number of particles inside it. The Dantec Dynamics software is used for images acquisition and images correlations to obtain the velocity. The resolution and precision of the measurements depends upon different factors, like the particle size, the quality of the seeding, the intensity of the laser sheet and the relation between the selected Δt and the range of investigated velocities (Raffel et al., 2007).

The 2D-2C PIV system is presented in Fig.2.6. It features a 2×400 mJ Nd:YAG laser doubled at 532 nm operated at 10 Hz and a 2048×2048 pixels CCD camera (Dantec Dynamics, FlowSense EO 4M). For measurements conducted in

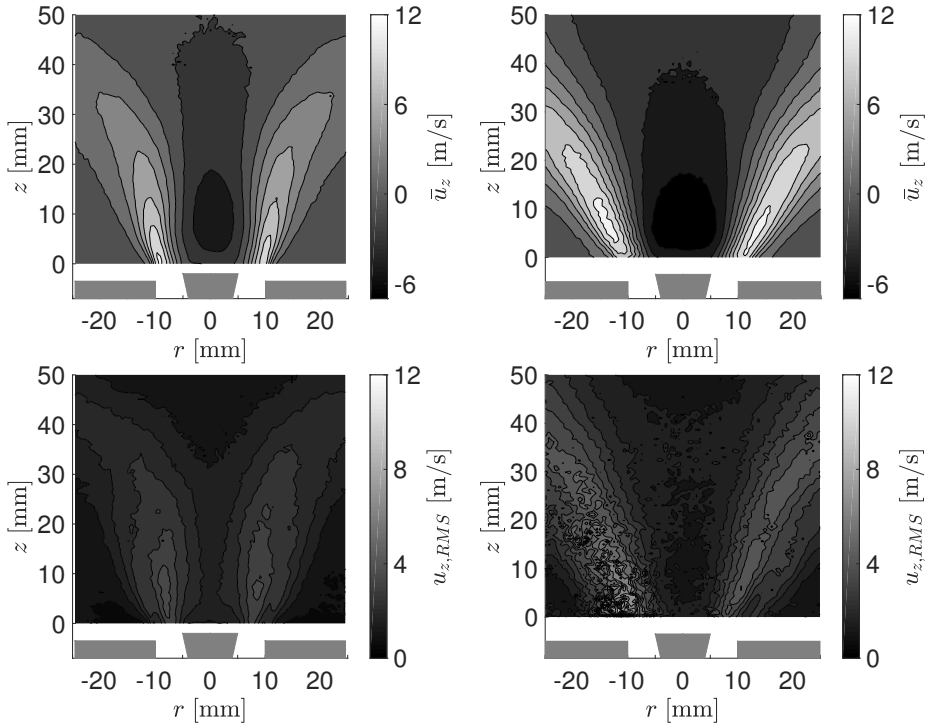

Figure 2.9: *Steady state scan of the mean (top) and root mean square RMS (bottom) axial velocity for swirler SW_3, $D_o = 20$ mm, $C = 10$ mm, $U_b = 5.44$ m/s obtained from post-processing of 800 PIV images. Left: cold flow conditions. Right: reactive conditions ($\phi = 0.82$).*

reactive conditions, a 10 nm bandpass filter centered at 532 nm was placed in front of the camera lens to avoid detecting light from the flame. A Delay-Pulse generator is used to synchronize the laser pulses and the camera apertures. Two different optical setups are used with a time interval between the two laser pulses $\Delta t = 10$ μs and a pixel pitch of 27.88 px/mm for measurements made in an axial plane crossing the burner axis and $\Delta t = 25$ μs and a pixel pitch of 40.14 px/mm for measurements made in a transverse plane at a distance of 2 ± 0.5 mm from the bluff-body.

In this last case, a mirror placed on top of the combustion chamber and inclined by an angle of 45° is used to visualize the horizontal laser sheet, which is obtained by a 90° rotation of the cylindrical lens as shown in Fig. 2.6. In both cases the laser sheet has a length/height of 50 mm and a thickness of about 1.5 mm in the region of interest. This large thickness helps minimizing out of sheet particle displacements of the swirling flow between the two laser pulses. Eight hundred images are taken to assure the convergence of the mean and rms values of the velocity field, which is computed from the cross-correlation of the PIV images by a three passes window deformation technique (from 64×64 pixels to 16×16 pixels interrogation areas), with an uncertainty of 0.1 pixel on

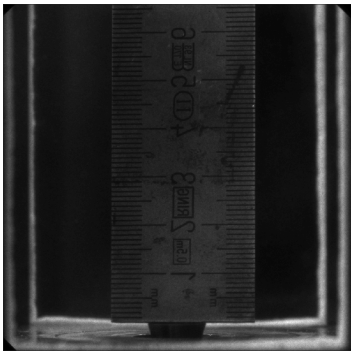

Figure 2.10: *Grid used to obtain flame dimensions.*

the calculated displacement.

Examples of measurements for the mean and root mean square RMS axial component of velocity are reported in Fig. 2.9 in steady cold (left) and hot (right) conditions. These measurements are conducted in the central axial plane. One can clearly observe the recirculation zone with negative velocities in the central region downstream the bluff-body, typical of swirling flows. This region is larger and longer in the right of Fig. 2.9 for reactive conditions. One can also identify the jets of high velocities at the sides of the central recirculation zones and observe that the radial expansion of the jet increases for reactive conditions. The RMS fluctuations feature high values in the shear layers of the flow, as reported also in Fig. 2.5 showing the LDV measurements.

2.4 Flame imaging

An intensified CCD camera (Princeton Instruments, PI-MAX 4, 1024×1024 pixels), mounted with an UV objective (Nikkor 105 mm f/4.5) is used to analyze the flame structures under steady and forced conditions. A narrow-bandpass filter (Asahi Spectra Co., ZBPA310) centered at 310 nm and with a 10 nm bandwidth is placed in front of the camera to detect the OH* chemiluminescence.
Figure 2.10 first shows a grid which is used in the image post-processing to detect the main dimensions of the flame. Figure 2.11 then shows examples of the OH* chemiluminescence signal recorded with the ICCD camera for a geometrical configuration with the swirler SW_3, $D_o = 20$ mm, $C = 10$ mm, a bulk flow velocity of $U_b = 5.44$ m/s and an equivalence ratio $\phi = 0.82$. Results are shown for steady (top) and forced (bottom) conditions. In this second case, the forcing frequency is $f = 185$ Hz, the forcing level is $u'/\bar{u} = 0.72$ RMS and only a selected phase in the forcing cycle is shown. For the phase-locked images, the ICCD camera is synchronized with the signal driving the loudspeaker (Fig. 2.1). A long exposure time of 20 ms is used to record the mean images.

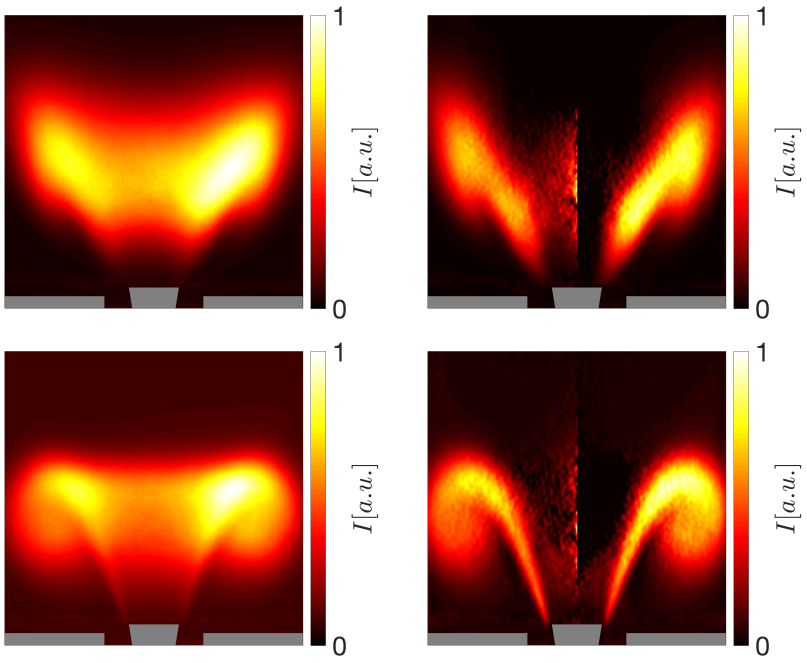

Figure 2.11: *OH* chemiluminescence for SW_3, $D_o = 20$ mm, $C = 10$ mm, $U_b = 5.44$ m/s, $\phi = 0.82$. Top row: without acoustic forcing. Bottom row: $f = 185$ Hz, $u'/\bar{u} = 0.72$ RMS. On the right an Abel deconvolution is applied to the line of sight integrated image shown on the left.*

The integration time needs to be reduced for phase-conditioned measurements in pulsed conditions with respect to the acoustic forcing signal. In these cases, an exposure time not exceeding $T/120$ was always selected, where $T = 1/f$ is the period of the harmonic forcing signal at the frequency f. In both cases, a hundred snapshot are averaged to obtain the final result.

The chemiluminescence signal shown in the left of Fig. 2.11 is integrated in the line of sight. Assuming that the flame is axisymmetric in average, an Abel deconvolution can be applied to the chemiluminescence images to get an information on the OH* light distribution in an axial slice of the flame in the symmetry axis (Poularikas, 2010). This is useful during images post-processing, for instance it allows to better determine the angle of the reaction layer at the base of the flame. An home-made Matlab routine is used to compute Abel transforms. Results are shown in Fig. 2.11-right. The high level of noise along the central axis is due to the mathematical formalism of the Abel transform that yields a singularity along the symmetry axis (Poularikas, 2010). Figure 2.12 shows 6 phase averaged pictures covering a full cycle of oscillation. The phase angle indicated on each picture in Fig. 2.12 is referred to the velocity signal recorded by the hot wire. The phase average imaging procedure is performed as follows.

When the flame is submitted to harmonic acoustic forcing, it oscillates at the forcing frequency. The harmonic forcing signal provided by the loudspeaker, is also used to trigger the ICCD camera. Each image in Fig. 2.12 is obtained by adding a constant time offset to the triggering signal. By recording simultaneously the velocity signal measured by the hot wire, each image is related to an instant in the cycle, as shown at the bottom in Fig. 2.12.

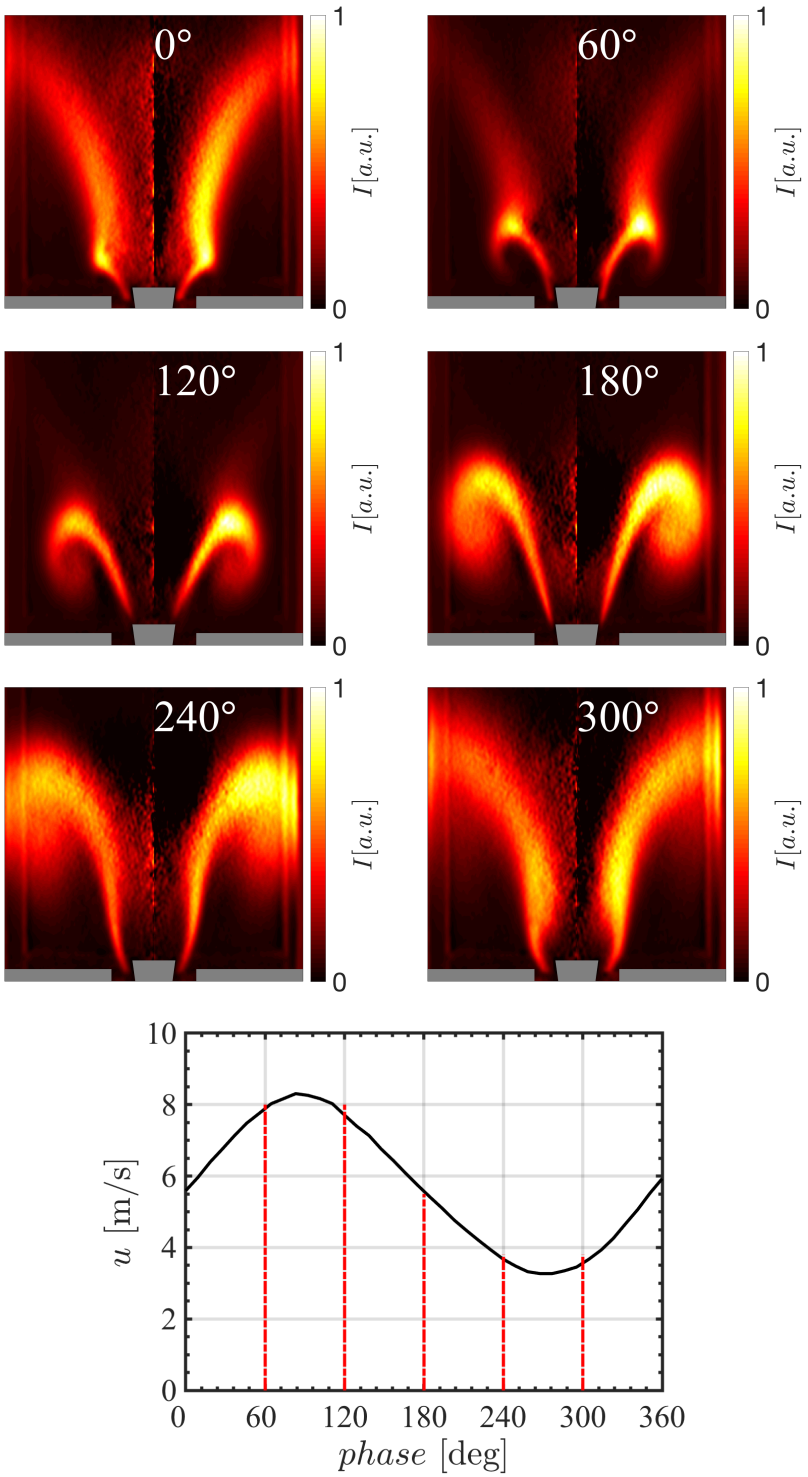

Figure 2.12: *Abel deconvoluted OH* chemiluminescence for SW_3, $D_o = 20$ mm, $C = 10$ mm, $U_b = 5.44$ m/s, $\phi = 0.82$. The flame is forced with a harmonic signal at $f = 185$ Hz and $u'/\bar{u} = 0.72$ RMS. The phase angle indicated on the figures is referred to the velocity signal recorded by the hot wire as shown in the bottom figure.*

Chapter 3

Numerical setup

This chapter is dedicated to the description of the numerical setup used throughout this work for the comparison between LES and experimental data. The code selected for the numerical simulations is briefly described. Simulations are carried out for one selected geometry of the injector, which is described in the second section of the chapter; together with details on the mesh and the boundary conditions applied. A comparison between numerical simulations and measurements for the flow in absence of acoustic forcing is presented in the last section of the chapter.

3.1 Large Eddy Simulations with AVBP

Large Eddy Simulations (LES) are dedicated to solve the turbulent compressible Navier-Stokes equations and are an intermediate numerical concept between Direct Numerical Simulations (DNS) and the Reynolds Averaged Navier-Stokes (RANS) methodology (Poinsot and Veynante, 2005).

A DNS solves the full instantaneous Navier-Stokes equations explicitly, without any modeling. RANS simulations compute only averaged values, without solving turbulent quantities. LES is an intermediate concept, since it resolves the large turbulent scales and models the small scales by applying a filter (Poinsot and Veynante, 2005). RANS, LES and DNS properties are summarized in terms of energy spectrum in Fig. 3.1. All spatial frequencies in the spectrum are resolved in direct numerical simulations. Only the largest ones, up to a cut-off wave number k_c, are computed in LES while the others are modeled. Turbulence is fully modeled in RANS.

In this thesis, LES are carried out with AVBP, a parallel CFD code developed by Cerfacs in partnership with IFP Energies Nouvelles (Schönfeld and Rudgyard, 1999; Moureau et al., 2005; Sengissen et al., 2007). AVBP solves the three-dimensional laminar and turbulent compressible non-reactive and re-

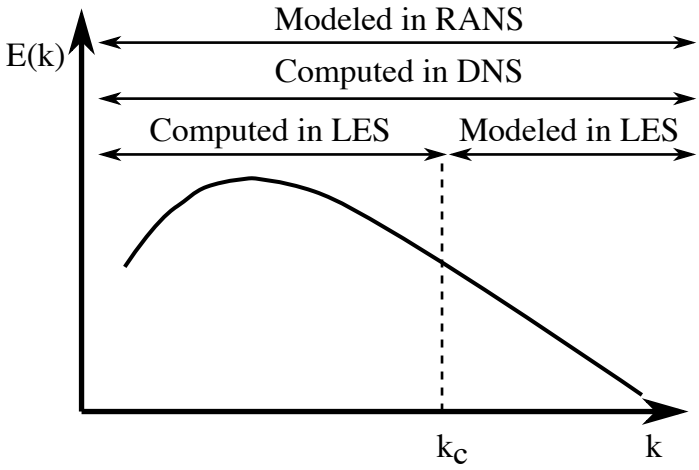

Figure 3.1: *Turbulence energy spectrum plotted as a function of wave numbers (proportional to the inverse of the length scales). RANS, LES and DNS are summarized in terms of spatial frequency range. k_c is the cut-off wave number used in LES (log-log diagram). Reproduced from Poinsot and Veynante, 2005.*

active Navier-Stokes equations, handling unstructured grids of any cell type. The code is not described here, as no developments have been made in this code during this work. The interested reader is referred to the cited references. Calculations are performed only for a non-reactive case and the AVBP code was chosen for its ability to retrieve the largest unsteady flow structures and the propagation of acoustic waves, two mandatory characteristics for the study that we wish to conduct.

3.2 Geometry, mesh and boundary conditions

The geometry sketched in Fig. 3.2 is selected for comparison between numerical simulations and measurements. The main geometrical parameters of the configuration are the following. The swirler vane SW_3 is selected. It is set at $\delta = 50$ mm upstream the injector outlet section. The injector outlet diameter is $D_o = 20$ mm. The injector unit is also equipped with the 6 mm diameter central bluff body with a $C = 10$ mm diameter end piece. One is referred to Fig. 1.3 for a detailed view of the injector geometry.

The inlet and outlet of the simulated domain correspond, respectively, to the end of the first convergent unit and the exit of the convergent exhaust on top of the combustion chamber, as shown in Fig. 3.2. Given that the first measurement point for comparison with experiments is at the hot-wire location, it seems reasonable to not take into account the long upstream plenum in the simulation and thus reduce the computational cost. The region of the experimental setup, corresponding to the simulated geometry, together with the fluid

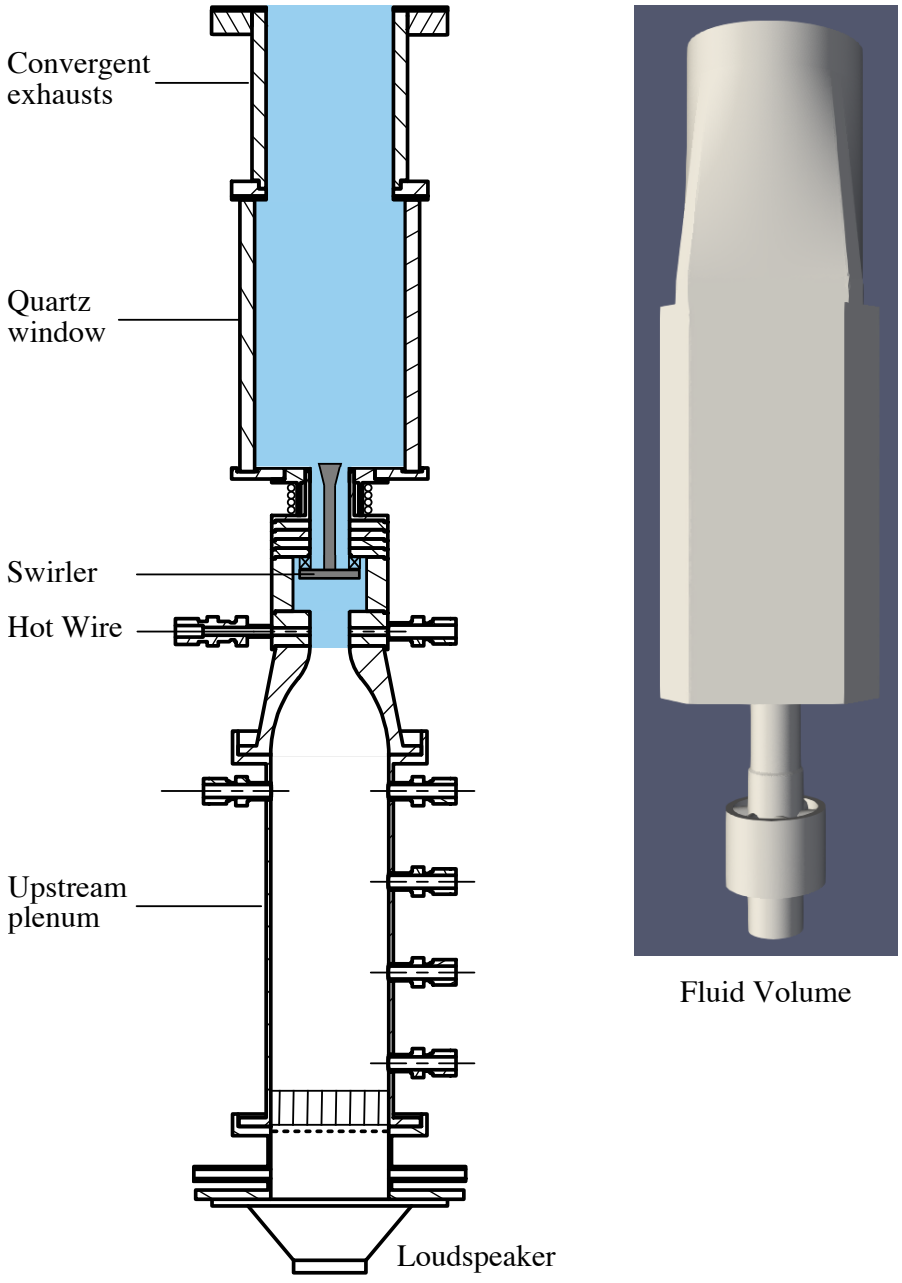

Figure 3.2: *Left: sketch of the burner geometry. Highlighted in blue, the region of the flow selected for the LES. Right: fluid volume generated with Inventor corresponding to the area highlighted in blue on the left.*

volume generated by the CAD software Inventor, are shown in Fig. 3.2.

A cut of the simulated geometry showing the mesh is also displayed in Fig. 3.3. The same figure also shows a zoom, focusing on the refined zones in the injection tube and at the chamber inlet. Full credits for the mesh of this geometry are to be given to F. Dupuy, a Ph.D. student at Cerfacs collaborating on this project by making reactive simulation of this same configuration. The fully unstructured grid is composed of 19.1 million cells corresponding to 3.4 million nodes, with refinement regions inside the swirler vanes and in the injector. The six radial vanes of 6 mm diameter are resolved by circa 1 million elements. The full injector, from the swirler up to the combustion chamber backplane, is resolved by about 5.5 million cells.

A small difference between the geometrical configuration depicted in Fig. 1.3 and that in Fig. 3.2 is the distance between the top cone of the central bluff body and the chamber backplane. This distance is equal to 2.5 mm in Fig. 1.3-a, since most of the injector configurations analyzed in this work feature a central insert with the tip of the top cone lying 2.5 mm above the combustion chamber backplane. The geometry simulated with AVBP features a slightly shorter distance of 1.5 mm, due to a reduced length of the central rod. All the remaining dimensions of the burner are not modified. This small geometrical difference is due to the fact that the NoiseDyn setup was shared between this thesis work and that of R. Gaudron (Gaudron, 2018). In Gaudron's work, this slightly shorter central rod is used. Many measurements conducted in common with R. Gaudron at the beginning of this work were done on this setup. This setup has also already been used as a validation tool for the numerical simulations conducted in the thesis work of M. Merk (Merk, 2018). Due to the abundance of experimental data on the flow field with a rod tip 1.5 mm above the injector plane, we also selected this geometry for the simulations conducted in this thesis work and in that of F. Dupuy working at CERFACS. In this work, simulations are conducted only for cold flow conditions, while F. Dupuy is working on simulations in reactive conditions. In the following, only when there could be a doubt about the value of the distance between the cone and the chamber backplane, its value will be specified.

The inlet and outlet boundary conditions are imposed through the non-reflecting Navier-Stokes Characteristic Boundary Condition (NSCBC) formulation (Poinsot and Lele, 1992), which avoids acoustic reflection by the use of a relaxation coefficient (Selle et al., 2004). This is an important aspect for the acoustically pulsed simulations presented in Chapter 7. The relaxation coefficient should be higher than zero in order to avoid drift of mean quantities (Poinsot and Lele, 1992), but low enough to avoid acoustic reflections on the boundary. Values used for reflection coefficients are indicated in Tab. 3.1. It will be shown in Chapter 7 that these selections let us match the experimental data in terms of

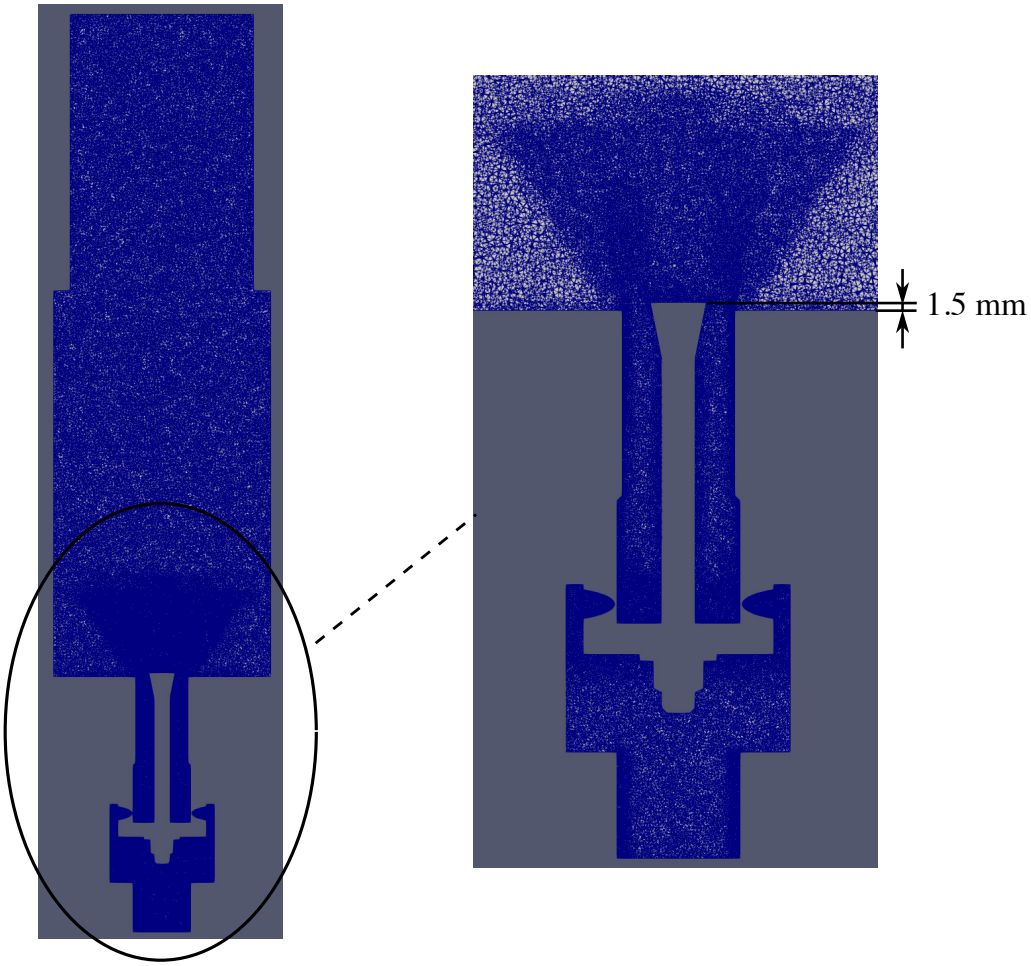

Figure 3.3: *Left: axial cut of the simulated geometry showing the mesh. Right: zoom showing the refined zones over the injector section.*

Table 3.1: *NSCBC conditions applied at the boundaries*

Patch	Boundary condition	Relaxation coefficient	Physical parameters
Inlet	Top-hat velocity profile (RELAX_UVW_T_Y)	$200s^{-1}$	$Q = 2.07\ m^3s^{-1}$ $T = 293$ K
Outlet	Target pressure (RELAX_P_3D)	$100s^{-1}$	$p = 101325$ Pa
Walls	No-slip adiabatic		

mean and oscillating quantities. At the inlet of the domain, a top-hat velocity profile like the one found in the experiments, is imposed. As in the experiment, the bulk flow velocity at a pressure $p_{atm} = 101325$ Pa and at a temperature $T = 293$ K, is set to a value $U_b = 5.44$ m/s. At the outlet of the domain the same atmospheric pressure is prescribed. Finally, all the solid walls are treated with a no-slip adiabatic boundary condition (Tab. 3.1). No attempt was made in this work to impose the correct thermal boundary condition (Mercier et al., 2016) as only cold flow simulations are envisaged.

The numerical integration relies on a two-step Taylor-Galerkin weighted residual central distribution scheme with a third order precision in space and time (Colin and Rudgyard, 2000). The Sigma model, developed by Nicoud et al., 2011, is used as a subgrid scale model for turbulent fluctuations.

3.3 Comparison with experiments

Simulation conducted with this numerical setup are validated against experimental data in the absence of external forcing. For these comparisons, the averaging LES time amounts to 50 ms. At first, LES data are compared to LDV measurements in Fig. 3.4. It is important to remember that the LDV measurements are conducted without confinement for optical reasons. Nonetheless, the average axial, azimuthal and radial velocity profiles obtained with LDV or LES compare well in the left of Fig. 3.4. The LES well captures both the shape and the amplitudes of the velocity profiles. The root-mean-square (rms) values are also compared in the right of Fig. 3.4. These quantities are generally more difficult to capture by LES. The shape of the rms profiles are here well captured by the simulation. The rms velocity values show a peak in the shear layers, close to the rim of the injector and near the central cone, in both the LDV and LES data. The rms velocities are underestimated by LES, especially in the central region of the jet in the wake of the bluff-body. One reason might be that the relatively short time in the LES over which averages were made is not long enough to converge toward the correct average values in this region characterized by very low recirculation velocities. The overall comparison yields, however, satisfying agreement for the cold flow condition explored.

LES data are compared to PIV measurements in Figs. 3.5 to 3.7. Figure 3.5 shows velocity fields in an axial plane (top) and in a transverse plane at a distance of 2 mm from the bluff-body. To take into account the fact that the PIV laser sheet has a thickness of about 1.5 mm, the LES results are obtained by averaging eleven equally separated cuts, from -0.75 mm to $+0.75$ mm with respect to the central one. The transverse scans in Fig. 3.5, show the velocities in the x direction. For a coordinate $x = 0$, this velocity would correspond to the azimuthal velocity, while for $y = 0$ it corresponds to the radial velocity.

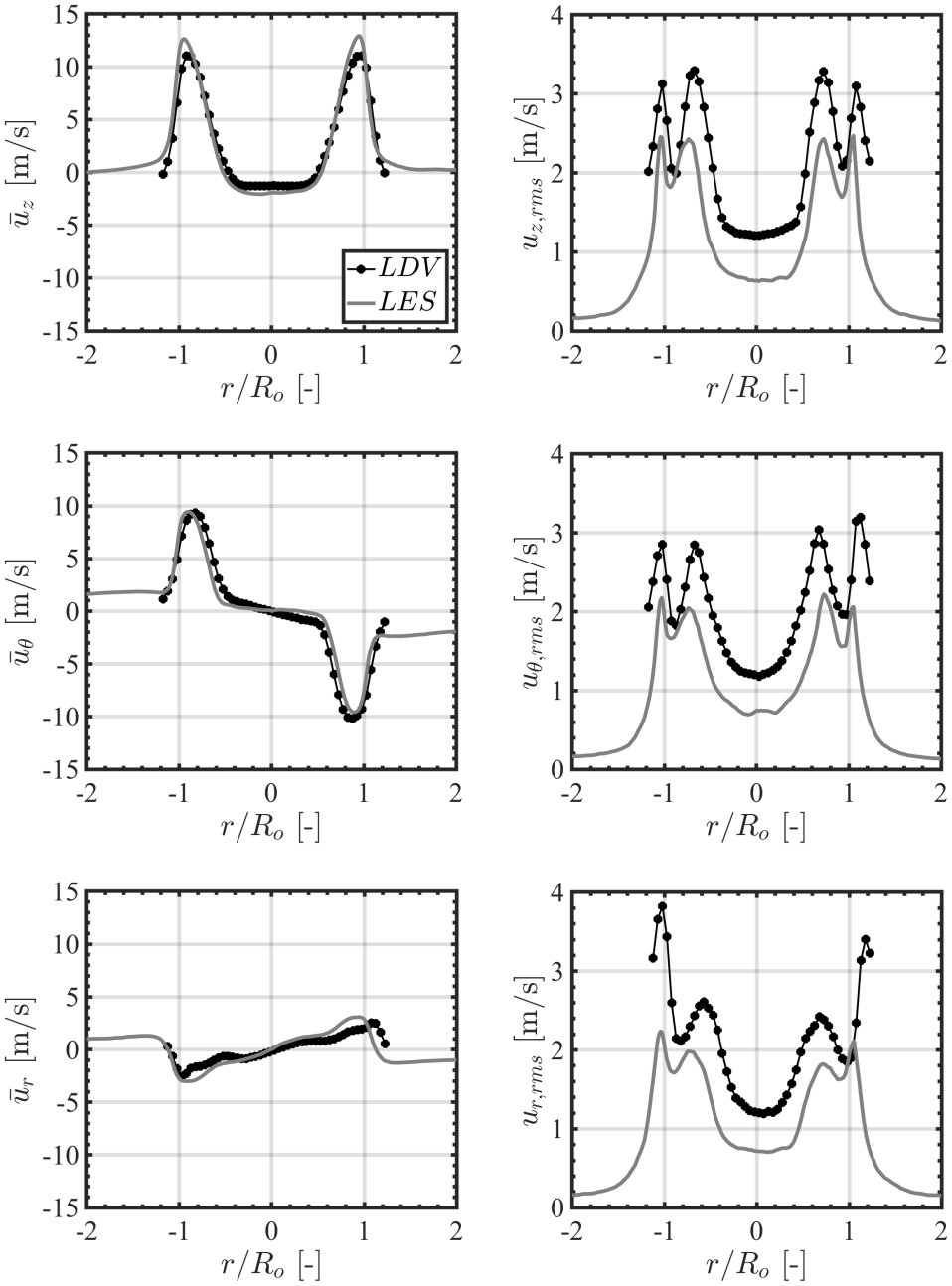

Figure 3.4: *Cold flow, steady state comparison of the axial (top), azimuthal (center), and radial (bottom) velocity profiles obtained with LDV measurements and LES at a distance of* 1.5 *mm from the bluff-body for the configuration of interest:* SW_3, $D_o =$ 20 *mm*, $C = 10$ *mm*, $\delta = 50$ *mm. Left: mean values. Right: RMS values.*

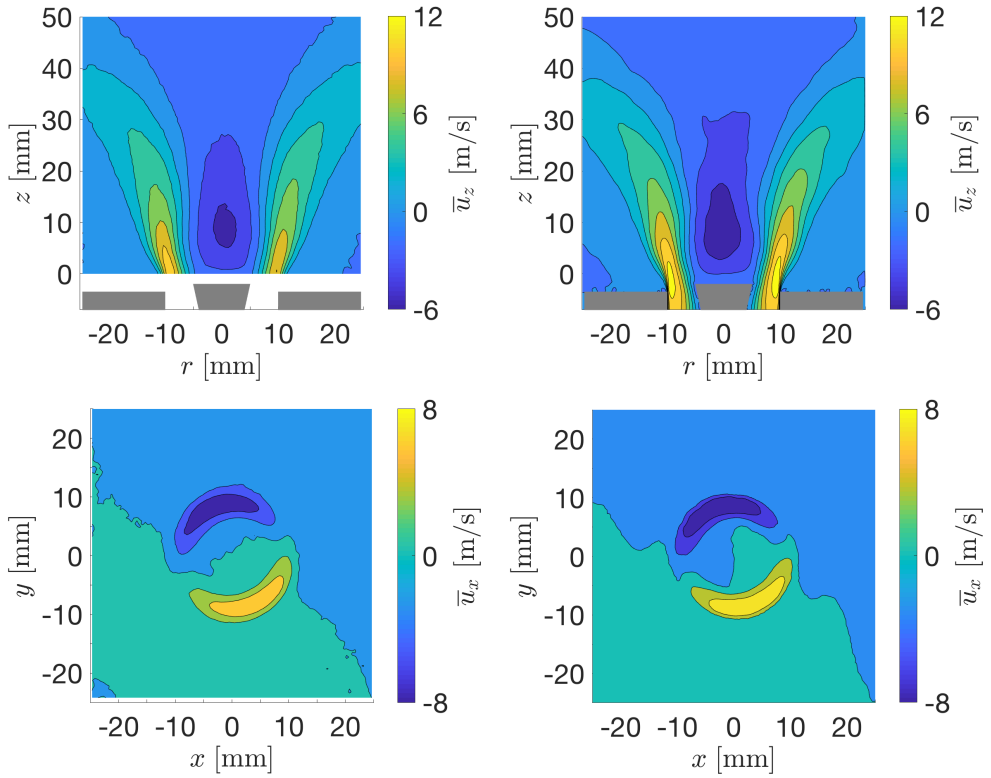

Figure 3.5: *Top: cold flow, steady state velocity field in an axial plane crossing the burner axis obtained from PIV measurements (left) and LES (right). Bottom: cold flow, steady state velocity field in a transverse plane at a distance of 2 mm from the bluff-body obtained from PIV measurements (left) and LES (right).*

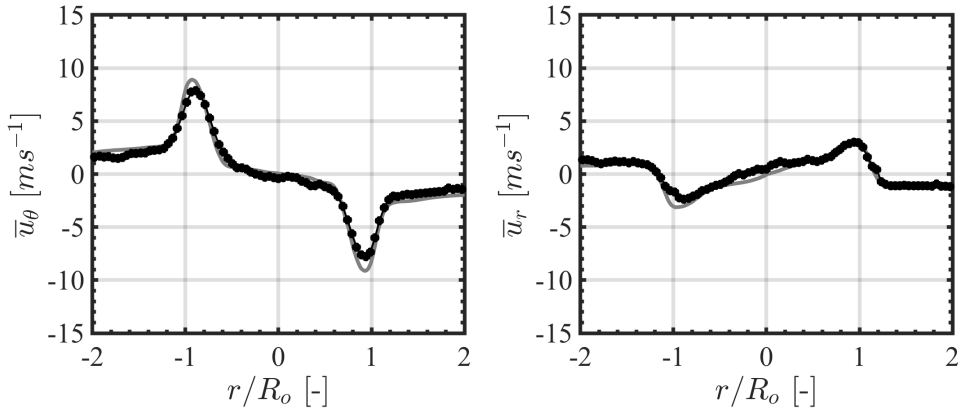

Figure 3.6: *Cold flow, steady state comparison of the azimuthal and radial velocity profiles obtained with PIV measurements and LES at 2 mm from the bluff-body. Configuration studied: SW_3, $D_o = 20$ mm, $C = 10$ mm, $\delta = 50$ mm.*

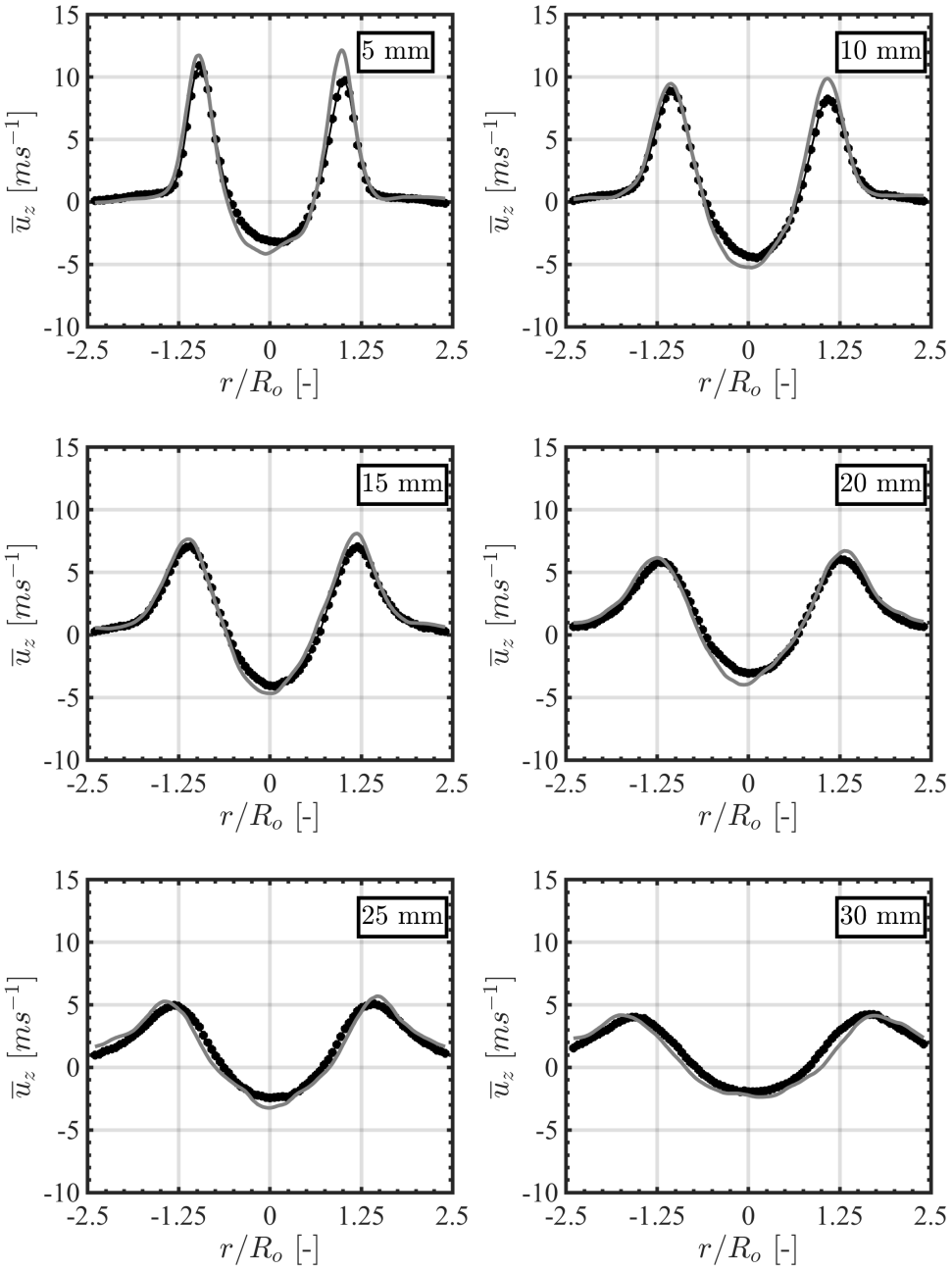

Figure 3.7: *Cold flow, steady state comparison of the axial velocity profiles obtained with PIV measurements and LES at different distances from the bluff-body. Configuration studied: SW_3, $D_o = 20\ mm$, $C = 10\ mm$, $\delta = 50\ mm$.*

Azimuthal and radial velocity profiles extracted from PIV and LES are compared in Fig. 3.6. These pictures show these profiles at a distance of 2 mm downstream the bluff-body. The shape of both profiles match very well, and only a slight overestimation of the peak velocities is observed with LES results. The axial velocity scans match well in the top of Fig. 3.5. One needs to pay attention to the fact that, in these two pictures, the coordinate z starts at a distance of $\simeq$ 2 mm from the bluff-body, corresponding to the first point measured by PIV. The inner recirculation zone with negative velocities is well captured by the LES. Also the spreading of the jet is well retrieved. This is confirmed in Fig. 3.7, showing radial profiles of the axial velocity at different distances z = 5, 10, 15, 20, 25 and 30 mm above the tip of the central bluff body. Axial velocity profiles obtained by PIV or by LES compare well.

3.4 Conclusions

LES are performed with the AVBP code and compared with measurements for one configuration of the injector featuring swirler SW_3, an injector outlet diameter D_o = 20 mm and a central insert ended by a cone of C = 10 mm. In the explored configuration, the conical end piece protrudes 1.5mm in the combustion chamber. The same configuration was used in the thesis of R. Gaudron and M. Merk (Gaudron, 2018; Merk, 2018). LES well reproduce the cold flow field of the configuration explored in the axial and transverse planes at which measurements and simulations were compared. This numerical setup is also used in Chapter 7 to investigate how a modulation of the flow rate alters the injector dynamics and the flow field in the combustion chamber.

Chapter 4

Flow and flame properties - without acoustic coupling

This chapter is dedicated to the analysis of steady mean flow and flame properties. A detailed investigation of the effects of modifications of the swirler and injector geometries is conducted. At first, a stabilization chart is obtained, separating three main regions where flames are respectively flash-backing into the injector, well-stabilized in the combustion chamber or have an elongated shape. These different shapes depend on a normalized flow passage area and on the swirl number. The analysis for well-stabilized flames is then taken to the next level, by analyzing the mean axial and transverse velocity fields and the flame structures, for some selected configurations.

4.1 Burner stabilization chart

The experimental setup used for the analyses described in this chapter is shown in Fig. 1.3. It was fully described in Chapter 1. Each injector could be equipped with a different swirling vane SW placed at a distance δ from the injector outlet, a different nozzle tube of diameter D_o and a different conical end piece of diameter C at the top of the central bluff body.

The different configurations analyzed are summarized in Table 4.1. Five different radial swirlers with tangential inlets, described in Section 1.2.1, are tested together with different values of the injector exit diameter D_o = 18, 20 and 22 mm and of the conical end piece diameter C = 10, 12 and 14 mm. These geometrical modifications lead to different values of the cross section area A_2 at the exit of the injector, while the cross section area $A_1 \simeq 380$ mm^2 at the hot wire location is fixed for all configurations.

It is known that the swirl number S controls the stabilization of swirling flames

Table 4.1: *Configurations explored. SW: Swirler design: D_o: injection tube diameter [mm], C: conical end piece diameter [mm], δ : distance between the swirler exit and the injection plane outlet [mm], U_b: bulk flow velocity at the convergent outlet [m/s], A_1/A_2 : normalized injector cross section area based on hydraulic diameters. S^* : Estimated swirl number. S : Swirl number deduced from LDV or PIV measurements.*

SW	D_o	C	δ	U_b	A_1/A_2	S
0	22	14	50	5.44	4.84	0.20
1	18	12	50	5.44	8.60	0.54*
1	18	14	50	5.44	13.44	0.48*
1	20	12	50	5.44	5.36	0.63
1	22	10	50	5.44	2.86	0.75*
1	22	12	50	5.44	3.66	0.71
1	22	14	50	5.44	4.84	0.65*
2	18	12	50	5.44	8.60	0.59
2	18	14	50	5.44	13.44	0.52*
2	20	10	50	5.44	4.00	0.73
2	20	12	50	5.44	5.36	0.69
2	20	14	50	5.44	7.56	0.63
2	22	10	50	5.44	2.86	0.84*
2	22	12	50	5.44	3.66	0.79
3	18	12	50	5.44	8.60	0.60
3	18	14	50	5.44	13.44	0.55*
3	20	10	35	5.44	4.00	0.80*
3	20	10	40	5.44	4.00	0.80*
3	20	10	45	5.44	4.00	0.80*
3	20	10	50	5.44	4.00	0.80
3	20	12	50	2.72	5.36	0.73*
3	20	12	50	4.08	5.36	0.73*
3	20	12	50	5.44	5.36	0.73
3	20	14	50	5.44	7.56	0.64*
3	22	10	50	5.44	2.86	0.86*
3	22	12	50	5.44	3.66	0.81
3	22	14	50	5.44	4.84	0.80
4	22	14	50	5.44	4.84	0.95*

and that changes in this quantity modify the flame mean and dynamic properties. To obtain the swirl number, LDV or PIV measurements of the axial u_z and azimuthal u_θ velocity components are carried out for the set of geometrical configurations indicated in Tab. 4.1 without star ($*$). The data issued from LDV and PIV measurements are used to determine the swirl number at the

injector outlet as:

$$S = \frac{2}{D_o} \frac{\int u_\theta u_z r^2 dr}{\int u_z^2 r dr}. \tag{4.1}$$

The values found for the swirl number are also indicated in the last column in Table 4.1 with a relative precision ±3% taking into account uncertainties on the measurements. For all other remaining configurations tested in this study, the analytic expression Eq. (1.5) is used to estimate the swirl number S^*.

Figure 4.1 shows, as an example, the LDV profiles obtained for three of the different configurations analyzed. LDV measurements are conducted, in cold flow conditions, 1.5 mm above the top cone of the central bluff-body (see sec. 2.2 in Chapter 2). The mean axial velocity profiles $\overline{u}_z$, Fig. 4.1-left, feature a central recirculation zone with slightly negative velocities, while the mean azimuthal velocities $\overline{u}_\theta$, Fig. 4.1-right, have a Rankine like shape profile in the center part of the flow.
We first consider the case when the swirler design SW is modified, but the cross-section area at the exit of the injector A_2 is fixed. The mean axial velocity $\overline{u}_z$ profile does not change, while the peak of the mean azimuthal component $\overline{u}_\theta$ augments from SW_1 to SW_2 and shifts to a slightly higher radial position. This is due to the increase of the distance $2H$ between the axes of the tangential inlets of the swirling vane. This leads to an increase of the swirl number S for SW_2 compared to SW_1. We now examine the case when the swirler design SW is fixed, but the cross-section area at the exit of the injector A_2

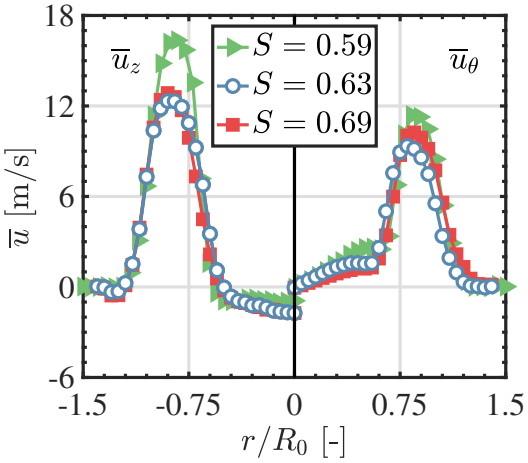

Figure 4.1: *Mean axial $\bar{u}_z$ and azimuthal $\bar{u}_\theta$ velocity profiles deduced from LDV for three selected configurations: SW_1, $D_o = 20$ mm, $C = 12$ mm (blue), SW_2, $D_o = 20$ mm, $C = 12$ mm (red), SW_2, $D_o = 18$ mm, $C = 12$ mm (green). The distance $\delta = 50$ mm and the bulk flow velocity $U_b = 5.44$ m/s at the hot-wire location, are fixed.*

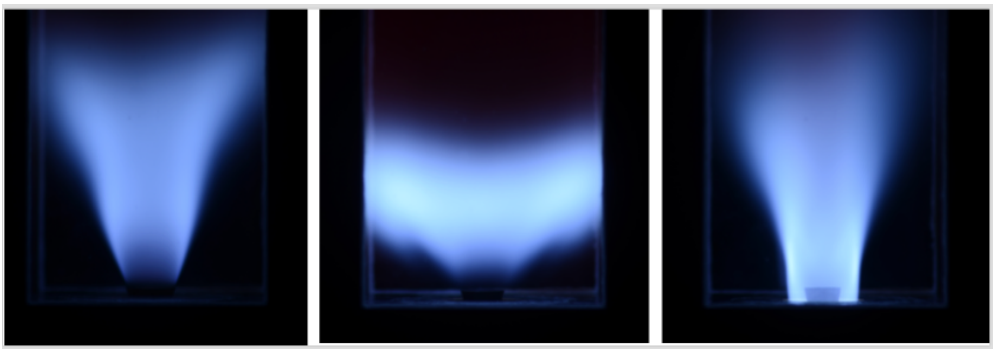

Figure 4.2: *Swirl number effect on flame stabilization. (a) SW_1, D_o = 18 mm, C = 14 mm, S=0.48*, elongated flame close to blow off. (b) SW_3, D_o = 20 mm, C = 12 mm, S=0.73, well-stabilized flame. (c) SW_3, D_o = 22 mm, C = 10 mm, S=0.86*, flash back. The equivalence ratio $\phi = 0.82$, the bulk flow velocity $U_b = 5.44$ m/s at the hot-wire location and the distance $\delta = 50$ mm, are fixed.*

is reduced. This corresponds to the data in red and green in Fig. 4.1. The azimuthal velocity $\overline{u}_\theta$ profile does not change much in this case, while there is a clear increase of the peak axial velocity $\overline{u}_z$, which leads to a strong reduction of the measured swirl number S between the two cases. From Table 4.1, one can see that the swirl number increases from swirler SW_0 to SW_4 when the cross-section area at the exit of the injector A_2 remains constant. Once again, this is due to the increase of the distance $2H$ between the axes of the swirler tangential inlets (see Fig. 1.4). For a fixed swirler design, the swirl number S increases if the injection nozzle diameter D_o increases or if the diameter C of the conical end piece decreases, i.e. when the flow passage area A_2 in the injection tube increases. This leads to a decrease in axial velocity with almost constant azimuthal velocity.

Flame stabilization is now investigated for the different injectors tested. Three stabilization modes are identified depending on the value of the swirl number S and the normalized injector nozzle cross section area A_1/A_2. These three regimes are presented in Fig. 4.2. Close to blow-off, when the swirl number is too low, the flame is elongated in the downstream direction as in the left image in Fig. 4.2 (a). In the middle image, when the swirl number is high enough, the flame is well stabilized inside the combustion chamber and has a compact "V" shape. In the right image, when the swirl level is too high, flash back takes place and the flames protrudes inside the injector.

The stabilization chart in Fig. 4.3 delineates the different regimes observed for the injectors tested in Tab. 4.1. When the swirl number is between 0.5 and 0.8, flames are well-stabilized over a wide range of injector dimensions and for a wide

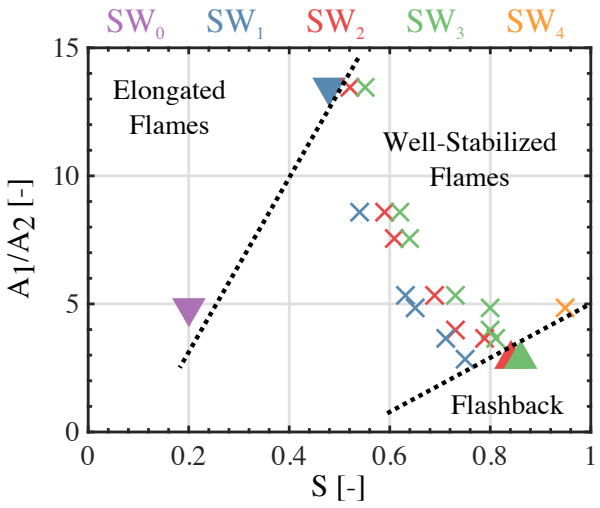

Figure 4.3: *Stabilization chart plotting different flame regimes as a function of the normalized flow passage area ratio A_1/A_2 and the swirl number S. The equivalence ratio $\phi = 0.82$, the bulk flow velocity $U_b = 5.44$ m/s at the hot-wire location and the distance $\delta = 50$ mm are fixed.*

set of swirler designs. When $S < 0.5$, the shape of the flame becomes elongated and one approaches the blow-off limit. When $S > 0.8$, flashback inside the injector can occur. As shown in Fig. 4.3, these critical boundaries also depend on the ratio A_1/A_2. It is worth recalling that these experiments were conducted at a fixed equivalence ratio $\phi = 0.82$ and bulk flow velocity $U_b = 5.44$ m/s and these boundaries obviously depend on these operating conditions and on the setup used in this study.

4.2 Mean flow properties

The mean flow properties are analyzed by comparing PIV results in an axial plane and in a transverse plane for four geometrical configurations of the injector as shown in Fig. 4.4. The first two rows in Fig. 4.4 show results obtained for fixed injector geometries with $D_o = 22$ mm and $C = 14$ mm but different swirler designs SW_0 and SW_3 and leading to different swirl numbers $S = 0.20$ and $S = 0.80$. Swirler SW_0 features radial injection channels aligned with the radial direction and, as a consequence, velocities in the transverse plane are much lower compared to those measured for SW_3, featuring injection channels shifted from the radial direction. This is also highlighted in Fig. 4.6-left, showing the azimuthal velocity profiles obtained from the transverse PIV results at 2 ± 0.5 mm above the bluff body. The central recirculation region is concentrated in a small area in the wake of the central bluff-body in the top row of Fig. 4.4, while it is much larger and extends further downstream in the second row obtained for swirler SW_3. When the swirl number is high enough,

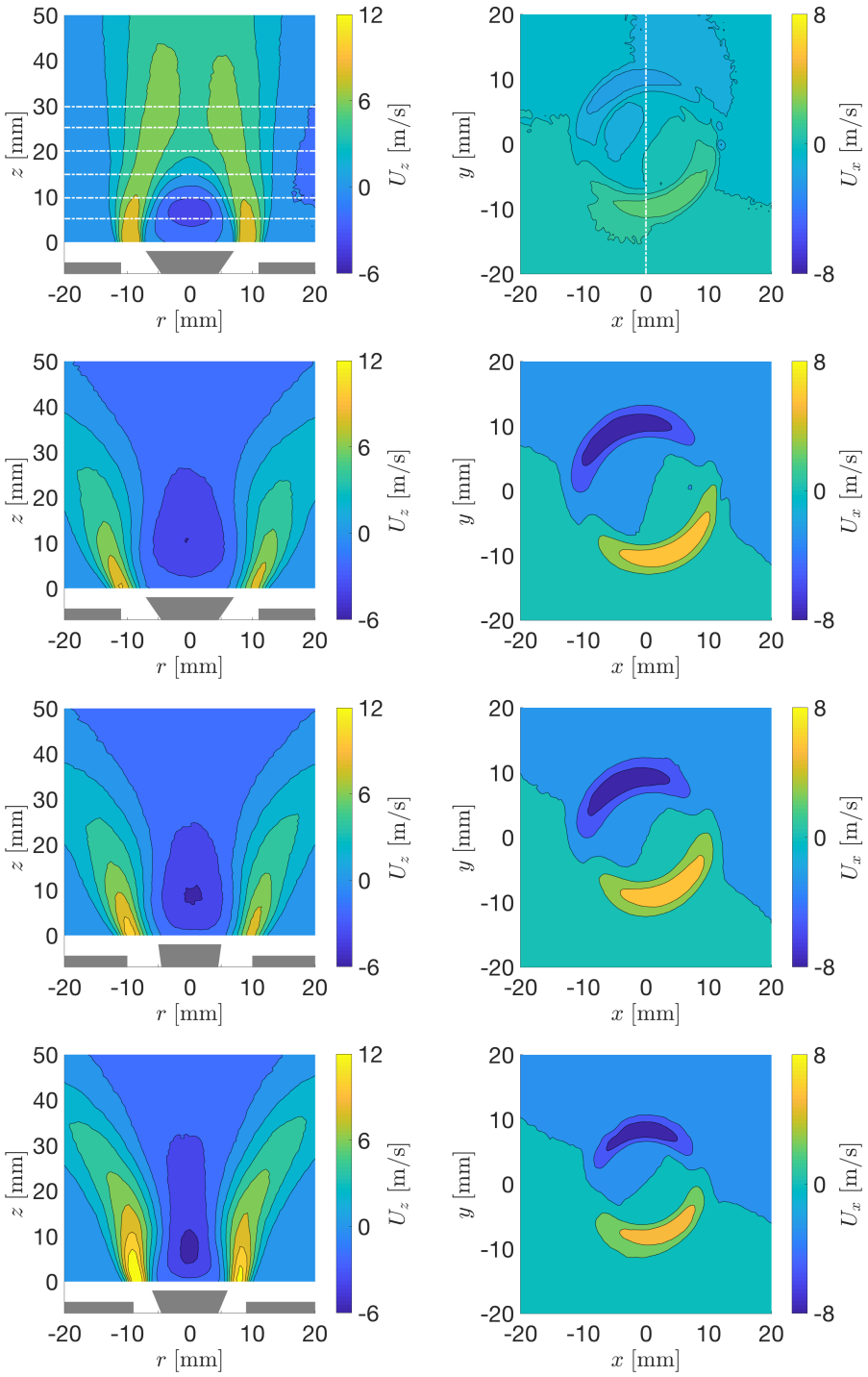

Figure 4.4: *Cold flow velocity field in an axial (left) and a transverse (right) plane obtained from PIV measurements for four different injectors. First row:* SW_0, $D_o = 22$ *mm*, $C = 14$ *mm*, $S = 0.20$. *Second row:* SW_3, $D_o = 22$ *mm*, $C = 14$ *mm*, $S = 0.80$. *Third row:* SW_3, $D_o = 20$ *mm*, $C = 10$ *mm*, $S = 0.80$. *Fourth row:* SW_3, $D_o = 18$ *mm*, $C = 12$ *mm*, $S = 0.60$.

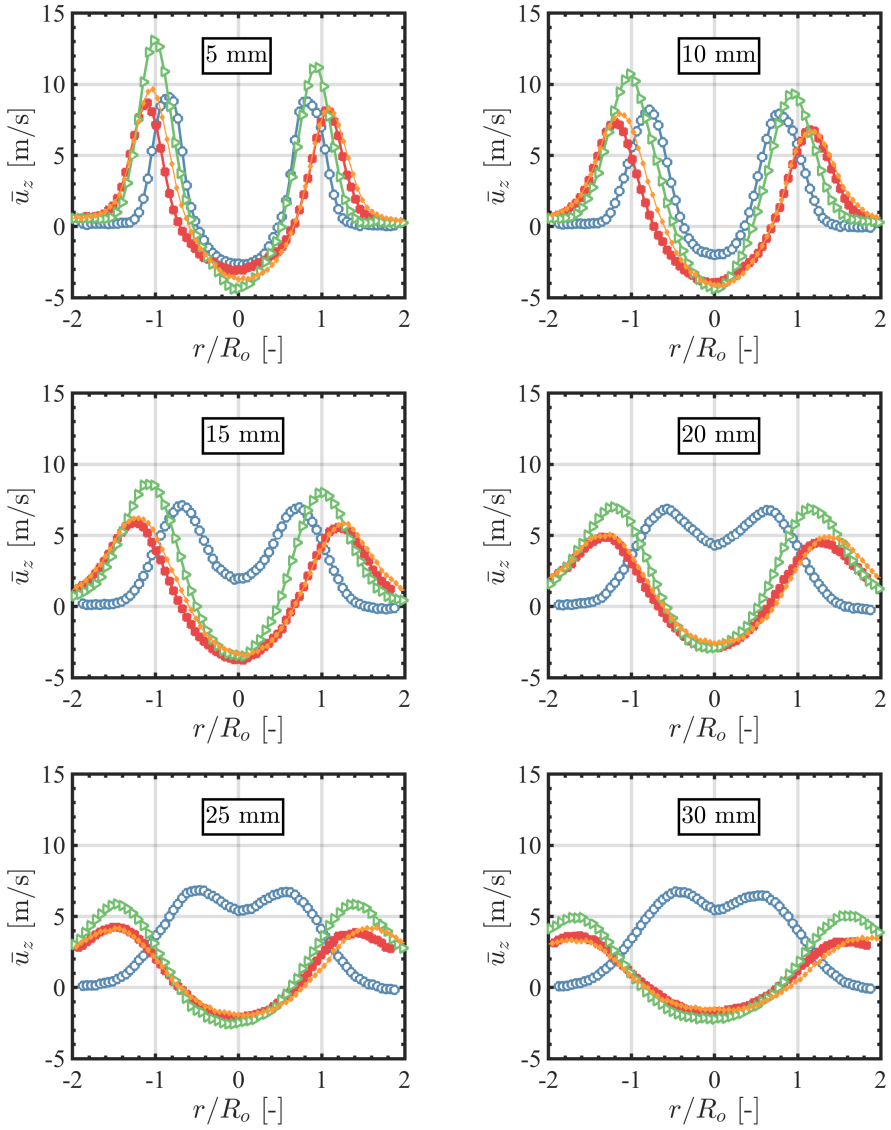

Figure 4.5: *Cold flow mean axial velocity profiles at different axial locations above the combustion chamber backplane, obtained from PIV measurements for four configuration of interest. Blue: SW_0, $D_o = 22$ mm, $C = 14$ mm, $S = 0.20$. Red: SW_3, $D_o = 22$ mm, $C = 14$ mm, $S = 0.80$. Orange: SW_3, $D_o = 20$ mm, $C = 10$ mm, $S = 0.80$. Green: SW_3, $D_o = 18$ mm, $C = 12$ mm, $S = 0.60$. The axial locations of these profiles are reported as dash-dotted white lines in Fig. 4.4.*

with a tentative threshold of S> 0.60 generally considered (Lucca-Negro and O'Doherty, 2001), the vortex breakdown phenomenon causes the recirculation zone in the wake of the bluff-body to merge with that due to the swirling flow. A stronger IRZ is thus established in this case.

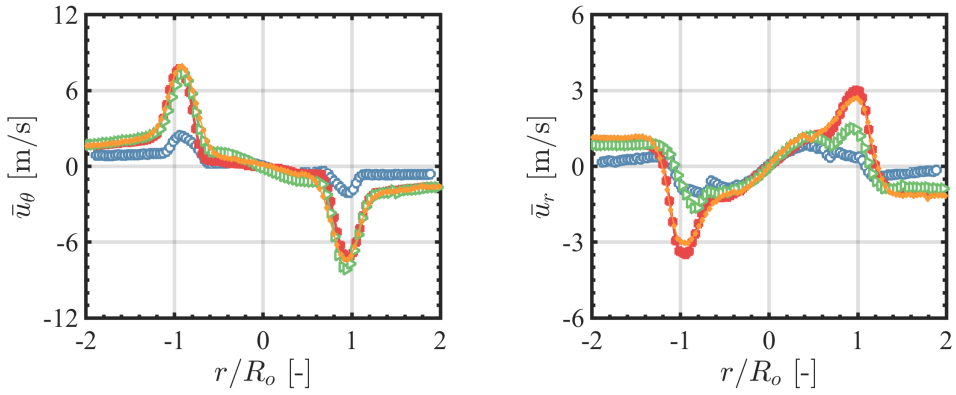

Figure 4.6: *Cold flow mean azimuthal (left) and radial (right) velocity profiles obtained from PIV measurements for four configuration of interest. Blue: SW_0, $D_o = 22$ mm, $C = 14$ mm, $S = 0.20$. Red: SW_3, $D_o = 22$ mm, $C = 14$ mm, $S = 0.80$. Orange: SW_3, $D_o = 20$ mm, $C = 10$ mm, $S = 0.80$. Green: SW_3, $D_o = 18$ mm, $C = 12$ mm, $S = 0.60$. The location of these profiles is reported as dashed dotted white lines in Fig. 4.4.*

Axial velocity profiles obtained from the axial PIV scan, are shown in Fig. 4.5. These profiles are shown at different axial locations inside the chamber, indicated as white lines on the first plot in Fig. 4.4. An asymmetry is observed between the left and the right parts of Figs. 4.4-4.5. This is due to small imperfections in machining and difficulty to center the bluff body over a relatively long distance from the swirler backplane, where it is screwed, to the injector outlet. Results for SW_0 are presented in blue in Fig. 4.5. Close to the chamber backplane, the IRZ strength is comparable for SW_0 and SW_3 (shown in red). But it is clear that the IRZ of SW_0 becomes weaker as the distance from the chamber backplane increases. At a distance of 15 mm, the axial velocity is positive all along the scan for SW_0 in Fig. 4.5, while negative velocities in the central region of the jet are observed for all the locations considered for SW_3. The angle of the jet is bigger for the configuration with SW_3 than with SW_0. This is also seen in Fig. 4.6-right, showing the radial velocity profiles obtained from the transverse PIV scan at 2 ± 0.5 mm above the bluff body. The radial velocity is much higher for SW_3 than for SW_0 in this figure.

Images in the third and fourth rows in Fig. 4.4 show the velocity field for configurations featuring the same swirler SW_3, but different values of the cross section area A_2 at the injector exit. These modifications were obtained by substituting the central injection nozzle $D_o = 18 - 20$ mm and the bluff body end piece $C = 12 - 10$ mm. The swirl number is $S = 0.80$ for the configuration shown in the third line, while it is reduced to $S = 0.60$ for that in the fourth line. From Fig. 4.6-left, one can check that this is not due to a change of the azimuthal flow component. As already seen in Fig. 4.1, when the swirler design is fixed, a

change of other geometrical parameters does not influence much the azimuthal velocity $\bar{u}_\theta$ profiles. The swirl number decrease is here due to a different shape of axial velocity profiles, plotted in orange and green in Fig. 4.5. When the size of the injector and bluff-body are modified, but the normalized cross section A_1/A_2 remains almost unchanged, as for the results shown in the second and third row in Fig. 4.4, the axial velocity profiles are almost superposed in Fig. 4.5 (red and orange curves). When the cross section at the exit of the injector is reduced, the axial velocity profile shifts to higher values (green curve in Fig. 4.5) and the swirl number S decreases as a consequence. The central recirculation region still spans the full axial scan for the configuration with swirler SW_3, $D_o = 18$ mm, $C = 12$ mm and a swirl number $S = 0.60$ shown in the last line in Fig. 4.4, but it is thinner in the radial direction compared to the results shown in the third line for the configuration with swirler SW_3, $D_o = 20$ mm, $C = 10$ mm and with $S = 0.80$.

4.3 Mean flame structure

Effects of the swirl number S on the shape taken by the flames are shown in Figs. 4.7 and 4.8. It is first worth recalling that the equivalence ratio $\phi = 0.82$ is fixed for all these experiments. These images are obtained by averaging a hundred snapshots, each with a long exposure time of 20 ms, that are recorded with the ICCD camera equipped with the OH* filter. Here again, a small asymmetry can be identified in the light distributions between the left and right part in these images.

Some general features about the shape of the flames can be inferred from these figures, obtained for several different injection conditions. As the swirl number decreases, either by a reduction of the injector exit diameter D_o (first row in Fig. 4.7) or by a increase of the bluff-body end piece diameter C (second row in Fig. 4.7), the flame becomes more elongated, moves further away from the injector outlet and closer to the chamber walls. This is due to the increase of axial velocity, as shown in Figs. 4.1-4.5. In the third line of Fig. 4.7, effects of the swirler design are highlighted. As the swirl level S decreases from 0.95 to 0.65, the flame length and its leading edge position with respect to the burner outlet remain roughly unaltered, while the flame angle with respect to the axial direction reduces. This is due to the strong change in azimuthal velocity imposed by the different swirler SW designs (Figs. 4.1-4.6), when all the other geometrical parameters are kept fixed. When the swirl number is reduced to $S = 0.20$ for SW_0, the light distribution takes a relatively long and narrow shape concentrated in the wake of the central bluff-body.

The OH* light distribution does not feature any visible change when the swirler is mounted at different distances δ with respect to the combustion chamber

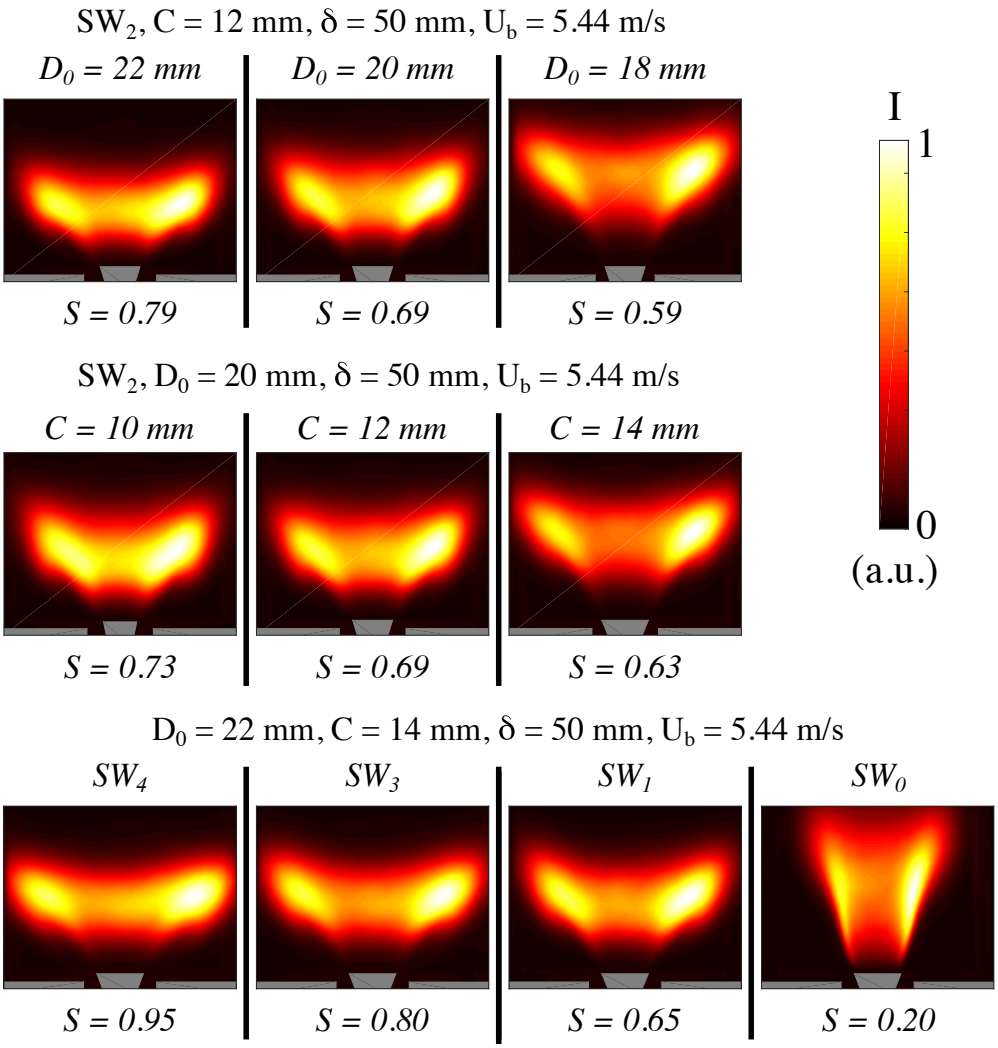

Figure 4.7: *OH* flame light distribution for different configurations tested with different swirl numbers. First line: effect of nozzle diameter D_o. Second line: effect of top cone central bluff body diameter C. Third line: effect of swirling vane SW.*

backplane, as observed in Fig. 4.8-first line. In fact the swirl number S is not expected to be modified by a change of the distance δ in a straight tube as long as δ is still big enough for the flow to fully develop and small enough to neglect dissipation altering the axial and azimuthal momentum given to the flow. Lastly, the flame size increases but keeps the same aspect ratio as the injection velocity is increased from $U_b = 2.72$ m/s to $U_b = 5.44$ m/s in the last line in Fig. 4.8. Here again, the swirl number is not expected to change when U_b is modified, if the dimensions of the injector and the swirler design are not modified.

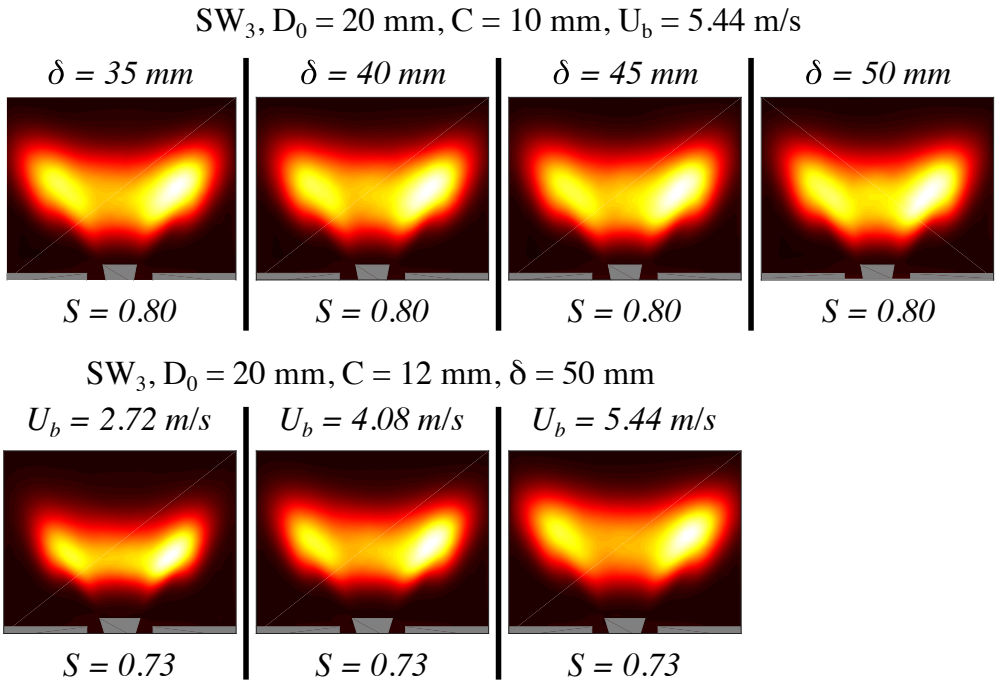

Figure 4.8: *OH* flame light distribution for different configurations tested. First line: effect of the distance δ between swirler exit and combustor backplane. Second line: effect of the injection velocity U_b. The swirl number is fixed in each line. The colorscale is the same as the one used in Fig. 4.7.*

4.4 Conclusions

The experiments reported in this chapter, done in the absence of acoustic forcing, show how to control the structure of the resulting flow field and flame shape when the injector design is modified by either changing the nozzle diameter, the top cone end piece diameter or the swirling vane.
It was shown that three different regimes could be obtained, with elongated flames close to blow-off, compact well stabilized flames and flames flash-backing inside the injector. The swirl level has been shown to largely determine the structure of the flow field and the resulting flame shape. The way the swirl level determines these properties, is by modifying the axial, azimuthal and radial velocity profiles in the combustion chamber.
A last set of experiment was conducted with modification of the swirling vane distance δ with respect to the injector outlet or of the bulk flow velocity U_b. It was shown that a change of the distance δ does not impact the flame structure, while an increase of the bulk flow velocity U_b increases the flame size but keeps the same flame aspect ratio. This is due to the fact that these two quantities are not expected to modify the swirl number S, once again confirming that the structure of the flow field and the flame shape largely depends on this quantity.

Chapter 5

Characterization of thermoacoustic instabilities

The test rig equipped with different exhaust tubes and injection devices features a set of self-sustained thermoacoustic instabilities. This chapter is dedicated to their analysis. After a brief description of the specific diagnostics used for the analysis of these instabilities, the first part of this chapter is dedicated to the characterization of one unstable regime. The rest of this chapter is dedicated to the description of the effects of modifications of the injector and swirler designs on the stability of the combustor.

5.1 Analysis of a naturally unstable regime

Lean premixed combustion systems achieve low pollutant emission levels, with compact flames and high power densities, but are sensitive to external perturbations. The absence of perforated liners, which are present in non-premixed designs, reduce the damping of premixed systems. These reasons make thermoacoustic instabilities one of the major drawbacks, that hinder the practical operation of lean premixed combustion systems. This matter has been studied since the early fifties (Crocco, 1951; Crocco, 1952) but, nonetheless, progress is still needed if one want to be able to predict and eventually control the onset of instabilities. In a simplified configuration, like the one investigated in this work, where the mixture composition remain uniform, combustion instabilities result from a resonant coupling between flow rate oscillations, unsteady combustion and acoustics (Ducruix et al., 2003; Candel et al., 2014).

The test-rig used for the analysis of thermoacoustic instabilities is sketched in Fig. 5.1. Only the components and instruments specific to this analysis are highlighted in this figure. A detailed description of the setup was already given in chapter 1. A mixture of air and methane is injected from two diametrically opposed apertures at the base of the burner. The air and methane mass flow rates

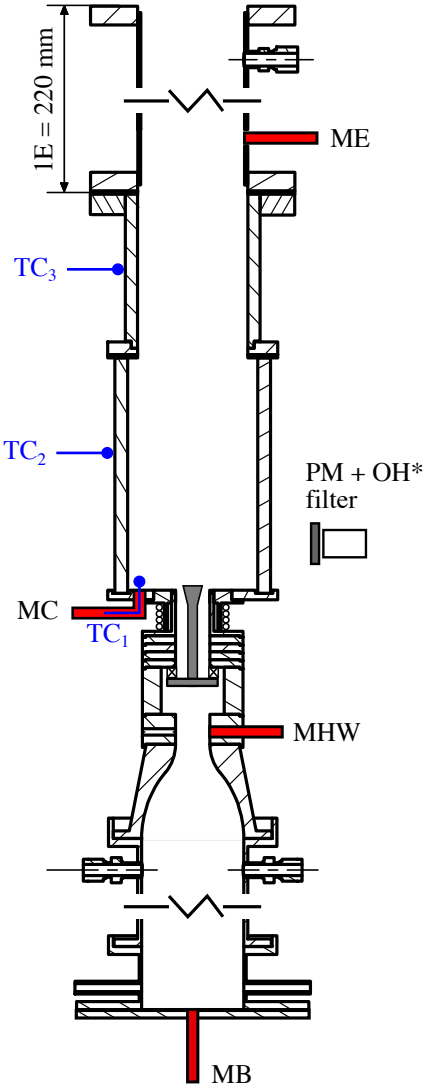

Figure 5.1: *Sketch of the burner used for combustion instabilities characterization.*

are fixed for these experiments to $\dot{m}_{air} = 2.28$ g/s and $\dot{m}_{CH_4} = 0.11$ g/s. This leads to an equivalence ratio $\phi = 0.82$ and a bulk flow velocity $U_b = 5.44$ m/s (at $T = 20^o$ C and $p = 1$ atm) at the convergent nozzle outlet where a microphone MHW (Bruel & Kjaer, 4938 with pre-amplifier 4938-A-011) is installed as in Fig. 5.1. The thermal power is thus fixed to $P = 5.44$ kW assuming total combustion.

The bottom side of the burner is closed by a rigid plate equipped with a pressure tap, as shown in Fig. 5.1, where microphone MB (B&K, 4938 with pre-amplifier 4938-A-011) is mounted. A second microphone, MHW (B&K, 4938 with pre-amplifier 4938-A-011), is mounted in the 22 mm diameter section

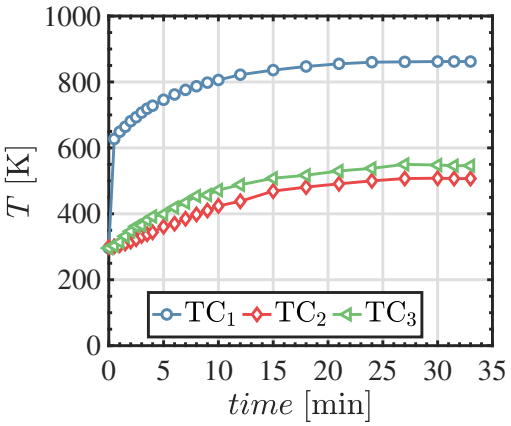

Figure 5.2: *Temperature measurements used to estimate the thermalization time. The position of the K-type thermocouples is indicated in Fig. 5.1.*

where normally the hot wire probe is placed. Microphones MC and ME in Fig. 5.1 are used to measure the pressure at the combustion chamber backplate and in the exhaust tube. In this hot gases region, microphones are mounted on water-cooled waveguides. More information on these waveguides are given in the Ph.D. thesis of Gaudron, 2018. All microphones are connected to a conditioning amplifier (Bruel & Kjaer, 2690).

The length of the exhaust tube downstream the second convergent unit can be modified by mounting up to three tubes of length $E = 220$ mm (Fig. 5.1). The configuration without any exhaust tube ($E = 0$ mm in Fig. 5.1) is the one used in chapter 4 to analyze the mean flame properties in the absence of acoustic forcing and is used here to get an estimate of the thermalization time of the system.

Three K-type thermocouples are used for temperature measurements. TC_1 is inserted in the combustion chamber through the pressure tap for microphone MC. It is used to estimate the burnt gases temperature, at a distance of approximately 2 ± 0.5 mm from the chamber backplane. TC_2 is located at approximately half the height of a quartz side window and inserted in one of the lateral steel rod at the corner of the combustion chamber. TC_3 is put in contact with the second convergent unit, at approximately half of its height. It is important to underline that these measurements are not intended to give a precise indication of the temperature at these locations, but are just used to get an indication of the system thermalization time.
Results of temperature measurements are shown in Fig. 5.2, with respect to the ignition time of combustion. After a rapid initial increase in the first 10 minutes, the temperature of combustion reaches a steady-state value at about 20-25 minutes. All the measurements conducted in this work in reactive con-

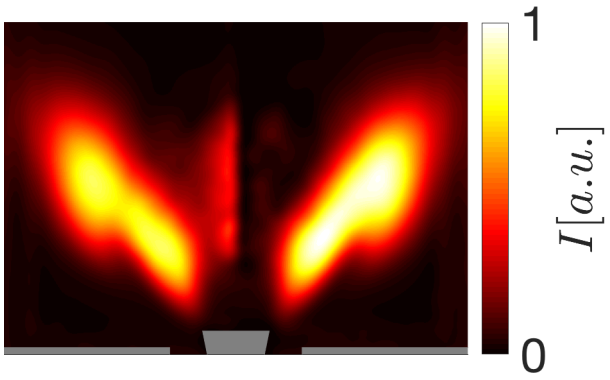

Figure 5.3: *Abel deconvoluted OH* chemiluminescence for the flame stabilized with the injector configuration featuring SW_3, $D_o = 20$ mm, $C = 10$ mm, $U_b = 5.44$ m/s, $\phi = 0.82$ without any exhaust tube ($E = 0$ mm in Fig. 5.1).*

ditions, for instance the ICCD imaging to analyze the flame structure in the absence of forcing as in chapter 4 or the FTF measurements presented in chapter 6, were done after 25 minutes from the flame ignition, to let the system reach its thermalization.

When the length of the exhaust tube downstream the second convergent is changed, the thermoacoustic state of the burner is modified. Without any exhaust tube ($E = 0$ mm in Fig. 5.1), the system is stable, and no distinct tone emerges from the pressure spectrum. This was confirmed for all the different geometrical configurations tested by modifying the injection unit. Figure 5.3 shows an example of a stable flame for a configuration featuring swirler SW_3, with a diameter at the exit of the injector $D_o = 20$ mm, a bluff-body diameter $C = 10$ mm, a distance $\delta = 50$ mm (Fig. 1.3) and no exhaust tube $E = 0$ mm. When the length of the exhaust tube is increased to $1E = 220$, $2E = 440$ or $3E = 660$ mm instabilities can be triggered. The sound power level (SPL) measured by microphone MC at the bottom of the combustion chamber shown in Fig. 5.1 for exhaust tube lengths of $1E$, $2E$ or $3E$ is shown in Fig. 5.4 for the same injector configuration as in Fig. 5.3. Signals were recorded at a sampling rate of $f_s = 8192$ Hz over 8 seconds and Welch periodograms are used to obtain statistically meaningful results. The SPL is then deduced:

$$SPL = 20log_{10}\left(\frac{p_{rms}}{p_0}\right) \tag{5.1}$$

where $p_0 = 2.10^{-5}$ Pa and p_{rms} is the RMS value of the acoustic pressure recorded. In Fig. 5.4, no distinct tone emerges from the pressure spectrum with an exhaust tube length of $1E = 220$ mm. In this case, the system is stable. For $2E = 440$ mm and $3E = 660$ mm exhaust tube lengths, the system is unstable and two peaks, respectively at $f = 185$ Hz and $f = 164$ Hz, emerge. Phase averaged OH* chemiluminescence images of the flame motion during one

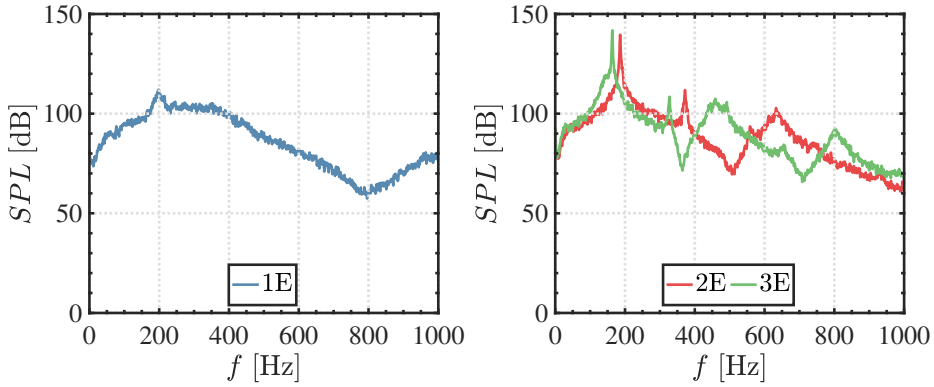

Figure 5.4: *Sound pressure spectrum measured in the combustion chamber after the thermalization time for different length E of the exhaust tube downstream the combustion chamber. Left: 1E. stable system. Right: 2E, 3E. Unstable systems.*

cycle of oscillation are shown in Fig. 5.5 for exhaust tube lengths $2E = 440$ mm (top) and $3E = 660$ mm (bottom). It is evident that the flame front depart considerably from its mean position shown in Fig. 5.3 when instabilities are triggered. The flame is stretched in the vertical direction during the cycle and its tip is rolled up by vortex interaction. This flame motion is further analyzed in chapter 7.

The configuration with an exhaust tube length of $2E = 440$ mm is now analyzed in more detail. The evolution of the SPL measured by microphone MC is plotted in Fig. 5.6-left at different times after ignition. The SPL rapidly builds up in the first minutes of the experiments to reach a maximum of 148 dB inside the combustion chamber around 7-8 minutes after the flame ignition in Fig. 5.6-left. In this first part of the experiment, the combustion chamber strongly vibrates leading to a large mechanical strain on the sealing between the quartz windows and the metal rods. It was checked that there was no air leakage from the chamber during the experiments and all measurements presented were conducted at least two times to check their repeatability. It was necessary to rebuild periodically the combustion chamber after each characterization to ensure a perfect joint sealing for subsequent experiments.

After the initial increase, the maximum SPL measured by MC drops a little to reach a plateau of about 140 dB for $t \geq 20$ minutes when the system has reached thermalization. The frequency f_I of the instability plotted in Fig. 5.6-right also increases with time. It reaches a limit cycle at $f_I \simeq 185$ Hz after $t \geq 20$ minutes. This analysis confirms the strong impact of thermal boundary conditions on the solid components of the combustion chamber (Mercier et al., 2016) on its thermo-acoustic state and in particular on the frequency and level reached by the instability at limit cycle.

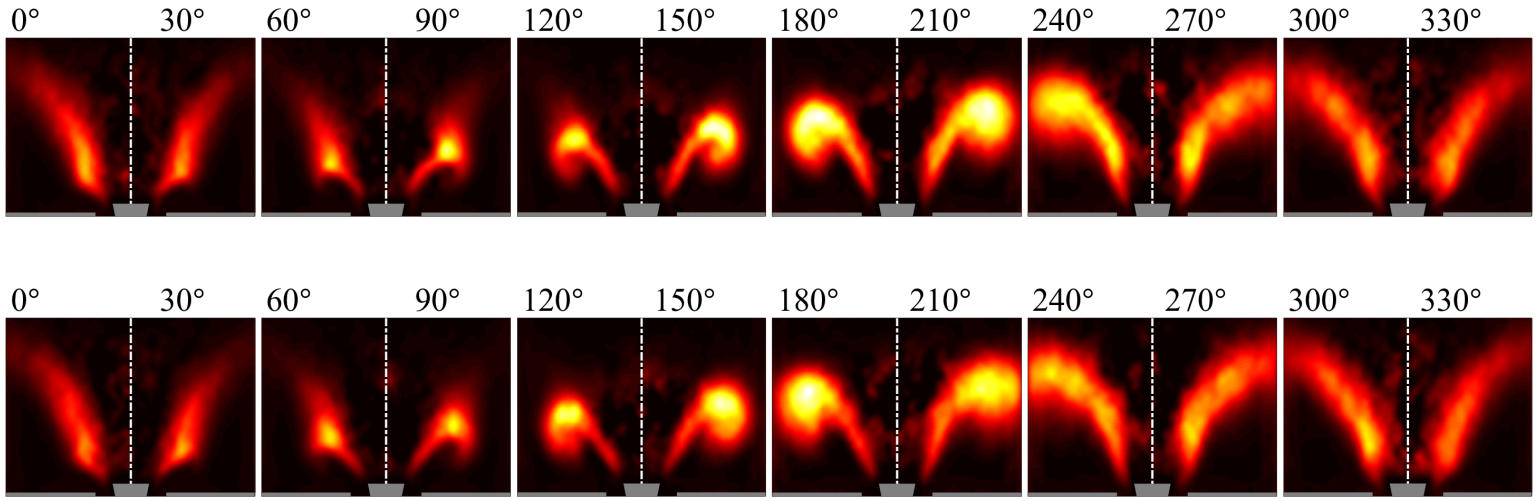

Figure 5.5: *Phase averaged OH* chemiluminescence of the flame during one cycle of oscillation for the flame stabilized with the injector configuration featuring SW_3, $D_o = 20$ mm, $C = 10$ mm, $U_b = 5.44$ m/s, $\phi = 0.82$. Top: $2E = 440$ mm exhaust length. Bottom: $3E = 660$ mm exhaust length. The colorscale is the same as the one used in Fig. 5.3. The phase angle indicated on the figures is referred to the velocity signal recorded by the hot wire.*

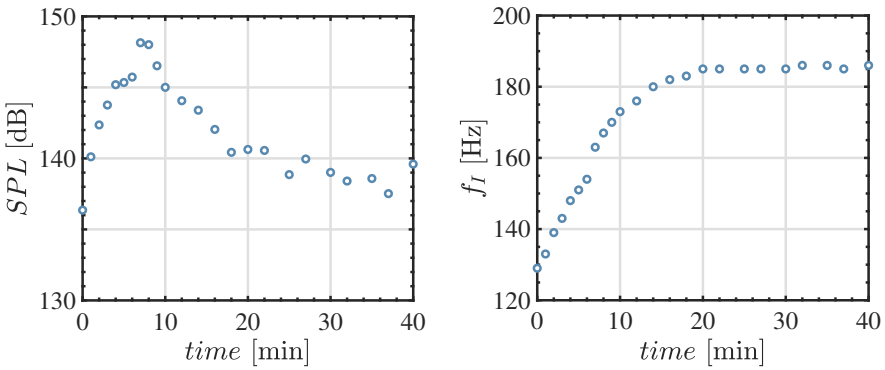

Figure 5.6: *Temporal evolution of the maximum SPL recorded by microphone MC at the combustion chamber backplane (left) and of the frequency of instability (right).*

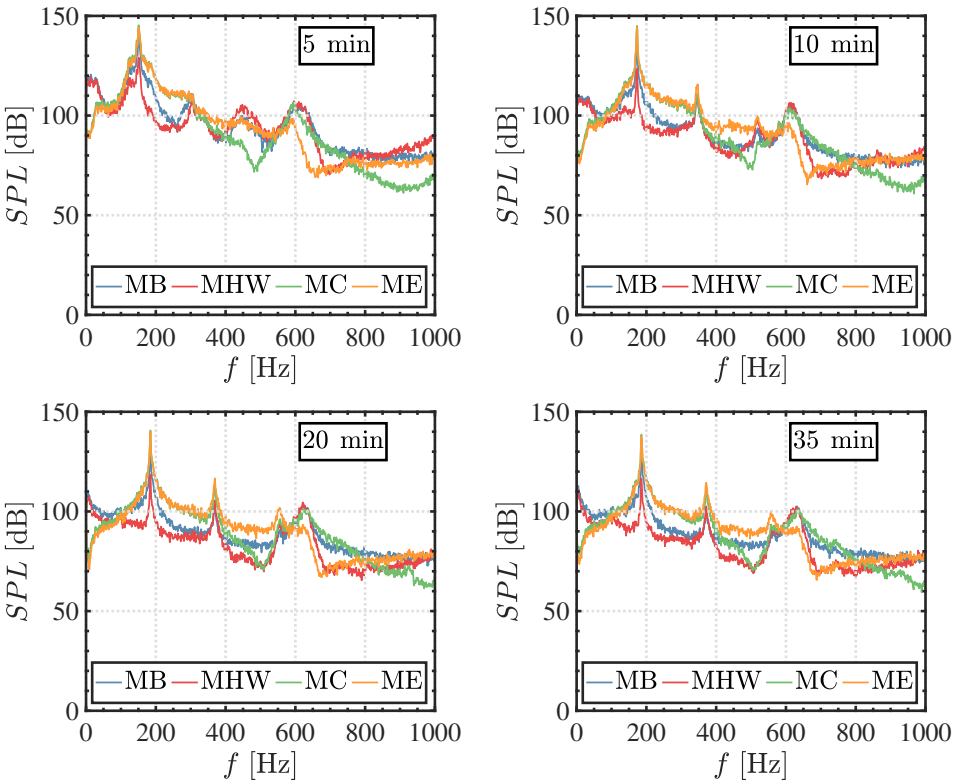

Figure 5.7: *Temporal evolution of the sound power spectral density at the bottom of the burner (MB), at the hot wire location (MHW), in the combustion chamber (MC) and in the exhaust tube (ME). Results are plotted in dB.*

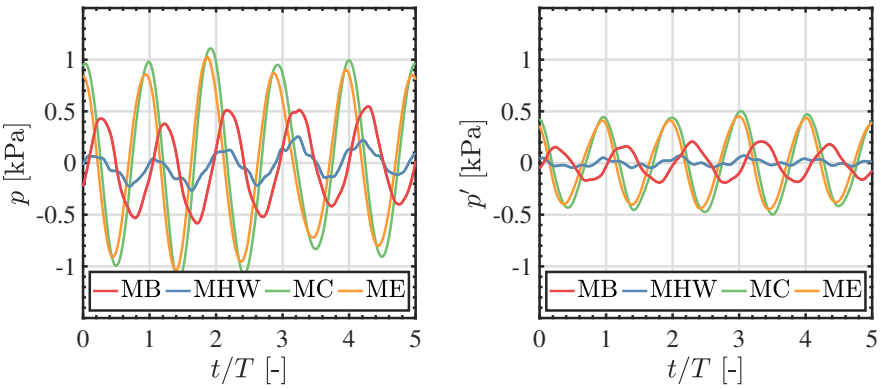

Figure 5.8: *Pressure measurements recorded with different microphones after* 5 *minutes from the beginning of the experiments (left) and after* 35 *minutes (right).*

The pressure spectra measured by the different microphones presented in Fig. 5.7 clearly feature a main peak at the instability frequency, but the level of the pressure fluctuations varies with time. Figure 5.7 also shows that the spectral distribution is altered with the second harmonic and moves as time increases highlighting how acoustic energy is redistributed.

Figure 5.8 shows that the pressure fluctuations measured by MC in the combustion chamber and ME in the exhaust tube are much higher than those measured by MB at the burner bottom and MHW at the hot wire location. Fluctuations as high as 1 kPa are measured in the first minutes of the experiments, while they drop to about half that level at 500 Pa when $t \geq 20$ minutes. The signals recorded by MB and MHW are almost out of phase with respect to the signals measured by MC and ME in Fig. 5.8. Considering that the system is closed at the bottom by a rigid plate and open at its exhaust, the acoustic boundary conditions correspond to a closed-open system. More information on the acoustic characterization of this setup with detailed measurements of these acoustic boundary can be found in Merk et al., 2018b. The modal structure depicted in Fig. 5.8 sugests that this instability is coupled to the 3/4 wave mode of the system, with a pressure node close to the hot wire location. This has been confirmed by a set of other experiments in the work of Gaudron (Gaudron, 2018).

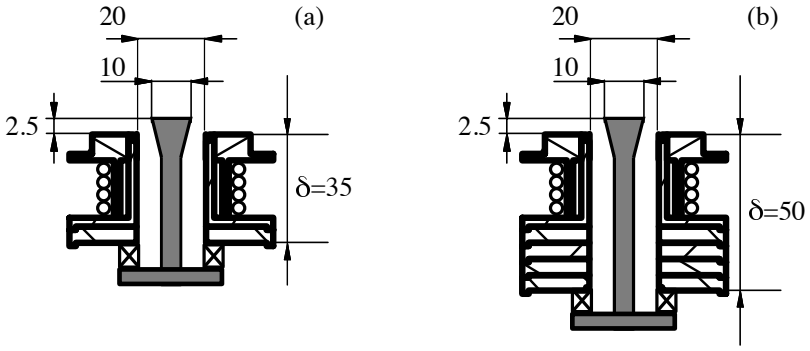

Figure 5.9: *Sketch of the different injectors tested. Left:* $\delta = 35$ *mm. Right:* $\delta = 50$ *mm.*

5.2 Effect of the swirler to injector outlet distance δ

Effects of modification of the injector design on the thermoacoustic instability properties is now investigated by first modifying the distance δ between the swirler outlet and the nozzle outlet as in Fig. 5.9. The thermoacoustic is here also modified by changing the exhaust tube length ($1E$, $2E$, $3E$). All the other parameters remain fixed. It is first recalled that the mean flame shape without any exhaust tube ($E = 0$ mm) is the same in these two cases as shown in Fig. 5.10. By modifying the length of the exhaust tube, the thermoacoustic state of the burner can be modified. The objective here is to analyze effects of modifications of the injector design on this thermoacoustic state. Figure 5.11 shows the SPL spectrum measured with the microphone MC for $\delta = 35$ mm (Fig. 5.11-left) and $\delta = 50$ mm (Fig. 5.11-right) with three different lengths of the exhaust tube ($1E$, $2E$, $3E$). When the swirler is mounted at a distance $\delta = 35$ mm from the chamber, a weak instability with a maximum SPL of 127 dB is observed at $f_I = 220$ Hz for the configuration with an exhaust tube

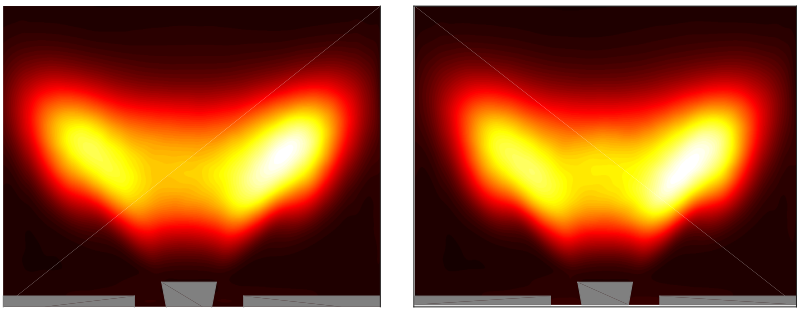

Figure 5.10: *OH* chemiluminescence for the flame stabilized with the injector configuration featuring* SW_3, $D_o = 20$ *mm,* $C = 10$ *mm,* $U_b = 5.44$ *m/s,* $\phi = 0.82$ *without any exhaust tube (*$E = 0$ *mm in Fig. 5.1). Left:* $\delta = 35$ *mm. Right:* $\delta = 50$ *mm. The colorscale is the same as the one used in Fig. 5.3.*

of length $1E = 220$ mm. By increasing this length to $2E = 440$ mm, the maximum SPL is reduced to 124 dB and the frequency of the instability drops to $f_I = 196$ Hz. When three tubes are mounted downstream the combustion chamber, the system is stable for $3E = 660$ mm.
The situation is reversed in Fig. 5.11-right when the swirler is mounted at $\delta = 50$ mm from the nozzle exhaust section. A much stronger instability is observed for the configuration with an exhaust tube of length $3E = 660$ mm with a maximum SPL of 142 dB at $f_I = 164$ Hz. The SPL slightly drops to 140 dB at $f_I = 185$ Hz for a $2E = 440$ mm exhaust length, but the system is still strongly unstable in this configuration, as described in section 5.1. The system is now stable for an exhaust length of $1E = 220$ mm.

In Fig. 5.12, the pressure fluctuations in the combustion chamber measured by MC are plotted along with the heat release rate fluctuations measured by the photomultiplier PM in Fig. 5.1 equipped with an OH* filter. Results are shown for the configuration with an exhaust length of $2E = 660$ mm for the two distances $\delta = 35$ mm and 50 mm. Both signals in left and right plots in Fig. 5.12 oscillate at the same frequency. The oscillations for the combustion pressure and heat release rate are much larger for the configuration with $\delta = 50$ mm shown on the right plot in Fig. 5.12 than when the swirler is set at $\delta = 35$ mm. This was already seen in Fig.5.11, showing that the instability is stronger when two tubes are mounted downstream the chamber and the distance δ is increased from 35 mm to 50 mm. One can conclude that this is not due to a different phasing between pressure and heat release rate fluctuations. One clearly sees in Fig. 5.12 that these signals are oscillating in phase in the left plot for $\delta = 35$ mm and right plot for $\delta = 50$ mm. The drop of pressure oscillations is thus not due to a shift of the heat release rate signal with respect to the pressure signal as

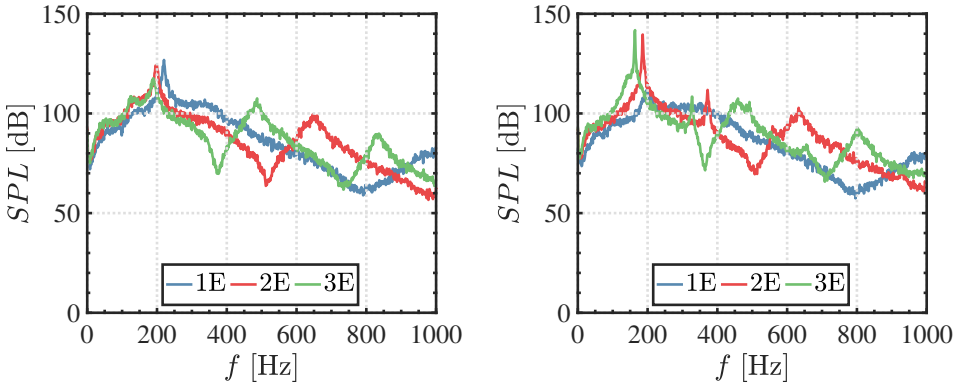

Figure 5.11: *Sound pressure spectrum measured in the combustion chamber (MC) at $t = 40$ minutes for three lengths $1E$, $2E$ and $3E$ of the exhaust tube downstream the combustion chamber and for two values of the distance δ between the swirler and the chamber backplane. Left: $\delta = 35$ mm. Right: $\delta = 50$ mm.*

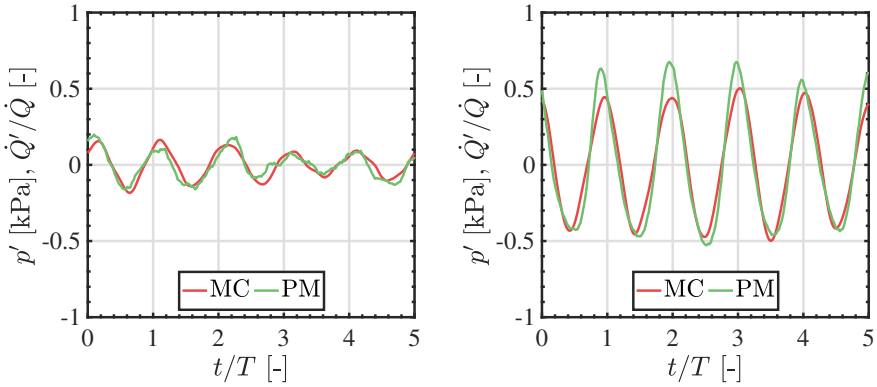

Figure 5.12: *Time series of acoustic pressure MC in the chamber and heat release rate fluctuations measured by the PM with an OH* filter for the self-triggered flame with* $2E = 440$ *mm at* $t = 35$ *minutes. Results are shown for two values of the distance* δ *between the swirler and the chamber backplane. Left:* $\delta = 35$ *mm. Right:* $\delta = 50$ *mm.*

the distance δ is reduced.

These observations confirms that small changes of the injector design can lead to dramatic changes of the thermoacoustic state of the system. An interpretation of the mechanisms leading to this differences in strength of the instability for different values of δ is given in chapter 6 with the help of FTF measurements.

5.3 Effect of the swirling vane

The investigation now proceeds by changing the swirling vane design SW. Measurements are conducted with the longest exhaust tube, $3E = 660$ mm. Two different radial swirlers SW_1 and SW_3 are tested. Their design is described in chapter 1. All the remaining geometrical parameters of the injector are fixed: $D_o = 20$ mm, $C = 10$ mm, $\delta = 50$ mm. The bulk flow velocity $U_b = 5.44$ m/s and equivalence ratio $\phi = 0.82$ remain also unchanged. The swirl level with this design and the radial vane SW_3 is $S = 0.80$ and it drop to $S = 0.69$ when SW_3 is replaced with SW_1.

The sound pressure spectrum measured by MC in the combustion chamber at a time $t = 40$ minutes after ignition is presented in Fig. 5.13-left. The pressure spectrum is basically superposed for the two swirler designs. The evolution of the instability frequency f_I and of the maximum SPL measured by MC is presented in Fig. 5.13-right. Data are presented only after the system has reached its thermalization. The frequency of the instability is close to $f_I \simeq 164$ Hz for both the explored configurations. The maximum SPL measured by microphone MC is close to 142 dB and is close for the two swirler designs while the flame

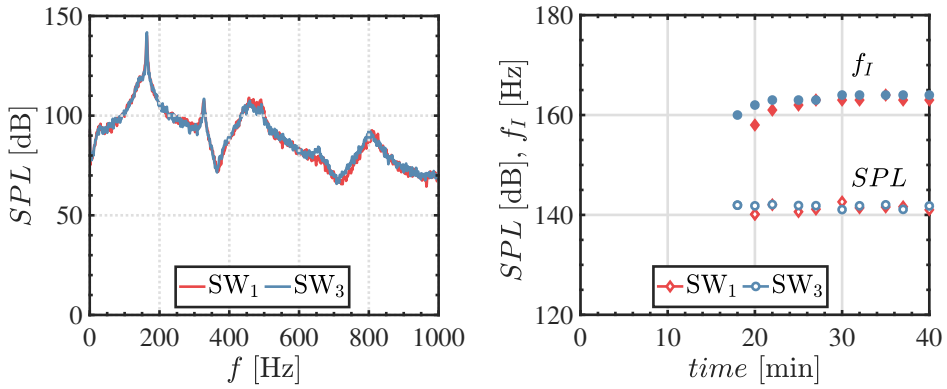

Figure 5.13: *Sound pressure spectrum measured in the combustion chamber (left) at $t = 40$ minutes and temporal evolution of the frequency of instability and of the SPL in the combustion chamber (right) for two different swirler designs.*

shape in the absence of acoustic forcing differs, as shown in Fig. 5.14 for a slightly different injector geometry.

These results show that the swirler design does not play an important role itself on the properties of the thermoacoustic instability, when all the other parameters are kept fixed. An interpretation of these observations is given in chapter 6 with the help of FTF measurements.

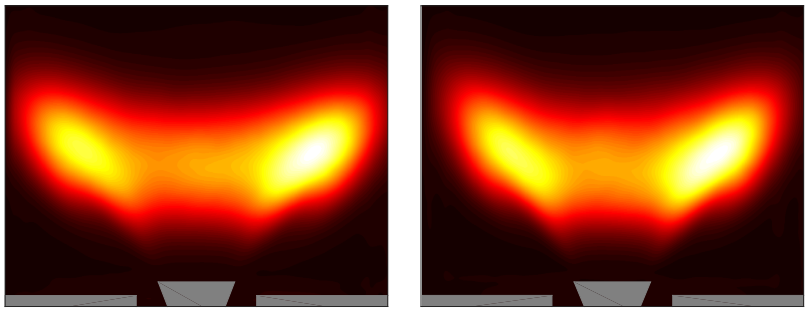

Figure 5.14: *OH* chemiluminescence for the flame stabilized with the injector configuration featuring SW_3 (left) or SW_1 (right), $D_o = 22$ mm, $C = 14$ mm, $U_b = 5.44$ m/s, $\phi = 0.82$ without any exhaust tube ($E = 0$ mm in Fig. 5.1). The colorscale is the same as the one used in Fig. 5.3.*

5.4 Conclusions

The thermoacoustic state of the test rig developed in this work has been analyzed when the combustion exhaust length is modified and some components of the injector are replaced. Experiments have been conducted at fixed equivalence ratio $\phi = 0.82$ and bulk flow velocity $U_b = 5.44$ m/s.

It has first been shown that the thermal state of the combustor strongly alters the thermoacoustic state of the system. This has been checked for one configuration of the injector. It is found that the sound power level (SPL) inside the combustion chamber strongly builds up in the first minutes after ignition and then reaches a plateau at about $t \simeq 20$ min. The instability frequency constantly increases in the first minutes and then reaches a limit cycle for $t \geq 20$ min. It is then necessary to wait for the system to reach its thermalization before one can conclude about its thermoacoustic state.

It has been shown that increasing the combustor exhaust length can lead to increasingly higher oscillation levels or lower oscillation levels depending on the distance between the swirler and injector outlet, if all other parameters are kept fixed. This has been shown for two different values of the distance δ between the swirler exit and the combustion chamber backplane. For a swirler mounted at a distance $\delta = 35$ mm, we observed a reduction of the SPL inside the combustion chamber for increasing length of the combustor exhaust, while the opposite was observed for a distance $\delta = 50$ mm. It has also been shown that modifying the swirling vane does not necessarily help to control the oscillation level in the combustion chamber. This was checked for two different designs of the radial swirling vane. Despite the fact that the shape of the flame stabilized with these different swirling vanes in the absence of acoustic forcing differs, the SPL measured in the combustion chamber for the two configurations is close. These two observations are discussed in more detail in chapter 6 with the help of FTF measurements.

Chapter 6

Effects of injector design and injection conditions on Flame Transfer Functions

The effects of different injector geometries and injection conditions on the flame transfer function are examined in this chapter. The objective here is to describe the shape taken by the FTF and assess the main parameters altering the flame response. The next chapter is dedicated to the analysis of the mechanisms controlling this response. The chapter is organized in the following way. After a brief introduction, a typical flame describing function determined for a given injector configuration is illustrated. It is shown that the shape of this response features the same characteristics for all forcing levels. In the second part of the chapter, results are reported at a fixed forcing level but for different geometrical configurations. The effects of modifications of the distance between the swirler exit and the combustion chamber backplane are considered first, followed by the effects of a change of the bulk flow velocity. In the last part of the chapter, results obtained while changing the injector exit diameter, the bluff-body end piece diameter or the swirler design are considered.

6.1 Introduction

In fully premixed systems and in absence of mixture composition disturbances, the flame transfer function (FTF) between heat release rate fluctuations $\dot{Q}'$ and harmonic velocity disturbances u' that produce them is defined as (Ducruix et al., 2003):

$$\mathcal{F}(f) = \frac{\dot{Q}'/\overline{\dot{Q}}}{u'/\overline{u}} = G(f)\exp(i\varphi(f)) \tag{6.1}$$

where G denotes the gain and φ stands for the phase lag of the FTF, both depending on the forcing frequency f. In recent developments, this linear concept has been extended to the Flame Describing Function (FDF) when effects of the perturbation level $|u'|/\bar{u}$ are explicitly considered (Noiray et al., 2008; Hosseini et al., 2012; Palies et al., 2011b; Ćosić et al., 2015):

$$\mathcal{F}(f,|u'|/\overline{u}) = \frac{\dot{Q}'/\overline{\dot{Q}}}{u'/\overline{u}} = G(f,|u'|/\overline{u})\exp(i\varphi(f,|u'|/\overline{u})). \tag{6.2}$$

The objective of this chapter is to characterize the differences between the FTF of swirled flames stabilized on various injection system designs. Only fully premixed flames at fixed equivalence ratio $\phi = 0.82$ stabilized on radial swirling injectors are considered. Their FTF is determined and the main elements leading to the largest drop of the FTF gain are analyzed with a set of experiments. The design modifications comprise changes of (1) the distance between the swirler exit and the combustion chamber backplate, (2) the main dimensions of the radial swirler, (3) the diameter of the injection nozzle and (4) the design of the top cone of variable diameter of the central bluff body. Experiments start by examining effect of the forcing level. All experiments are conducted for fixed flow injection conditions with a bulk flow velocity $U_b = 5.44$ m/s at the outlet of the convergent nozzle, except in a specific set of experiments conducted to analyze the effects of a change of this velocity.

The experimental setup used to determine the FTF/FDF is shown in Fig. 6.1 and was described in detail in Chapter 1. The FTFs are determined from Eq. (6.1) by submitting the flame to harmonic modulations of the flowrate. The velocity fluctuation u' is controlled by the hot wire anemometer HW. This probe is located in the nozzle of the convergent unit in Fig. 6.1 at a distance of 40 mm upstream the swirling vane. It has been checked that the velocity has a top hat profile and is laminar at this location. The photomultiplier equipped with an OH* filter is used to determine the mean $\bar{I}$ and fluctuating I' luminosity signals integrated over the flame volume and over the line of sight. These signals are assumed to be a good tracer of the heat release rate for the lean premixed flames investigated here (Hurle et al., 1968). The transfer function is then deduced from the cross and power-spectral densities between the photomultiplier and hot wire signals examined at the forcing frequency f. These signals are recorded at a sampling rate of $f_s = 8192$ Hz over 4 seconds and Welch periodograms are used to obtain statistically converged results. More details were given in chapter 2.

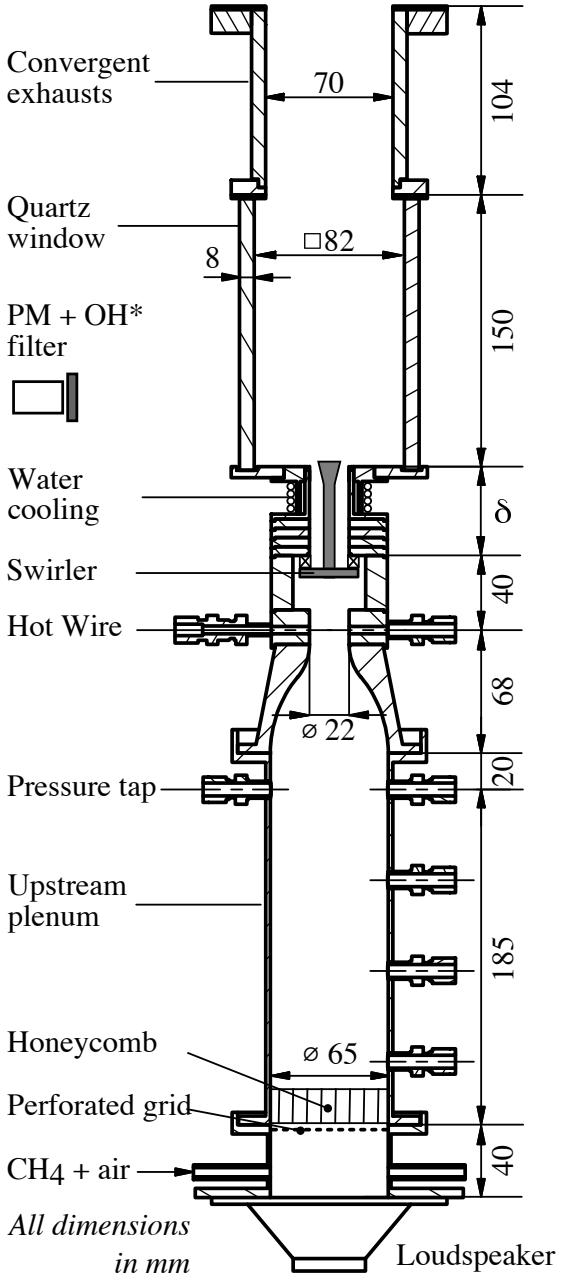

Figure 6.1: *Experimental setup used to determine the FTF/FDF.*

6.2 Effect of the forcing level - Flame Describing Function

The case considered here is also analyzed by LES and was presented in chapter 3. This geometry features the radial swirling vane SW_3, an injector outlet diameter $D_o = 20$ mm, a bluff body with a top cone of diameter $C = 10$ mm and a 1 mm shorter central rod with respect to that shown in Fig. 1.3-a. The distance between the top of the cone and the chamber backplane is 1.5 mm. The bulk flow velocity is $U_b = 5.44$ m/s and the equivalence ratio is $\phi = 0.82$. The mean shape of the flame stabilized with this injector configuration without acoustic forcing is shown in Fig. 6.2.

Figure 6.3 shows FDF data in the frequency range $20-250$ Hz, with a 10 Hz resolution, for velocity perturbation levels ranging from $u'/\overline{u} = 0.10$ to $u'/\overline{u} = 0.72$, where $\overline{u}$ and u' denote the mean and root-mean-square values of the signal measured by the hot wire HW. The full frequency range could not be covered for all the forcing levels because of power limitations of the actuation system.

The shape of the FDF in Fig. 6.3 is very similar to that found by Palies et al., 2010a and in many other studies (Komarek and Polifke, 2010; Bunce et al., 2013). At zero frequency the FDF gain approaches unity. The FDF gain then first increases with the frequency to reach a maximum at a frequency close to 50 Hz for all forcing levels. But the maximum gain value at this peak frequency depends on the forcing level. In particular it regularly drops as $u'/\overline{u}$ increases. This is a clear manifestation of a non-linear behavior. The gain curve then features a sudden drop with a valley and reaches a minimum value at a frequency close to 120 Hz for all forcing levels. This frequency also corresponds to an inflection point in the FTF phase plot. The minimum value reached by the gain does not depend on $u'/\overline{u}$. So, at the minimum gain frequency, the behavior may be considered roughly linear with the forcing level. At higher frequencies, the FTF gain increases again to reach a second maximum, around

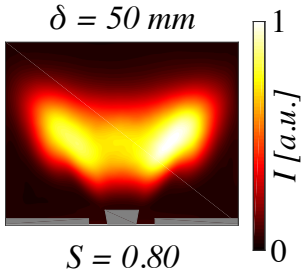

Figure 6.2: *OH* flame light distribution for the geometrical configuration featuring SW_3, $D_o = 20$ mm, $C = 10$ mm, $\delta = 50$ mm. The bulk flow velocity is $U_b = 5.44$ m/s and the equivalence ratio is $\phi = 0.82$.*

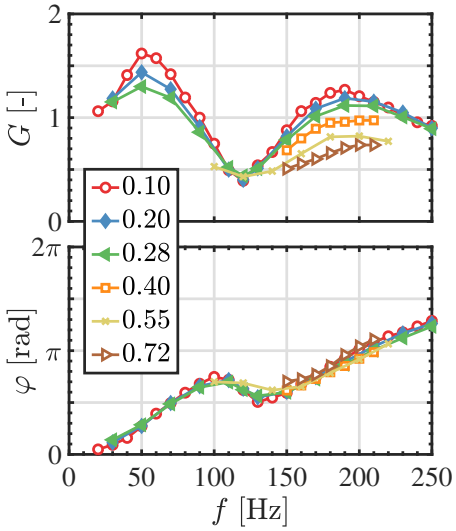

Figure 6.3: *Flame Describing Function measurement. Geometrical configuration: SW_3, $D_o = 20$ mm, $C = 10$ mm. The forcing level is varied between $u'/\overline{u} = 0.10 - 0.72$ RMS.*

190 Hz. Once again, this frequency is independent of the forcing level $u'/\overline{u}$ and the FDF gain at this second peak frequency drops regularly as $u'/\overline{u}$ increases. At zero frequency the FDF phase-lag approaches zero. The phase-lag curve then increases with an almost constant slope between $20 - 100$ Hz. It then features a sudden drop with an inflection point around $100 - 150$ Hz, in the region where the FDF gain features its minimum value. At higher frequencies, the phase-lag curve still increases with a constant slope. It is important to notice that the curves obtained at all forcing levels are superposed, meaning that the delay between incoming velocity perturbations and resulting heat release rate fluctuations is not a function of the forcing level $u'/\overline{u}$.

As indicated in the introduction, the objective of this chapter is to identify the main elements of the injector leading to the largest drop of the FTF gain. Figure 6.3 clearly shows that the forcing level does not lead to a change of the minimum gain value and that results are independent of the forcing level at this peculiar frequency. For this reasons, results presented in the following sections are obtained at a fixed forcing level.

6.3 Effect of the distance δ and of the bulk flow velocity U_b

Effects of modifications of the distance δ between the swirler exit and the combustion chamber backplate on the flame response are now analyzed. This distance is modified here between $\delta = 35 - 50$ mm, while it is fixed to 50 mm for

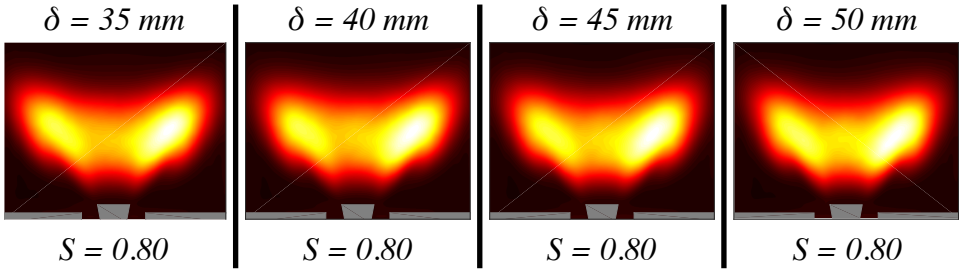

Figure 6.4: *OH* flame light distribution for the geometrical configuration featuring SW_3, $D_o = 20$ mm, $C = 10$ mm, $\delta = 35 - 50$ mm. The bulk flow velocity is $U_b = 5.44$ m/s and the equivalence ratio is $\phi = 0.82$. The colorscale is the same as the one used in Fig. 6.2.*

all the other configurations investigated in this chapter. The other geometrical parameters of the injector are fixed to SW_3, $D_o = 20$ mm, $C = 10$ mm. The mean shape taken by these flames in the absence of acoustic forcing is reported in Fig. 6.4. It is found that the OH* light distribution does not feature any obvious change when the swirler is mounted at different distances δ with respect to the combustion chamber backplane. The swirl number $S = 0.80$ was measured only for the configuration with $\delta = 50$ mm and it is assumed to be the same for the other configurations tested with different distances δ. FTF results for these flames are reported in Fig. 6.6-left at a forcing level $u'/\overline{u} = 0.30$ RMS.

A second set of experiments is also reported when the distance δ is again fixed to $\delta = 50$ mm, but the bulk flow velocity is modified. This velocity, deduced from the air and methane mass flowrate indications (at 20^oC and $p = 1$ atm) and referred to the hot wire location, is here set to $U_b = 2.72$, 4.10 and 5.44 m/s. One reminds that it is kept constant and fixed to 5.44 m/s for all the other configurations presented in this chapter. This injector is equipped with swirler SW_3, an injector nozzle of diameter $D_o = 20$ mm and a bluff body with a con-

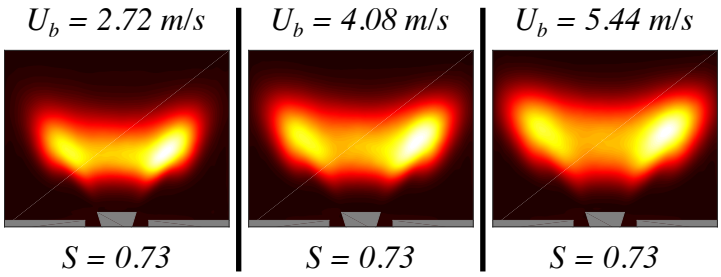

Figure 6.5: *OH* flame light distribution for the geometrical configuration featuring SW_3, $D_o = 20$ mm, $C = 12$ mm, $\delta = 50$ mm. The bulk flow velocity is here set to $U_b = 2.72$, 4.10 and 5.44 m/s. The equivalence ratio is $\phi = 0.82$. The colorscale is the same as the one used in Fig. 6.2.*

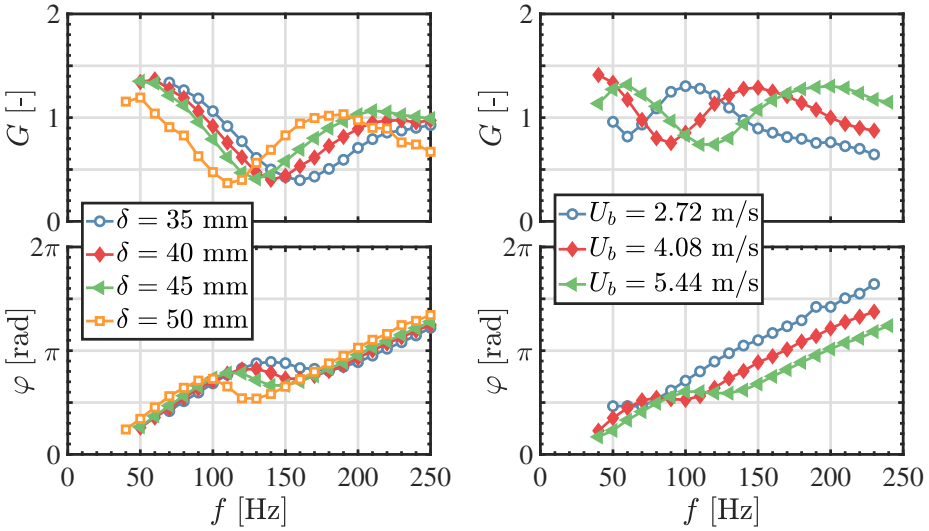

Figure 6.6: *Flame Transfer Function measurements. Geometrical configurations: (left) SW_3, $D_o = 20$ mm, $C = 10$ mm, $\delta = 35 - 50$ mm; (right) SW_3, $D_o = 20$ mm, $C = 12$ mm, $U_b = 2.77 - 5.44$ m/s. Forcing level: $u'/\overline{u} = 0.30$ RMS.*

ical end piece diameter $C = 12$ mm. The shape of these flames in the absence of forcing is reported in Fig. 6.5, showing that the flame size increases, keeping the same aspect ratio, as the injection velocity U_b is increased. The swirl number $S = 0.73$ was measured only for the configuration with $U_b = 5.44$ m/s and is here assumed to remain the same for the other configurations with a lower velocity. FTF results for these flames are reported in Fig. 6.6-right at a forcing level $u'/\overline{u} = 0.30$ RMS.

The FTFs reported in the left and right plot in Fig. 6.6 are both characterized by alternating regions with first a maximum and then a minimum value of the gain as the excitation frequency increases. Their phase lag also features an inflection point around the frequency of the gain minimum. One retrieves the same features observed for the FDF shown in Fig. 6.3. The peculiarity of the results shown in Fig. 6.6 is that the FTF gain and phase-lag curves are basically shifted in the frequency range, without any important modification of their shape, as δ or U_b are modified. The minimum value reached by the FTF gain remains the same in Fig. 6.6-left for the different cases explored with changes of the distance δ and in Fig. 6.6-right for the different cases explored with changes of the bulk flow velocity U_b, but the frequency corresponding to this minimum gain value changes as δ or U_b are modified. In particular, this frequency increases as δ is reduced or as U_b is increased. This is due to a change of the time required for the convected disturbances generated at the swirler trailing edge to reach the burner outlet. This time lag decreases as the distance δ decreases or as the bulk velocity in the injection tube increases.

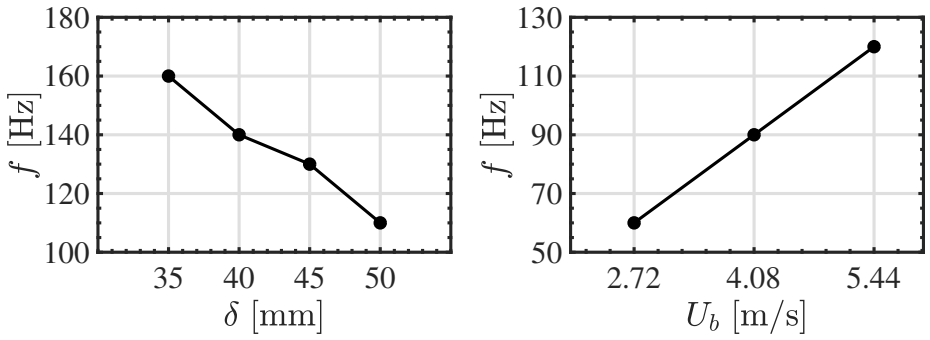

Figure 6.7: *Evolution of the frequency corresponding to the minimum FTF gain value for different values of the distance δ between the swirler exit and the combustion chamber backplane (left) and of the bulk flow velocity U_b (right).*

The minimum gain value is close to $G = 0.40$ for all configurations in Fig. 6.6-left. The frequency where this minimum is observed reduces as δ increases: $f = 160$ Hz ($\delta = 35$ mm), $f = 140$ Hz ($\delta = 40$ mm), $f = 130$ Hz ($\delta = 45$ mm) and $f = 110$ Hz ($\delta = 50$ mm). It is interesting to note that the product of f and δ is almost constant in these four cases. This is also highlighted in Fig. 6.7-left, showing the evolution of the frequency corresponding to a minimum FTF gain value with respect to the distance δ. It is also important to remember that the FTF measurements are conducted with a frequency resolution of 10 Hz, which can justify the slight change of slope of the line in Fig. 6.7-left. The minimum gain is close to $G = 0.75$ for all configurations in Fig. 6.6-right. The frequency where this minimum is observed increases as U_b increases: $f = 60$ Hz ($U_b = 2.72$ m/s), $f = 90$ Hz ($U_b = 4.10$ m/s) and $f = 120$ Hz ($U_b = 5.44$ m/s). It is again interesting to observe that the ratio of f and U_b is remains also constant in this three cases. This is highlighted in Fig. 6.7-right, showing the evolution of the frequency corresponding to a minimum FTF gain value with respect to the bulk flow velocity U_b.

6.4 Effect of geometrical modifications of the injector unit

6.4.1 Effect of the outlet diameter D_o of the injector

Figure 6.8 presents the effects of modifications of the injector exit diameter ($D_o = 18$, 20, 22 mm) on the flame transfer functions for flames stabilized with SW_2 (left) or SW_1 (right), with a bluff-body featuring a conical end piece diameter of $C = 12$ mm. The shapes of these flames for the configurations featuring the swirling vane SW_2 are reported in Fig. 6.9, showing that as D_o decreases and thus the swirl number decreases, the flame becomes more elongated, moves

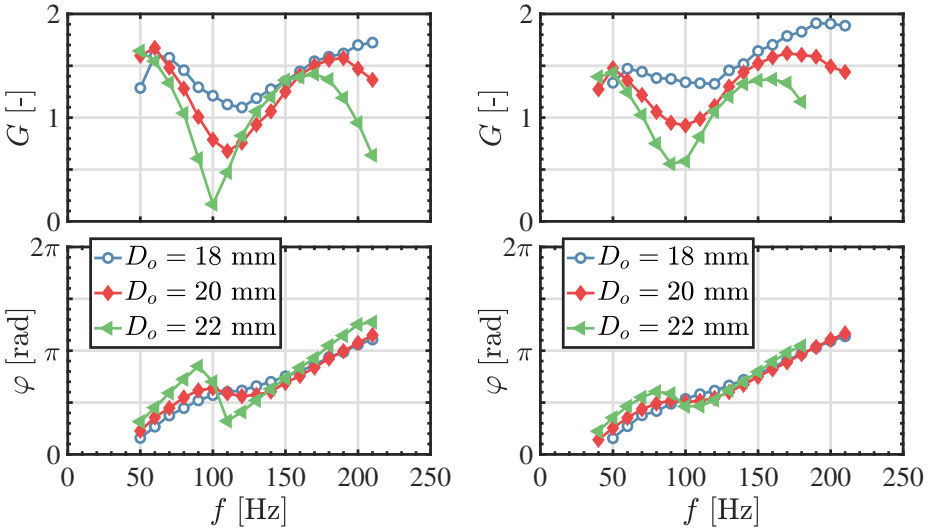

Figure 6.8: *Flame Transfer Function measurements. Geometrical configurations: (left) SW_2, $D_o = 18 - 22$ mm, $C = 12$ mm; (right) SW_1, $D_o = 18 - 22$ mm, $C = 12$ mm. The forcing level is fixed at $u'/\overline{u} = 0.10$ RMS.*

further away from the injector outlet and closer to the chamber walls.

FDF data are plotted in the frequency range $50 - 210$ Hz, with a 10 Hz resolution, for a velocity perturbation level fixed to $u'/\overline{u} = 0.10$ RMS in Fig. 6.8. The shape of the FTFs shows the same characteristics as the ones reported in Fig. 6.3 and in Fig. 6.6. The gain features a first maximum around $f = 50 - 60$ Hz. It is found here that this maximum gain value is almost unaltered by the geometrical configuration chosen for the injector. Then the gain curve features a drop with a valley to reach its minimum value. The most important difference for the gain curves in Fig. 6.8 with respect to results presented in Fig. 6.3 and in Fig. 6.6 is that the minimum FTF gain value largely differs depending on the

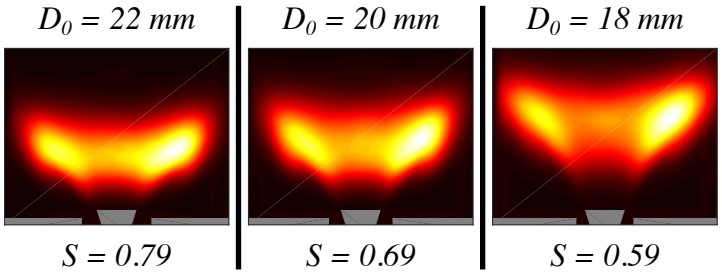

Figure 6.9: *OH* flame light distribution for the geometrical configuration featuring SW_2, $D_o = 18 - 22$ mm, $C = 12$ mm, $\delta = 50$ mm. The bulk flow velocity is $U_b = 5.44$ m/s and the equivalence ratio is $\phi = 0.82$. The colorscale is the same as the one used in Fig. 6.2.*

geometrical configuration of the injector tested. Reduction of the FTF gain is very slight for configurations with $D_o = 18$ mm in Fig. 6.8 for both swirling vanes SW_2 and SW_1 associated to slightly different swirl levels $S = 0.59$ and $S = 0.54$ respectively. The minimum gain value does not drop below unity in both cases. The minimum FTF gain drops below unity when the injector diameter is increased to $D_o = 20$ mm for both swirling vanes SW_2 and SW_1. In these cases the swirl levels are $S = 0.69$ and $S = 0.63$ respectively. The drop of the FTF gain is the largest for the biggest injector diameter $D_o = 22$ mm. In this case, a gain as low as $G \simeq 0.15$ is measured for SW_2 ($S = 0.79$), while the minimum gain is $G \simeq 0.5$ for swirler SW_1 ($S = 0.71$). FTF measurements for swirler SW_3 were attempted in the same configuration. Results cannot be presented since, for this geometry featuring a swirl number $S = 0.81$, the flame flashed back into the injection tube when submitted to flowrate modulations at frequencies close to 100 Hz even for a forcing level as low as $u'/\overline{u} = 0.05$ RMS.

At higher forcing frequencies the FTF gain increases again in Fig. 6.8 to reach a second maximum. It is worth noting that the maximum gain values of the FTF obtained with swirlers SW_1 and SW_2 are close in Fig. 6.8 when the diameter D_o is the same. The differences in the amplitude response between these two swirler designs are the largest at the frequency corresponding to the minimum FTF gain. It is also interesting to observe that the frequencies corresponding to this peculiar minimum values of the FTF gain are slightly shifted to higher values as the injector nozzle diameter D_o is reduced and the flow velocity in the tube between the swirler exit and the chamber backplane increases. This is once again due to a change of the time required for the convected disturbances generated at the swirler trailing edge to reach the burner outlet. This time lag decreases since the bulk velocity in the injection tube increases.

The phase-lag curves in Fig. 6.8 also feature a sharp transition with an inflection point around the FTF gain minimum frequency. This transition is sharper when the FTF gain drop is higher. In the rest of the frequency range investigated, the phase-lag increases regularly with frequency, showing a constant slope that increases as the injector diameter D_o increases.

6.4.2 Effect of the bluff-body end piece diameter C

Figure 6.10 shows effects of modifications of the conical bluff-body diameter $C = 10$, 12, 14 mm on the FTF for flames stabilized with the radial swirler SW_2 and an injector diameter fixed at $D_o = 20$ mm. The mean shape taken by these flames is reported in Fig. 6.11. One reminds that as the swirl number decreases, here by increasing the diameter C, the flame becomes more elongated, moves further away from the injector outlet and closer to the chamber walls.

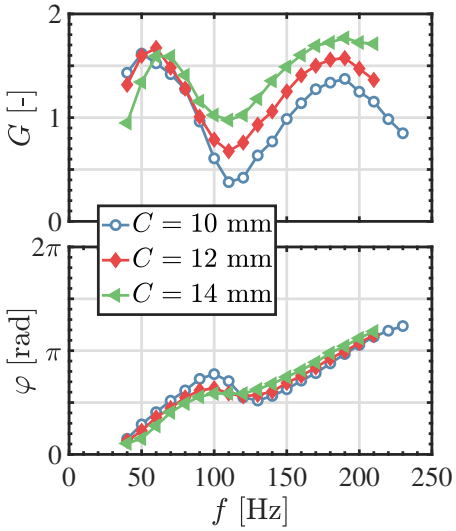

Figure 6.10: *Flame Transfer Function measurements. Geometrical configurations: SW_2, $D_o = 20$ mm, $C = 10 - 14$ mm. Forcing level: $u'/\overline{u} = 0.10$ RMS.*

FTF data are plotted in the frequency range $40 - 230$ Hz, with a 10 Hz resolution, for a velocity perturbation level fixed to $u'/\overline{u} = 0.10$ RMS in Fig. 6.10. The shape of the FTFs is again close to the ones shown previously in the chapter. The gain features a first maximum in the range $f = 50 - 60$ Hz. Once again this maximum gain value is almost independent of the geometrical configuration of the injector. As the forcing frequency increases, the gain curves still feature a drop with a valley and reach a minimum value, which decreases as the swirl number increases, when the cone diameter C is reduced. The gain minimum in Fig. 6.10 reaches a value close to unity for $C = 14$ mm and $S = 0.61$. It reduces to $G \simeq 0.65$ for $C = 12$ mm and $S = 0.69$ and it drops to $G \simeq 0.4$ for $C = 10$ mm and $S = 0.73$. For increasing forcing frequencies the gain level increases again to reach a second maximum around $f = 190$ Hz.

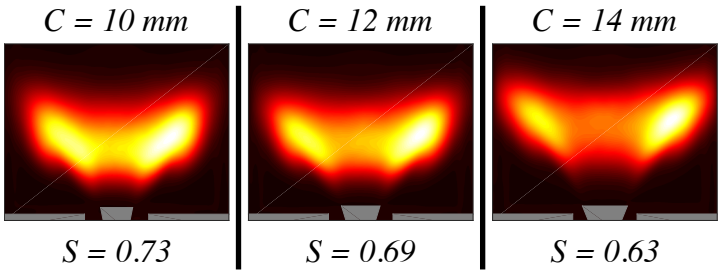

Figure 6.11: *OH* flame light distribution for the geometrical configuration featuring SW_2, $D_o = 20$ mm, $C = 10 - 14$ mm, $\delta = 50$ mm. The bulk flow velocity is $U_b = 5.44$ m/s and the equivalence ratio is $\phi = 0.82$. The colorscale is the same as the one used in Fig. 6.2.*

It is important to underline that, for all these configurations sharing the same flow velocity in the injection tube between the swirler exit and the chamber backplane, the frequencies corresponding to minimum or maximum gain values are exactly the same.

The shape of the phase-lag curves in Fig. 6.10 is the same as in Figs .6.3 and 6.8. The results obtained for different diameters C in Fig. 6.10 are roughly superposed. The only difference is that the sharp change at the inflection point where the FTF gain reaches a minimum increases as the swirl level increases and the minimum FTF gain drops.

6.4.3 Effect of the swirling vane

Effects of modifications of the swirling vane SW_0, SW_1, SW_3 and SW_4 on the FTF are now presented in Fig. 6.12, for flames stabilized with the nozzle diameter $D_o = 22$ mm and a conical end piece diameter $C = 14$ mm. Results are plotted in the frequency range $20 - 250$ Hz, with a 10 Hz resolution and for a velocity perturbation level fixed to $u'/\overline{u} = 0.30$ RMS in this case. The mean shape taken by these flames is reported in Fig. 6.13.

The FTFs obtained with swirlers SW_1, SW_3 and SW_4 have the same characteristics as those shown in Figs. 6.3, 6.6, 6.8 and 6.10. The FTF gain features an alternating behavior with first a maximum followed by a minimum value. The minimum gain decreases as the swirl level S increases when SW_1 ($S = 0.65$) is

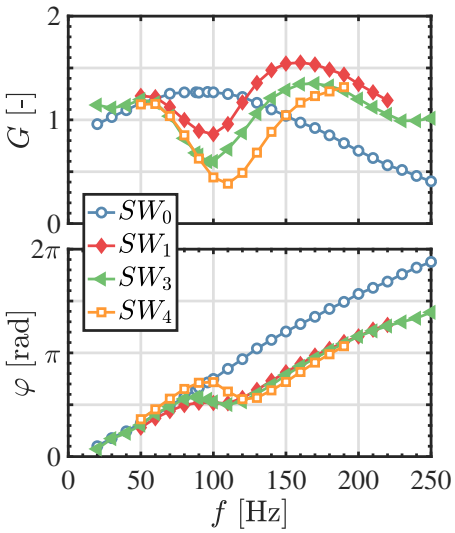

Figure 6.12: *Flame Transfer Function measurements. Geometrical configurations:* $SW_{0,1,3,4}$, $D_o = 22$ *mm*, $C = 14$ *mm. Forcing level:* $u'/\overline{u} = 0.30$ *RMS.*

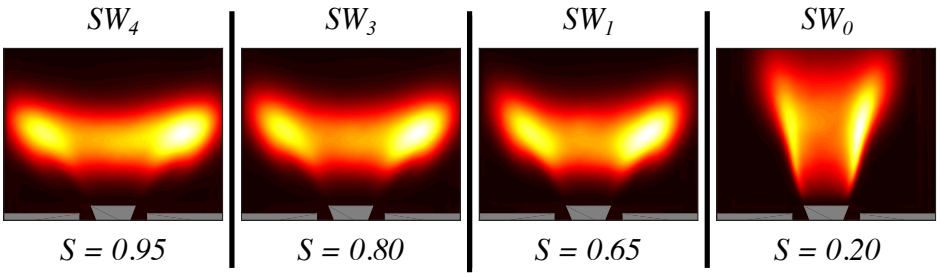

Figure 6.13: *OH* flame light distribution for the geometrical configuration featuring* $SW_{0,1,3,4}$, $D_o = 22$ *mm*, $C = 14$ *mm*, $\delta = 50$ *mm. The bulk flow velocity is* $U_b = 5.44$ *m/s and the equivalence ratio is* $\phi = 0.82$. *The colorscale is the same as the one used in Fig. 6.2.*

replaced by SW_3 ($S = 0.80$). The lowest gain is obtained for the highest swirl number $S = 0.95$ for SW_4.

The flame stabilized with the low swirl injector SW_0 ($S = 0.20$) behaves in a singular manner. In this case, the FTF gain curve $G(f)$ smoothly increases to reach a maximum $G \simeq 1.27$ at $f \simeq 100$ Hz and then smoothly decreases towards zero as the forcing frequency further increases. This low-pass filter behavior, with gain values exceeding unity in the frequency range $40 - 150$ Hz, is a well known feature of the acoustic response of laminar premixed non-swirling V-flames, as first theoretically demonstrated in Schuller et al., 2003 and confirmed experimentally in Durox et al., 2005. The same type of smooth behavior with large gain overshoots at low frequencies is also a characteristic of the response of turbulent non-swirling flames (Balachandran et al., 2005). The shape of this flame is actually closer to that of a non-swirling flame, as shown in Fig. 6.13. Indeed, the swirl number $S = 0.20$ is very low in this case.

The FTF phase-lag of the low swirling flame SW_0 also behaves like that of a non-swirling V-flame. It regularly increases in Fig. 6.12 with an almost constant slope in the full frequency range investigated. There is no inflection point in this case. The FTF phase lag increases linearly also for the other swirling flames presented in Fig. 6.12, except in the frequency region close to the minimum value of the FTF gain, where an inflection point and a rapid change of the phase lag characterize the responses of the highly swirled flames.

6.5 Discussion

Some general features about the FTF/FDF of highly swirled flames ($S \geq 0.60$) can be drawn from the results presented in this chapter.

The flame response is characterized by alternating regions with maximum and minimum gain values. With respect to the forcing level, Fig. 6.3, the behavior of the FTF gain is strongly non-linear around the maximum response and roughly linear at the minimum response. The FDF phase-lag does not depend on the forcing level.

When the time required for the convected disturbances generated at the swirler trailing edge to reach the burner outlet is modified, either by a change of the distance δ between the swirler exit and the combustion chamber backplane or by a change of the bulk flow velocity U_b, but all the other geometrical parameters of the injector unit are fixed, Fig. 6.6, the FTF gain curve is shifted in the frequency range without any important change of its shape. In particular, the minimum gain level is constant for these configurations with a constant swirl number.

When the injector geometry is modified in such a way to modify the swirl number, either by changing the injector outlet diameter D_o, the conical end piece diameter C or the swirling vane SW, the minimum FTF gain value decreases as the swirl level increases. This is confirmed through 4 different set of experiments presented in Figs.6.8, 6.10 and 6.12. One should however be careful that the swirl level is not the only parameter influencing the minimum gain level. Two different flames, stabilized with the same swirl level but on two injectors featuring more than one different component, can lead to a different value of the gain minimum. This is highlighted in blue in Tab. 6.1, that summarizes the FTF results presented in this chapter. Moreover, if we consider two flames with different swirl numbers, the one with the higher swirl can lead to an higher minimum response if the two flames are stabilized on injectors featuring more than one different component. This is highlighted in red in Tab. 6.1.

These results are used to explain some of the differences in the properties of the combustion instabilities analyzed in chapter 5.

In Fig. 5.11, it was found that the amplitude of the instability differs when the distance δ is set to 35 mm or to 50 mm and the length of the exhaust tube is modified from $1E$ to $2E$ and $3E$. These self sustained oscillations were analyzed in a configuration with an injector equipped with the radial swirler SW_3, a nozzle diameter $D_o = 20$ mm and a conical end piece diameter $C = 10$ mm. The FTF of this injector is shown in Fig. 6.6-left. With $\delta = 35$ mm, a strong instability was detected at a frequency close to 220 Hz with an exhaust length

of $1E$. From Fig. 6.6-left, we observe that this frequency is close to the one where the FTF gain features a maximum value $G \simeq 1$. With $\delta = 50$ mm, the strongest instability was detected at a frequency close to 164 Hz, with an exhaust tube length of $3E$. Once again, this configuration features a maximum response with $G \simeq 1$ around this frequency in Fig. 6.6-left. With the same exhaust tube length $3E$, the instability could be suppressed for the injector equipped with the same swirling vane but a smaller distance $\delta = 35$ mm. One clearly sees that the FTF gain in Fig. 6.6-left is close to its minimum value $G \simeq 0.4$ at $f = 164$ Hz for $\delta = 35$ mm.

In Fig. 5.13, it was observed that the intensity of the instability is close when the swirler design is modified but all the other geometrical parameters of the injector are fixed. These self sustained oscillations were analyzed in a configuration with a nozzle diameter $D_o = 20$ mm, a conical end piece diameter $C = 10$ mm and the swirling vanes SW_1 and SW_3. Unfortunately the FTFs of these injectors were not measured. One can try to comment by analyzing FTF results obtained for SW_1 and SW_3 while all other geometrical parameters are fixed as shown in Fig. 6.12. These data are obtained for a configuration featuring a nozzle diameter $D_o = 22$ mm and a conical end piece diameter $C = 14$ mm, which is slightly different with respect to the one analyzed in Fig. 5.13 . One sees that the maximum gain value is $G \simeq 1.5$ for SW_1 and $G \simeq 1.4$ for SW_3. These values are also observed in the same frequency range $f = 160$-170 Hz. It is thus evident that a change of the swirling vane when all the other parameters of the injector are fixed does not lead to a sensible change of the maximum gain value or of the frequency at which this value is observed. FTF data for the same injectors studied in Fig. 5.13 are necessary to strengthen this conclusion.

Table 6.1: *Evolution of the minimum gain level for the different configurations explored. SW: Swirler design: D_o: injection tube diameter [mm], C: conical end piece diameter [mm], δ : distance between the swirler exit and the injection plane outlet [mm], U_b: bulk flow velocity at the convergent outlet [m/s], A_1/A_2 : normalized injector cross section area based on hydraulic diameters. S^* : Estimated swirl number. S : Swirl number deduced from LDV or PIV measurements. G_{min}: minimum gain level. Fig.: corresponding figure reporting the full FTF measurements.*

SW	D_o	C	δ	U_b	A_1/A_2	S	G_{min}	Fig.
1	18	12	50	5.44	8.60	0.54*	1.32	6.8-right
2	18	12	50	5.44	8.60	0.59	1.10	6.8-left
1	20	12	50	5.44	5.36	0.63	0.93	6.8-right
2	20	12	50	5.44	5.36	0.69	0.68	6.8-left, 6.10
1	22	12	50	5.44	3.66	0.71	0.55	6.8-right
2	22	12	50	5.44	3.66	0.79	0.16	6.8-left
2	20	14	50	5.44	7.56	0.63	0.98	6.10
2	20	10	50	5.44	4.00	0.73	0.38	6.10
1	22	14	50	5.44	4.84	0.65*	0.86	6.12
3	22	14	50	5.44	4.84	0.80	0.59	6.12
4	22	14	50	5.44	4.84	0.95*	0.38	6.12
3	20	10	35	5.44	4.00	0.80*	0.39	6.6-left
3	20	10	40	5.44	4.00	0.80*	0.40	6.6-left
3	20	10	45	5.44	4.00	0.80*	0.40	6.6-left
3	20	10	50	5.44	4.00	0.80	0.37	6.6-left
3	20	12	50	2.72	5.36	0.73*	0.80	6.6-right
3	20	12	50	4.08	5.36	0.73*	0.76	6.6-right
3	20	12	50	5.44	5.36	0.73	0.75	6.6-right

6.6 Conclusion

Experiments were carried out to investigate changes in the acoustic response of swirl-stabilized lean premixed methane/air flames, when the system is operated at constant equivalence ratio $\phi = 0.82$ for different injection conditions and injector designs.

It was first shown that the flame response depends on the excitation frequency and amplitude. The transfer function measurements show that the FTF gain curve of swirling flames is characterized by a low frequency gain peak followed by a sudden drop and that the minimum gain value decreases as the swirl number increases. This was confirmed in different configurations obtained by modifying the diameter of the injection nozzle, the diameter of the conical end piece at the top of the central bluff body and the dimensions of the radial swirler. On the other side, the FTF of a low-swirled flame was shown to be similar to that of a non-swirling V-flame, for which the gain exhibits values exceeding unity over a large frequency span before smoothly being reduced at higher frequencies.

It was shown that the behavior of the FTF gain with respect to the forcing level is highly non-linear at frequencies corresponding to maximum values of the gain, while it is roughly linear at the FTF gain minimum. The phase lag curve remains independent of the forcing level.

It was then found that a shift in the frequency range of the FTF gain and phase lag curves is obtained, when the distance between the swirler and the combustion chamber or the bulk flow velocity in the injection channel downstream the swirler are modified. This is due to a change of the time required for the convected disturbances generated at the swirler trailing edge to reach the burner outlet. It was observed that the product between the distance δ and the frequency f corresponding to a minimum flame response or the ratio between U_b and f remains constant.

These results were used to interpret some of the features of combustion instabilities observed in the previous chapter. In particular, the fact that a maximum or a minimum value of the FTF gain can be obtained at a same frequency for different values of the distance δ between the swirler and the combustion chamber backplane, explains the different intensity of the instability observed at that same frequency for different values of the distance δ.

The following two chapters are dedicated to the interpretation of the results presented here by scrutinizing the flow and the flame with optical diagnostics and with the help of numerical simulations.

Chapter 7

Flow and flame dynamics

In this chapter we focus on the mechanisms leading to the high or low FTF gain values observed in chapter 6. Strong swirl number fluctuations leading to a strong flame-flow interaction at the flame base and hindering the development of vortical structures generated at the burner rim are currently interpreted as the reason for the low FTF gain at peculiar frequencies. These fluctuations are weaker at the FTF gain maximum frequency which means that vortical structures are free to fully develop and interact with the flame at its tip. These mechanisms are here questioned through a set of experimental and numerical observations. Phase-locked OH chemiluminescence images first reveal that the motion of highly swirled flames is qualitatively similar at the two frequencies of interest, while a general decrease of flame luminosity and flame volume fluctuations is observed as the gain level is reduced. Cold flow, phase-locked PIV measurements in an axial and in a transverse plane are then considered. These measurements show a general reduction of the strength of vortical structures at the FTF gain minimum frequency with respect to the FTF gain maximum frequency as reported in the literature. Phase conditioned Large Eddy Simulations are lastly exploited in cold flow conditions at the two frequencies. These data first confirm the PIV results in terms of different strength of vortical structures shed from the burner rim. More importantly, swirl number fluctuations are found to be comparable at the two frequencies. This result is in contrast with the current understanding from the literature. The different strength of vortical structures shed from the burner rim is here not related to a different flame-flow interaction resulting from a different swirl number oscillations, since this effect is already observed in cold flow conditions and swirl number fluctuations are comparable at the two frequencies. The origin of this mechanism is here purely hydrodynamic, resulting from the complex interaction between the axial and the azimuthal velocity components inside the injector and leading to a different shape of velocity profiles at the burner rim.*

7.1 Introduction

It has been emphasized in the introduction that the mechanisms leading to a drop of the FTF gain are not fully elucidated and different scenarios were envisaged to explain this drop. Palies *et al.* (Palies et al., 2010a; Palies et al., 2011e; Palies et al., 2011d) came to the conclusion that interferences between vortex shedding at the injector lip with a flapping motion of the flame base do not let these vortices to grow in strength before they rollup the flame. Bunce et al., 2013 consider that the Kelvin-Helmholtz instability in the external shear layer of the forced jet cannot fully develop due to thermal dilation from the combustion reaction.

Results in the previous chapter showed that progressively increasing the swirl level led to a progressive reduction of the FTF minimum gain value. It has also been shown that the details of the injector geometry need to be considered as well. Different injectors featuring the same swirl level, led to slightly different reduction of the FTF gain.

The origin of the physical mechanisms leading to a drop of the FTF gain curve in the low frequency range needs further investigation. This is the main scope of this chapter. The following section is dedicated to the investigation of the forced flame dynamics by phase conditioned analysis of the OH* signal emitted by the pulsated flames obtained for different injectors. This is followed by phase conditioned analysis of PIV measurements made under cold flow conditions and by phase conditioned Large Eddy Simulations. These simulations are first compared to PIV measurements and then further exploited to complete the analysis.

7.2 Flame dynamics

Four different injector geometries are considered for the analysis of flame dynamics. The corresponding flame transfer function measurements are reported in Fig. 7.1. The mean shape taken by these flames is exemplified in Figs. 7.2-b and 7.3-b.

7.2.1 Difference between non-swirling and high swirling flame dynamics - Effect of the swirling vane

The first configuration of interest is the one stabilized with the non-swirling injector SW_0 with the nozzle diameter $D_o = 22$ mm and the top cone diameter $C = 14$ mm. It is here taken as the basis to compare the dynamics of non-swirling and swirling flames. The second configuration features the same injector dimensions ($D_o = 22$ mm, $C = 14$ mm) but is equipped with swirler

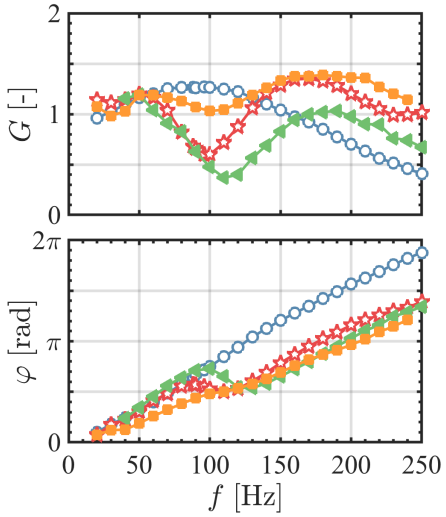

Figure 7.1: *Flame Transfer Function measurements. Geometrical configurations: SW_0, $D_o = 22$ mm, $C = 14$ mm, (blue); SW_3, $D_o = 18$ mm, $C = 12$ mm, (orange); SW_3, $D_o = 22$ mm, $C = 14$ mm, (red); SW_3, $D_o = 20$ mm, $C = 10$ mm, (green). The forcing level is fixed to $u'/\bar{u} = 0.30$ RMS.*

SW_3. The response of these flames is analyzed in Fig. 7.2 at the forcing frequency $f = 96$ Hz corresponding to a maximum FTF gain value for the injector equipped with the vane SW_0 (blue curve in Fig. 7.1) and a minimum gain value when it is replaced by the swirler SW_3 (red curve in Fig. 7.1). The last row in Fig. 7.2 shows the response observed at a forcing frequency $f = 170$ Hz corresponding to the maximum FTF gain value for the injector with SW_3. The forcing level $u'/\bar{u} = 0.30$ RMS is the same as the one used for the FTF measurements shown in Fig. 7.1. Six phase conditioned images covering the full cycle of oscillation are shown. Images are separated by a phase angle of 60 degrees and each image is formed by accumulating one hundred snapshots with an exposure time of 40 μs each. The angles indicated in the figure are the phase delays with respect to the hot wire signal. An Abel deconvolution reveals the trace of the flame luminosity in an axial plane crossing the burner axis. These images were obtained with the same camera and optical setup. The same color scale, at the bottom in Fig. 7.2, is used for all images to better highlight both the flame motion and changes of the flame luminosity during the forcing cycle.

The first sequence in Fig. 7.2 highlights the large motion executed by the flame at the low swirl level $S = 0.20$ with the device SW_0 and the forcing frequency $f = 96$ Hz when the FTF gain is maximum in Fig. 7.1. Large roll-up of the flame tip is seen at phase angles 195° and 255°. The flame is stretched in the vertical direction during the forcing cycle with relatively minor changes of the OH* luminosity along the flame arms.

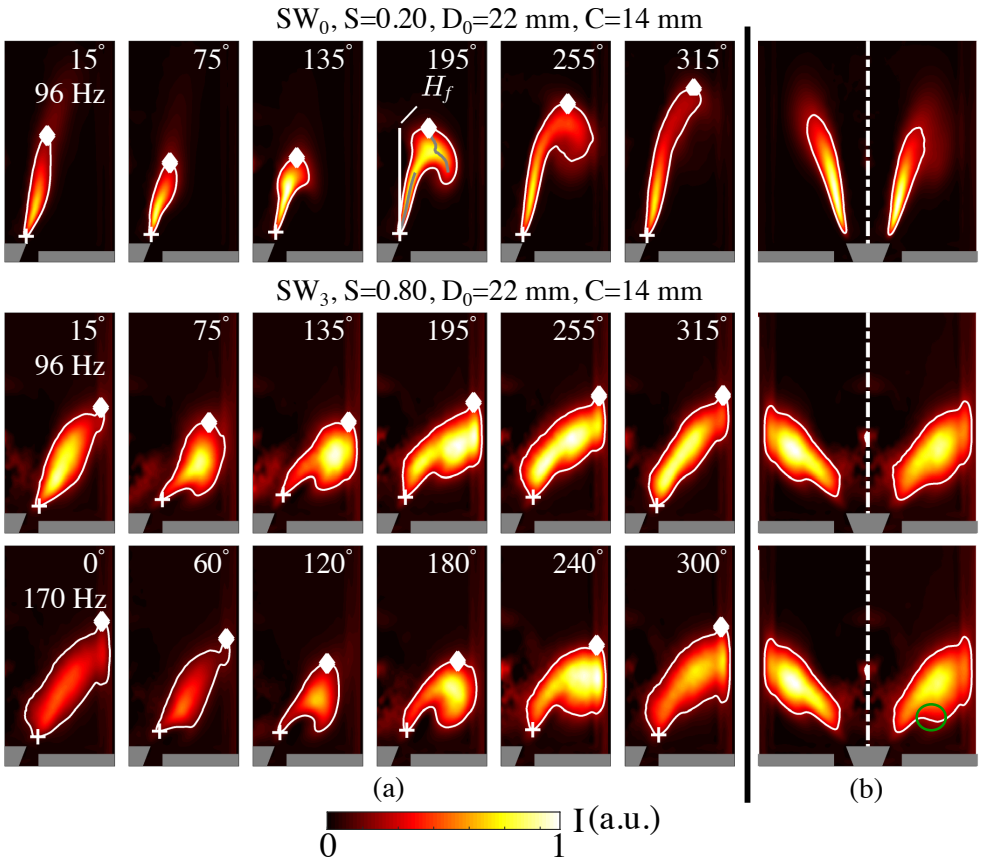

Figure 7.2: *(a): Abel deconvoluted phase conditioned images of the flame OH* signal for a forcing level $u'/\bar{u} = 0.30$ RMS. The phase angle is referred to the hot wire signal. The flame contours used to determine the flame volume V are superimposed on the flame images. (b): comparison between unforced flame (left of the chamber axis) and mean flame determined from the phase conditioned images (right of the chamber axis).*

The second and third sequences in Fig. 7.2 show the flame response for a higher swirl number $S = 0.80$ stabilized with the swirler SW_3, at the frequencies $f_0 = 96$ Hz, corresponding to a FTF gain minimum and $f = 170$ Hz, corresponding to the FTF gain maximum in Fig. 7.1. The motion executed by the flame at these two forcing frequencies does not differ significantly. It is mainly changes of the flame luminosity along the flame arms that explain the large differences observed for the FTF gain at $f_0 = 96$ Hz and $f = 170$ Hz in Fig. 7.1. At $f_0 = 96$ Hz, there is a relatively weak flame roll-up motion accompanied by weak changes of the flame luminosity over the phases of the forcing cycle. At $f = 170$ Hz, the flame roll-up motion is a bit further pronounced, but the OH* luminosity undergoes large regular changes over the phases in the forcing cycle, explaining the large value taken by the FTF gain at this frequency in Fig. 7.1.

7.2.2 Difference between high swirling flame dynamics - Effect of the injector unit geometry

This behavior is confirmed in the first and second rows in Fig. 7.3 showing the response of a flame stabilized with swirler SW_3, but an injector equipped with a nozzle cone diameter $D_o = 20$ mm and a top cone diameter $C = 10$ mm. This flame features the same swirl level $S = 0.80$ as the previous one, but a different level of the minimum FTF gain in Fig. 7.1. The flame luminosity along the flame arms again barely changes for the flow forced at $f_0 = 110$ Hz in the first row in Fig. 7.3. This low response explains the minimum FTF gain value reached at this frequency in Fig. 7.1. This again contrasts with the large fluctuations of the OH* intensity signal observed in the second row in Fig. 7.3 when the flame is forced at $f = 190$ Hz that corresponds to a large FTF gain in Fig. 7.1. The qualitative differences between the motion executed by the flame at these two forcing frequencies $f = 110$ and 190 Hz are less pronounced.

A last case is considered in the third and fourth sequences in Fig. 7.3 for an injector still equipped with swirler SW_3 but with a slightly smaller nozzle diameter $D_o = 18$ mm and a slightly larger top cone diameter $C = 12$ mm. This flame features a lower swirl level $S = 0.60$ than the flame shown at the top in Fig. 7.3. In this latter case, both the flame motion and the OH* luminosity fluctuations are important at the two forcing frequencies $f = 110$ Hz and $f = 180$ Hz investigated. Indeed, the FTF gain level remains high in Fig. 7.1 at these two frequencies for this injector characterized by a moderately high swirl number $S = 0.60$.

One can get further insight by a closer examination of the OH* light distributions averaged over the forcing excitation cycle that can be compared to the OH* light distribution in the absence of acoustic forcing. These images are gathered in Figs. 7.2-b and 7.3-b. The OH* light distributions from the unperturbed flames are compared to the mean flame light distributions averaged over all phase conditioned images in the row. One can see that in all cases this average distribution remains essentially unaltered at the two forcing frequencies investigated, characterizing the minimum and maximum flame responses. In all forced configurations explored, the average light distribution over a forcing cycle also barely differs from the unperturbed flame light distribution, even for a forcing level as high as $u'/\bar{u} = 0.30$ RMS. The main differences when the flame is pulsated are (i) a small decrease of the mean flame lift-off distance, (ii) a small modification of the flame height and (iii) an increase of the flame volume in the region where vortical structures impinge the flame. This is emphasized by the green circle in the third sequence in Fig. 7.2-b.

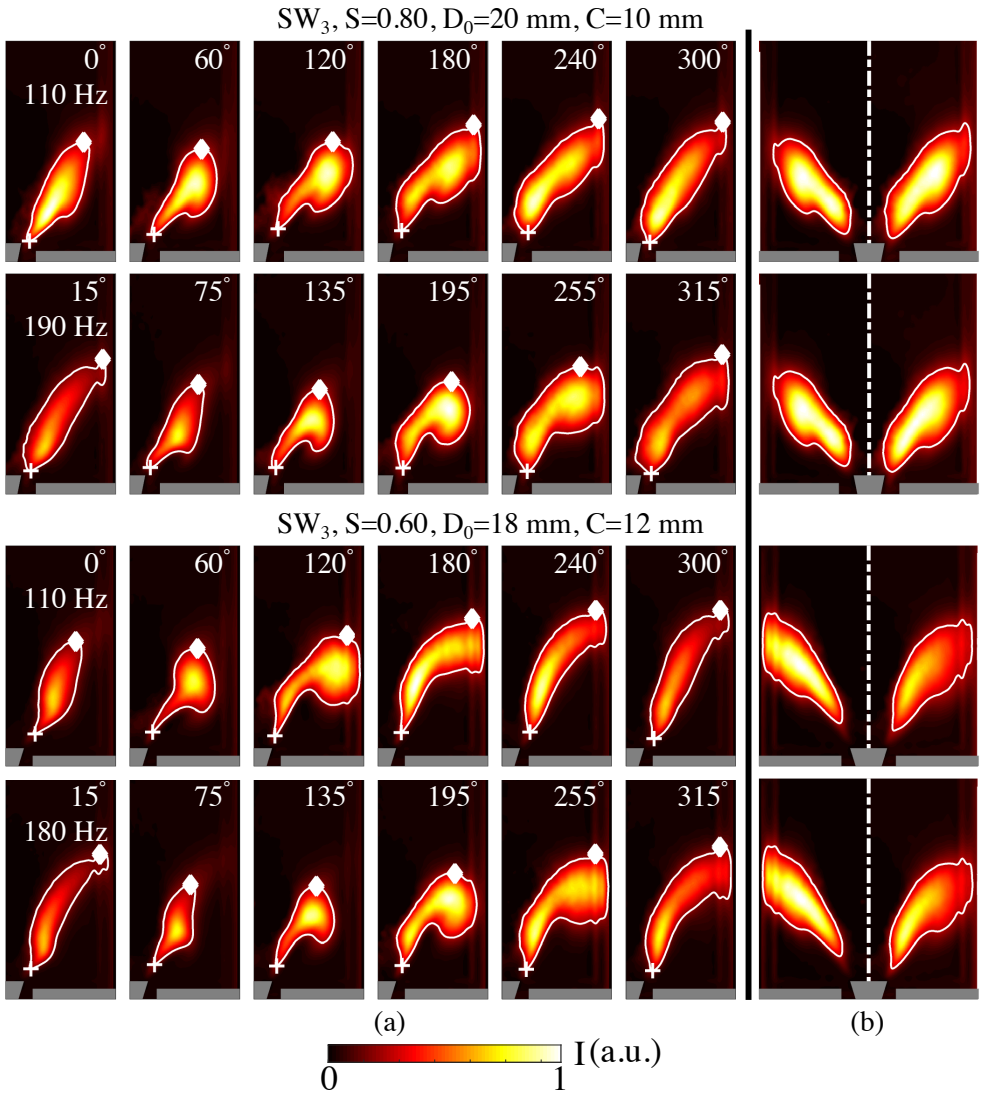

Figure 7.3: *(a): Abel deconvoluted phase conditioned images of the flame OH* signal for a forcing level $u'/\bar{u} = 0.30$ RMS. The phase angle is referred to the hot wire signal. The flame contours used to determine the flame volume V are superimposed on the flame images. (b): comparison between unforced flame (left of the chamber axis) and mean flame determined from the phase conditioned images (right of the chamber axis).*

7.2.3 Flame motion analysis

Further analysis is now made by determining the flame contours, highlighting the region of the flame where the luminosity is higher than a threshold level, for each image recorded. The threshold is taken here equal to 25% of the maximum flame luminosity in each phase averaged picture, a value found to be suitable for the determination of the flame contours. It was checked that the results presented hereafter are only weakly sensitive to this threshold level, when this

is chosen in the range $15-35\%$ of the maximum flame luminosity. The flame contours are used to determine the flame height H_f, which is deduced by calculating the vertical distance between the lowest point, shown as a plus sign in Figs. 7.2-7.3, and the highest point, shown as a diamond sign in Figs. 7.2-7.3, of the flame contours. The flame angle α with respect to the vertical direction is also determined at the flame leading edge position.

Finally, the swirl number S is also determined, for each selected phase in the forcing cycle. These data are deduced from the phase conditioned PIV fields measured in a longitudinal plane crossing the chamber axis and in a transverse plane 2 ± 0.5 mm above the top cone of the central bluff-body in the absence of combustion. The precision on the deduced swirl number is $\pm 5\%$. Evolutions of H_f and α are plotted over two periods in Fig. 7.4 together with the evolution of the swirl number S.

The top graph in Fig. 7.4 is obtained for the injector with swirler SW_0, an injector outlet diameter $D_o = 22$ mm and a bluff-body end piece diameter $C = 14$ mm at the forcing frequency $f = 96$ Hz. One reminds that in this case the flame features a weak swirl number $S = 0.20$ and that this case serves as a reference. The flame undergoes large fluctuations of its height $H'_f/\overline{H}_f$, but no oscillation of the flame base angle $\alpha'/\overline{\alpha} \simeq 0$. The small oscillations of the swirl number S around the mean value 0.2 observed in this plot are meaningless here due to the low values of the swirl number.

The situation differs for the results obtained with swirler SW_3 in the other graphs in Fig. 7.4 independently of the forcing frequency and injector design. The flame response now exhibits both flame base angle $\alpha'/\overline{\alpha}$ oscillations and flame height $H'_f/\overline{H}_f$ oscillations in the second and third rows in Fig. 7.4, obtained for a swirl number $S = 0.80$, but different injection nozzle diameters $D_o = 22$ and 20 mm and top cone diameters $C = 14$ and 10 mm respectively. The same conclusions can be drawn for the results shown in the fourth row obtained for the same swirler SW_3, but at a slightly lower swirl number $S = 0.60$ with $D_o = 18$ mm and $C = 12$ mm. These swirled flames undergoing large oscillations of their flame base angle and large oscillations of their flame height all feature large oscillations of the swirl number in Fig. 7.4. These observations contrast with data reported by Palies *et al.* (Palies et al., 2010a; Palies et al., 2011e; Palies et al., 2011d) in which the flame base angle and swirl number oscillations differed at frequencies corresponding to maximum and minimum of the FTF gain.

The main striking features in Fig. 7.4 are that the oscillations of the swirl number S, the flame base angle oscillations $\alpha'/\overline{\alpha}$ and the flame height oscillations $H'_f/\overline{H}_f$ experienced by these flames, are very similar in the left and right plots corresponding the minimum and maximum flame responses respectively.

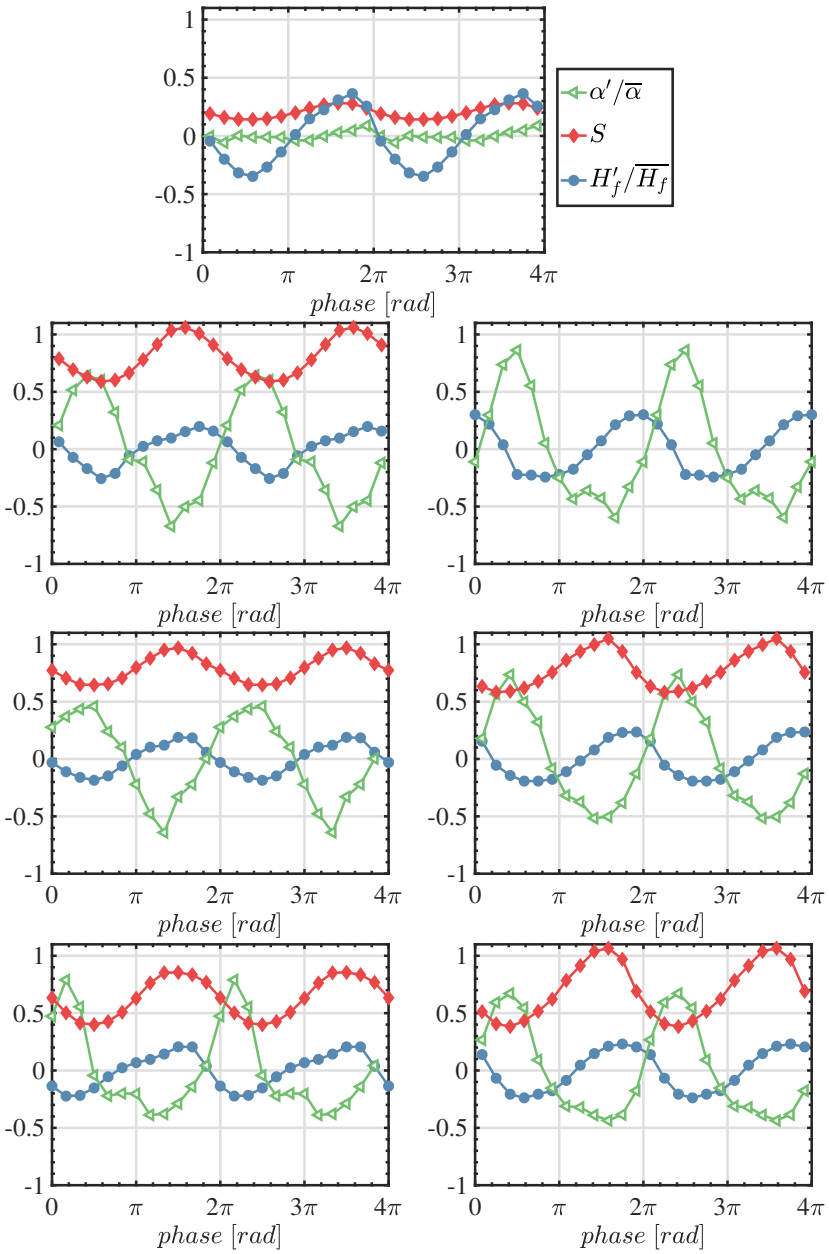

Figure 7.4: *Evolution of the swirl number S, the flame height normalized fluctuation* $H'_f/\overline{H_f}$ *and flame angle normalized fluctuation* $\alpha'/\overline{\alpha}$ *at the flame base. First line:* SW_0, $S = 0.20$, $D_o = 22$ *mm*, $C = 14$ *mm*, $f = 96$ *Hz. Second line:* SW_3, $S = 0.80$, $D_o = 22$ *mm*, $C = 14$ *mm. Left:* $f = 96$ *Hz, right:* $f = 170$ *Hz. Third line:* SW_3, $S = 0.80$, $D_o = 20$ *mm*, $C = 10$ *mm. Left:* $f = 110$ *Hz, right:* $f = 190$ *Hz. Fourth line:* SW_3, $S = 0.60$, $D_o = 18$ *mm*, $C = 12$ *mm. Left:* $f = 110$ *Hz, right:* $f = 180$ *Hz. The phase is referred to the hot wire signal. Two cycles are represented for better readability.*

The synchronization between these different signals is also roughly the same for the different cases explored. This confirms that there are no significant differences between the motions executed by these flames, when they are forced at a frequency corresponding to a minimum or a maximum in the FTF gain curve. Another important finding is that large swirl number oscillations are detected for flames featuring low, but also large, FTF gain values. These two last observations contrast with current interpretations of flame responses to swirl oscillations (Palies et al., 2011e; Bunce et al., 2013). They however need to be confirmed by further analysis.

7.2.4 Heat release rate fluctuations analysis

The origin of the heat release fluctuations observed at these excitation frequencies is now scrutinized by decomposing the heat release rate disturbances $\dot{Q}'/\overline{\dot{Q}}$ as the sum of fluctuations associated to changes of the volumetric rate of change of the heat released averaged over the flame volume $< \dot{q}' > / < \overline{\dot{q}} >$ and fluctuations associated to the flame volume $V'/\overline{V}$, with the methodology fully described in Gaudron et al., 2017:

$$\frac{\dot{Q}'}{\overline{\dot{Q}}} = \frac{< \dot{q}' >}{< \overline{\dot{q}} >} + \frac{V'}{\overline{V}} \tag{7.1}$$

The evolution of these three quantities is shown in Fig. 7.5 for the cases explored in Figs. 7.2-7.4. For the flame stabilized on the injector featuring SW_0, $D_o = 22$ mm and $C = 14$ mm leading to a low swirl number $S = 0.20$, heat release rate oscillations are mainly driven by changes of the flame volume $\dot{Q}'/\overline{\dot{Q}} \simeq V'/\overline{V}$, with only a slight contribution from local changes of the volumetric heat release rate in the top row in Fig. 7.5. In this case, the flame luminosity remains roughly constant along the flame arms over the forcing cycle in Fig. 7.2. In the second, third and fourth rows in Fig. 7.5, results are plotted for flames stabilized with the swirling vane SW_3. These injectors feature high swirl numbers $S \geq 0.60$. The contributions to heat release rate fluctuations from $V'/\overline{V}$ and $< \dot{q}' > / < \overline{\dot{q}} >$ reach both comparable and relatively high levels in the right plots, when the flame response feature large FTF gain values. This means that large vortical structures impinging the flame modulate the flame shape but also change the local consumption rate. For the flames sharing the same swirl level $S = 0.80$, both signals $V'/\overline{V}$ and $< \dot{q}' > / < \overline{\dot{q}} >$ largely drop in the second and third rows in the left column in Fig. 7.5, for frequencies corresponding to low FTF gain values. At a slightly lower swirl level $S = 0.60$, there is no large drop of $V'/\overline{V}$ and $< \dot{q}' > / < \overline{\dot{q}} >$ and the level reached by these signals are comparable in the left and right graphs in the last row in Fig. 7.5 obtained at $f = 110$ and 180 Hz. In this latter case, one recalls that the FTF gain level remains high at these two frequencies as shown

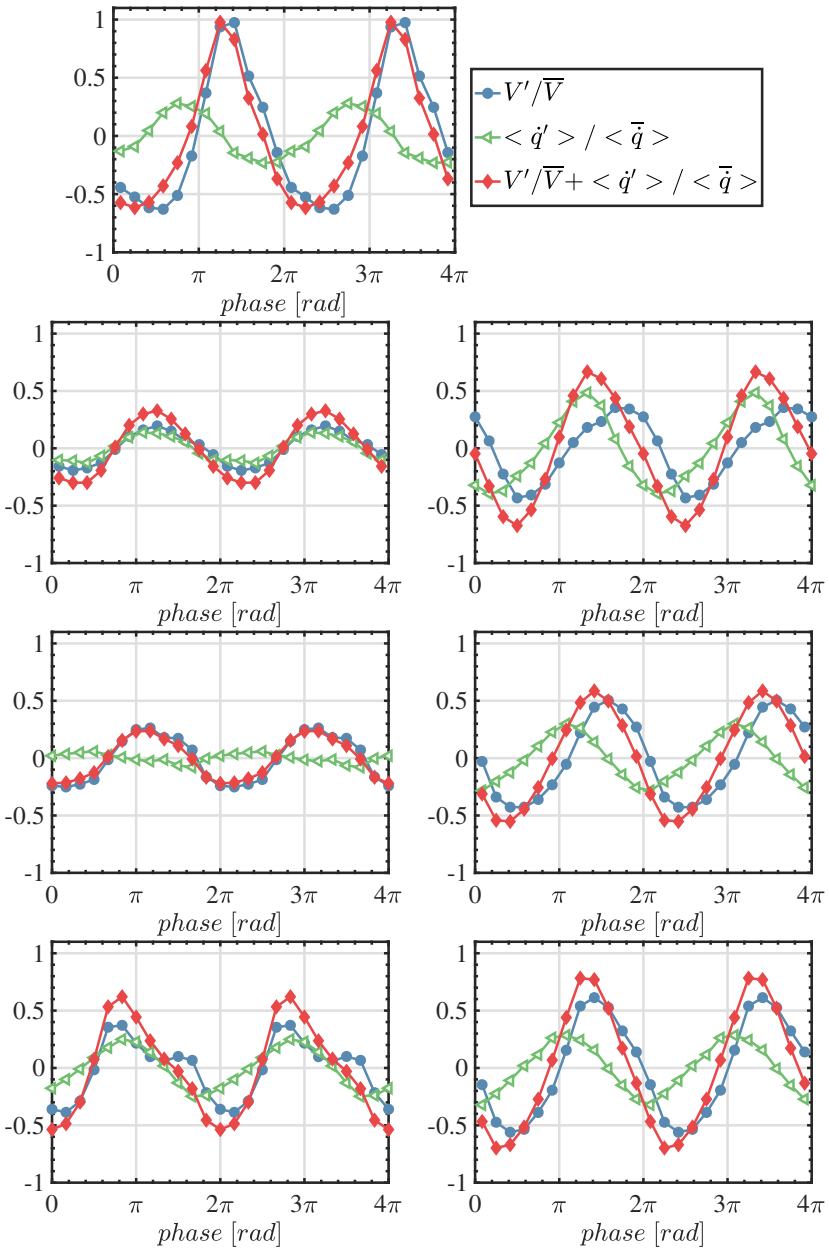

Figure 7.5: *Evolution of the spatially-averaged volumetric heat release rate fluctuation* $< \dot{q}' > / < \overline{\dot{q}} >$*, flame volume fluctuation* $V'/\overline{V}$ *and sum of these contributions. First line:* SW_0*,* $S = 0.20$*,* $D_o =$ *22 mm,* $C = 14$ *mm,* $f = 96$ *Hz. Second line:* SW_3*,* $S = 0.80$*,* $D_o = 22$ *mm,* $C = 14$ *mm. Left:* $f = 96$ *Hz, right:* $f = 170$ *Hz. Third line:* SW_3*,* $S = 0.80$*,* $D_o = 20$ *mm,* $C = 10$ *mm. Left:* $f = 110$ *Hz, right:* $f = 190$ *Hz. Fourth line:* SW_3*,* $S = 0.60$*,* $D_o = 18$ *mm,* $C = 12$ *mm. Left:* $f = 110$ *Hz, right:* $f = 180$ *Hz. The phase is referred to the hot wire signal. Two cycles are represented for better readability.*

in Fig. 7.1.

This analysis confirms the qualitative descriptions made in the discussion of Figs. 7.2-7.3. At the frequencies corresponding to the lowest flame responses, (i) the flame luminosity barely changes during the forcing cycle and (ii) the flame shape may execute a relatively large motion during the forcing cycle, but the overall surface and volume variation remains low. These two mechanisms explain the low FTF responses observed in this work. They also confirm that the reduced response of the heat release rate observed at specific frequencies is not associated here with some compensation mechanism between out of phase contributions to heat release rate oscillations associated to modifications of the flame base angle dynamics with respect to the flame tip dynamics and resulting from different swirl number oscillations. They were shown to be the consequence of significant reductions of both flame volume variations and local changes of the reaction rate compared to flames featuring a high response. It is now worth examining if these differences could be interpreted with an analysis of the cold flow response.

7.3 Cold flow dynamics - PIV measurements

The investigation proceeds by examining phase conditioned PIV measurements with the acoustic pulsation gathered in an axial plane of the combustor in cold flow conditions. The PIV setup is described in chapter 2. To identify vortical structures, the Q criterion (Jeong and Hussain, 1995) is selected:

$$Q = \frac{1}{2}(|\Omega|^2 - |\mathbf{S}|^2) \tag{7.2}$$

where $\mathbf{S}$ and Ω are the symmetric and anti-symmetric components of the velocity gradient respectively. Iso-contours of Q are inferred from velocity measurements conducted in the axial plane crossing the center of the combustion chamber. Only positive values of Q are retained, while negative values, indicating areas of the flow where shear is present but no swirling motion, are forced to a zero value. As the velocity field is only known in the axial plane, Q is here calculated on a 2D basis:

$$Q = \frac{\partial u_z}{\partial z}\frac{\partial u_x}{\partial x} - \frac{\partial u_x}{\partial z}\frac{\partial u_z}{\partial x}. \tag{7.3}$$

where u_x and u_z are the transverse and axial velocity components. This approximation of course does not reproduce the full complexity of the swirled 3D flow response to the flow modulation, but it is reasonable because the analysis of the phase averaged flame response in Figs. 7.2-7.3 revealed that their dynamics also differs in the axial plane.

Results are presented in Fig. 7.6 and Fig. 7.7 for the same injectors as in Fig. 7.2 and 7.3 respectively, except that combustion is not initiated. Vortical structures are detected both in the external and internal shear layers of the jet. The structures in the internal shear layer can however not develop in reacting flow conditions because the flame leading edge is anchored on the central bluff body. This is why the following analysis only considers the response of the external shear layer to acoustic forcing.

The first and third sequences in Fig. 7.6 reveal that large coherent vortical structures are shed within the cold flow from the external lips of the burner at the forcing frequencies $f = 96$ Hz and $f = 170$ Hz when the same injector ($D_o = 22$ mm and $C = 14$ mm) is equipped with swirler SW_0 ($S = 0.20$) and SW_3 ($S = 0.80$) respectively. These excitation conditions correspond to FTF gain maxima in Fig. 7.1. In both cases, a large vortical structure is generated at the rim of the injector and is convected downstream in the chamber. This is highlighted by the high values taken by Q in these figures that exceeds $Q > 2.10^6$ s^{-2}. The displacement of the center of these structures is emphasized by the superposed dashed lines. The same observations can be made for the results shown in the second and fourth rows in Fig. 7.7 obtained for an injector equipped with swirler SW_3 but different nozzle and top cone diameters. The forcing conditions in the second row at $f = 190$ Hz and in the fourth row at $f = 180$ Hz are associated to a maximum of the FTF gain plots in Fig. 7.1. These data reveal that large coherent vortical structures shed in the external shear layer of the flow are responsible for the high gain values taken by the FTF gain independently of the injector design.

Results are now analyzed for excitation conditions leading to minimum FTF gain values. The second sequence in Fig. 7.6 and the first in Fig. 7.7 correspond to the response of the flow for the injector with the swirler SW_3 but different nozzle and top cone diameters leading to the same swirl level $S = 0.80$. These two flames feature a minimum of the FTF gain in Fig. 7.1 at $f = 96$ Hz and 110 Hz respectively. In both cases, the large coherent structures shed from the burner lip in the external shear layer can hardly be identified with Q values lower than $Q < 1.10^6$ s^{-2}. These weak structures are also rapidly dissipated by the flow as they are convected downstream.

When the swirl level is slightly decreased to $S = 0.60$ for an injector with the same swirler SW_3, but a reduced nozzle diameter $D_o = 18$ mm and a top cone diameter $C = 12$ mm, one now again may identify a weak vortical structure shed from the burner lip and travelling in the external shear layer of the flow in the third sequence in Fig. 7.7 for an excitation frequency $f = 110$ Hz. The strength of this structure with $Q < 1.5.10^6$ s^{-2} is however much lower at this forcing frequency than that observed for the same injector when the flow is forced at $f = 180$ Hz in the last sequence in Fig. 7.7 for which $Q > 2.5.10^6$ s^{-2}. One

reminds that $f = 110$ Hz corresponds to a FTF gain minimum and $f = 180$ Hz to a FTF gain maximum in Fig. 7.1.

Interactions of the flame with large vortical structures shed from the burner rim is a well known mechanism leading to nonlinearities in the flame response (Balachandran et al., 2005; Thumuluru and Lieuwen, 2009; Oberleithner et al., 2015). In Fig. 6.3, it was shown that nonlinearities are strong at the FTF gain maximum, but are drastically reduced at the FTF gain minimum. Figures 7.6-7.7 indicate that this behavior is linked to the lower strength of the vortical structures shed from the burner rim at forcing frequencies corresponding to minimum FTF gain values.

Reduction of the strength of large vortical structures at the frequency corresponding to the FTF gain minimum was already identified in previous works on swirling flame dynamics (Palies et al., 2011e; Bunce et al., 2013). In these studies, however, the origin of this reduction was in both cases attributed to some interference mechanism between the flame dynamics and the forced shear layer. Figures 7.6-7.7 obtained in cold flow conditions reveal that these vortical structures are also damped even in the absence of heat release. This in turn leads to the conclusion that the strong reduction of the FTF of swirled flames anchored on a central bluff body at peculiar frequencies is a purely hydrodynamic mechanism, which finds its origin from the complex interactions taking place between acoustic waves and the vorticity field of the swirled flow dynamics. This is why this problem is further investigated with the help of LES calculations of the pulsed cold flow.

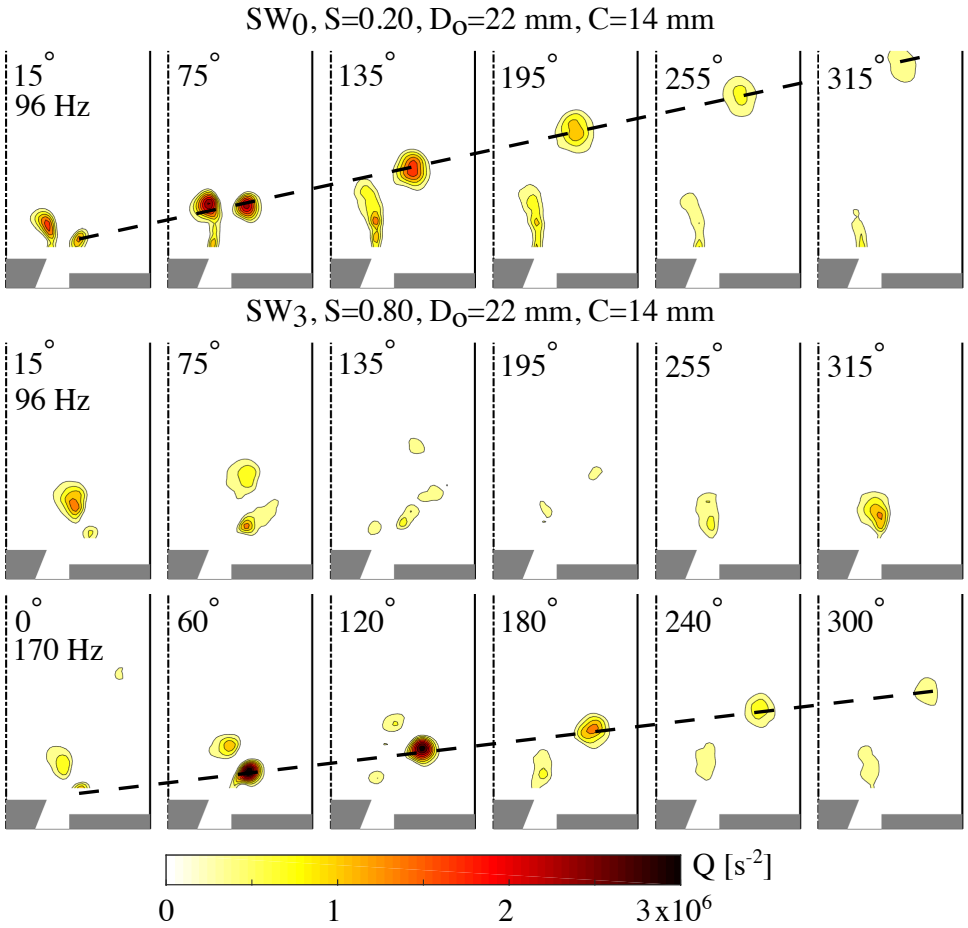

Figure 7.6: *Q criterion contours deduced from PIV data in cold flow conditions for a forcing level $u'/\bar{u} = 0.30$ RMS. The same colorbar, set from 0 to 3.10^6 s^{-2}, is applied to all figures. Only positive values of Q are retained. The indicated phase angle is referred to the signal measured by the hot wire.*

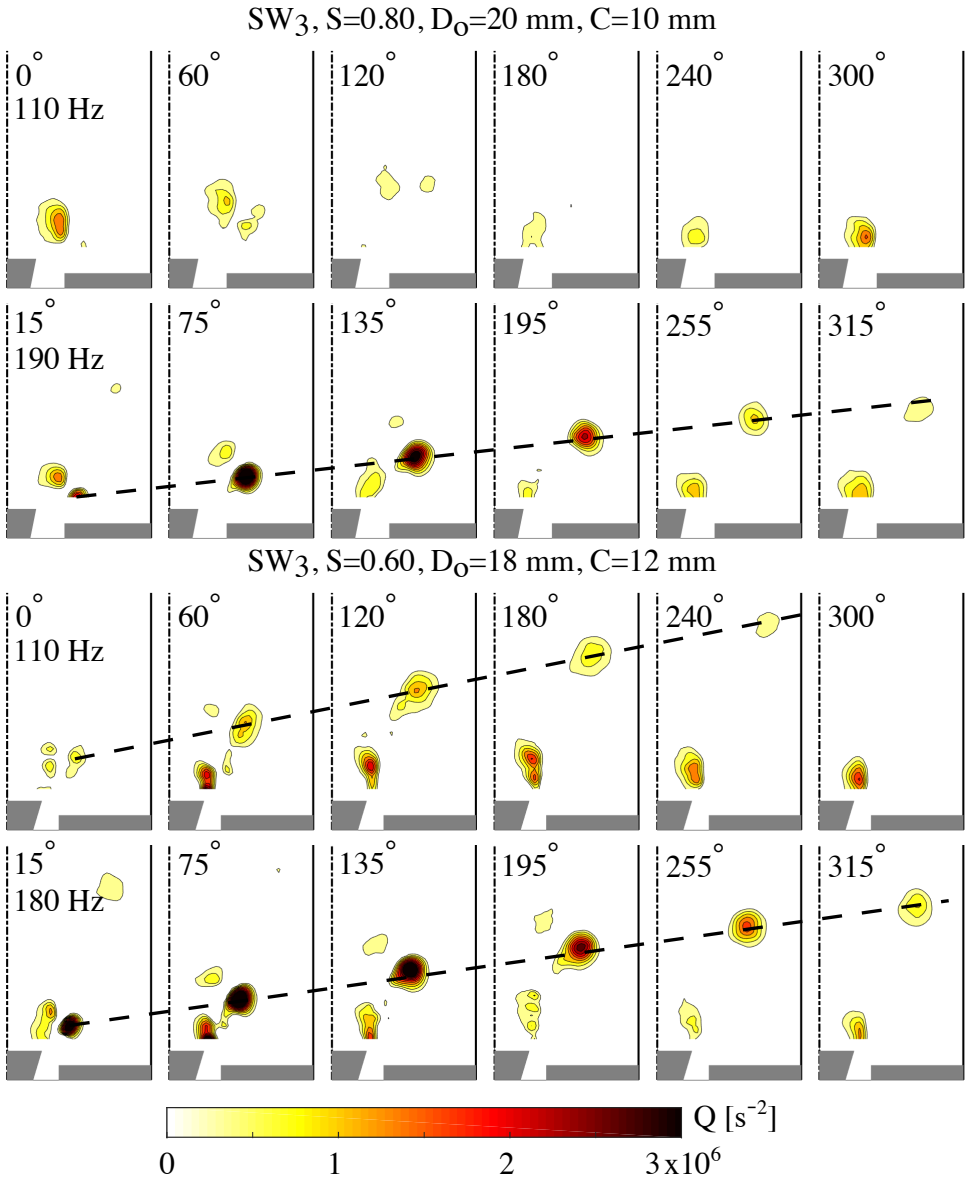

Figure 7.7: *Q criterion contours deduced from PIV data in cold flow conditions for a forcing level $u'/\bar{u} = 0.30$ RMS. The same colorbar, set from 0 to 3.10^6 s^{-2}, is applied to all figures. Only positive values of Q are retained. The indicated phase angle is referred to the signal measured by the hot wire HW.*

7.4 Cold flow dynamics - LES

7.4.1 Comparison with experimental measurements

The objective of these simulations is to better highlight the mechanisms leading to a reduction of the strength of vortical structures at the forcing frequencies corresponding to minimum FTF gain levels. To do so, Large Eddy Simulations were carried out on the configuration described in Chapter 3 for the injector equipped with the swirler SW_3, a nozzle injection diameter $D_o = 20$ mm and a bluff body with a conical top cone diameter $C = 10$ mm. One recalls that this configuration is slightly different from those presented so far, since it features a 1 mm shorter central rod. The flow is forced at two frequencies, $f = 120$ Hz and $f = 190$ Hz, respectively corresponding to a FTF minimum and maximum gain value in Fig. 6.3. The question arises whether the observations highlighted by PIV in the previous section originate from a modification of the response of the swirled flow to acoustic forcing outside the burner or if this could already be explained by the dynamics of the flow within the burner.

Figure 7.8 highlights some cross sections inside the injector that are used in this chapter to analyze the data obtained from LES. Two of these sections are located upstream the swirler unit. Section HW corresponds to the one where the hot wire probe is inserted within the flow in the experiments. Section S-E, corresponds to the sudden expansion of the cross section between the 22 mm diameter tube where the hot wire is inserted and the enlargement of 40 mm diameter necessary to mount the swirler unit. The other sections are located downstream the swirling vane SW_3. Section AS_{08mm} located in the injection nozzle at a distance of 8 mm downstream the swirler backplane. Section AS_{56mm} corresponds to the injector outlet section which is flush mounted to the combustion chamber backplane.

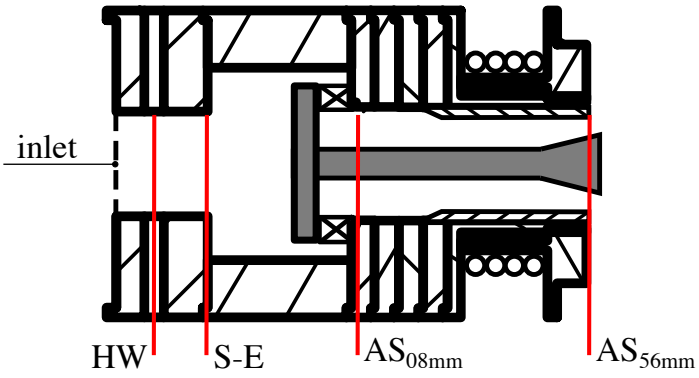

Figure 7.8: *Details of the injector studied with LES with indication of some sections of interest.*

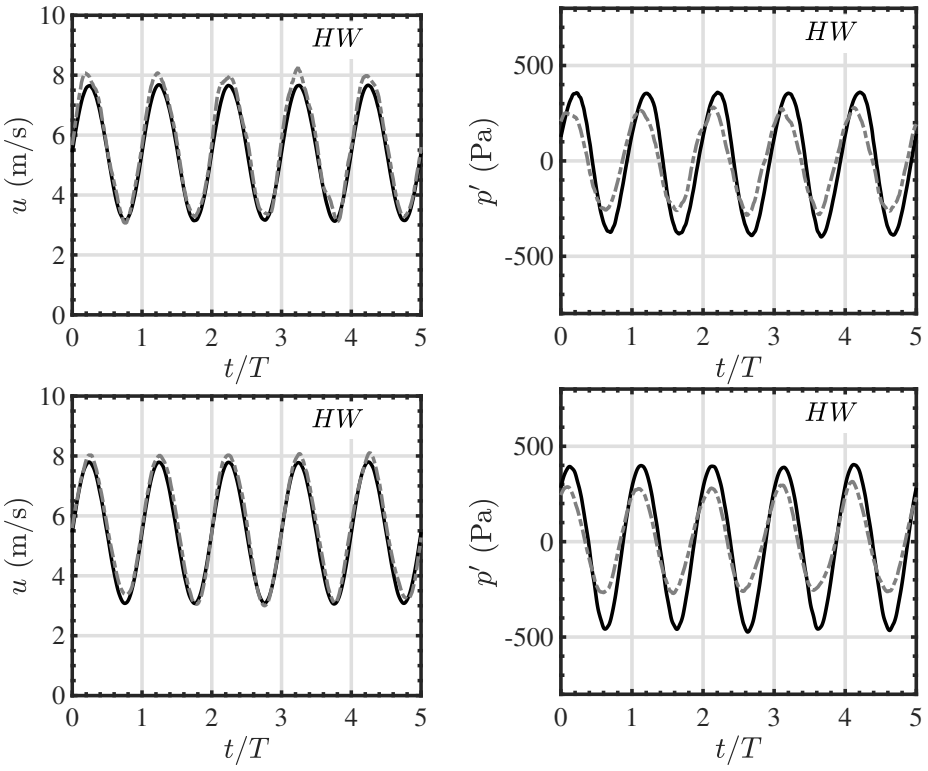

Figure 7.9: *Comparison between experimental and numerical velocity and pressure signals at the hot wire (HW) location. Experimental data : dashed gray lines. Numerical data (solid black lines) are integrated over the HW section as indicated in Eq. (7.4). Top: $f = 120$ Hz. Bottom: $f = 190$ Hz.*

Acoustic forcing is introduced in the numerical simulations at the inlet section in Fig. 7.8 through the INLET_RELAX_UVW_T_Y_PULSE boundary condition from the AVBP solver. This boundary condition allows to superpose a harmonic acoustic fluctuation of desired frequency and amplitude to the mean flow. Acoustic excitation is introduced in the simulation by starting from a converged solution for the flow field in the absence of acoustic forcing as described in chapter 3. Simulations are then carried out until the transient response of the flow is evacuated for several forcing periods, typically more than 10, before comparing the simulations and experiments.

It is important to underline that all the data presented at the different locations illustrated in Fig. 7.8 are obtained after a spatial integration over the cross section of interest. For example the axial velocity shown in Fig. 7.9-left is obtained as:

$$u_z(t) = \frac{1}{A} \int 2\pi r u_z(r,t) dr. \tag{7.4}$$

The temporal evolution of the velocity and acoustic pressure signals obtained

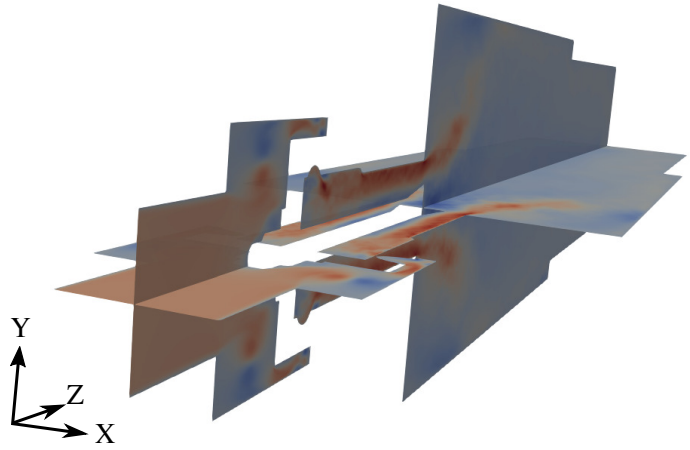

Figure 7.10: *Examples of two axial cuts used for the determination of velocity profiles and Q criterion contours.*

with LES are compared to hot wire and microphone measurements in the HW section in Fig. 7.9. It is worth recalling that the flow is laminar in this section at the outlet of the convergent unit with a top hat velocity profile. Five cycles of excitation are shown. Results are presented at the top in Fig. 7.9 for $f = 120$ Hz corresponding to a minimum FTF gain as shown in Fig. 6.3. The response at $f = 190$ Hz at the bottom in Fig. 7.9 corresponds to a maximum FTF gain. In both cases, the measured and simulated velocity signals are well superposed in the left graphs in Fig. 7.9.

The corresponding acoustic pressure signals in the right plots are a bit overestimated by the LES. This is due to the difficulty to adjust the correct acoustic forcing level at the inlet of the numerical domain. One cannot prescribe the desired acoustic velocity and desired acoustic pressure wave in section HW in the numerical solver. One prescribes the forcing frequency and amplitude of the Riemann invariant at the numerical domain inlet, which corresponds to the amplitude of the characteristic wave entering the numerical domain, while the characteristic wave leaving the domain through the inlet is adjusted with a relax coefficient (Selle et al., 2004). One then needs to correctly adjust the value of the relax coefficient with an iterative procedure to get the desired level on both the acoustic velocity and acoustic pressure in section HW. This procedure is a crude way to mimic the impedance of the real system in the section HW. Overall, we consider that the comparisons in Fig. 7.9 are satisfactory for the sake of the analysis to be conducted.

The next step, after having checked that the correct acoustic perturbation is introduced in the computational domain at the two frequencies of interest, is to compute the Q criterion contours deduced from LES to get phase averaged

results with respect to the excitation signal. This is done in a two steps process. Two types of averaging are performed. A phase-average procedure is applied over 25 cycles of excitation at both excitation frequencies. This procedure is applied for 24 phases in one acoustic cycle separated by 15^o. The phase reference for averaging is the velocity signal in the HW section. To further improve the results, an azimuthal average is then performed over 10 equally separated axial cuts crossing the burner axis with different azimuths. Two cuts at azimuths separated by 90^o are illustrated in Fig. 7.10. All these data are projected to the $x-z$ plane. The resulting scan of LES data are post-processed to calculate the two dimensional Q criterion contours with Eq. (7.3) as done for the PIV data.

Results of this procedure are shown in Fig. 7.11 for 6 phases in the forcing cycle. Only the Q criterion contours inside the chamber are shown. It is evident that vortical structures are much stronger in the bottom sequence in Fig. 7.11 for the forcing frequency $f = 190$ Hz corresponding to a maximum FTF gain value, than for the sequence of images shown at the top for $f = 120$ Hz corresponding to a minimum FTF gain value. At both frequencies, the formation of a coherent vortex starts at the external rim of the injector at a phase between 300^o and 0^o with respect to the velocity signal in section HW. This vortical structure is then convected through the combustion chamber along the shear layer of the swirled jet and it is eventually dissipated. Its trajectory is represented by the dashed-dotted blue line. Figure 7.11 shows that the structure is dissipated much faster at the forcing frequency $f = 120$ Hz, corresponding to a minimum FTF gain value than at $f = 190$ Hz corresponding to a maximum FTF gain.

7.4.2 Discussion

One may first wonder if this behavior may be linked to some preferential Strouhal number. A number of studies indicate that staggered vortical structures are released in the shear layer of an acoustically forced jet or in the wake flow downstream a bluff-body at a preferential characteristic frequency given by:

$$f = St\frac{\bar{u}}{D} \tag{7.5}$$

where $\bar{u}$ is the bulk flow velocity at the injection nozzle outlet, D is the outlet diameter of the injector and the Strouhal number $St \simeq 0.20 - 0.30$ independently of the Reynolds number (Crow and Champagne, 1971; Cantwell and Coles, 1983; Prasad and Williamson, 1997; Emerson et al., 2012). These studies however do not deal with the response of swirling flows. Nonetheless, it is worth estimating the Strouhal numbers in the case explored in this study. Taking the

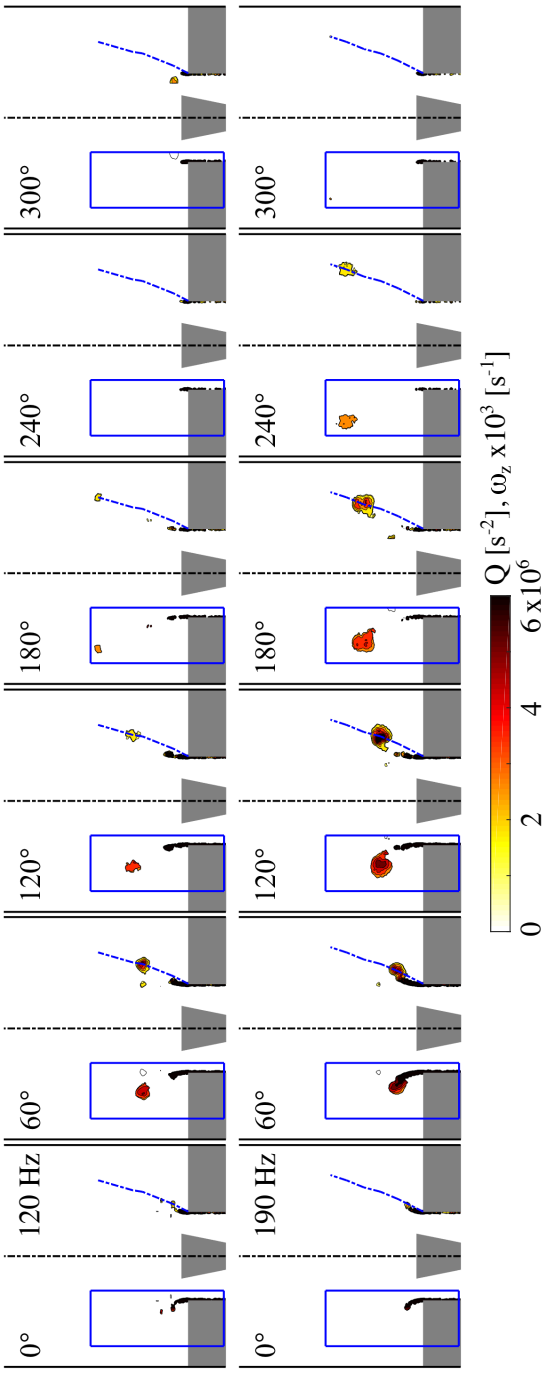

Figure 7.11: *Vorticity (left of symmetry axis) and Q criterion contours (right of symmetry axis) of the cold flow inside the combustion chamber deduced from LES at frequencies corresponding to a minimum FTF gain ($f = 120$ Hz, top row) and to a maximum FTF gain ($f = 190$ Hz, bottom row).*

average axial velocity at the injector outlet in section AS_{56mm}, $\bar{u} = 8.5$ m/s, and the hydraulic diameter of this cross section, $D = 10.6$ mm, Eq. (7.5) yields $St = 0.15$ at $f = 120$ Hz and $St = 0.24$ at $f = 190$ Hz. One confirms that the Strouhal number obtained for $f = 190$ Hz, corresponding to a FTF gain maximum, lies within the range $0.20 - 0.30$. This however cannot be used to interpret the low and high responses of the flow at these two frequencies as demonstrated below.

At this stage, it is worth taking a step back to the FTF measurements presented in chapter 6. One focus on FTF results shown in Fig. 6.6-left obtained for the same injector and flow conditions but different values of the distance δ between the swirling vane and the combustion chamber backplane. The configuration with the swirler set at $\delta = 50$ mm, features a maximum gain value at $f = 190$ Hz. One could argue that this is related to a preferential Strouhal number, for example $St = 0.24$ leading to the largest coherent structures released within the flow. A change in the distance δ does however not alter any value in Eq. (7.5), while in Fig. 6.6-left, the FTF gain at the same forcing frequency, and thus the same Strouhal number, corresponds to a minimum value when the distance is set to $\delta = 35$ mm.

The same conclusion can be drawn from the analysis of results presented in Fig. 6.12. In these cases, the swirler design was modified, but the other geometrical parameters were fixed so that the velocity $\bar{u}$ and the hydraulic diameter D remain unchanged in Eq. (7.5). Nonetheless, at a same frequency $f \simeq 100$ Hz, maximum and minimum gain values are observed for the FTF obtained with the different swirlers tested.

Figures 7.6-7.7 and 7.11 show that maximum and minimum gain values are respectively linked to high and low strengths of vortical structures released in the flow. This strength cannot be related to a preferential Strouhal number since for a same Strouhal number St, low and high FTF gain value are observed in Fig. 6.6-left and 6.12.

7.4.3 Analysis of signals inside the injector unit

The Large Eddy Simulations of the cold flow response inside the combustor confirm the results obtained by PIV discussed in the previous section. LES signals are now analyzed inside the injector in a region where experimental measurements could not be achieved. Figure 7.12 presents the temporal evolution of axial and azimuthal velocity components and pressure signals in sections HW, AS_{08mm} and AS_{56mm}. At a first glance, it is hard to find any difference between the results reported on the left obtained for $f = 120$ Hz (corresponding to a FTF minimum gain) and those plotted on the right for $f = 190$ Hz (maximum

FTF gain). The axial velocity signals, in red, are the same at the two frequencies in section HW. This was already illustrated in Fig. 7.9. Even downstream the swirler, in section AS_{08mm}, the axial velocity signals remain unaltered in phase and amplitude by the swirler at the two excitation frequencies. The only small difference is seen in section AS_{56mm} where the average axial velocity u_z increases due to the flow passage constriction shown in Fig. 7.8 at the injector outlet. This acceleration however is the same in both cases and does not change the phase lag of these axial velocity signals. One may also conclude that flow dissipation does not alter axial velocity disturbances at $f = 120$ and 190 Hz. These confrontations confirm the acoustic nature of the axial forcing as already discussed in Palies et al., 2011a.

The flow is purely axial in section HW in Fig. 7.12. The swirler introduces a certain amount of rotation in the flow. The average azimuthal velocity component conferred to the flow is roughly the same at both forcing frequencies $f = 120$ Hz and $f = 190$ Hz in section AS_{08mm}. In particular there is no phase lag between the left and right plots in Fig. 7.12. Contrarily to results found for the axial velocity disturbances, azimuthal disturbances are higher in section AS_{08mm} than at the outlet of the burner in section AS_{56mm} due to dissipation and this is true at both forcing frequencies. One may also see that the phase lag of the azimuthal with respect to the axial component of velocity also differs between sections AS_{08mm} and AS_{56mm} and differs in the same section AS_{56mm} between results found at $f = 120$ Hz and $f = 190$ Hz.

Finally, Fig. 7.12 also shows that the mean pressure $\overline{p}$ and pressure amplitude p' drop between section HW and the injector outlet. Their phase lag in the left and right plots obtained for $f = 120$ Hz and $f = 190$ Hz remains unaltered through the swirler, but their amplitude drops significantly.

The main difference between data shown in Fig. 7.12 at $f = 120$ Hz and $f = 190$ Hz originate from the phase-lag $\Delta\varphi_{u'_\theta - u'_z}$ between the axial u_z and azimuthal u_θ velocity signals. These signals are almost in phase in section AS_{08mm}, but their phase lags differ in section AS_{56mm}. At this location, u_z and u_θ are still almost in phase at $f = 190$ Hz, while they are close to out of phase for the excitation at $f = 120$ Hz.

The phase lag between the axial or the azimuthal velocity component in different sections downstream the swirler outlet with respect to the axial velocity signal in section HW is determined. Results are shown in Fig. 7.13-left. The phase-lag $\Delta\varphi_{u'_z - u'_z}$ between the axial components u_z in section HW and the u_z signals at the different AS locations is first considered. This phase-lag is always close to zero at all locations downstream the swirler backplane. This confirms that axial velocity disturbances propagate at the speed of sound through the swirler and injection tube up to the burner outlet. The distance $l \simeq 60$ mm

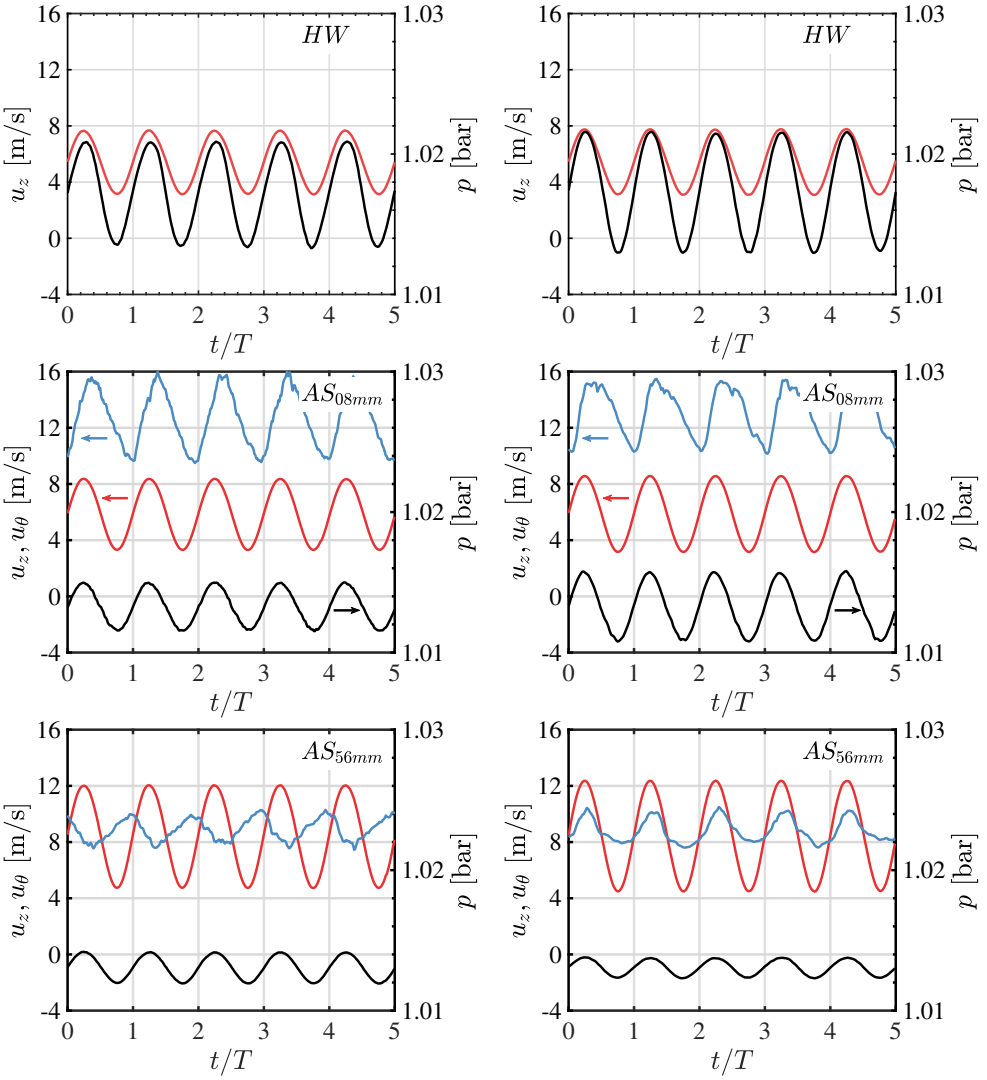

Figure 7.12: *Temporal evolution of axial velocity (red), azimuthal velocity (blue) and pressure (black) signals in sections HW, AS_{08mm} and AS_{56mm}. Left: $f = 120$ Hz. Right: $f = 190$ Hz.*

covered by the acoustic waves between the swirler backplane and the burner outlet remains small with respect to their wavelengths at $f = 120$ and 190 Hz, $\mathrm{He} = \omega c/l \ll 1$. One can neglect this contribution to the overall phase lag and consider that axial disturbances remain in phase through the injector.

One can also see in Fig. 7.13-left that $\Delta\varphi_{u'_\theta - u'_z}$ corresponding to the phase lag of the azimuthal velocity u'_θ in the different AS locations downstream the swirler backplane with respect to the axial velocity in section HW increases roughly linearly with the frequency of perturbation. Considering that azimuthal flow

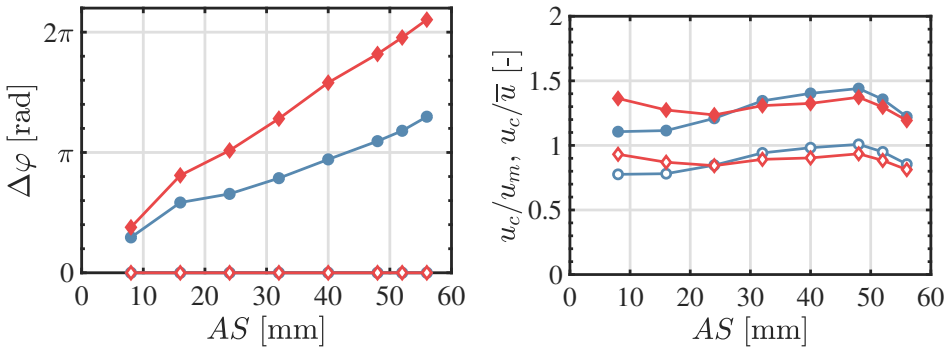

Figure 7.13: *Left: evolution of the phase-lags $\Delta\varphi_{u'_\theta - u'_z}$ (full symbols) and $\Delta\varphi_{u'_z - u'_z}$ (empty symbols) with respect to the distance AS to the swirler backplane. Right: evolution of the convective velocity u_c of azimuthal perturbations normalized by the bulk flow velocity $\overline{u}$ (full symbols) and the maximum velocity u_m (empty symbols) reached by the flow in each section as a function of the distance to the swirler backplane. Blue: $f = 120$ Hz. Red: $f = 190$ Hz.*

disturbances are transported by the mean flow, the phase lag $\Delta\varphi_{u'_\theta - u'_z}$ can be expressed as (Komarek and Polifke, 2010; Palies et al., 2011a):

$$\Delta\varphi_{u'_\theta - u'_z} = 2\pi f \frac{\delta}{u_c} \tag{7.6}$$

where u_c is the convective velocity of azimuthal perturbations and δ is the distance from the swirler exit where azimuthal perturbations are generated. Taking the slope of the curve in Fig. 7.13-left yields the velocity u_c which is plotted in Fig. 7.13-right. It is either normalized by the bulk flow velocity $\overline{u}$ in the corresponding cross section or the maximum velocity u_m reached by the flow in the section of interest. It is interesting to observe that u_c lies in between $\overline{u}$ and u_m, but is not modified by the forcing frequency f. The phase lag difference observed at $f = 120$ Hz and $f = 190$ Hz between azimuthal perturbations in Fig. 7.12 at the burner outlet in section AS_{56mm} is not due to changes of the phase speed at which these disturbances travel.

These velocity signals are further analyzed in Fig. 7.14 by considering their relative fluctuations to deduce the resulting swirl number fluctuations S' with:

$$\frac{S'}{\overline{S}} = \frac{u'_\theta}{\overline{u}_\theta} - \frac{u'_z}{\overline{u}_z} \tag{7.7}$$

This linearized expression for perturbations of the swirl number was used by Palies *et al.* (Palies et al., 2010a; Palies et al., 2011e) to show that, due to the different phase lags between u_z and u_θ signals with frequency, the largest swirl number oscillations S' are obtained when the axial and azimuthal velocity components are out of phase at the burner outlet. Conversely, the smallest swirl

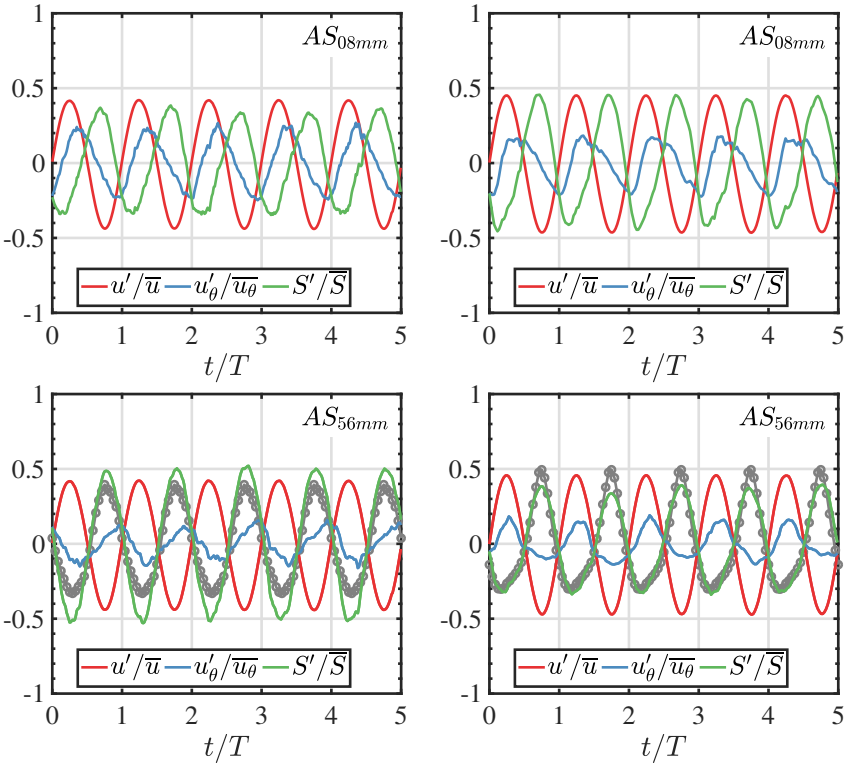

Figure 7.14: *Temporal evolution of axial velocity (red), azimuthal velocity (blue) and swirl number (green) in sections AS_{08mm} and AS_{56mm}. Superposed in gray the swirl number deduced from Eq. (5.1). Left: $f = 120$ Hz. Right: $f = 190$ Hz.*

number oscillations correspond to situations in which the axial and azimuthal velocity components are in phase at the burner outlet. They used this model to show that the amplitude of the oscillations of the flame angle at the flame base increases with the amplitude of the swirl number oscillations. They also found that at a frequency corresponding to a minimum FTF gain, the swirl number oscillations were the largest, while they were considerably reduced at forcing frequencies corresponding to a maximum FTF gain. This in turn was used to develop a scenario in which strong interactions between a flapping flame and vortices shed in the shear layer from the injector rim led to a reduction of the strength of the shed vortical structures.

It has already been shown in Fig. 7.4 that swirl number oscillations S' reach comparable levels at the two frequencies $f = 120$ and 190 Hz respectively corresponding to a minimum FTF gain and a maximum FTF gain. It was also shown that the strength of these vortical structures is reduced at $f = 120$ Hz compared to those released at $f = 190$ Hz even in the absence of combustion. It is now found that the swirl number fluctuations deduced from Eq. (7.7) are slightly higher at $f = 120$ Hz than at $f = 190$ Hz in Fig. 7.14, but they reach

in both cases quite high levels. One hardly sees how the slight different levels observed in Fig. 7.14 for S' could explain the large differences in vortex strength highlighted in Fig. 7.11.

One possibility is that Eq. (7.7) is an oversimplified model that does not well reproduce the swirl number disturbances seen by the flow at the burner outlet. The swirl number can also be deduced from the original definition Eq. (5.1). It is here deduced from the axial and azimuthal velocity profiles at the outlet of the burner in section AS_{56mm} for 24 phases in the forcing cycle from the axial cuts shown in Fig. 7.10. Results are superposed in Fig. 7.14. The values of $S'/\overline{S}$ deduced from the velocity profiles and calculated with the exact expression Eq. (5.1) or those deduced from the simplified linearized model Eq. (7.7) are close in Fig. 7.14. This means that the simplified expression Eq. (7.7) is well suited to get an estimate of the swirl fluctuation level. The value of S' deduced from the exact expression Eq. (5.1) is now slightly higher at $f = 190$ Hz than at $f = 120$ Hz. More importantly, it is once again shown that the swirl number fluctuations are strong at both forcing frequencies. This confirms that the large differences observed for the vortical structures shed at these two frequencies in the cold flow do not directly result from changes of the level of swirl number fluctuations.

7.4.4 Vortex formation without swirl

To get more insight, the mechanisms leading to shedding of large coherent structures with and without swirl are now examined. The formation of vortical structures in a purely axial flow is analyzed first at section S-E upstream the swirler corresponding to a sudden expansion of the cross flow section passage in Fig. 7.8. Results post-processed with the same procedure already described for the analysis of the data shown in Fig. 7.11 are presented in Fig. 7.15.

This figure reveals that the strength of vortical structures shed at an excitation frequency $f = 120$ Hz and $f = 190$ Hz in the absence of swirl is the same. In both cases, a large vortex is formed between phases 300^o and 0^o and then fully detaches from the rim between phases 60^o and 120^o. The vorticity and the Q criterion reach about the same values for both results presented at $f = 120$ Hz and $f = 190$ Hz. This test highlights without any ambiguity that the two different responses of the injector at $f = 120$ Hz and $f = 190$ Hz is linked to the dynamics downstream the swirling vane.

Velocity profiles in section S-E are also analyzed in Fig. 7.16 as a function of their phase lag with respect to the acoustic velocity in section HW. Without surprise, the axial profiles coincide in the left and right top graphs obtained for the two forcing frequencies $f = 120$ Hz and $f = 190$ Hz respectively. An

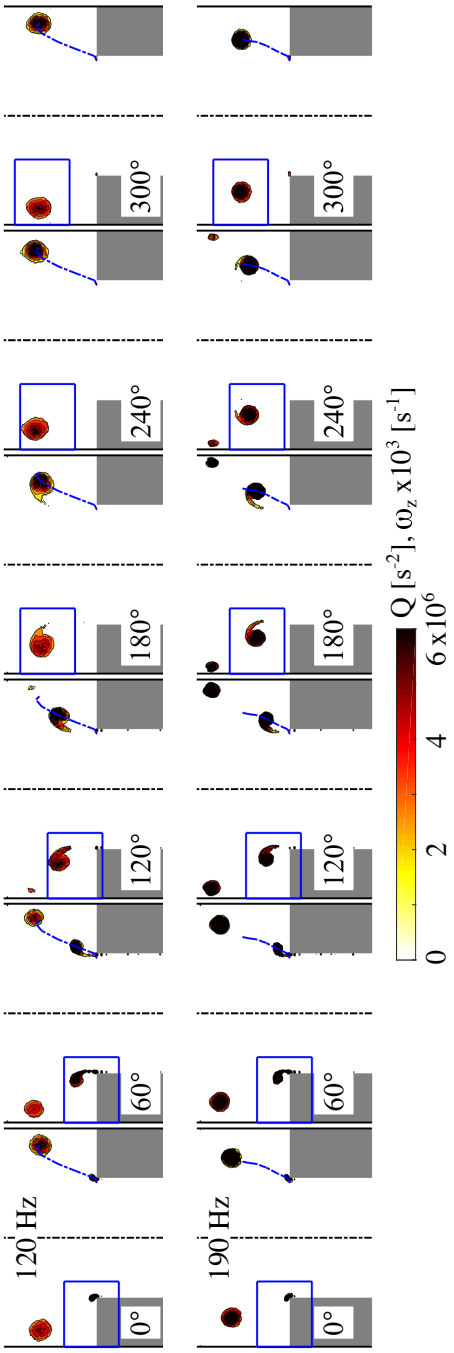

Figure 7.15: *Vorticity (left of symmetry axis) and Q criterion contours (right of symmetry axis) from LES at frequencies corresponding to a minimum ($f = 120$ Hz, top row) and to a maximum FTF gain value ($f = 190$ Hz, bottom row) in the section S-E upstream the swirler.*

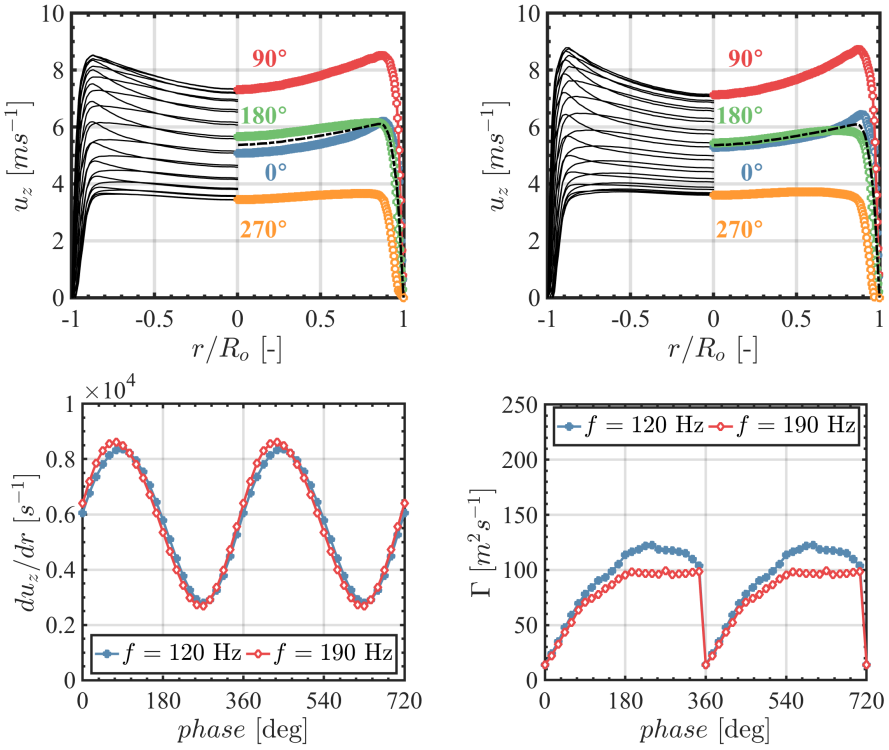

Figure 7.16: *Top: axial velocity profiles in section S-E ($D_o = 22$ mm) at frequencies corresponding to a minimum ($f = 120$ Hz, left) and to a maximum FTF gain value ($f = 190$ Hz, right). The profiles at all the 24 phases are shown for negatives r/R_o values. Four characteristic phases are shown for positives r/R_o values. The average profile is also superposed as a dashed-dotted line. Bottom: radial gradient of the axial velocity at the channel wall (left) and circulation (right) along the closed contour shown in Fig. 7.15.*

attempt is also made to explore the dynamics leading to the detachment of these vortical structures with respect to changes of the axial velocity profile at the channel wall. The gradient du_z/dr is plotted in Fig. 7.16. This velocity gradient, obtained for $0.9 \leq r/R \leq 1$, is proportional to the shear on the channel wall. One again sees that the shear wall follows exactly the same law for the two excited flows when the signal is plotted as a function of the phase in the oscillation cycle. As the axial velocity increases for phases between 270^o to 90^o, a vortex is first generated at the channel outlet and then detaches. In the following part of the forcing cycle, this structure is convected along the dashed-dotted blue line in Fig. 7.15.

Another attempt is made to characterize the strength of the shed vortical structures. This is done by measuring their circulation Γ along their trajectory, around the boundary of a closed surface surrounding and following the struc-

ture. The circulation Γ corresponds to the flux of vorticity through this surface. Only the vorticity linked to the vortical structure needs to be considered. For this purpose, a binarization procedure is applied: (i) a threshold is selected on the Q criterion contours; (ii) a binary matrix is constructed by assigning 1 for all values above this threshold and assigning 0 for all values below; (iii) the vorticity is multiplied by this binary matrix. The vorticity scan resulting from this procedure is shown in Fig. 7.15, on the left of the symmetry axis. The surface used to obtain the circulation is superposed on the images as well.

The results in the bottom right plot in Fig. 7.16 are again very close for both excitation frequencies. One begins with the analysis of results obtained for $f = 190$ Hz. At phase 0^o with respect to the acoustic velocity, the circulation Γ is the lowest. It then linearly grows in the forcing cycle up to phase 75^o. The rate of increase of the circulation Γ then slows down up to a phase lag 180^o. After this stage it remains almost constant up to the end of the forcing cycle. At phase 360^o, one follows the circulation of a new vortical structure. The same observations are made for the excitation frequency $f = 120$ Hz. The only difference is that Γ saturates at a higher level and then slightly drops. This figure confirms that the strength and the circulation of the shed vortical structures at $f = 120$ Hz and $f = 190$ Hz are very close in the absence of swirl. It was also checked that these results are only weakly sensitive to the selected threshold level to determine the circulation.

7.4.5 Vortex formation with swirl

The same analysis is repeated at the outlet of the injector in the cross section AS_{56mm}. In this section, the flow is swirled with a strong azimuthal velocity component. It was already shown in Fig. 7.11 that vortical structures shed from the burner lip are stronger at an excitation frequency $f = 190$ Hz compared to those produced at $f = 120$ Hz. Further insight into the mechanisms leading to this behavior of the swirled flow response can be gained by analyzing the velocity profiles shown in Figs. 7.17 and 7.18.

In Fig. 7.17, the axial velocity profiles superposed at regularly distributed instants in the forcing cycle show that the envelope of the axial velocity close to the central bluff body is wider at $f = 120$ Hz in the left plot than in the right plot obtained for a forcing frequency $f = 190$ Hz. The situation is reverse for the envelope covered by the axial velocity close to the solid wall of the injection channel. The peak axial velocity close to the channel wall is bounded between 9 and 16 m.s^{-1} in the left plot obtained for an excitation at $f = 120$ Hz. The peak velocity in the boundary layer between $0.8 < r/R_o < 1$ spans from 7.5 to 17.5 m.s^{-1} when the flow is excited at $f = 190$ Hz in the right plot. As a consequence, the axial velocity profile is steeper at $f = 190$ Hz close to the channel

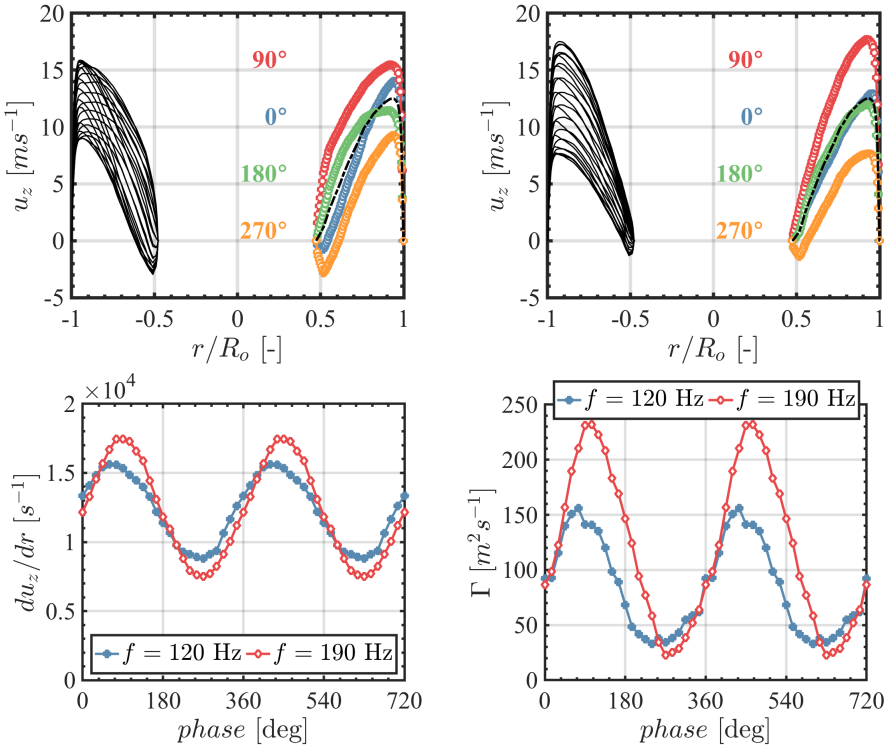

Figure 7.17: *Top: axial velocity profiles at the burner outlet section AS_{56mm} (D_o = 20 mm) at frequencies corresponding to a minimum (f = 120 Hz, left) and to a maximum FTF gain value (f = 190 Hz, right). The profiles at all the 24 phases are shown for negatives r/R_o, while 4 characteristic phases are shown for positives r/R_o. The average profile is also superposed as a dash-dotted line. Bottom: radial gradient of the axial velocity at the injector rim (left) and circulation (right) along the closed contour shown in Fig. 7.11.*

wall than at $f = 120$ Hz. Close to the central cone between $0.5 < r/R_o < 0.7$, the largest span between the velocity profiles is reached at $f = 120$ Hz.

These observations for the axial velocity are completed by examining the two other velocity components in Fig. 7.18. The evolution of the azimuthal velocity profiles are very close in shape and level in the two top graphs for acoustic excitation at $f = 120$ Hz and $f = 190$ Hz. Changes of the radial velocity profiles in the bottom plots in Fig. 7.18 are more significant between the two forced cases. Close to the annular channel walls, the envelope covered by the radial profiles at $f = 120$ Hz and 190 Hz does not differ much. The largest changes are observed close to the central bluff-body. Changes of the radial velocity close to the central bluff body are much larger when the flow is excited at $f = 120$ Hz than at $f = 190$ Hz. As a synthesis, the dynamics of the swirled flow at the injector outlet exhibit larger changes of the axial velocity close to the channel

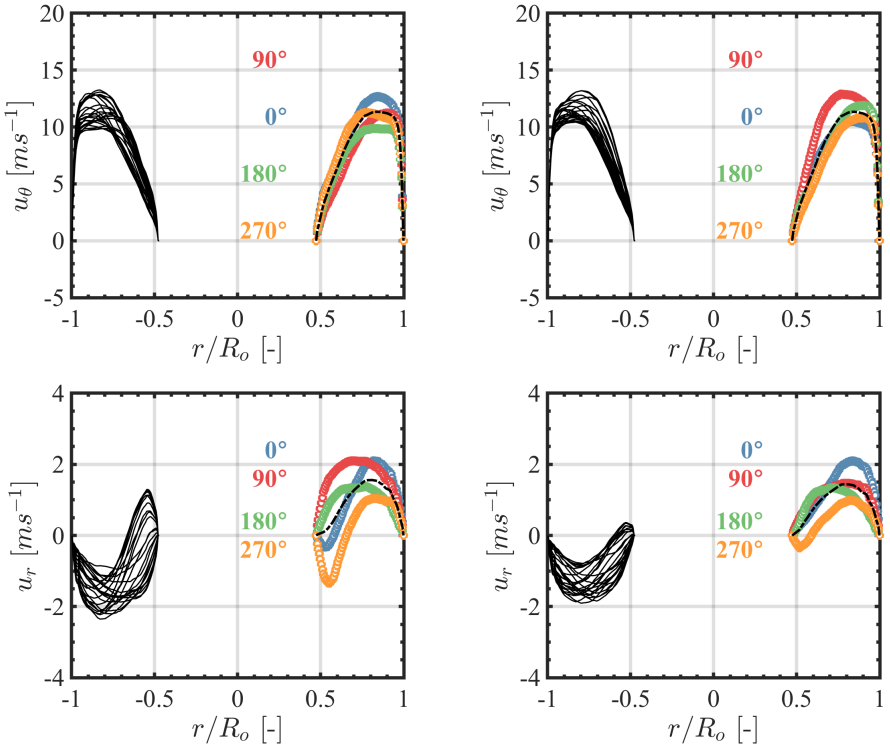

Figure 7.18: *Azimuthal (top) and radial (bottom) velocity profiles at the burner outlet section AS_{56mm} (D_o = 20 mm) at frequencies corresponding to a minimum (f = 120 Hz, left) and to a maximum FTF gain value (f = 190 Hz, right). The profiles at 24 phases in the cycle are shown for negatives r/R_o values. Four characteristic phases are shown for positives r/R_o values. The average profile is also superposed as a dashed-dotted line.*

walls when the flow is excited at f = 190 Hz and larger changes of the radial velocity close to the central injector when the flow is excited at f = 120 Hz.

The minimum axial velocity -3 m.s^{-1} reached by the flow at a phase 270^o for an excitation at f = 120 Hz is much lower in Fig. 7.17 compared to the value -1 m.s^{-1} found for the axial flow velocity when the flow is excited at f = 190 Hz. This may explain the higher propensity of flashback during FTF measurements when the forcing frequency is set close to f = 120 Hz as discussed in chapter 6. As the velocity profile features larger variations close to the solid wall of the injection channel at f = 190 Hz than at f = 120 Hz, this leads to larger wall gradients du_z/dr (determined at a distance of 1 mm from the rim) in the bottom left plot in Fig. 7.17 when the flow is excited at f = 190 Hz. There is no phase lag between excitation at f = 120 and 190 Hz. The only difference is the amplitude of the oscillation experienced by the shear at the wall.

Finally, the circulation Γ around a contour shown in Fig. 7.11 following the vortex convected by the flow is extracted from the simulations with the same method described for results in Fig. 7.16. The circulation Γ in the bottom right plot in Fig. 7.17 reaches values of about 250 $m^2.s^{-1}$ at $f = 190$ Hz compared to the flow forced at $f = 120$ Hz for which circulation is limited to 150 $m^2.s^{-1}$. The initial growth of circulation is the same for $f = 120$ and 190 Hz for phases lower than 70^o. Saturation and dissipation then alters the circulation of the vortical structure shed at $f = 120$ Hz, while the circulation of the vortical structure continues to grow for the flow forced at $f = 190$ Hz until phases of about 90-100^o. This confirms that after the initial phase of vortex formation and growth, dissipation of the coherent structure circulation is much faster at the frequency $f = 120$ Hz corresponding to a minimum FTF gain value than at $f = 190$ Hz corresponding to a maximum FTF gain value.

7.5 Conclusion

Experimental measurements and numerical simulations have been carried out to investigate the flame and flow dynamics above a swirled injector at frequencies $f = 190$ Hz and $f = 120$ Hz leading to maximum and minimum values of the FTF gain as shown in the previous chapter.

Phase conditioned OH* chemiluminescence images revealed that the flame motion is qualitatively similar at these two frequencies. For flames stabilized by a central bluff body with a vanishingly small level of swirl ($S = 0.20$), the flame height fluctuation is dominant with respect to flame angle fluctuations, while as the swirl number increases ($S > 0.60$) both contributions are important. The difference in flame dynamics between low and high values of the FTF gain has been analyzed by comparing the flame luminosity fluctuations and flame volume fluctuations. A general decrease of these two contributions to the heat release rate oscillation has been observed as the gain level is reduced.

Phase conditioned PIV measurements have then been considered to analyze the cold flow response to these acoustic excitations. These data confirmed that vortical structures shed from the burner rim are stronger at the frequency of the FTF gain maximum, as reported in the literature. They also revealed that these vortical structures vanish at forcing frequencies corresponding to a minimum value of the FTF gain. The originality lies here in the fact that these data were obtained in cold flow conditions, while interaction of the flame with the flow dynamics was so far believed to be responsible of this phenomenon.

Phase conditioned numerical simulations have lastly been conducted in cold flow conditions at the two excitation frequencies respectively leading to a maximum and a minimum value of the FTF gain. These data first confirmed the

PIV results in terms of different strength of vortical structures shed from the burner rim. The velocity and pressure signals inside the injector, at locations where experimental measurements were not available, have then been analyzed. No important differences could be observed in this internal response of the injector except in the phase lag between the axial and the azimuthal velocity profiles at the burner outlet. In particular, the swirl number fluctuations, often considered to be a discriminating parameter for the different behaviors of a swirled injector at different frequencies, was shown to reach comparable level of oscillation in these simulations at the two frequencies of interest.

The higher strength of the vortical structures shed from the burner lip and convected in the combustion chamber at the frequency corresponding to the maximum FTF gain level, has been here found to be related to a different shape of the envelope of the axial and radial velocity profiles at the burner outlet. The flow is submitted to a much higher shear du/dr at the channel wall at $f = 190$ Hz corresponding to a FTF gain maximum than when the flow is forced at $f = 120$ Hz. The envelope of the radial velocity profile also significantly differs between the two excitation conditions, with much larger changes close to the central bluff body at $f = 120$ Hz compared to results obtained at $f = 190$ Hz.

These observations lead to the conclusion that the mechanism leading to high and low gain values of the FTF of swirled flames stabilized by a bluff body is purely hydrodynamic. Further effort needs to be made to model this behavior.

Chapter 8

Flame Transfer Function scaling

An attempt is made to determine dimensionless quantities allowing a scaling of FTF results obtained for different injector designs. Following previous studies, a Strouhal number based on the forcing frequency and the ratio between a flame length scale and the convective velocity of vortical perturbations shed in the external shear layer of the swirled jet is considered first. It is shown that this Strouhal number allows to scale many of the FTF measurements reported in chapter 6. This scaling law is however also shown to fail when the distance δ between the swirler exit and the combustion chamber backplane is modified. A new definition of the Strouhal number is introduced that takes this distance into account which yields a better match to rescale the measured FTFs.

8.1 Introduction

The determination of the parameters describing the flame transfer function (FTF) with a reduced set of dimensionless numbers is an important issue for engineers. This type of scaling law allows to reduce the set of experiments or simulations needed to determine the FTF for different flow operating conditions. An attempt is made in this study to find such a scaling law when the flow operating conditions and the burner design are modified.

In the cases of laminar premixed conical and V-flames submitted to flowrate perturbations, this issue has been extensively covered (Merk, 1957; Fleifil et al., 1996; Ducruix et al., 2000). These studies came out with two main dimensionless numbers that were shown to govern the flame frequency response to incoming flowrate disturbances (Schuller et al., 2003). For a flame with a laminar burning velocity S_L stabilized over a burner of radius R with a bulk flow velocity U_b and submitted to small flowrate perturbations at angular frequency ω, the two main independent dimensionless numbers controlling its response are (i) a reduced frequency $\omega^* = \omega R/(S_L \cos\alpha)$, where $\sin\alpha = S_L/U_b$ yields the mean position of the flame sheet, and the ratio of laminar burning to the

mean flow velocity S_L/U_b.

In the case of premixed swirling flames submitted to incoming flowrate disturbances in constant equivalence ratio mixtures, a Strouhal number based on the ratio of a flame length scale to a convective velocity is generally used to adimensionalize the FTF results (Kulsheimer and Buchner, 2002; Kim et al., 2010a; Kim et al., 2010b; Palies et al., 2010b; Jones et al., 2011) :

$$\mathrm{St} = f\frac{L_f}{u_{vc}} \tag{8.1}$$

where L_f is a flame length scale and u_{vc} is an effective convection velocity. Kim et al., 2010a used this scaling law to reduce their FTF data gathered for premixed swirled flames at equivalence ratios varying from $\phi = 0.65$ to 0.75 and a fixed bulk flow velocity $U_b = 30$ m/s on the same curve with a reasonable match. The distance L_f was defined as the center of mass of CH* emission images recorded over one forcing period and was found to be a function of the equivalence ratio and the forcing frequency. The effective convective velocity was determined as $u_{vc} = L_f/\tau$, where τ is deduced from the slope of the FTF phase lag. This type of scaling law can only be used once the FTF is determined and does not consider the impact of the swirler.

Many recent investigations of the FTF of swirling flames by modeling tools (Hirsch et al., 2005; Palies et al., 2011d; Acharya et al., 2012), numerical simulations (Palies et al., 2011e; Acharya and Lieuwen, 2015) and by experimental means (Huang and Yang, 2009; Palies et al., 2010b; Komarek and Polifke, 2010), indicate that the injector dynamics and the response of the swirler to flow perturbations need to be considered to interpret the key features of the FTF of swirling flames. These studies revealed that an acoustic pulsation impinging on a swirler generates a vorticity wave which is then convected downstream at the local flow velocity. This in turn leads to interferences between axial acoustic and azimuthal convective disturbances, along the distance from the swirler exit to the combustion chamber inlet (Palies et al., 2010b; Komarek and Polifke, 2010; Palies et al., 2011a). Straub and Richards, 1999 firstly described the influence of the axial swirler position on the self-excited instabilities in a gas turbine combustor. Komarek and Polifke, 2010 and later Kim and Santavicca, 2013b observed a strong dependence of the Flame Transfer Function (FTF) upon swirler-combustor distance.

In a series of works dedicated to understanding the key mechanisms controlling the dynamics of swirling flames, Palies and co-workers (Palies et al., 2011b; Palies et al., 2010b; Palies et al., 2011e) found that (i) the same mechanisms take place for radial or axial swirlers, (ii) the same FTF shape is obtained when velocity fluctuations are measured on the upstream or downstream side of the swirler and (iii) the frequencies at which the lowest FTF gain values are ob-

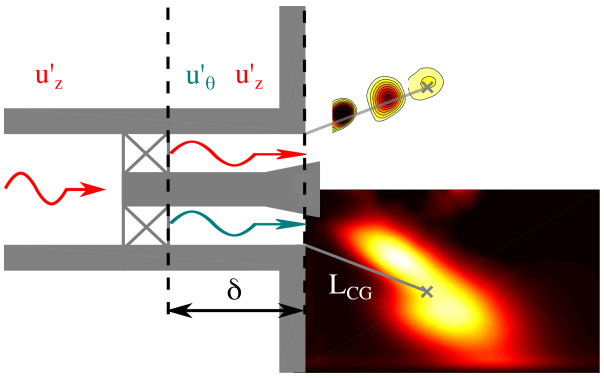

Figure 8.1: *Sketch of the key mechanisms controlling the FTF.*

served are associated to out of phase azimuthal and axial flow disturbances at the injector outlet. Gaudron et al., 2018 showed that the FTF results obtained by pulsating the flame from the upstream or downstream side of the combustion chamber are almost the same, if the velocity fluctuations are measured at a same location upstream of a swirler.

To take the response of the swirler into account, Kim and Santavicca, 2013a introduced two Strouhal numbers $\mathrm{St}_1 = fL_f/U_b$ and $\mathrm{St}_2 = f\delta/U_b$ to reduce their data set of FTF from swirled flames over a wide range of inlet mixture temperatures $T_i = 100^o$C to $T = 250^o$C, mean inlet velocities $U_b = 25$ to 40 m/s, equivalence ratios $\phi = 0.60$ to 0.75, CO_2 concentrations $X_{CO_2} = 0$ to 0.50 of the oxidizer stream, and two positions of the axial swirler $\delta = 77$ and 96 mm. In these experiments, L_f is deduced from CH* images in the absence of acoustic forcing. The best collapse of their data was obtained by plotting the FTF as a function of $\mathrm{St}_1 + \mathrm{St}_2$, which may also be rewritten as :

$$\mathrm{St} = f\frac{(L_f + \delta)}{U_b} \tag{8.2}$$

Note that only the bulk flow velocity U_b is involved in this expression instead of a convective velocity u_{vc}.

This problem is revisited here. One takes advantage of the results shown in the previous chapters to sum up the main physical mechanisms leading to the peculiar shape of the FTF of swirling flames.

8.2 Mechanisms controlling the FTF of swirling flames

In the following analysis, two dominant mechanisms, illustrated in the sketch in Fig. 8.1, are considered to be at the origin of the response of lean premixed swirling flames submitted to acoustic perturbations.

The first mechanism is associated to the interaction between acoustic and convective disturbances. When an acoustic wave, with acoustic velocity u'_z, impinges on a swirler, two waves are generated on the downstream side of the swirler (Wang and Yang, 2005; Palies et al., 2010b; Hirsch et al., 2005; Kim and Santavicca, 2013b). They correspond to a transmitted acoustic wave, with the same acoustic velocity u'_z if the swirler is transparent to acoustic waves in the absence of a large pressure drop, and a vorticity wave, with azimuthal velocity u'_θ that is generated at the swirler trailing edge and is convected by the mean flow. These waves travel at different speeds inside the injector from the swirler exit up to the combustion chamber backplane. Their phase lag can be expressed as:

$$\varphi_{u'_\theta - u'_z} = 2\pi f \delta \left(\frac{1}{u_c} - \frac{1}{c} \right) \simeq 2\pi f \frac{\delta}{u_c} \tag{8.3}$$

where u_c is the velocity at which azimuthal velocity fluctuations are convected inside the injector and $c \gg u_c$ is the speed of sound. This phase lag controls the frequency f at which the FTF gain reaches a minimum (Palies et al., 2010b; Palies et al., 2011e; Kim and Santavicca, 2013b). In particular, it was shown in Palies et al., 2010b that the frequency corresponding to the lowest FTF gain value is associated to out of phase azimuthal and axial flow disturbances at the injector outlet.

The second mechanisms controlling the FTF is flame-vortex interaction (Kulsheimer and Buchner, 2002; Balachandran et al., 2005; Durox et al., 2009; Oberleithner et al., 2015). Vortices are generated at the rim of the injector, convected in the swirled jet external shear layer through the combustion chamber and interact with the flame. In Fig. 8.1, a same vortex is represented at three instants during a forcing cycle. The delay τ, appearing in the FTF phase lag, $\varphi = 2\pi f \tau$, can be expressed as the ratio of the convective velocity of these structures, u_{vc}, to the distance they cover before interacting with the flame, L_{CG}.

8.3 Scaling of the transfer functions of swirling flames

Attempt is first made to scale the FTF data with:

$$\mathrm{St}_a = f \frac{L_{CG}}{u_{vc}} \tag{8.4}$$

where L_{CG} is a characteristic flame dimension, which is here taken equal to the distance between the injector rim and the flame center of gravity (Kim and Santavicca, 2013a; Ćosić et al., 2015) and u_{vc} is the convective velocity of vortical structures inside the combustion chamber. The coordinates of the

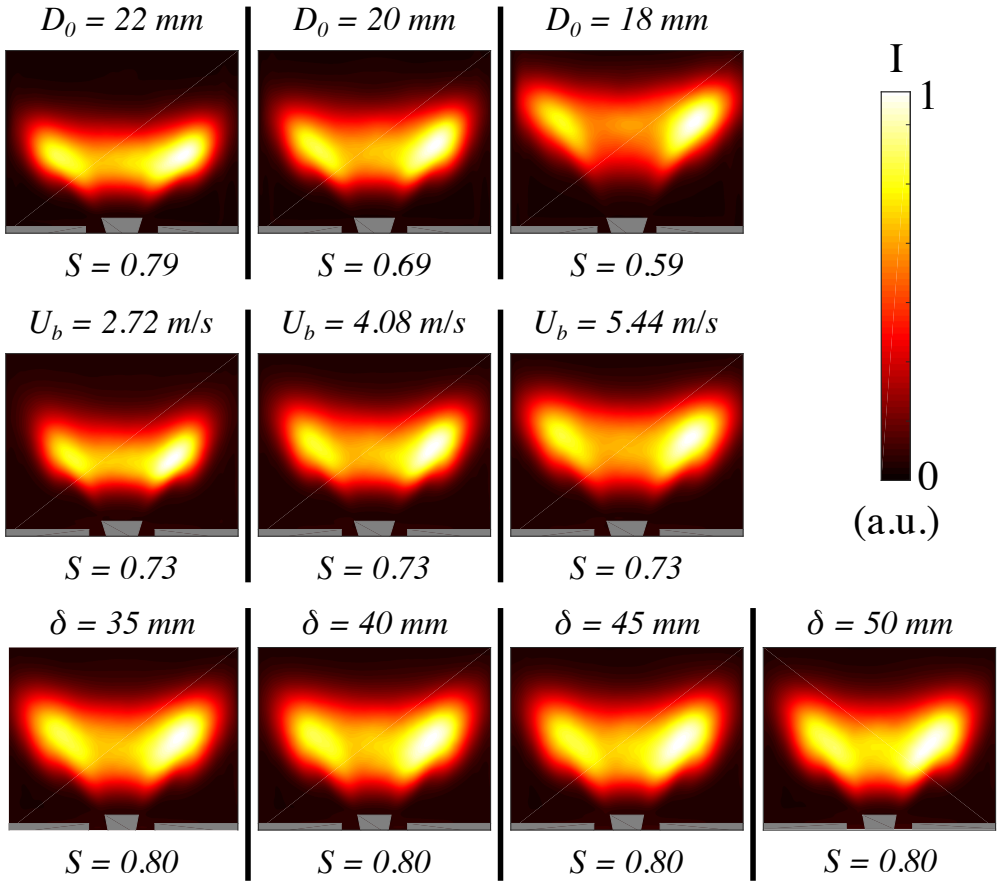

Figure 8.2: *OH* flame light distribution for the different configurations tested. First line: effect of nozzle diameter D_o. Second line: effect of the injection velocity U_b. Third line: effect of the distance δ between swirler exit and combustor backplane.*

center of gravity x_{cg}, y_{cg} are calculated as (Ćosić et al., 2015):

$$x_{cg} = \frac{\sum_{i,j} x_{i,j} y_{i,j} I_{OH^*,i,j}}{\sum_{i,j} y_{i,j} I_{OH^*,i,j}}; \quad y_{cg} = \frac{\sum_{i,j} y_{i,j} y_{i,j} I_{OH^*,i,j}}{\sum_{i,j} y_{i,j} I_{OH^*,i,j}}, \tag{8.5}$$

where i and j are pixel indexes, $x_{i,j}$ and $y_{i,j}$ the pixel coordinates and $I_{OH^*,i,j}$ the measured OH* intensity. The distance L_{CG} is obtained from Eq. (8.5) through long exposure time OH* flame images shown in Fig. 8.2 after an Abel deconvolution as in the sketch of Fig. 8.1.

The velocity u_{vc} is deduced from the phase conditioned PIV measurements and LES presented in Figs. 7.6 and 7.11. The velocity is deduced by following the displacement of the center of the vortical structure at different instants along the forcing cycle. Results are presented in Fig. 8.3. Four different configurations are compared. In each case, the velocity u_{vc} slightly oscillates along the

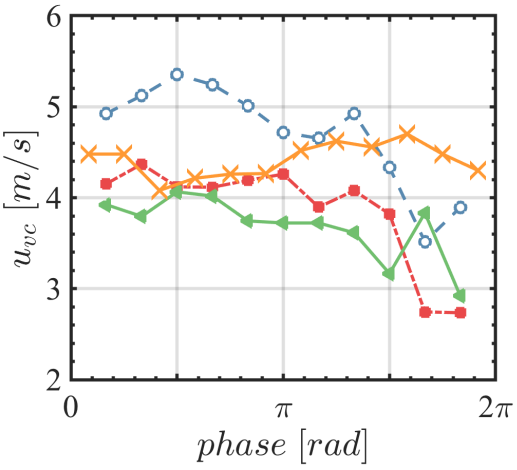

Figure 8.3: *Vortex convection velocity u_{vc} determined from the Q criterion contours shown in Figs. 7.6 and 7.11. Blue: SW_3, $D_o = 18$ mm, $C = 12$ mm, $f = 180$ Hz (PIV). Orange: SW_3, $D_o = 20$ mm, $C = 10$ mm, $f = 190$ Hz (LES). Red: SW_3, $D_o = 20$ mm, $C = 10$ mm, $f = 190$ Hz (PIV). Green: SW_3, $D_o = 22$ mm, $C = 14$ mm, $f = 170$ Hz (PIV).*

cycle around a mean value that increases when the flow passage cross section, area A_2, decreases as indicated in Table 4.1. One can also see that u_{vc} drops in the final portion of the cycle. This could be due to the fact that it is more difficult to discern vortices from the Q criterion plots shown in Fig. 7.6 for the latest phases, since the vortex intensity is dissipated during its convection in the chamber. Nonetheless, an average value of u_{vc} can be determined from these data and is used in Eq. (8.4) as indicated in Table 8.1, also reporting the value of L_{CG}.

FTF measurements shown in Figs. 6.6 and 6.8 are reported in Fig. 8.4-left with respect to the Strouhal number St_a. This scaling law is well suited for the configurations where the bulk flow velocity U_b is modified, but it does not allow to reduce the data for the other two configurations, where the injector diameter D_o or the swirler to injector outlet distance δ are modified.

Inspired from Kim and Santavicca, 2013a, a new definition of the Strouhal number is considered that takes into account the distance δ from the swirler exit to the injector outlet section. The main difference with Eq. (8.2) is that the reference velocity is not U_b, but two convective velocities are considered. Azimuthal perturbations inside the injector are convected at the phase velocity u_c. Large vortical structures shed from the burner rim are convected at the velocity u_{vc} through the combustion chamber :

$$\mathrm{St}_b = f(\frac{\delta}{u_c} + \frac{L_{CG}}{u_{vc}}). \tag{8.6}$$

Table 8.1: *Parameters used to determine the Strohual numbers* St_a *and* St_b. δ_1 *[mm]: distance between the swirler exit and the central insert of diameter* D_o, $u_{c,1}$ *[m/s]: convective velocity of* u'_θ *along the distance* δ_1, δ_2 *[mm]: length of the central insert of diameter* D_o, $u_{c,2}$ *[m/s]: convective velocity of* u'_θ *along the distance* δ_2, L_{CG} *[mm]: distance between the injector rim and the flame center of gravity,* u_{vc} *[m/s]: convective velocity of vortical structures.*

		δ_1	$u_{c,1}$	δ_2	$u_{c,2}$	L_{CG}	u_{vc}
D_o [mm]	18	16	5.88	34	9.14	31.0	4.8
	20		5.88		7.23	24.0	4.2
	22		5.88		5.88	21.5	3.8
U_b [m/s]	2.72	16	2.94	34	3.61	22.0	2.10
	4.08		4.41		5.42	24.5	3.15
	5.44		5.88		7.23	26.0	4.2
δ [mm]	35	1	5.88	34	7.23	24.0	4.0
	40	6					
	45	11					
	50	16					

The velocity u_c is determined from LES calculations and is shown in Fig. 7.13-right. One can see that this velocity lies in between the average and the maximum velocity in the section where it is measured. As a consequence, a mean velocity $u_c = 1.2\overline{u}$ is taken in Eq. (8.6), where $\overline{u}$ is the bulk flow velocity determined from mass balance in the injector cross section between the swirler exit and the combustion chamber backplane. Two different values of u_c are used for the configurations of the injector featuring a different diameter over the section of length δ_1 and δ_2 (see Fig. 1.3-a).

Scaled FTF measurements with St_b are reported in Fig. 8.4-right. One can see that the inclusion of δ in the definition of the Strouhal number leads to a good superposition of the FTFs obtained for different values of the injection diameter D_o, bulk flow velocity U_b and distance δ between the swirler outlet and the injector outlet section. The minimum gain value appears for all the investigated cases at a Strouhal number $St_b \simeq 1.3-1.4$. These results highlight the fact that the timescales of both the mechanisms shown in Fig. 8.1 should be considered for the proper scaling of FTF results of premixed swirling flames. Some differences can also be identified in the FTFs in Fig. 8.4-right. This is probably due to the strong assumption made on the value taken for the convective velocity u_c inside the injector. Some improvement would likely be obtained with a better knowledge of the value of u_c.

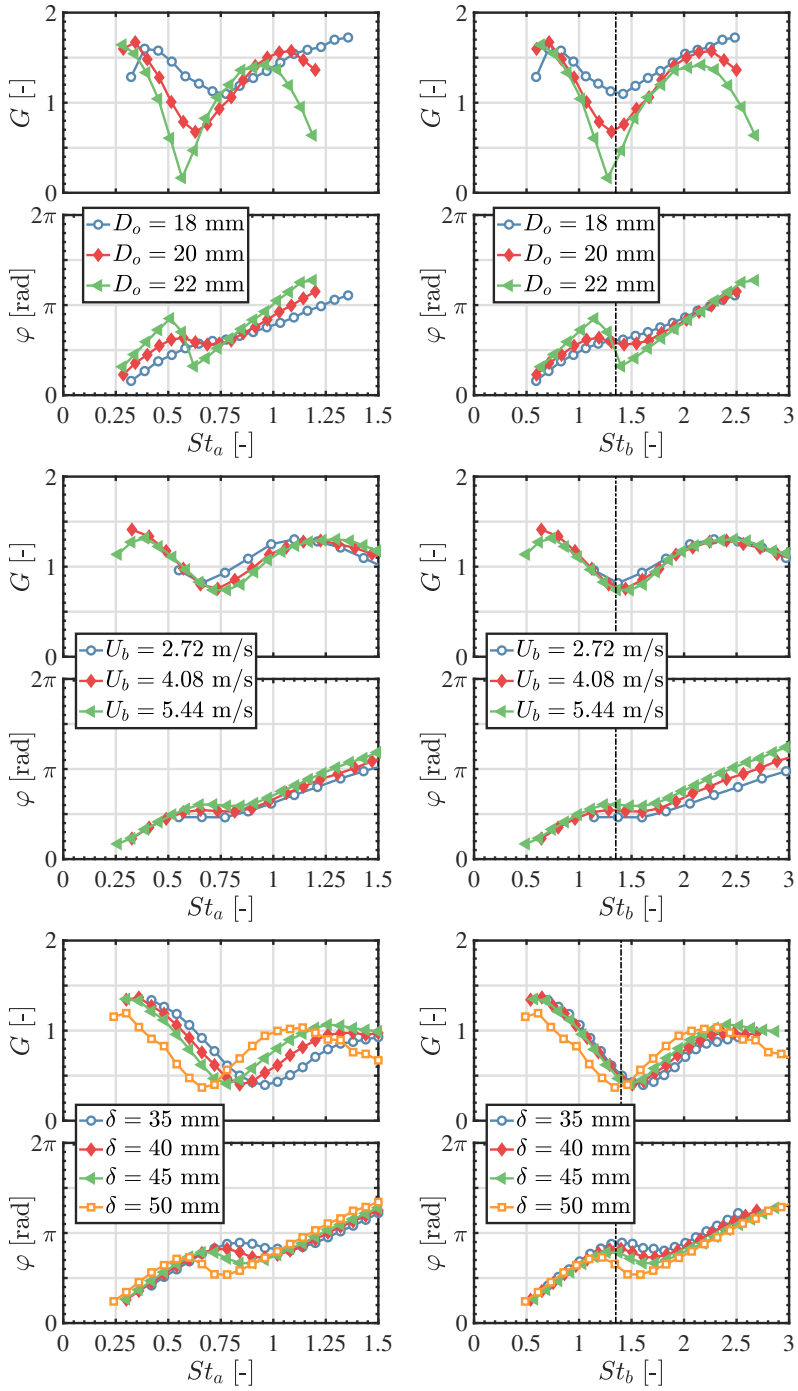

Figure 8.4: *FTF generalization based on Strouhal number. First line: effect of the injector diameter D_o. Second line: effect of injection velocity U_b. Third line: effect of distance δ between swirler exit and combustor backplane. Left: St_a. Right: St_b.*

8.4 Conclusions

The transfer function measurements reported in chapter 6 showed that the FTF gain curve of swirling flames is characterized by peaks and valleys and that the frequencies corresponding to these values are shifted when the bulk flow velocity U_b inside the injector or the distance δ between the swirler trailing edge and the combustion chamber backplane is modified. Two mechanisms are retained as dominant for the description of the observed flame dynamics: interferences between the acoustic pulsation and azimuthal flow disturbances generated at the swirler outlet and interaction of the flame with vortical structures generated at the burner rim.

In the literature, FTF measurements are usually scaled through a Strouhal number St taking into account a flame length scale and a characteristic convection velocity of the vortical structures shed from the burner rim and convected in the combustion chamber. Kim and Santavicca, 2013a also considered the response of the swirler. They introduced a new Strouhal number also considering the propagation time of vortical disturbances from the swirler to the combustor dump plane. They however considered the same characteristic velocity for the convection of vortical disturbances inside the injector and that of vortical structures in the combustion chamber.

These velocities can actually be quite different depending upon the injector geometry. Following the analysis of Kim and Santavicca, 2013a, a slightly different definition of the Strouhal number, based on the different convective time scales of the two dominant phenomena, is shown to be suited to nondimensionalize FTF results obtained for different values of the injection diameter D_o, bulk flow velocity U_b and distance δ between the swirler outlet and the injector outlet section.

Chapter 9

Impact of central bluff body

This chapter has been published in the Proceedings of the Combustion Institute with the title "Impact of swirl and bluff-body on the transfer function of premixed flames". It is reproduced here as is. The objective is to analyze the role of the central bluff body on the FTF of swirled flames. To do so, the frequency response of three lean methane/air flames submitted to flowrate perturbations is analyzed for flames featuring the same equivalence ratio and thermal power, but a different stabilization mechanism. The first flame is stabilized by a central bluff body without swirl, the second one by the same bluff body with the addition of swirl and the last one only by swirl, without central insert. In the two last cases, the swirl level is roughly the same. These three flames feature different shapes and heat release distributions, but their Flame Transfer Function (FTF) feature about the same phase lag at low frequencies. The gain of the FTF also shows the same behavior for the flame stabilized by the central insert without swirl and the one fully aerodynamically stabilized by swirl. Shedding of vortical structures from the injector nozzle, that grow and rollup the flame tip, controls the FTF of these flames. The flame stabilized by the swirler-plus-bluff-body system features a peculiar response, with a large drop of the FTF gain around a frequency at which large swirl number oscillations are observed. Velocity measurements in cold flow conditions reveal a strong reduction of the size of the vortical structures shed from the injector lip at this frequency. The flame stabilized aerodynamically only by swirl and the one stabilized by the bluff body without swirl don't exhibit any FTF gain drop at low frequencies. In the former case, large swirl number oscillations are still identified, but large vortical structures shed from the nozzle also persist at the same forcing frequency in the cold flow response. These different flame responses are found to be related to the dynamics of the internal recirculation region, which response strongly differs depending upon the mechanism adopted to stabilize the flame.

9.1 Introduction

The frequency response of premixed swirling flames submitted to flow rate modulations is a topic of high scientific and technical interest due to the problems raised by combustion instabilities in gas turbines (Lieuwen and Zinn, 2005; Huang and Yang, 2009; Poinsot, 2017). This response is often characterized by a Flame Transfer Function (FTF) or more recently by a Flame Describing Function (FDF) when the level of flow disturbances is considered (Candel et al., 2014).

Changing the shape of the FTF/FDF by modifying the injector design is a way to augment the stability margins of a combustor. However, there is still no systematic way to make these changes, because the dynamics of swirling flames is not fully understood (Thumuluru and Lieuwen, 2009; Candel et al., 2014). Improved combustor stability is thus gained by a costly trial and error iterative process and there is a need for better knowledge of the fundamental mechanisms controlling the shape of the FTF of swirling flames.

The FTF of premixed swirling flames can be determined analytically in simplified configurations (Hirsch et al., 2005; Palies et al., 2011d; Acharya et al., 2012) or by numerical flow simulations in more complex geometries (Tay Wo Chong et al., 2010; Biagioli et al., 2013; Acharya and Lieuwen, 2015). Most often this response is determined experimentally by using well proven optical techniques (Kulsheimer and Buchner, 2002; Kim et al., 2010a; Palies et al., 2011b; Ćosić et al., 2015) even in engine like conditions (Schuermans et al., 2010).

Since shear layers are highly responsive to acoustic forcing, the FTF of premixed flames stabilized by a bluff body is mainly controlled by the shedding of large coherent structures, which are then convected by the mean flow and roll-up the flame. This flame roll-up process around a coherent vortical structure constitutes the main contribution controlling the FTF phase lag of premixed laminar (Durox et al., 2005) and turbulent non-swirling jet flames (Balachandran et al., 2005). It also constitutes one of the fundamental process controlling the dynamics of premixed swirling flames (Palies et al., 2011e; Bunce et al., 2013; Oberleithner et al., 2015).

It has been demonstrated that the response of the swirling vane needs to be taken into account in the dynamics of swirling flames (Komarek and Polifke, 2010; Palies et al., 2010b; Bunce et al., 2013). Vortical transverse perturbations triggered by the axial flow disturbances at the swirler outlet lead to oscillations of the swirl level at the burner outlet. This in turn leads to oscillations of the flame angle at the anchoring point location (Palies et al., 2011e). This swirl oscillation mechanism and its impact on the FTF have been identified in sev-

eral setups in which the flame is stabilized by a central bluff body (Komarek and Polifke, 2010; Palies et al., 2010b; Bunce et al., 2013). The same dynamics is observed when the acoustic pulsation is introduced from the upstream or downstream side of the swirler (Gaudron et al., 2018).

In high power systems, the flame is most often fully aerodynamically stabilized without the help of any solid central insert. Giuliani et al., 2002 also report large swirl number oscillations in the response of an aeronautical injector powered by kerosene when it is submitted to flow rate modulations. They however provide no FTF data. Biagioli et al., 2013 analyzed the FTF of aerodynamically swirl-stabilized flames and found that the position of the Internal Recirculation Zone (IRZ) and the flame leading edge respond to the acoustic forcing by a large axial motion, but the tangential flow component is not considered in their analysis and one cannot conclude about the role of swirl oscillations.

There is yet no detailed investigation on the impact of swirl number oscillations on the FTF of swirling flames aerodynamically stabilized away from all solid components. This response is analyzed here for flames stabilized either only by a bluff body, only by swirl or by both swirl and bluff body. The premixed flames investigated feature the same equivalence ratio and the same thermal power.

The experimental setup and diagnostics are presented in section 9.2, followed by a description in section 9.3 of their flame structure in the absence of forcing. Their frequency response is analyzed in section 9.4 for the different injectors tested. The flow and flame dynamics at selected frequencies are investigated in section 9.5 to infer the swirl number fluctuations and the mechanisms controlling the response of these flames. Conclusions are finally drawn in section 9.6.

9.2 Configurations explored

The experimental setup is sketched in Fig. 9.1. The burner is powered by a methane/air mixture. Experiments are conducted at a fixed equivalence ratio $\phi = 0.82$ and bulk velocity $U_b = 5.44$ m/s ($T = 20^o$ C and $p = 1$ atm) in the $D = 22$ mm diameter section before the swirler unit. These conditions correspond to a constant thermal power $\mathcal{P} = 5.44$ kW assuming total combustion. Two different radial swirlers can be fixed in the injection unit. They both feature six radial injection channels of $d_c = 6$ mm diameter. The design of swirlers SW_0 and SW_3 only differ by the distance x indicated in Fig. 9.1. In the first device, designated as SW_0, the channels are aligned with the radial direction ($x = 0$ mm). In the second one, designated as SW_2, the channels are shifted from the radial direction by $x = 6$ mm, to impart a strong rotation to the flow.

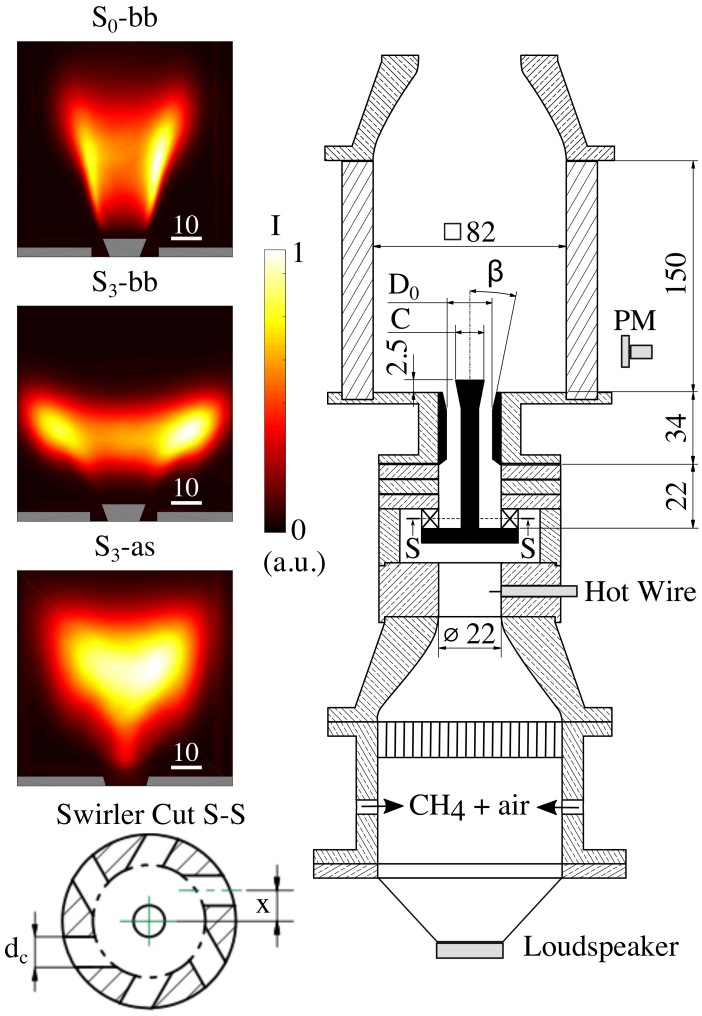

Figure 9.1: *Experimental setup. S_0-bb : Non-swirling flame anchored by a bluff-body, $D_0 = 22$ mm, $C = 14$ mm. $S_3 - bb$: Flame stabilized by swirl $S = 0.8$ and the bluff-body, $D_0 = 22$ mm, $C = 14$ mm. S_3-as : Swirling flame $S = 0.75$ stabilized aerodynamically, $D_0 = 12$ mm, $\beta = 15°$. The main dimensions are indicated in millimeters.*

A detailed description of swirler designs were also given in chapter 1. The flow leaves the swirler through an injector that can take two different designs. It is a straight tube of diameter $D = 22$ mm with a central rod of diameter $d = 6$ mm, topped by a cone of diameter $C = 14$ mm and 10 mm length, to stabilize flames S_0-bb and S_3-bb shown in Fig. 9.1. The cone protrudes 2.5 mm inside the combustion chamber from the injector backplane. The distance between the swirler backplane and the chamber backplane is $L = 56$ mm.

For flame S_3-as at the bottom in Fig. 9.1, the central rod is removed and the flame is fully stabilized aerodynamically. The central injection tube is in this

case slightly modified and comprises a tube with diameter $D = 22$ mm over a first section of length $L_1 = 22$ mm, followed by a nozzle of length $L_2 = 34$ mm, which is terminated by a diverging cup with an angle $\beta = 15°$ over an height of 6 mm. The nozzle throat diameter is in this case $D_0 = 12$ mm in Fig. 9.1.

The combustion chamber has an 82 mm square cross-section and a length of 150 mm, and is equipped with four quartz windows. At the base of the burner, a loudspeaker (Monacor SP-6/108PRO, 100 W RMS) is mounted to pulsate the flow. The velocity is measured with a hot wire anemometer probe (Dantec Dynamics - Probe 55P16 with a mini-CTA 54T30) below the swirler unit where the velocity has a top hat profile. A photomultiplier (Hamamatsu, H5784-04), equipped with a narrowband filter (Asahi Spectra, ZBPA310) centered around 310 nm and with a 10 nm bandwidth, is used to record the OH* chemiluminescence signal.

A 2D-2C Particle Image Velocimetry (PIV) system is also used to analyze the flow structure at the injector outlet under cold flow operation. Small oil droplets of diameter 3 μm are, in this case, seeded in the flow. The PIV system consists of 2×400 mJ Nd:YAG laser doubled at 532 nm operated at 10 Hz and a 2048×2048 px^2 CCD camera (Dantec Dynamics, FlowSense EO 4M). Two different optical setups are used for longitudinal and transverse measurements, with a time delay between the two laser pulses Δt =10 μs and a pixel pitch of 27.9 px/mm in the first case and Δt =25 μs with a pixel pitch of 40.1 px/mm in the second one. Eight hundred images are taken to obtain converged mean and rms values of the velocity field, which is deduced from the cross-correlation of the PIV images by a three passes window deformation technique (from 64×64 px^2 to 16×16 px^2 interrogation areas), with an uncertainty of 0.1 px on the calculated displacement.

An intensified CCD camera (Princeton Instruments, PI-MAX 4, 1024×1024 px^2), mounted with an UV objective (Nikkor 105 mm f/4.5) and equipped with the same filter as the photomultiplier, is also used to analyze the flame structure under steady and forced conditions. Phased averaged images of the OH* signals and the PIV fields are synchronized by the signal driving the loudspeaker.

9.3 Steady injection conditions

The PIV data gathered in the axial plane and a transverse plane 2 mm above the top cone of the central bluff-body (flames S_0-bb, S_3-bb) and 2 mm above the injector outlet (flame S_3-as) are first used to determine the swirl number S (Candel et al., 2014) at the injector outlet : S=0.20 for S_0-bb, S=0.80 for S_3-bb and S=0.75 for S_3-as, with a relative precision ±3%.

The swirl level for flame S_0-bb slightly differs from zero due to small imperfections in the swirler manufacturing. Several PIV measurements were made to check this feature that was found to be reproducible, with the same velocity profile, from tests to tests by mounting and demounting the swirler and the rod. Nonetheless, the swirl number $S = 0.2$ remains in this case small and the configuration S_0-bb will be referred in the following as a non-swirling flame.

Effects of the swirl number S on the shape taken by the flames are shown in Fig. 9.1. The flame S_0-bb is anchored on the bluff body at the top in Fig. 9.1 with a relatively narrow reaction layer spreading over a long distance in the wake of the central bluff-body. The flame S_3-bb produced by the same injector but with a higher swirl $S = 0.8$ is more compact in Fig. 9.1. When the central rod is removed, Fig. 9.1 shows that the lifted flame S_3-as has about the same axial extent as flame S_0-bb but with an emission intensity peaking in the central region.

9.4 Flame transfer functions

The FTF of the three preceding flames is determined from the velocity signal measured by the hot wire anemometer and the OH* chemiluminescence intensity I measured by the photomultiplier gathering light from the whole combustion region. This signal is assumed to be a good tracer of the heat release rate. Flames are excited by the loudspeaker in the frequency range 20-260 Hz with a constant modulation level $u'/\overline{u}$=0.3, where $\overline{u}$ and u' denote the mean and root-mean-square (RMS) values of the velocity signal measured by the hot wire. The FTF is deduced from the cross- and power-spectral densities of the hot wire and photomultiplier signals evaluated at the forcing frequency f:

$$\mathcal{F}(f) = \frac{I'/\overline{I}}{u'/\overline{u}} = G(f)\exp(i\varphi(f)) \tag{9.1}$$

Results are plotted in Fig. 9.2. The FTF gain curve of flame S_0-bb shows a typical low-pass filter behavior with a large gain overshoot at low frequencies, a well known feature of the acoustic response of laminar and turbulent premixed non-swirling V-flames anchored on a central bluff body (Schuller et al., 2003; Durox et al., 2005; Balachandran et al., 2005).

The FTF of the flame S_3-bb obtained with the same injector design, but a swirl level $S = 0.80$, differs from flame S_0-bb by several aspects in Fig. 9.2. The FTF gain of S_3-bb shows a succession of a peak, a valley at $f_0 = 96$ Hz and another peak over a short frequency range, over which the non-swirling flame S_0-bb response remains maximum. These features are now well understood and documented in a series of theoretical, numerical and experimental

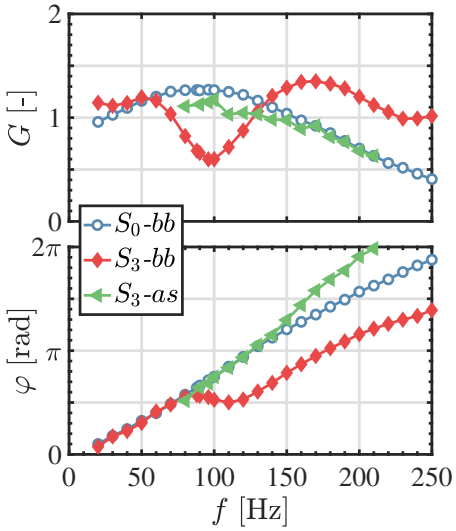

Figure 9.2: *Gain G and phase lag φ of the FTF for the three configurations investigated at the forcing level $u'/\overline{u} = 0.30$ RMS.*

studies (Komarek and Polifke, 2010; Palies et al., 2010b; Palies et al., 2011d; Kim and Santavicca, 2013b). They result from interferences between axial and azimuthal velocity fluctuations that are produced at the swirler outlet. It has been demonstrated that the frequency f_0 at which the FTF gain of a swirling flame reaches its minimum is obtained for the largest swirl number oscillation, *i.e.* a situation where azimuthal and axial velocity fluctuations are out of phase at the burner outlet (Palies et al., 2010b).

The frequency f_0 can be roughly estimated by considering the phase-lag $\varphi_{u'_\theta - u'_z}$ between azimuthal and axial velocity fluctuations at the injector outlet (Palies et al., 2011a; Kim and Santavicca, 2013b):

$$\varphi_{u'_\theta - u'_z} = 2\pi f_0 \delta \left(\frac{1}{u_c} - \frac{1}{c} \right) \tag{9.2}$$

where u_c is the convection velocity of azimuthal disturbances and $c \gg u_c$ is the speed of sound. The condition leading to the highest swirl number oscillation amplitude, *i.e.* a minimum FTF gain, corresponds to $\varphi_{u'_\theta - u'_z} = \pi$. The distance δ in Eq. (9.2) is between the top of the swirler injection channels, where azimuthal disturbances are generated, and the combustor backplane. It is thus slightly smaller than the distance $L = 56$ mm between the swirler and the combustor backplanes. The velocity u_c is close to the maximum velocity reached by the flow in the injection channel (Palies et al., 2010b; Palies et al., 2011a; Acharya and Lieuwen, 2015). This velocity remains unknown in the present study, but a rough estimate is made here by taking it equal to the highest axial velocity $u_c = 9$ m/s measured close to the injector outlet with PIV (Figs. 4.4-4.5). The same choice was made in Palies et al., 2010b. One finds $f_0 = 90$ Hz

for $u_c = 9$ m/s and $\delta = 50$ mm. This estimate is close to $f_0 = 96$ Hz determined experimentally in Fig. 9.2 for flame S_3-bb. The largest uncertainty comes from the value of the convection velocity u_c, which depends on the flow structure between the swirler injection channel outlets and the burner outlet.

The FTF of the swirling flame S_3-as obtained without central insert does not feature any significant FTF gain drop in Fig. 9.2 even though the swirl level $S = 0.75$ is close to the value $S = 0.80$ for flame S_3-bb anchored on the bluff body. One may again roughly estimate the frequency f_0 associated to the largest swirl number oscillations. Considering the reduction of the injection tube diameter, one now takes $u_{c,1} = 5.44$ m/s over $\delta_1 = 16$ mm and $u_{c,2} = 18.2$ m/s over $\delta_2 = 34$ mm deduced from mass balance (see Fig. 9.1) and finds $f_0 = 104$ Hz. This frequency is well inside the range investigated but, nonetheless, there is no drop of the FTF gain in Fig. 9.2 for flame S_3-as.
Other interesting features, which seem to have not been reported previously, are observed for the FTF phase lag in Fig. 9.2. The phase lag curve of the non-swirling S_0-bb and highly swirled S_3-bb flames anchored on the central bluff body are the same at low frequencies $f < f_0$. This is not an obvious feature since the time lag τ appearing in the FTF phase lag $\varphi = 2\pi f\tau$ is generally proportional to the flame length L_f and to the inverse of the bulk flow velocity $1/U_b$. In Fig. 9.1, obtained for steady injection conditions, the flame length L_f and flame aspect ratio largely differ between S_0-bb and S_3-bb while the bulk flow velocity remains the same. At higher frequencies $f > f_0$, the FTF phase lag of the non-swirling flame S_0-bb keeps increasing with an almost constant slope in the full frequency range investigated. An inflection point and a rapid change of the phase lag characterize the response of the highly swirled flame S_3-bb at frequencies close to $f \sim f_0$. At higher forcing frequencies, the data for the FTF phase lag of flame S_3-bb are found to be parallel to the FTF phase lag plot of the non-swirling flame S_0-bb offset by a constant value of $\varphi_0 \simeq -1.3$ rad. The FTF phase lag of the aerodynamically stabilized swirled flame S_3-as regularly increases with a different slope than flame S_0-bb and does not exhibit any inflection point.

9.5 Flame dynamics

Phase averaged images of the OH* chemiluminescence conditioned by the harmonic excitation are examined in Fig. 9.3 to elucidate some of the previous observations. The forcing level $u'/\overline{u} = 0.30$ RMS is the same as in Fig. 9.2 showing the FTF results. The intensified CCD camera is synchronized with the signal driving the loudspeaker at the bottom of the burner. Images are taken for each configuration at the same phases separated by a constant interval of 30^o. The phase angles are indicated in Fig. 9.3 with respect to the hot-wire signal below the radial swirler and a phase shift arises between flames

forced at 96 Hz and 170 Hz which correspond to the minimum and maximum gain of the FTF for flame S_3-bb. An Abel deconvolution reveals the trace of the flame luminosity in an axial plane crossing the burner axis for flames S_0-bb and S_3-bb. This post-processing was not possible for flame S_3-as due to the too high intensity values close to the symmetry axis (see Fig. 9.1). The same color scale is used for all images to better highlight both the flame motion and changes of the flame luminosity during the forcing cycle.

The first sequence in Fig. 9.3 highlights the large motion undergone by the non-swirling flame S_0-bb at the forcing frequency $f = 96$ Hz when the FTF gain is maximum in Fig. 9.2. Large roll-up of the flame tip is seen at 195° and 255°. The flame is stretched in the vertical direction during the forcing cycle with relatively minor changes of the OH* luminosity.

The second and third sequences in Fig. 9.3 show the responses of flame S_3-bb, at the FTF gain minimum at $f_0 = 96$ Hz and at the FTF gain maximum at $f = 170$ Hz in Fig. 9.2. The motion undergone by the flame does not differ significantly at these two forcing frequencies, but it is mainly changes of the flame luminosity that explain the large differences observed for the FTF gain at $f_0 = 96$ Hz and $f = 170$ Hz in Fig. 9.2. At $f_0 = 96$ Hz, there is a relatively weak flame roll-up motion accompanied by weak changes of the flame luminosity over the forcing cycle in Fig. 9.3. At $f = 170$ Hz, the flame roll-up process is a bit further pronounced, but the OH* luminosity undergoes large changes during the forcing cycle explaining the high value taken by the FTF gain at this frequency in Fig. 9.2.

The last sequence in Fig. 9.3 shows the dynamics of the aerodynamically stabilized flame S_3-as at $f = 96$ Hz corresponding to its peak FTF gain value in Fig. 9.2. The flame is rolled-up by vortex interaction (75°-195°) and is stretched in the vertical direction, but also undergoes large changes of its luminosity as flame S_3-bb at $f = 170$ Hz. The position of the leading edge of flame S_3-as also exhibits a large vertical oscillation during the forcing cycle, as highlighted by the white crosses in this sequence, while flames S_0-bb and S_3-bb remain anchored on the bluff body in Fig. 9.3.

Further analysis is made at the forcing frequency $f_0 = 96$ Hz by determining the average flame position for each image sequences. This profile is obtained by finding the maximum row-wise intensity of the pixel luminosity, weighted by the distance from the burner axis as expressed by: $\int I(r,x)2\pi r dr$. A threshold of 25% is selected to delineate the lower (cross symbol) and upper (diamond symbol) flame boundaries. For flame S_3-as in the last sequence in Fig. 9.3, the flame contour is used in place of the average flame position for the analysis. This post-processing is used to deduce the flame height H corresponding to the vertical distance between the upper (diamond sign) and lower (plus sign) flame

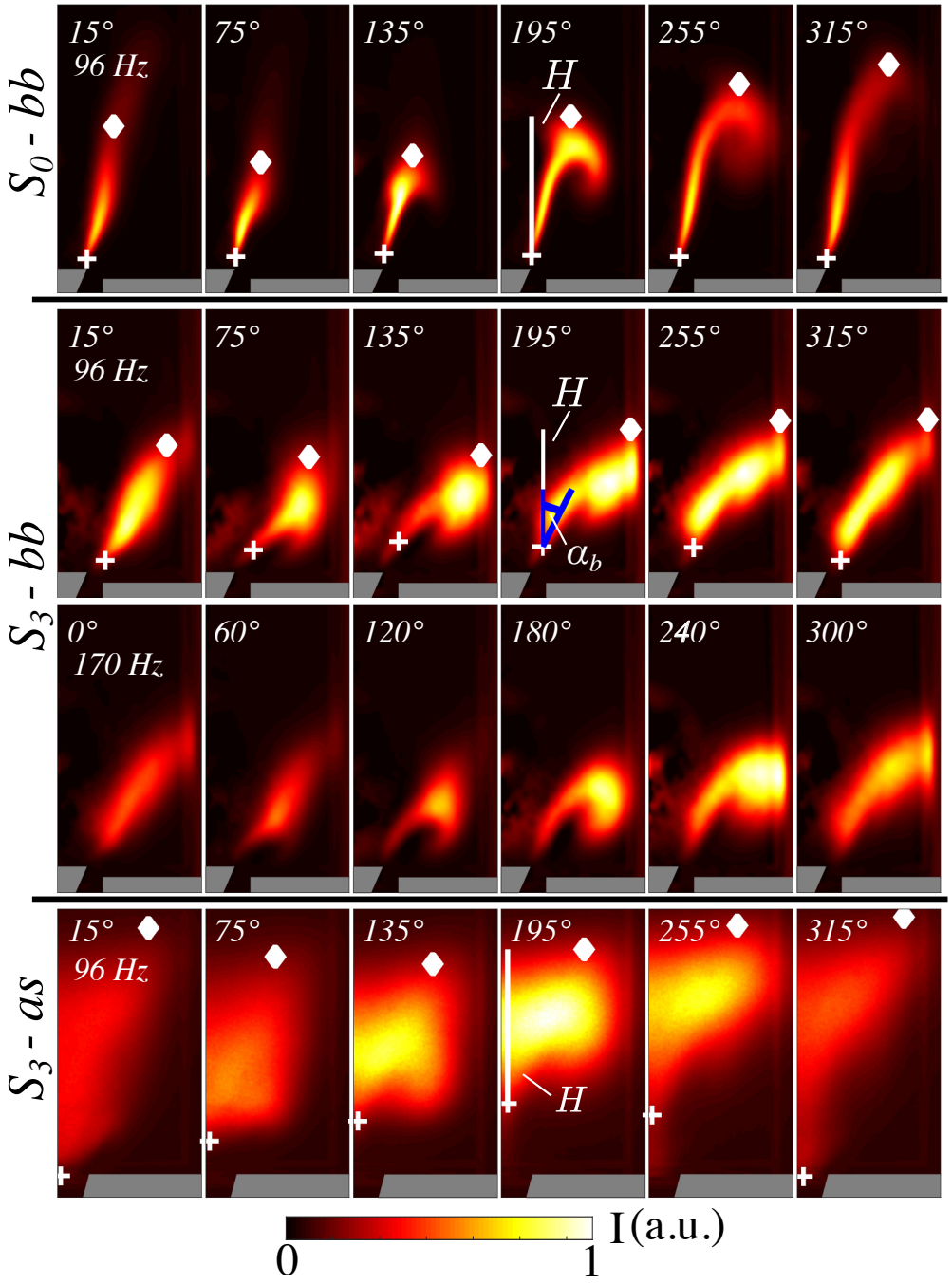

Figure 9.3: *OH^* intensity phase averaged images at a forcing level $u'/\overline{u} = 0.30$ RMS. + : flame root position. ◇ : flame tip position.*

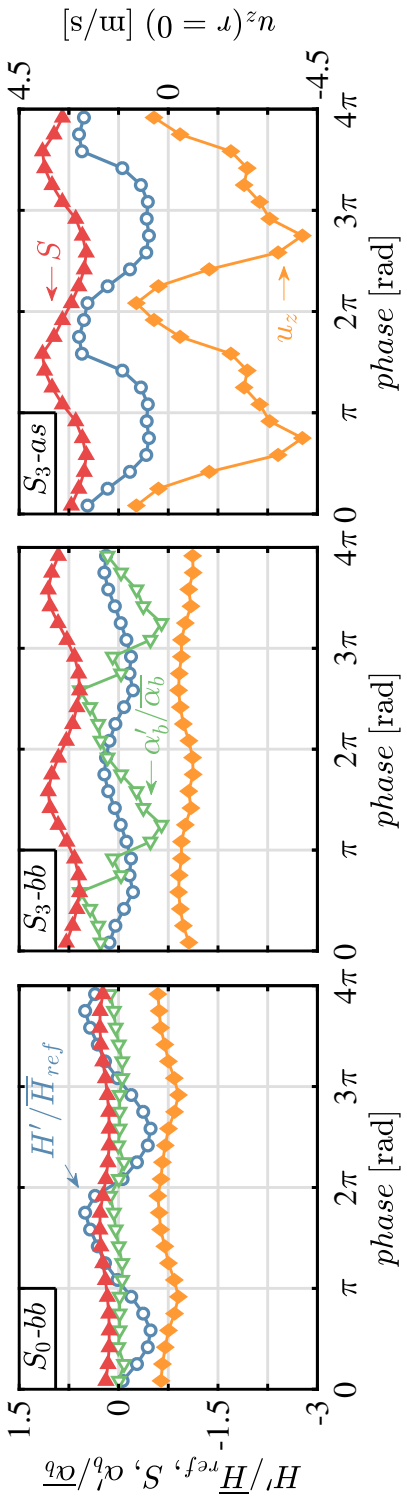

Figure 9.4: *Evolutions of the swirl number S and axial velocity $u_z(r = 0)$ at the burner outlet with respect to the phase of the hot-wire signal. The relative flame height $H'/\overline{H}_{ref}$ and flame base angle $\alpha_b'/\overline{\alpha_b}$ oscillations are also plotted. Two oscillation cycles are represented for better readability.*

boundaries *i.e.* the length of the vertical white segment shown in Fig. 9.3 at the phase 195^o. This process proves to be efficient and robust even when the flame is strongly modulated by vortex interaction. The flame angle α_b with respect to the vertical direction is also determined at the flame leading edge position as shown in the second sequence in Fig. 9.3 at 195^o. Evolutions of H and α_b are plotted in Fig. 9.4 over two periods for the three flames S_0-bb, S_3-bb and S_3-as excited at $f = 96$ Hz. The same reference height $\overline{H}_{ref} = 25$ mm is used to normalize the results. The three flames exhibit a modulation of their height H during the forcing cycle, but the oscillation amplitude H' is a bit lower for S_3-bb compared to S_0-bb and S_3-as. The swirling flame S_3-bb stabilized by the bluff body also features a large oscillation of the flame angle α_b at its base at $f_0 = 96$ Hz. These flame angle oscillations are not observed for the non-swirling flame S_0-bb and could not be determined for the fully aerodynamically stabilized flame S_3-as.

Figure 9.4 also shows the evolution of the swirl number S at the injector outlet, determined, for each selected phase in the cycle, by PIV measurements conducted in cold flow conditions, with a relative precision of $\pm 5\%$. One clearly identifies a large modulation of the swirl level at $f = 96$ Hz for the swirling flames S_3-bb with and S_3-as without bluff body, while at the same frequency there are no swirl oscillations for the flame S_0-bb. This analysis confirms that both flames, S_3-bb and S_3-as, undergo large swirl number oscillations at $f = 96$ Hz, but their FTF largely differ even though they share about the same swirl level $S \sim 0.8$.

Finally, the axial velocity signal u_z on the symmetry axis $r = 0$ is examined in Fig. 9.4. This signal measured 2 mm above the top cone is barely altered by the flow modulation at $f_0 = 96$ Hz for flames S_0-bb and S_3-bb anchored in the wake of the central bluff body. This contrasts with the large oscillation in Fig. 9.4 observed for the same signal measured 2 mm above the injector outlet for the swirling flame S_3-as without bluff body. This large modulation is responsible for the displacement of the leading edge position of the aerodynamically stabilized flame S_3-as in the bottom image sequences in Fig. 9.3.

Further analysis is now carried out under cold flow conditions by examining the dynamics of coherent vortical disturbances synchronized by the acoustic pulsation. Results are presented in Fig. 9.5. To identify vortical structures, the Q criterion (Jeong and Hussain, 1995) is selected:

$$Q = \frac{1}{2}(|\mathbf{\Omega}|^2 - |\mathbf{S}|^2) \tag{9.3}$$

where $\mathbf{S}$ and $\mathbf{\Omega}$ are the symmetric and anti-symmetric components of the velocity gradient respectively. Iso-contours of Q are inferred from PIV measurements in the axial plane. Only positive values of Q are retained. Negative values, in-

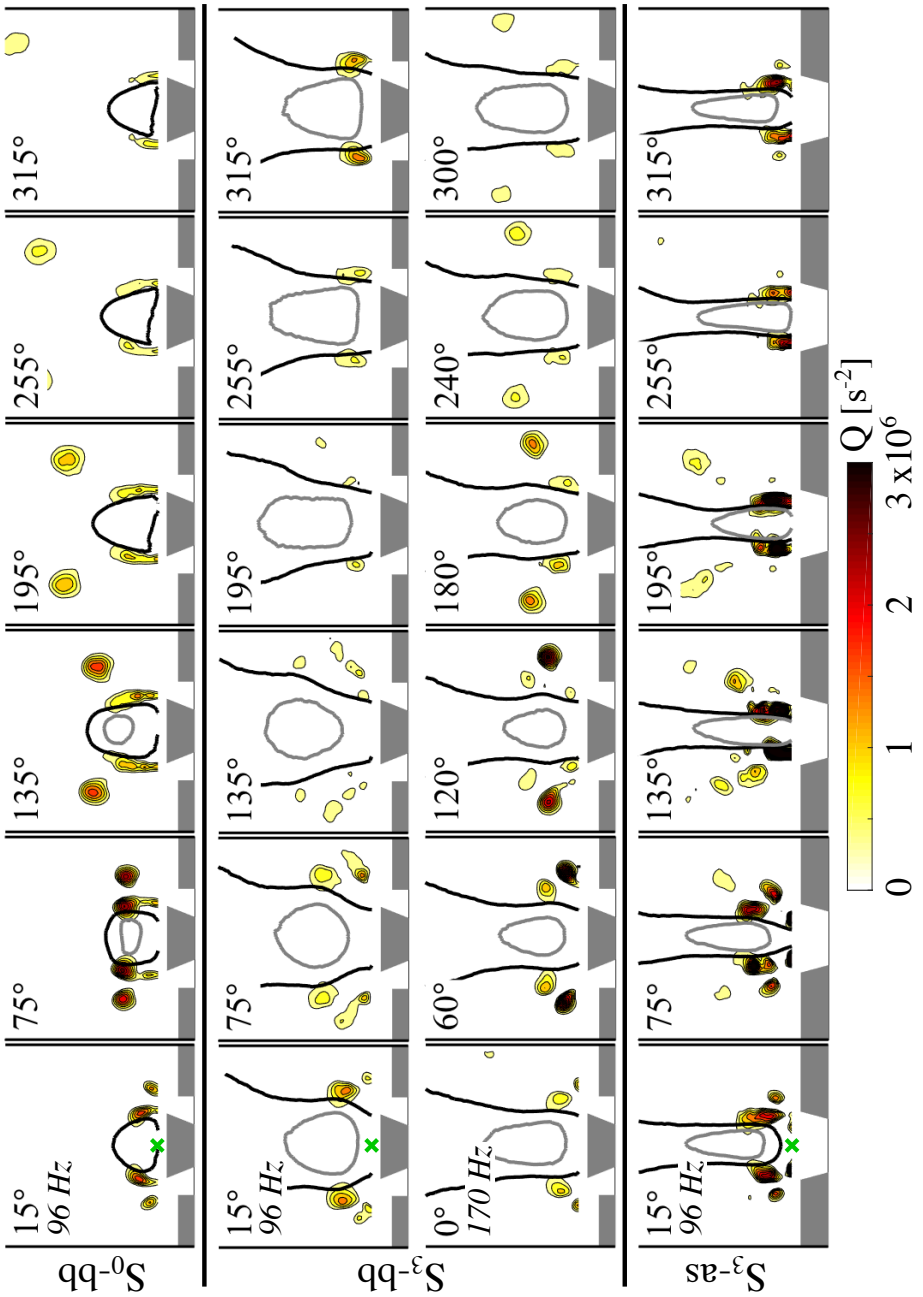

Figure 9.5: *Q criterion contour obtained from PIV measurements in cold flow conditions, for a forcing level $u'/\overline{u} = 0.30$ RMS. Isolines of axial velocity are superimposed. Black contour: $u_z = 0$ m/s. Gray contour: $u_z = -2.5$ m/s. The position where the axial velocity u_z for the analysis of Fig. 9.4 is measured, is shown as a green cross at the phase 15^o.*

dicating regions where shear is present but no swirling motion, are forced to a zero value.

In the first, third and last sequences in Fig. 9.5, corresponding to FTF gain maxima in Fig. 9.2, large vortical structures generated at the rim of the injector are produced by the acoustic forcing and convected downstream in the chamber. In the second sequence in Fig. 9.5, corresponding to the FTF gain minimum in Fig. 9.2 for flame S_3-bb at $f_0 = 96$ Hz, vortical structures are much weaker as emphasized by the much lower values taken by the Q criterion. As a consequence, the flame response remains low at this forcing frequency.

Isolines of axial velocity are also shown in Fig. 9.5, to highlight the different dynamics of the internal recirculation zone depending upon the flame stabilization mechanism. Flame S_0-bb feature a small recirculation region in the wake of the bluff-body. Flame S_3-bb feature a larger IRZ, undergoing a flapping motion during the forcing cycle, which is more evident at $f_0 = 96$ Hz. When the flame is stabilized without bluff-body, S_3-as, the IRZ is much thinner and oscillates vertically in and out of the injector.

These observations are confronted with current interpretations of the response of swirling flames associated with the combined effects of swirl number oscillations and flame vortex roll-up. Palies et al., 2011e explained that at the FTF gain minimum, large swirl number oscillations modulate the strength of the IRZ. This oscillation weakens the formation of eddies and also leads to flame base angle oscillations. When the flame angle fluctuates, vortex growth is rapidly hindered by the flame flapping motion and the flame response is low. When the flame angle oscillation weakens, the response is high because vortices can fully develop before interacting with the flame. Interaction of vortex shedding and flame angle fluctuations has been further analyzed in Bunce et al., 2013. These authors argue that as the flame moves closer to the shear layer, the vorticity of the flow is dissipated due to its interaction with the flame and the flame response is low. In contrast, when the mean flame position is stationary, the vorticity of the flow is not dissipated before interacting with the flame, which leads to a large flame response.

The observations made in this work are for some aspects consistent with these conclusions, but also reveal new mechanisms. Figure 9.4 confirms that swirl number and flame base angle oscillations are large for flame S_3-bb stabilized by a bluff body at $f_0 = 96$ Hz where the FTF gain is at a minimum. It is however found that the formation of large vortical structures are damped even without combustion. This phenomenon is here not related to the flapping motion of the flame, but is found to be related to the geometry of the injector. At the same excitation frequency, large vortical structures are shed from the injector without bluff-body, while large swirl level oscillations are also observed. In

this case, the response of flame S_3-as remains high. This flame also exhibits a large vertical oscillation of its leading edge and a peak value of the FTF gain at $f = 96$ Hz. This analysis reveals that the mechanisms controlling the frequency response of swirled flames largely differ when they are stabilized by a bluff body or when they are stabilized aerodynamically, the main differences being related to the dynamics of the IRZ.

9.6 Conclusion

Transfer functions of flames stabilized with different injector designs have been investigated for different swirl levels, with and without a central insert in the injector. Depending on the stabilization mechanism, flame vortex roll-up, oscillations of the flame base angle induced by swirl level oscillations and vertical oscillations of the flame leading edge, are found to be the competing mechanisms controlling the flame response. When the FTF gain is at a maximum, the three flames investigated are strongly modulated by the interaction with large vortical structures convected in the external shear layer of the flow, regardless of changes of the swirl level and stabilization mechanisms. In contrast, the formation of large vortical structures is hindered, even in cold flow conditions, at the frequency corresponding to a minimum in the FTF gain curve, which is observed in the present study only for the swirling flame stabilized by a bluff body. At this frequency, large swirl number oscillations lead to a modulation of the flame base angle and weak vortex formation. At the same frequency, but for the aerodynamically stabilized flame without central insert, swirl number oscillations of the same order of magnitude are observed, but the gain of the FTF remains high. In this case, large vortical structures are shed and the flame leading edge oscillates vertically. The origin of the low response of swirling flames at specific frequencies is found to not only be related to large oscillations of the swirl level, but also to the flame stabilization mechanism and more specifically to the dynamics of the internal recirculation region.

Conclusion

The dynamics of lean premixed swirling flames was investigated in this manuscript. The main concern was to assess the effects of different injection conditions on the properties of flame stabilization, thermoacoustic instability and flame response to acoustic perturbations. In particular we considered effects of different (i) design of the swirler device, (ii) dimensions of the injector, (iii) bulk flow velocities and (iv) flame stabilization mechanisms.

Flame stabilization

A stabilization chart was obtained and three flame regimes were identified depending on the value of the swirl number and a normalized injector cross section area:

- at low level of swirl ($S < 0.5$), flames are elongated in the downstream direction with a shape similar to that of non-swirling V-flames
- in the intermediate swirl range ($0.5 < S < 0.8$) flames are well stabilized with a compact shape
- when the swirl number is too elevated ($S > 0.8$) flames flashback inside the injector.

These limits on the swirl number should only be taken as an indication and are also dependent upon the main dimensions of the injector. For a fixed swirl number, an injector with an higher nozzle cross section has more propensity to flashback.

Thermoacoustic instability

One of the major drawback for the application of lean premixed combustion systems, is their sensitivity to thermoacoustic instabilities. In this work, we concentrated on the effects of different geometries of the injector on this phenomenon. In particular, we showed that it was possible to lower the intensity of the instability by properly modifying the distance between the swirler device and the combustion chamber backplane. On the other hand, when the dimension of the injector are fixed, a different design of the swirler did not lead to any important difference on the properties of the thermoacoustic instability.

Flame response to acoustic perturbations

FTF measurements were conducted by submitting flames to well controlled acoustic perturbations. It was shown that the FTF gain curve of highly swirled flames is characterized by peaks and valleys while, when the swirl number is low ($S = 0.20$), the FTF behaves like a low-pass filter, with the gain increasing to reach a maximum higher than unity and then constantly decreasing towards zero for increasing forcing frequencies. Surprisingly, the same low-pass filter behavior was observed for an high swirling flame fully aerodynamically stabilized, without the help of a bluff-body. A low FTF gain value in the low frequency range could only be observed for highly swirled flames stabilized with the help of a bluff-body. The FTF phase-lag is characterized by a linear behavior and by a jump with an inflection point around the minimum gain frequency, if this minimum is present.

In terms of the effects of different injector geometries, it was observed that:

- as the swirl number is increased, either by an increase of the injector exit diameter, a decrease of the bluff-body diameter or a different swirler device, the minimum gain value is decreased and the phase-lag jump increased
- by modifying the velocity inside the injector, either by a change of injector diameter or bulk flow velocity, it is possible to shift the FTF curves in the frequency range
- the same effect can be obtained by modifying the distance between the swirler and the combustion chamber backplane.

Mechanisms behind the acoustic response

Phase-locked (i) OH* chemiluminescence images, (ii) Particle Image Velocimetry (PIV) measurements and (iii) Large Eddy Simulations (LES) were exploited for an interpretation of the main mechanisms behind the acoustic response of lean premixed swirling flames. The focus was on the differences between low and high value of the FTF gain, to assess those conditions possibly leading to a reduction of the sensitivity of LPM systems to acoustic waves.

Qualitatively, the motion of the investigated flames at these two peculiar frequencies is not different. The flame motion is the results of swirl number fluctuations and interaction with vortical structures, leading to a modulation of flame length and angle. Swirl fluctuations are due to the interaction of axial acoustic and azimuthal convective perturbations, which are formed at the swirler exit when this is impinged by acoustic waves. Due to the convective nature of azimuthal perturbations, this interaction depends upon swirler-combustion chamber distance and mean flow velocity inside the injector. This explains the effects on the FTF of these parameters.

Quantitatively, fluctuations are stronger at frequencies corresponding to a maximum gain value. It was shown that this is due to a different strength of vortical structures at the two frequencies, which is not linked to flame/flow interaction since it was observed even in cold flow conditions. By post-processing of LES data, this was linked to a different phase-shift between the axial and the azimuthal velocity perturbations, that lead to a different shape of the velocity profiles at the injector rim. The low strength of vortical structures at the FTF gain minimum frequency is behind the low flame response and the drift from linearity of the FTF phase-lag.

By considering the time scales of these two dominant mechanisms (interferences between the acoustic pulsation and the azimuthal flow disturbances generated at the swirler outlet and interaction of the flame with vortical structures generated at the burner rim), a nondimensionalization of the FTF results obtained with different injection conditions could be obtained.

The flame motion of a fully aerodynamically stabilized flame, analyzed at last, is somehow different. In this case, a vertical oscillation of the flame leading edge is observed as a consequence of the vertical oscillation of the internal recirculation region (IRZ) while, when the bluff-body is present, this vertical oscillation is hindered and the IRZ mainly oscillates laterally.

Perspectives

- All the results presented in this manuscript refer to fully premixed system at a fixed value of the equivalence ratio ($\Phi = 0.82$). It would be interesting to see if the mechanisms observed can be confirmed for different values of Φ. Even more interesting would be to conduct a same analysis for technically premixed systems.

- FTF measurements are a powerful tool to analyze the response of the flame to incoming perturbations, but are time consuming. A step forward towards the identification of the main parameters controlling this response was taken in this manuscript, but work still need to be done. In particular, the different behavior of flames stabilized with or without the help of a bluff-body, deserves further attention.

- The mechanisms leading to a different strength of vortical structures at the FTF gain minimum and maximum frequencies were identified through PIV and LES in cold flow conditions. It would be interesting to check whether the same conclusions could be drawn when performing the same analysis in reactive conditions.

- FTF measurements were performed only in the low and intermediate frequency range in this work. It would be interesting to extend these

data to the high frequency range and see if new minimum or maximum FTF gain values are present. In this case, it would be worth to conduct the same analysis at these other peculiar frequencies and check if the same mechanisms are in action.

- It would be interesting to compare LES with experimental data for the configuration without the bluff-body, in cold but also reactive conditions. This analysis would show the different flow properties inside the injector, leading to the different responses of swirling flames stabilized with/without bluff-body.

Appendix A

Comparison of naturally unstable and externally excited flame motion

Flame transfer function are used in low-order models, in conjunction with descriptions of the burner acoustic field, to predict stability maps of combustion systems. However, they do not give access to qualitative informations about the flame motion, in response to the acoustic excitation. To analyze the mechanisms behind the flame response, phase-locked images of the flame motion were exploited in this thesis.

The experimental setups, used to characterize combustion instabilities and to mimic them by external excitation, are sketched in Fig. A.1. In the first case, the bottom of the burner was closed by a plate and the exhaust length could be modified by adding tubes of length $T = 220$ mm. Up to three tubes, $3T = 660$ mm, were mounted during this study. Doing so, the thermoacoustic state of the burner was modified and instabilities could be triggered.

The fluctuating velocity was measured with an hot wire probe and pictures of the flame motion were taken with an ICCD camera, synchronized by the HW signal.

In the second case, the exhaust tubes were removed and a loudspeaker was mounted at the bottom of the burner, to introduce the same acoustic excitation measured during self-triggered instability, controlled by the HW signal. Pictures of the flame motion were then taken with the ICCD camera, synchronized by the HW signal.

Figure A.2 shows the flame motion obtained with these two different setups. The phase angles indicated in the figure, refers to the hot wire signal. The geometrical configuration analyzed was presented in Ch. 5. The flame movement shown at the left of the symmetry axis in Fig. A.2, obtained by introducing the acoustic excitation with the loudspeaker, correctly reproduces the flame motion observed at the right of the symmetry axis and measured during self-triggered

instabilities. This was checked for two configuration with different exhaust tube length.
This check was important to confirm that the analysis of flame motion conducted by externally exciting the flow with a loudspeaker, correctly reproduces the same mechanisms observed during self-triggered instabilities.

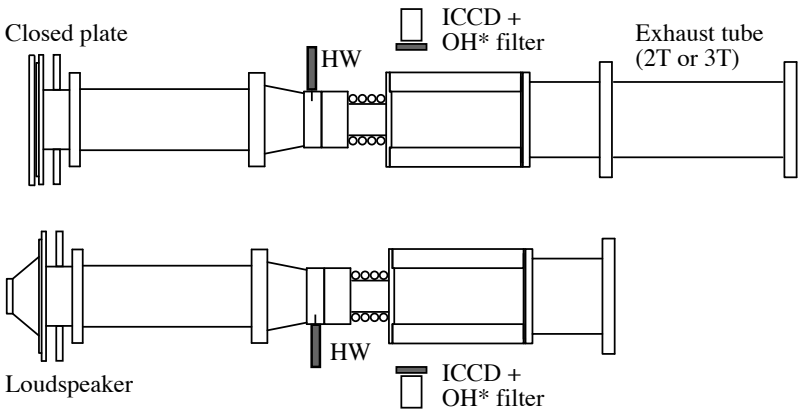

Figure A.1: *Setup used for the imaging of naturally unstable (top) or externally excited (bottom) flames.*

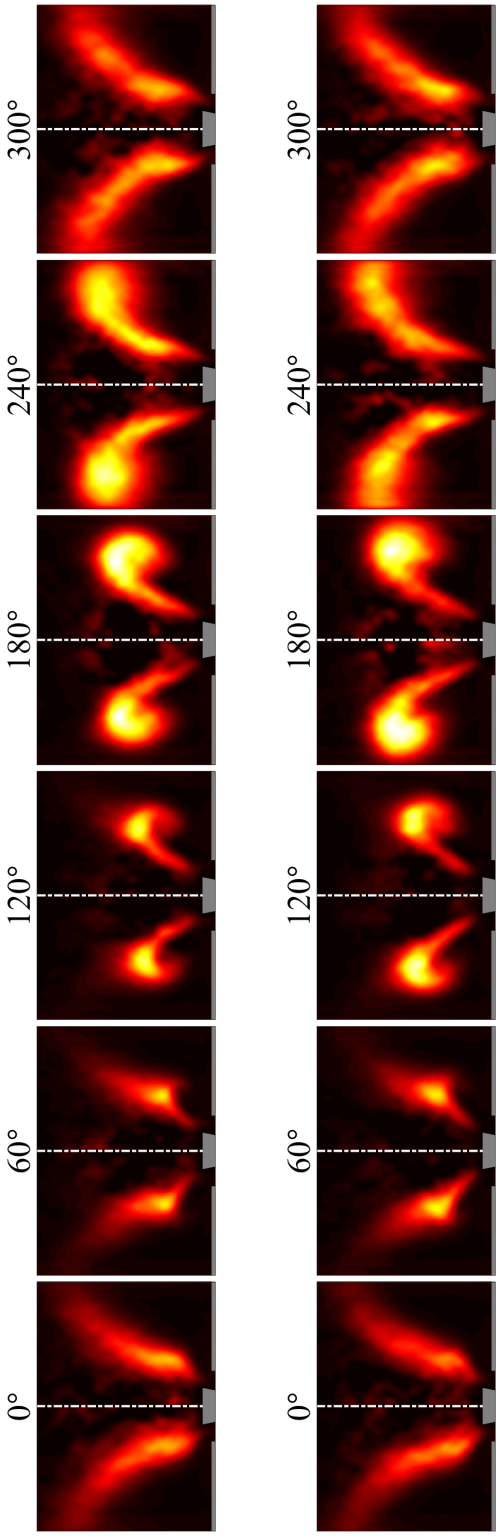

Figure A.2: *Phase averaged OH* chemiluminescence of the flame during one cycle of oscillation for the forced flame (left of the symmetry axis) and for the self-triggered flame (right of the symmetry axis). Top: 2T exhaust length, $f_1 = 181$ Hz. Bottom: 3T exhaust length, $f_1 = 164$ Hz. Geometrical configuration: SW_3, $D_o = 20$ mm, $C = 10$ mm, $\delta = 50$ mm. Full details were given in Ch. 5.*

Appendix B

Comparison of phase-locked flow fields for different injector geometries

Steady and dynamic properties of flames stabilized with different injector geometries, were analyzed in this work. The mechanisms behind the response to acoustic perturbations of these flames were studied with different diagnostics, including PIV measurements. The main objective was to investigate the conditions leading to an high or low flame response at different frequencies. The different strength of vortical structures, generated at the burner rim and then convected in the combustion chamber, was individuated as one of the peculiar mechanisms. This strength was estimated by analyzing the Q criterion contour plots, issued from PIV data as:

$$Q_{2D} = \frac{\partial u_z}{\partial z}\frac{\partial u_r}{\partial r} - \frac{\partial u_r}{\partial z}\frac{\partial u_z}{\partial r}. \tag{B.1}$$

The PIV scans, used to derive the Q criterion plots, are shown in Fig. B.1 for two configurations featuring different injector geometries and in Fig. B.2 for the same geometrical configuration but at two different forcing frequencies. The corresponding Q criterion plots were shown and discussed in Figs. 7.6-7.7.

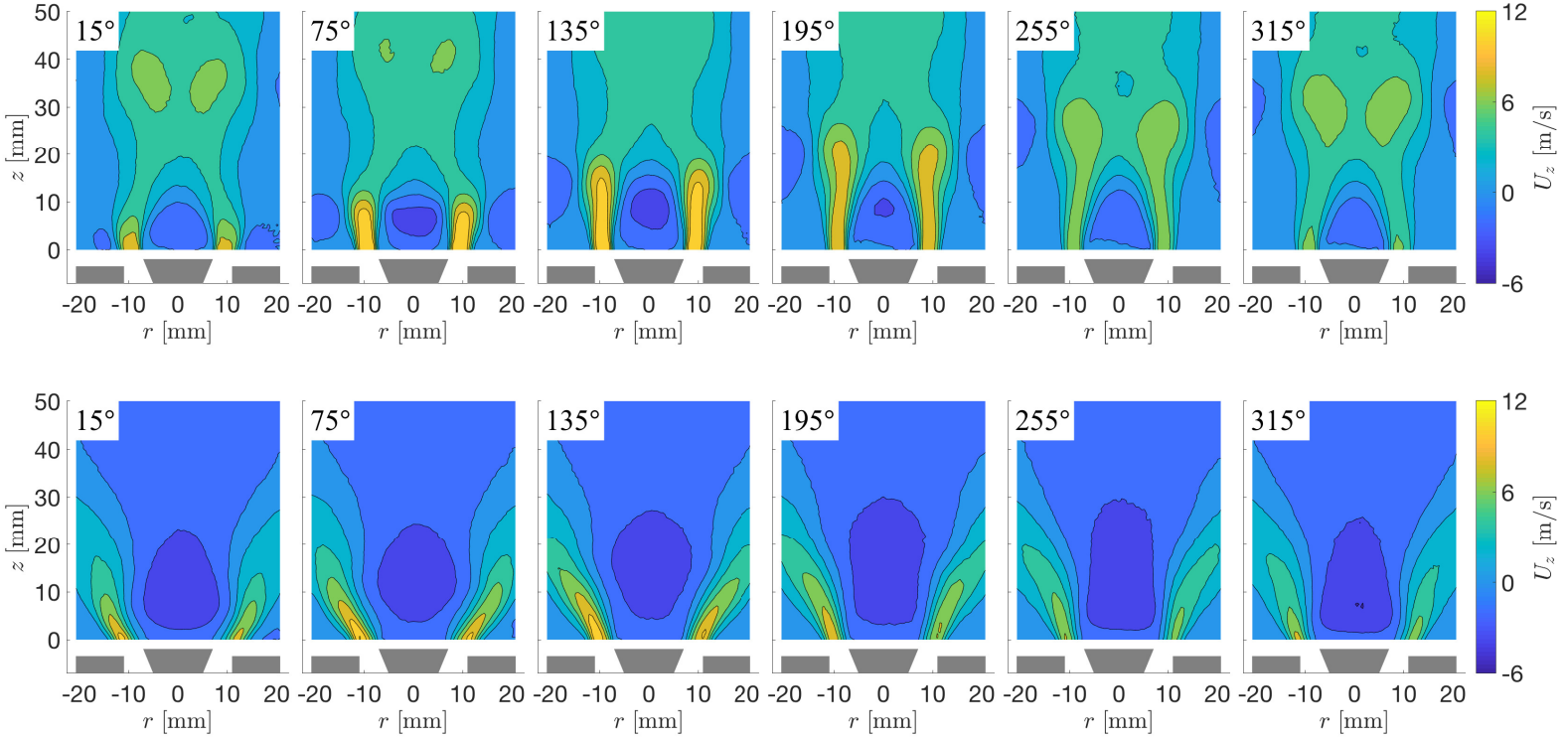

Figure B.1: *Phase averaged, cold flow, axial PIV scan for two configurations of interest. Top:* SW_0, $D_o = 22$ *mm*, $C = 14$ *mm*, $f = 96$ *Hz. Bottom:* SW_3, $D_o = 22$ *mm*, $C = 14$ *mm*, $f = 96$ *Hz.*

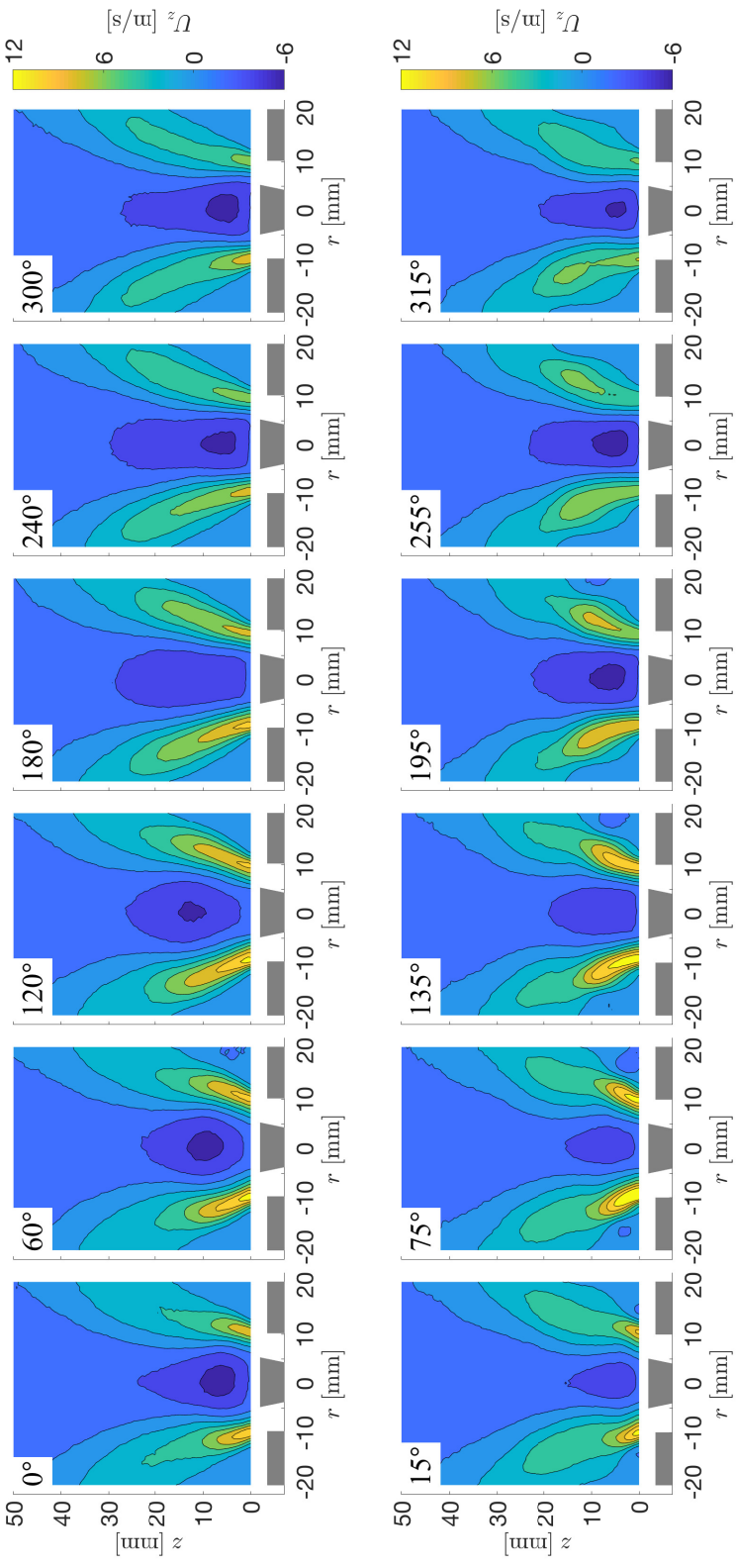

Figure B.2: *Phase averaged, cold flow, axial PIV scan for two configurations of interest. Top: SW_3, $D_o = 20$ mm, $C = 10$ mm, $f = 110$ Hz. Bottom: SW_3, $D_o = 20$ mm, $C = 10$ mm, $f = 190$ Hz.*

References

Abom, M. and Boden, H. (1988). Error analysis of two-microphone measurements in ducts with flow. *The Journal of the Acoustical Society of America*, 83(6):2429–2438. *(p. 10)*

Acharya, V. and Lieuwen, T. (2015). Effect of azimuthal flow fluctuations on flow and flame dynamics of axisymmetric swirling flames. *Physics of Fluids*, 27(10):105106. *(p. 148, 158, 163)*

Acharya, V., Shreekrishna, Shin, D.-H., and Lieuwen, T. (2012). Swirl effects on harmonically excited, premixed flame kinematics. *Combustion and Flame*, 159(3):1139–1150. *(p. 148, 158)*

Bahr, D, W. (1996). Aircraft Turbine Engine NOx Emission Abatement. In Culick, F., Heitor, M., and Whitelaw., J., editors, *Unsteady Combustion*, chapter 10, pages 243–264. Springer, Dordrecht. *(p. 2)*

Balachandran, R., Ayoola, B. O., Kaminski, C. F., Dowling, A. P., and Mastorakos, E. (2005). Experimental investigation of the nonlinear response of turbulent premixed flames to imposed inlet velocity oscillations. *Combustion and Flame*, 143:37–55. *(p. 9, 12, 107, 125, 150, 158, 162)*

Beer, J. M. and Chigier, N. A. (1972). *Combustion Aerodynamics*. Applied Science Publishers Ltd, London. *(p. 3, 37)*

Bellows, B. D., Bobba, M. K., Forte, A., Seitzman, J. M., and Lieuwen, T. (2007). Flame transfer function saturation mechanisms in a swirl-stabilized combustor. In *Proceedings of the Combustion Institute*, volume 31, pages 3181–3188. *(p. 10, 11, 12)*

Bellows, D., Bobba, K., Seitzman, M., and Lieuwen, T. (2006). Nonlinear Flame Transfer Function Characteristics in a Swirl-Stabilized Combustor. *Journal of Engineering for Gas Turbines and Power*, 129(4):954–961. *(p. 9, 48)*

Biagioli, F., Paikert, B., Genin, F., Noiray, N., Bernero, S., and Syed, K. (2013). Dynamic response of turbulent low emission flames at different vortex breakdown conditions. *Flow, Turbulence and Combustion*, 90(2):343–372. *(p. 158, 159)*

Borghesi, G., Biagioli, F., and Schuermans, B. (2009). Dynamic response of turbulent swirling flames to acoustic perturbations. *Combustion Theory and Modelling*, 13(3):487–512. *(p. 7)*

Bothien, M. R., Noiray, N., and Schuermans, B. (2015). Analysis of

Azimuthal Thermo-acoustic Modes in Annular Gas Turbine Combustion Chambers. *Journal of Engineering for Gas Turbines and Power*, 137(6):61505–61508. *(p. 7)*

Brear, M. J., Nicoud, F., Talei, M., Giauque, A., and Hawkes, E. R. (2012). Disturbance energy transport and sound production in gaseous combustion. *Journal of Fluid Mechanics*, 707:53–73. *(p. 6)*

Brown, D., M. (1995). Combustion control apparatus and method. European Patent Application No. 0 677 706 A1. 95/42. General Electric Company. *(p. 2)*

Bunce, N. A., Quay, B. D., and Santavicca, D. A. (2013). Interaction Between Swirl Number Fluctuations and Vortex Shedding in a Single-Nozzle Turbulent Swirling Fully-Premixed Combustor. *Journal of Engineering for Gas Turbines and Power*, 136(2):021503. *(p. 18, 20, 21, 98, 114, 121, 125, 158, 159, 170)*

Candel, S. (2002). COMBUSTION DYNAMICS AND CONTROL : PROGRESS AND CHALLENGES. In *Proceedings of the Combustion Institute*, volume 29, pages 1–28. *(p. 5, 6)*

Candel, S., Durox, D., Schuller, T., Bourgouin, J.-F., and Moeck, J. P. (2014). Dynamics of Swirling Flames. *Annu. Rev. Fluid Mech.*, 46:147–173. *(p. 9, 15, 18, 81, 158, 161)*

Candel, S., Durox, D., Schuller, T., Palies, P., Bourgouin, J. F., and Moeck, J. P. (2012). Progress and challenges in swirling flame dynamics. *Comptes Rendus - Mecanique*, 340(11-12):758–768. *(p. 3, 5)*

Cantrell, R. H. and Hart, R. W. (1964). Interaction between Sound and Flow in Acoustic Cavities: Mass, Momentum, and Energy Considerations. *The Journal of the Acoustical Society of America*, 36(4):697–706. *(p. 6)*

Cantwell, B. and Coles, D. (1983). An experimental study of entrainment and transport in the turbulent near wake of a circular cylinder. *J. Fluid Mech.*, 136:321–374. *(p. 131)*

Colin, O. and Rudgyard, M. (2000). Development of High-Order Taylor-Galerkin Schemes for LES. *Journal of Computational Physics*, 162(2):338–371. *(p. 64)*

Correa, S. M. (1993). A review of NOx formation under gas-turbine combustion conditions. *Combustion Science and Technology*, 87(1-6):329–362. *(p. 2)*

Ćosić, B., Terhaar, S., Moeck, J. P., and Paschereit, C. O. (2015). Response of a swirl-stabilized flame to simultaneous perturbations in equivalence ratio and velocity at high oscillation amplitudes. *Combustion and Flame*, 162(4):1046–1062. *(p. 96, 150, 151, 158)*

Crocco, L. (1951). Aspect of Combustion Stability in Liquid Propellant Rocket Motors Part I. *ARS Journal*. *(p. 5, 48, 81)*

Crocco, L. (1952). Aspect of Combustion Stability in Liquid Propellant Rocket Motors Part II. *ARS Journal*. *(p. 81)*

Crow, S. C. and Champagne, F. H. (1971). Orderly structure in jet turbu-

lence. *Journal of Fluid Mechanics*, 48(3):547–591. *(p. 131)*

Docquier, N. and Candel, S. (2002). Combustion control and sensors: a review. *Progress in Energy and Combustion Science*, 28:107–150. *(p. 3)*

Dowling, A. P. (1995). The calculation of thermoacoustic oscillations. *Journal of Sound and Vibration*, 180(4):557–581. *(p. 8)*

Dowling, A. P. (1999). A kinematic model of a ducted flame. *Journal of Fluid Mechanics*, 394:51–72. *(p. 8)*

Dowling, A. P. and Morgans, A. S. (2005). FEEDBACK CONTROL OF COMBUSTION OSCILLATIONS. *Annual Review of Fluid Mechanics*, 37(1):151–182. *(p. 6)*

Dowling, A. P. and Stow, S. R. (2003). Acoustic Analysis of Gas Turbine Combustors. *Journal of Propulsion and Power*, 19(5):751–764. *(p. 7)*

Ducruix, S., Durox, D., and Candel, S. (2000). Theoretical and experimental determinations of the transfer function of a laminar premixed flame. *Proceedings of the Combustion Institute*, 28(1):765–773. *(p. 7, 147)*

Ducruix, S., Schuller, T., Durox, D., and Candel, S. (2003). Combustion Dynamics and Instabilities: Elementary Coupling and Driving Mechanisms. *Journal of Propulsion and Power*, 19(5):722–734. *(p. 6, 7, 81, 95)*

Durox, D., Ducruix, S., and Lacas, F. (1999). Flow seeding with an air nebulizer. *Experiments in Fluids*, 27:408–413. *(p. 49)*

Durox, D., Moeck, J. P., Bourgouin, J. F., Morenton, P., Viallon, M., Schuller, T., and Candel, S. (2013). Flame dynamics of a variable swirl number system and instability control. *Combustion and Flame*, 160(9):1729–1742. *(p. 24, 25, 26, 37)*

Durox, D., Schuller, T., and Candel, S. (2005). Combustion dynamics of inverted conical flames. *Proceedings of the Combustion Institute*, 30(2):1717–1724. *(p. 8, 11, 12, 107, 158, 162)*

Durox, D., Schuller, T., Noiray, N., and Candel, S. (2009). Experimental analysis of nonlinear flame transfer functions for different flame geometries. *Proceedings of the Combustion Institute*, 32 I(1):1391–1398. *(p. 6, 8, 48, 150)*

Emerson, B., O'Connor, J., Juniper, M., and Lieuwen, T. (2012). Density ratio effects on reacting bluff-body flow field characteristics. *Journal of Fluid Mechanics*, 706:219–250. *(p. 131)*

Fleifil, M., Annaswamy, A. M., Ghoneim, Z. A., and Ghoniem, A. F. (1996). Response of a laminar premixed flame to flow oscillations: A kinematic model and thermoacoustic instability results. *Combustion and Flame*, 106(4):487–510. *(p. 147)*

Freitag, M. and Janicka, J. (2007). Investigation of a strongly swirled unconfined premixed flame using les. *Proceedings of the Combustion Institute*, 31 I(1):1477–1485. *(p. 7)*

Gaudron, R. (2018). *Acoustic Response of Premixed Flames Submitted to Harmonic Sound Waves*. PhD thesis. *(p. 31, 49, 62, 68, 83, 88)*

Gaudron, R., Gatti, M., Mirat, C., and Schuller, T. (2017). Impact of the

injector size on the transfer functions of premixed laminar conical flames. *Combustion and Flame*, 179:138–153. *(p. 121)*

Gaudron, R., Gatti, M., Mirat, C., and Schuller, T. (2018). FLAME DESCRIBING FUNCTIONS OF A CONFINED PREMIXED SWIRLED COMBUSTOR WITH UPSTREAM AND DOWNSTREAM FORCING. *Proceedings of ASME Turbo Expo*. *(p. 21, 22, 23, 149, 159)*

Gaydon, A. G. (1957). *The Spectroscopy of Flames*. Chapman and Hall, London, 1st edition. *(p. 47)*

Giuliani, F., Gajan, P., Diers, O., and Ledoux, M. (2002). Influence of pulsed entries on a spray generated by an airblast injection device: An experimental analysis on combustion instability processes in aeroengines. *Proceedings of the Combustion Institute*, 29(1):91–98. *(p. 159)*

Guiberti, T. F. (2015). *Analysis of the topology of confined premixed swirling flames*. PhD thesis, Ecole Centrale Paris. *(p. 47)*

Gupta, A. K., Lilley, D. G., and Syred, N. (1984). *Swirl flows*. Tunbridge Wells, Abacus Press, Kent. *(p. 3)*

Han, Z. and Hochgreb, S. (2015). The response of stratified swirling flames to acoustic forcing: Experiments and comparison to model. *Proceedings of the Combustion Institute*, 35(3):3309–3315. *(p. 7)*

Hirsch, C., Fanaca, D., Reddy, P., Polifke, W., and Sattelmayer, T. (2005). Influence of the swirler design on the flame transfer function of premixed flames. In *ASME Turbo Expo 2005*, number GT2005-68195. *(p. 148, 150, 158)*

Hochgreb, S., Dennis, D., Ayranci, I., Bainbridge, W., and Cant, S. (2013). FORCED AND SELF-EXCITED INSTABILITIES FROM LEAN PREMIXED, LIQUID-FUELLED AEROENGINE INJECTORS AT HIGH PRESSURES AND TEMPERATURES. In *Proceedings of ASME Turbo Expo*, pages GT2013–95311. *(p. 21)*

Hosseini, S. M., Gardner, C., and Lawn, C. (2012). The non-linear thermoacoustic response of a small swirl burner. *Combustion and Flame*, 159(5):1909–1920. *(p. 96)*

Howe, M. S. (1998). *Acoustics of Fluid-Structure Interactions*. Cambridge University Press, Cambridge. *(p. 6)*

Huang, Y. and Yang, V. (2005). Effect of swirl on combustion dynamics in a lean-premixed swirl-stabilized combustor. *Proceedings of the Combustion Institute*, 30 II(2):1775–1782. *(p. 3, 4)*

Huang, Y. and Yang, V. (2009). Dynamics and stability of lean-premixed swirl-stabilized combustion. *Progress in Energy and Combustion Science*, 35(4):293–364. *(p. 3, 5, 148, 158)*

Hurle, I. R., Price, R. B., Sugden, T. M., Thomas, A., Sudgen, T. M., and Thomas, A. (1968). Sound emission from open turbulent premixed flames. *Proc. Roy. Soc. A*, 303(1475):409–427. *(p. 7, 96)*

IEA (2016). Energy and Air Pollution. *(p. 2)*

IEA (2017a). Key World Energy statistics. Technical report, International

Energy Agency. *(p. 1)*

IEA (2017b). World Energy Balances: Overview. Technical report, International Energy Agency. *(p. 1)*

Jeong, J. and Hussain, F. (1995). On the identification of a vortex. *Journal of Fluid Mechanics*, 285:69–94. *(p. 123, 168)*

Jones, B., Lee, J. G., Quay, B. D., and Santavicca, D. A. (2011). Flame Response Mechanisms Due to Velocity Perturbations in a Lean Premixed Gas Turbine Combustor. *Journal of Engineering for Gas Turbines and Power*, 133(2):021503. *(p. 148)*

Keller, J. J. (1995). Thermoacoustic oscillations in combustion chambers of gas turbines. *AIAA Journal*, 33(12):2280–2287. *(p. 5)*

Kim, D., Lee, J. G., Quay, B. D., Santavicca, D. A., and Kim, K. (2010a). Effect of Flame Structure on the Flame Transfer Function in a Premixed Gas Turbine Combustor. *Journal of Engineering for Gas Turbines and Power*, 132:757–765. *(p. 7, 148, 158)*

Kim, K. T., Lee, J. G., Lee, H. J., Quay, B. D., and Santavicca, D. A. (2010b). Characterization of Forced Flame Response of Swirl-Stabilized Turbulent Lean-Premixed Flames in a Gas Turbine Combustor. *Journal of Engineering for Gas Turbines and Power*, 132(4):041502. *(p. 148)*

Kim, K. T. and Santavicca, D. A. (2013a). Generalization of Turbulent Swirl Flame Transfer Functions in Gas Turbine Combustors. *Combustion Science and Technology*, 185(7):999–1015. *(p. 149, 150, 152, 155)*

Kim, K. T. and Santavicca, D. A. (2013b). Interference mechanisms of acoustic / convective disturbances in a swirl-stabilized lean-premixed combustor. *Combustion and Flame*, 160(8):1441–1457. *(p. 148, 150, 163)*

Komarek, T. and Polifke, W. (2010). Impact of Swirl Fluctuations on the Flame Response of a Perfectly Premixed Swirl Burner. *Journal of Engineering for Gas Turbines and Power*, 132(June 2010). *(p. 7, 15, 16, 17, 20, 98, 136, 148, 158, 159, 163)*

Kulsheimer, C. and Buchner, H. (2002). Combustion Dynamics of Turbulent Swirling Flames. *COMBUSTION AND FLAME*, 131:70–84. *(p. 7, 148, 150, 158)*

Laera, D., Schuller, T., Prieur, K., Durox, D., Camporeale, S. M., and Candel, S. (2017). Flame Describing Function analysis of spinning and standing modes in an annular combustor and comparison with experiments. *Combustion and Flame*, 184:136–152. *(p. 7)*

Lee, J. G. and Santavicca, D. A. (2003). Experimental Diagnostics for the Study of Combustion Instabilities in Lean Premixed Combustors. *Journal of Propulsion and Power*, 19(5):735–750. *(p. 9)*

Lieuwen, T. C. and Yang, V., editors (2005). *Combustion Instabilities In Gas Turbine Engines: Operational Experience, Fundamental Mechanisms, and Modeling*. American Institute of Aeronautics and Astronautics, Inc. *(p. 5, 6)*

Lieuwen, T. C. and Zinn, B. T. (2005). Combustion Instabilities: Basic Con-

cepts. In Lieuwen, T. C. and Yang, V., editors, *Combustion Instabilities in Gas Turbine Engines*, chapter 1, pages 3–24. American Institute of Aeronautics and Astronautics. *(p. 5, 9, 158)*

Lucca-Negro, O. and O'Doherty, T. (2001). Vortex breakdown: A review. *Progress in Energy and Combustion Science*, 27(4):431–481. *(p. 3, 75)*

McManus, K. R., Poinsot, T., and Candel, S. M. (1993). A review of active control of combustion instabilities. *Progress in Energy and Combustion Science*, 19(1):1–29. *(p. 6)*

Mercier, R., Guiberti, T. F., Chatelier, A., Durox, D., Gicquel, O., Darabiha, N., Schuller, T., and Fiorina, B. (2016). Experimental and numerical investigation of the influence of thermal boundary conditions on premixed swirling flame stabilization. *Combustion and Flame*, 171:42–58. *(p. 64, 85)*

Merk, H. J. (1957). An analysis of unstable combustion of premixed gases. *Symposium (International) on Combustion*, 6(1):500–512. *(p. 147)*

Merk, M. (2018). *No Title*. PhD thesis. *(p. 31, 62, 68)*

Merk, M., Gaudron, R., Silva, C., Gatti, M., Mirat, C., Schuller, T., and Polifke, W. (2018a). Prediction of combustion noise of an enclosed flame by simultaneous identification of noise source and flame dynamics. *Proceedings of the Combustion Institute*. *(p. 7)*

Merk, M., Polifke, W., Gaudron, R., Gatti, M., Mirat, C., and Schuller, T. (2018b). Measurement and Simulation of Combustion Noise and Dynamics of a Confined Swirl Flame. *AIAA Journal*, 56(5):1930–1942. *(p. 88)*

Mirat, C. (2015). *Analyse des instabilites de combustion dans des foyers de centrale thermique fonctionnant au fioul lourd*. PhD thesis. *(p. 49, 50)*

Moureau, V., Lartigue, G., Sommerer, Y., Angelberger, C., Colin, O., and Poinsot, T. (2005). Numerical methods for unsteady compressible multi-component reacting flows on fixed and moving grids. *Journal of Computational Physics*, 202(2):710–736. *(p. 59)*

Nicoud, F., Benoit, L., Sensiau, C., and Poinsot, T. (2007). Acoustic Modes in Combustors with Complex Impedances and Multidimensional Active Flames. *AIAA Journal*, 45(2):426–441. *(p. 7)*

Nicoud, F. and Poinsot, T. (2005). Thermoacoustic instabilities: Should the Rayleigh criterion be extended to include entropy changes? *Combustion and Flame*, 142(1):153–159. *(p. 6)*

Nicoud, F., Toda, H. B., Cabrit, O., Bose, S., and Lee, J. (2011). Using singular values to build a subgrid-scale model for large eddy simulations. *Physics of Fluids*, 23(8). *(p. 64)*

Noiray, N., Durox, D., Schuller, T., and Candel, S. (2008). A unified framework for nonlinear combustion instability analysis based on the flame describing function. *J. Fluid. Mech.*, 615:139–167. *(p. 7, 8, 96)*

Oberleithner, K., Schimek, S., and Paschereit, C. O. (2015). Shear flow instabilities in swirl-stabilized combustors and their impact on the amplitude dependent flame response: A linear stability analysis. *Combustion and*

Flame, 162(1):86–99. *(p. 9, 12, 13, 14, 125, 150, 158)*

Oefelein, J. C. and Yang, V. (1993). Comprehensive Review of Liquid-Propellant Combustion Instabilities in F-1 Engines. *Journal of Propulsion and Power*, 9(5):657–677. *(p. 7)*

Palies, P. (2010). *Dynamique et instabilites de combustion des flammes swirlees*. PhD thesis, Ecole Centrale Paris. *(p. 37)*

Palies, P., Durox, D., Schuller, T., and Candel, S. (2010a). Swirling flame dynamics and describing function. In *48th AIAA Aerospace Sciences Meeting Including the New Horizons Forum and Aerospace Exposition*, Orlando. *(p. 8, 98, 114, 119, 136)*

Palies, P., Durox, D., Schuller, T., and Candel, S. (2010b). The combined dynamics of swirler and turbulent premixed swirling flames. *Combustion and Flame*, 157(9):1698–1717. *(p. 17, 18, 19, 20, 47, 148, 150, 158, 159, 163)*

Palies, P., Durox, D., Schuller, T., and Candel, S. (2011a). Acoustic-convective mode conversion in an aerofoil cascade. *Journal of Fluid Mechanics*, 672:545–569. *(p. 15, 134, 136, 148, 163)*

Palies, P., Durox, D., Schuller, T., and Candel, S. (2011b). Experimental study on the effect of swirler geometry and swirl number on flame describing functions. *Combustion Science and Technology*, 183(7):704–717. *(p. 96, 148, 158)*

Palies, P., Durox, D., Schuller, T., and Candel, S. (2011c). Nonlinear combustion instability analysis based on the flame describing function applied to turbulent premixed swirling flames. *Combustion and Flame*, 158(10):1980–1991. *(p. 12)*

Palies, P., Schuller, T., Durox, D., and Candel, S. (2011d). Modeling of premixed swirling flames transfer functions. *Proceedings of the Combustion Institute*, 33(2):2967–2974. *(p. 7, 17, 114, 119, 148, 158, 163)*

Palies, P., Schuller, T., Durox, D., Gicquel, L. Y., and Candel, S. (2011e). Acoustically perturbed turbulent premixed swirling flames. *Physics of Fluids*, 23(3):037101. *(p. 17, 18, 114, 119, 121, 125, 136, 148, 150, 158, 170)*

Poinsot, T. (2017). Prediction and control of combustion instabilities in real engines. *Proceedings of the Combustion Institute*, 36(1):1–28. *(p. 5, 158)*

Poinsot, T. and Veynante, D. (2005). *Theoretical and Numerical Combustion, 2/E*. R.T. Edwards, Inc. *(p. 5, 59, 60)*

Poinsot, T. J. and Lele, S. K. (1992). Boundary conditions for direct simulations of compressible viscous flows. *Journal of Computational Physics*, 101(1):104–129. *(p. 62)*

Poularikas, A. D. (2010). *Transforms and Applications Handbook*. CRC Press, Inc, 3rd edition. *(p. 56)*

Prasad, A. and Williamson, C. H. K. (1997). The insability of the shear layer separating from a bluff body. *Journal of Fluid Mechanics*, 333:375–402. *(p. 131)*

Providakis, T. (2011). *Compétition entre structures aérodynamiques et modes acoustiques dans une flamme swirlée : Influence de la répartition de carburant*. PhD thesis, Ecole Centrale Paris. *(p. 49)*

Raffel, M., Willert, C. E., Wereley, S. T., and Kompenhans, J. (2007). *Particle Image Velocimetry, a practical guide*. Springer-Verlag Berlin Heidelberg. *(p. 51, 53)*

Rayleigh, J. (1878). The explanation of certain acoustical phenomena. *Nature*, 18(455):319–321. *(p. 6)*

Sattelmayer, T. and Polifke, W. (2003). Assessment of methods for the computation of the linear stability of combustors. *Combustion Science and Technology*, 175(3):453–476. *(p. 7)*

Schimek, S., Moeck, J., and Paschereit, C. (2011). Experimental investigation of the influence of high amplitude forcing and swirl fluctuations on the flow field and the transfer function of a swirl-stabilized flame. In *47th AIAA/ASME/SAE/ASEE Joint Propulsion Conference & Exhibit*, number August, San Diego. *(p. 12, 13)*

Schönfeld, T. and Rudgyard, M. (1999). Steady and Unsteady Flow Simulations Using the Hybrid Flow Solver AVBP. *AIAA Journal*, 37(11):1378–1385. *(p. 59)*

Schuermans, B., Guethe, F., Pennell, D., Guyot, D., and Paschereit, C. O. (2010). Thermoacoustic Modeling of a Gas Turbine Using Transfer Functions Measured Under Full Engine Pressure. *Journal of Engineering for Gas Turbines and Power*, 132(11):111503. *(p. 158)*

Schuller, T., Durox, D., and Candel, S. (2002). Dynamics of and noise radiated by a perturbed impinging premixed jet flame. *Combustion and Flame*, 128(1):88–110. *(p. 7)*

Schuller, T., Durox, D., and Candel, S. (2003). A unified model for the prediction of laminar flame transfer functions: comparisons between conical and V-flame dynamics. *Combustion and Flame*, 134(1-2):21–34. *(p. 8, 9, 107, 147, 162)*

Selle, L., Nicoud, F., and Poinsot, T. (2004). Actual Impedance of Nonreflecting Boundary Conditions: Implications for Computation of Resonators. *AIAA Journal*, 42(5):958–964. *(p. 62, 130)*

Sengissen, A. X., Van Kampen, J. F., Huls, R. A., Stoffels, G. G., Kok, J. B., and Poinsot, T. J. (2007). LES and experimental studies of cold and reacting flow in a swirled partially premixed burner with and without fuel modulation. *Combustion and Flame*, 150(1-2):40–53. *(p. 59)*

Straub, D. L. and Richards, G. A. (1999). Effect of axial swirl vane location on combustion dynamics. In *International Gas Turbine and Aeroengine Congress and Exhibition, Paper 99-GT-109*. ASME. *(p. 148)*

Syred, N. (2006). A review of oscillation mechanisms and the role of the precessing vortex core (PVC) in swirl combustion systems. *Progress in Energy and Combustion Science*, 32:93–161. *(p. 4)*

Tay Wo Chong, L., Kaess, R., Komarek, T., Foller, S., and Polifke, W.

(2010). Identification of Flame Transfer Functions Using LES of Turbulent Reacting Flows. In *ASME Turbo Expo 2010*, number GT2010-22769, pages 623–635. ASME. *(p. 158)*

Thumuluru, S. K. and Lieuwen, T. (2009). Characterization of acoustically forced swirl flame dynamics. *Proceedings of the Combustion Institute*, 32(2):2893–2900. *(p. 125, 158)*

Wang, S. and Yang, V. (2005). Unsteady flow evolution in swirl injectors with radial entry . II . External excitations. *Physics of Fluid*, 17. *(p. 150)*

ÉCOLE DOCTORALE
Sciences mécaniques et énergétiques, matériaux et géosciences (SMEMAG)

Titre: Dynamique de la combustion des flammes de prémélange swirlées avec des différentes conditions d'injection

Résumé: Les systèmes de combustion à prémélange pauvre (PP) sont l'une des technologies les mieux adaptées pour la réduction des émissions de polluants, mais ils sont très sensibles aux phénomènes d'extinction, aux retours de flamme (flashback) dans l'injecteur et aux instabilités de combustion. La plupart des chambres de combustion des turbines à gaz utilisent de swirleurs pour stabiliser des flammes compactes et permettre une combustion efficace et propre avec des densités de puissance élevée. Une meilleure connaissance des mécanismes de la dynamique de la combustion d'écoulements swirlés PP présente un intérêt aussi bien pratique que fondamental. Ce travail est une contribution pour atteindre ce but. Le brûleur Noisedyn, avec une geometrie modifiable, a été spécialement conçu pour répondre à cet objectif. Une analyse expérimentale a etait conduite pour examiner les paramètres qui reduisent la sensibilité des systèmes PP aux phénomènes dynamiques. Mesures de fonction de transfert de flamme (FTF), diagnostiques laser (LDV et PIV) et imagerie des flammes sont les principaux techniques utilisé dans ce travail. Large eddy simulation sont aussi utilisé pour expliquer les mécanismes derrière les observations experimentaux.

Title: Combustion dynamics of premixed swirling flames with different injection conditions

Abstract: Lean premixed (LPM) combustion systems achieve low pollutant emission levels, with compact flames and high power densities, but are highly sensitive to dynamic phenomena, e.g, flashback, blowout and thermoacoustic instabilities, that hinder their practical application. Most LPM gas turbine combustors use swirling flows to stabilize compact flames for efficient and clean combustion. A better knowledge of the mechanisms of steady and unsteady combustion of lean premixed swirled mixtures is then of practical, as well as fundamental interest. This thesis is a contribute towards the achievement of this goal. A burner, made of several components with variable geometry, was specifically designed for this scope. An experimental analysis was conducted to investigate the main parameters leading to a reduction of the sensitivity of LPM systems to dynamic phenomena. The diagnostics applied include flame transfer function (FTF) measurements, laser diagnostics (LDV and PIV) and flame imaging. Large eddy simulations were also exploited to elucidate the mechanisms behind the experimental observations.